Maintaining Functionality of Biological Materials during Fluid–based Manufacturing

Susannah Elizabeth Evans

Department of Engineering

University of Cambridge

This dissertation is submitted for the degree of

Doctor of Philosophy

Churchill College

March 2021

To my parents, Liz and Richard

Declaration

I hereby declare that except where specific reference is made to the work of others, the contents of this dissertation are original and have not been submitted in whole or in part for consideration for any other degree or qualification in this, or any other University. This dissertation is the result of my own work and includes nothing which is the outcome of work done in collaboration, except where specifically indicated in the text. This dissertation contains less than 65,000 words including appendices, bibliography, footnotes, tables and equations and has less than 150 figures.

Susannah Elizabeth Evans

March 2021

Acknowledgements

Firstly, I would like to thank my supervisor Ronan Daly for his guidance and support throughout this PhD process. Your encouragement and feedback have been valuable, and I am sincerely grateful. It has been a pleasure to work alongside you these past few years and to be a member of the FIAM research group. This work would not have been possible without you and the funding from EPSRC.

Within the FIAM research group I am particularly grateful for help from Niamh, Etienne, Cristina and Cassi who have also imparted much of their wisdom with me and have assisted in furthering my research. I will also treasure all the random conversations we had over coffee in the common room with members of the nanomanufacturing group, Chris, Kate, Maxime, Sammy, Charlie, Sarah and Davor. I have made some great friends from the IfM who have made me feel so at home. The reception wouldn't be the same without Sharn, I have loved all of our chats, your honesty and mischievousness are the best, don't ever change. The adventures paddle boarding, kayaking, climbing and festivaling with James have been a highlight. Also, the unforgettable times with Niamh and Chris who have the profound ability to escalate a casual after work on Friday pub trip into a vow to never drink again on Saturday morning. And I can't forget all those virtual moments laughing at glitches and poor graphics with Kate.

Outside the IfM, when it was still possible, I was welcomed into an amazing gymnastics community, first meeting Nathan who made even putting the horse away exciting and Jasmin for always being there for me through ups and downs. I am so grateful for your friendship Jasmin, showing me Cambridge through a

local's eyes, always up for a spontaneous night and averting disaster for me when I forget my keys.

Although these people may not be in Cambridge, I am eternally thankful to my family, my parents for raising me and helping me get to where I am today. I don't think any words can serve justice to fully articulate how amazing all that you have done for me is. I am grateful to my siblings, Max and Frances for keeping me grounded by taking the piss out of me just the right amount. My school friends Becky, Izzy, Laura and Nina for only ever being a text or phone call away and the beauty of picking up right where we left off when we are reunited. Hannah for being an inspiration to me in getting your PhD so young and Olivia for helping me retain some sense of normality walking in Sale Water Park.

An extra special shout out goes to Will, impressing me every day with how much you have achieved yet how humble and modest you are. Despite how hard working you are, you always have time for me, whether it be debating, giving advice, or playing games, I appreciate you so much. Although we are on separate continents, I'd also like to mention Maté, your stubbornness is endearing and arguing with you can be beyond frustrating but also a lot of fun.

People come and go in life, yet despite our paths no longer crossing I can't forget Martí for the times we shared together, whether bartending in the MCR or teaching me how to program, I am grateful for them all. You taught me a lot about just living life and that I really should just relax.

Abstract

Drop on demand inkjet printing and extrusion–based printing enable 2D and 3D structures to be produced with high spacial resolution, highly applicable for the pharmaceutical industry where constructs can be used for tissue engineering, drug discovery and drug delivery applications. However, both of these fluid–based manufacturing techniques impart extensive shear forces to the ink during processing. When inks contain functional materials such as proteins, these forces are reported to be large enough to disrupt the resulting structure and activity of the ink after printing. Yet the precise cause of this damage is poorly understood and factors such as adsorption and drying can be conflated with observations of activity loss.

This research aims to build a better understanding of the impact inkjet printing and extrusion have on the ink and functional material being printed. For inkjet systems, the elements of the printing process, ink formulation, ancillary equipment, printhead choice, nozzle flow, droplet formation and drying are examined in isolation. Techniques that are more controlled than previously reported are used to determine protein activity losses for each element to assess the contribution from each stage of printing. With this knowledge, strategies to retain protein activity are then investigated, particularly focusing on ink formulation and the losses due to drying and adsorption. A similar approach is taken to examine the damage the extrusion process causes to collagen gels separating the manufacture of the gel and its subsequent processing.

Overall, this work has determined for the enzyme systems studied, adsorption and drying are the reasons inkjet printed enzymes have been observed to lose activity through separating out and controlling each element of the inkjet

printing process. Methods to print without activity losses have been achieved through formulating inks with sugars and coating printheads with a sacrificial protein to prevent adsorption. A quality control technique using piezo axial vibration rheometry has also been validated for extrusion–based printing, to assess the damage to hydrogel–based inks during manufacture and printing, demonstrated with collagen gels. The forces endured during extrusion have also been mapped out with a simulation. These results pave the way forward for more extensive industrial adoption of inkjet and extrusion–based printing.

Contents

List of Figures

List of Tables

Nomenclature

ABTS	2, 2'–Azino–Bis–3–Ethylbenzothiazoline–6–Sulfonic Acid
BSA	Bovine Serum Albumin
CIJ	Continuous Inkjet Printing
CMC	Carboxymethyl cellulose
DMP	Dimatix Materials Printer
DoD	Drop–on–demand
Dpi	Dots per inch
EBB	Extrusion based bioprinting
ECM	Extra cellular matrix
FPS	Frames per second
G’	Storage Modulus
G”	Loss Modulus
GFP	Green fluorescent protein
GOx	Glucose Oxidase
HDMS	Hexamethyldisilazone solution
HRP	Horse Radish Peroxidase (type VI)
IJ	Inkjet

LVE	Linear Viscoelastic Region
MEM	Minimum Essential Media
MF	Microfab
NP	Nanoparticle
PAV	Piezo Axial Vibrator
PEG	Polyethylene glycol
PCC	Phantom Camera Control
PMMA	Poly(methyl methacrylate)
PTFE	Polytetrafluoroethylene
PVA	Poly(vinyl alcohol)
SOx	Sarcosine Oxidase
SEM	Scanning Electron Microscope
TIJ	Thermal Inkjet Printing

Symbols

A	Area (m^2)
ω	Angular Frequency (rad/s)
d	Characteristic length of a print system (m)
μ	Viscosity (Pa s)
η^*	Complex viscosity (Pa s)
g	Standard gravitational acceleration (m/s^2)
G'	Storage Modulus (Pa)
G''	Loss Modulus (Pa)
ρ	Density (kg/m^3)
v	Velocity (m/s)
$\dot{Q}$	Flow rate (ml/hour)
ε	Molar excitation coefficient (L/mol cm)
l	Cuvette path length (cm)
γ'	Shear rate (1/s)
γ	Surface tension (N/m)

Chapter 1 Introduction

Fluid based manufacturing covers a broad range of techniques including inkjet printing, 3D printing, electrohydrodynamic printing and hot melt extrusion. It is a term that encompasses all manufacturing techniques that handle material in a liquid or gel phase. The techniques of particular interest in this thesis are drop on demand inkjet printing and extrusion based bioprinting.

Inkjet printing is a rapid, non–contact technique that can precisely and reliably generate picolitre scale droplets. A single input signal results in a single droplet being produced and sent towards a surface. Controlled droplet deposition is desirable for many applications including bioprinting, where inks consist of a combination of cells, enzymes, structural proteins and gels; and the pharmaceuticals industry, where inks are printed in applications ranging from drug discovery through to drug delivery and continuous manufacturing. Extrusion based bioprinting utilises the same technology seen in polymer and metal processing, but for biological and pharmaceutical applications the ink is typically made up of hydrogels, polymers or extracellular matrix–based materials. Extrusion of gels is gaining increasing popularity within tissue engineering where the technology is often referred to as direct–write. 3D structures can be produced by forcing the ink through a nozzle and controlling the location of deposition onto a surface or previously deposited material within the x, y and z directions.

When inks contain functional materials, such as proteins or cells, there are concerns that these delicate materials can be detrimentally affected by these printing processes. An inkjet system imparts large stresses and strains to the

working fluid due to the pressure variation within the printhead for droplet generation and the elongating flow upon droplet ejection. The shear rate is typically of the order of 100,000 s^{-1} [1] and the droplet can be ejected at speeds up to 10ms^{-1} for a drop–on–demand printer [2],[3]. The severity of these forces have previously been cited as the reason enzymes lose activity in studies focusing on inkjet printing [4], [5] and within the wider literature, generally examining the effect shear has upon protein structure and function [6]. Concurrently, the ink is exposed to a variety of interfaces within the print head, ancillary equipment or upon ejection and impact with the surface being printed onto. Research has also indicated that exposing proteins to air interfaces or different materials can result in an observed drop in activity [7], [8]. Therefore, attributing an activity loss to a single factor during inkjet printing, whether it be due to forces or interfaces, seems to be simplifying the problem of observed protein activity loss after inkjet printing when there are clearly multiple contributing factors. To build a better understanding of the observed protein activity losses after inkjet printing, it is vital that each factor that could contribute to an activity loss is isolated and rigorously controlled. This must include examination of the ink formulation and ancillary equipment through to droplet formation, deposition and drying. This research will break down each of these considerations and assess the relative magnitude of each contributing factor to activity losses seen after inkjet printing of protein–based inks. This is critical for transitioning towards more commercial and industrial pharmaceutical applications of inkjet in the future, where a greater understanding of the inkjet printing process is essential.

Research examining extrusion based bioprinting has reported similar concerns to inkjet printing when inks contain functional materials, although the focus of research in this space has been around the resulting post–printing cell viability [9] and improving the printability of extruded inks [10]. Hydrogels are often used for extrusion based bioprinting due to their high water content and resemblance to the extracellular matrix seen *in vivo.* Hydrogels formulated with the structural

protein collagen are increasingly being used due to its low immunogenicity for use *in vivo* and abundance in nature. Extrusion based bioprinting imparts shear rates in the order of magnitude of 100 – 1000s^{-1} to the ink and is dependent upon the fluid flow rate and nozzle geometry [11]. These forces have been shown to be sufficient to damage hydrogels [12], this is particularly important for hydrogel formulations containing structural proteins, such as collagen, where shear rates as low as 8.3s^{-1} have an observable effect on collagen fibre alignment [13]. Before hydrogels are seeded with cells for a specific application, it is important to understand the impact extrusion–based printing has on the gel itself prior to considering the effect on cells. This research will therefore approach the manufacture of collagen–based gels and processing of the gel separately to understand how each of these elements affects the resulting mechanical properties of the gel. This is important because changes to the mechanical properties of gels used to replicate the extracellular matrix influence cell behaviour.

This thesis starts with a literature review of inkjet printing and extrusion–based printing to provide a background into their operating mechanisms, applications, challenges with using these manufacturing techniques and an insight into future trends in applications of these technologies. This chapter will highlight the research gaps seen within the literature that will be addressed in subsequent chapters of this thesis. Chapter 3 details the experimental setup and material used. Chapters 4 to 7 inclusive present results from research conducted towards answering the research questions set out at the end of chapter 2 presenting notable results with discussion and analysis. To conclude with, chapter 8 summarises the main findings in this thesis and provides suggestions for future research that could be conducted.

Chapter 2 Background and Literature Review

2.1 Fluid Based Manufacturing Techniques

Fluid based manufacturing is an umbrella term that captures all technologies that handle materials in a liquid or gel phase. It is used extensively across many industries and is of significant interest within the pharmaceutical industry. Fluid based manufacturing techniques are used from drug discover through to applications for the end user such as needle–free injections with continuous manufacturing and direct fabrication of tablets and medical devices in–between [14]. A general trend in the healthcare sector is to move away from a one size fits all approach towards personalised and precision medicine, which is projected to have a market value of $194.4 billion by 2024 from an estimated $92.4 billion in 2017 [15]. Fluid based manufacturing is an enabling technology that will allow the healthcare sector to move in this direction. Inkjet printing and extrusion are gaining increasing interest in the field of personalised medicine as demonstrated by the increase in publications on these topics year on year as shown in

Figure 2.1.

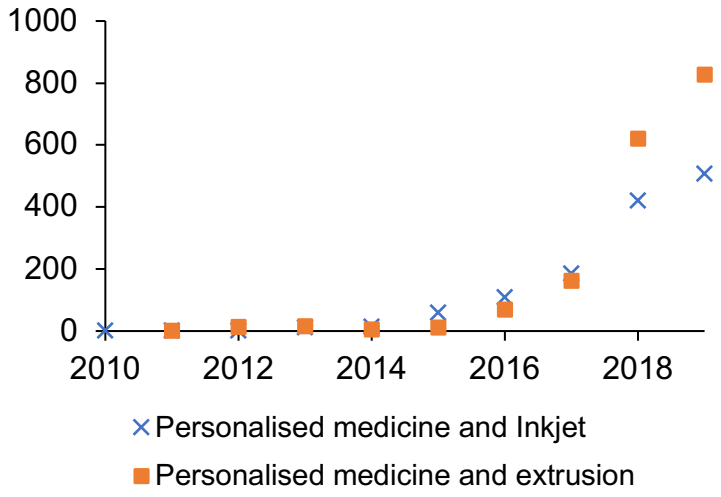

Figure 2.1: Citations on the topics of personalised medicine and inkjet/extrusion [16].

In contrast, research on bioprinting, defined as producing three dimensional constructs that incorporate living cells to form tissues and organs, has gained even more interest, evidenced in Figure 2.2.

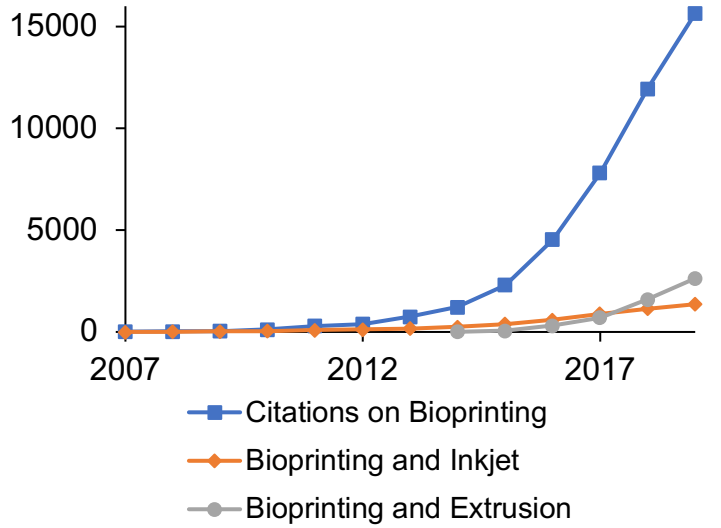

Figure 2.2: The number of citations on the topics of bioprinting and within this field, the topics of inkjet and extrusion [16].

Because of the interest in inkjet and extrusion, this thesis will focus on their application for using biological materials. In this section the mechanisms of inkjet (IJ) printing techniques and pneumatic extrusion will be presented along with print systems that are used at the lab scale and commercially at an industrial scale.

2.1.1 Inkjet Printing Overview

Inkjet printing is a non–contact additive manufacturing process where fluids are dispensed dropwise onto a surface from a small distance referred to as the stand–off height, typically around 1mm [2]. The technology, developed commercially in the 1970s and 80s, is already extensively used in small and home offices, printing ticketing, signage, banners, ceramic tiles, and printing onto textiles. Droplets are formed and ejected through any of a wide range of actuation techniques, an overview of which is provided in Figure 2.3. Continuous inkjet printing (CIJ) and the two most common drop–on–demand (DoD) mechanisms, thermal and piezoelectric actuation will be presented in this section. These two broad categories, CIJ and DoD, refer to the control that the actuator has over a droplet generating event. In summary, CIJ, a continuous stream of droplets is generated and the printhead is designed to select which of these droplets is sent to the surface, with the remaining being recycled back to the ink reservoir. For DoD, a single droplet is produced for each actuation event and sent to the surface. More detail on droplet generation will be given in 2.1.1.1 and 2.1.1.2, to aid in the identification of forces experienced by functional components in the inks in later sections.

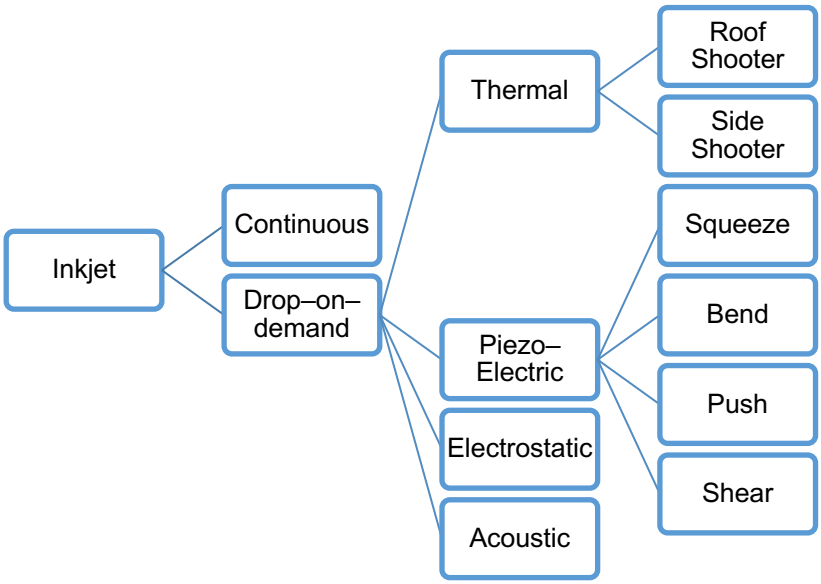

Figure 2.3: A breakdown of the different subcategories of inkjet printing, adapted from [17].

Research and development of inkjet printing technology is ongoing and the capabilities of standard inkjet technology in 2018 compared to its projected capabilities going into 2023 and beyond is shown in Table 2.1.

Table 2.1: A summary of the capabilities of industrial inkjet systems in 2018 compared to projected capabilities in 2023, adapted from [18].

	2018 status	2023 projection
Print quality	Equivalent to good flexographic printing and typical lithography processing.	Equivalent to sheetfed. Indistinguishable from litho, gravure and very good flexographic.
Printheads	1200 dpi at 200m per minute speed. Some printheads on robot arms.	1200 dpi at 300m per minute. Higher reliability and direct–to–shape printing capability.
Inks	Solvent, aqueous, UV curable with LED curing growing. Electron beam curing introduced and hybrid inks. However, inks are expensive.	Less solvents, more water based. Ink prices are becoming more economic.
Applications	Varnishes, coatings, packaging. Direct to shape printing growing.	New embellishments, tactile finishes. Ceramic and novel 3D printing applications growing.
Economics	Short runs	Medium and long runs, mainstream for most products.

2.1.1.1 Continuous Inkjet Printing

Continuous Inkjet (CIJ) technology was born from the Rayleigh instability theory [19]: a falling stream of fluid will break up into droplets when its wavelength is greater than the circumference and the distance between the resulting droplets formed is approximately 4.5 times the jet diameter. The pressure driving the jet is most commonly from a piezoelectric crystal that

deforms to cause ultrasonic vibrations within the printhead, and the droplets selected to reach the surface are normally sorted electrostatically. The operating principle is shown in Figure 2.4. Compared to drop–on–demand (DoD) printing, a larger stand–off height, typically 1–10cm [2] is utilised and the ink continuously circulates throughout the ink system which can result in contamination through the recycling system [20]. CIJ is a mature technology that does not achieve as high of a resolution as DoD printing and is not typically used for bioprinting due to the large volumes of ink required to be in circulation, higher droplet velocities and potential for ink contamination through recycling. Therefore, DoD systems will be examined in more detail.

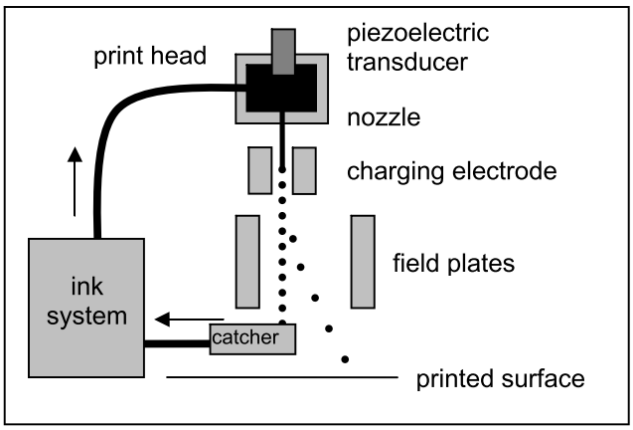

Figure 2.4: Schematic of a typical piezoelectric continuous inkjet printing system [3].

2.1.1.2 Drop–on–demand Inkjet Printing

The two most common actuation methods for DoD printing are thermal and piezoelectric, as shown in Figure 2.3. Each mechanism of droplet generation will be presented in this section.

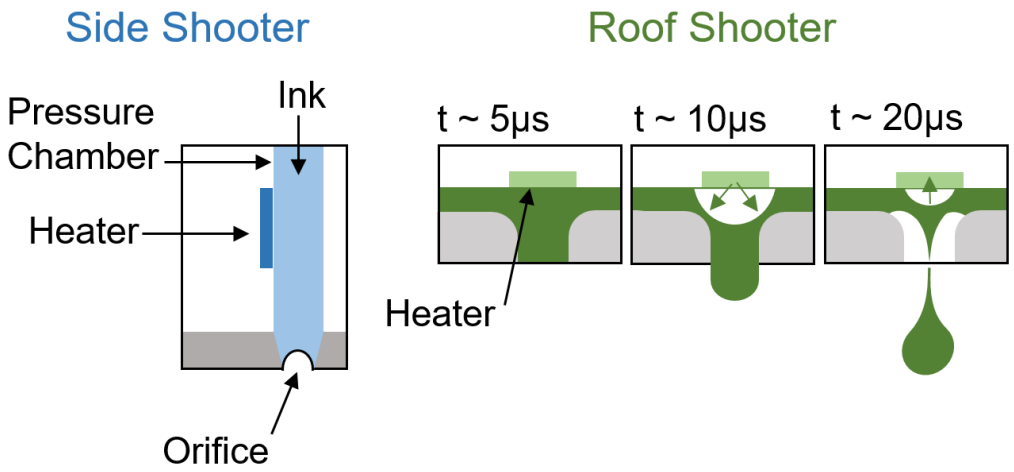

Figure 2.5 shows the location of the resistive heating element on TIJ and the mechanism of droplet formation from a roof shooter, adapted from [17].

The mechanism of Thermal Inkjet Printing (TIJ) is illustrated in Figure 2.5. A resistive heating element, located perpendicular to the orifice in the case of a side shooter, and directly above the orifice for a roof shooter, superheats the ink to temperatures up to 400°C in less than 10µs [21]. This increase in temperature is minimal as the short duration at the elevated temperature only causes the temperature of the printhead to rise by $4 - 10^0$C [22]. The rapid heating, triggered by an input electrical signal, causes a bubble to form increasing the pressure in the chamber. The propagation of this pressure wave through the ink results in droplet ejection. This cyclic heating is associated with degradation of the heating element by adherence of ink residue to the heater surface and thermally induced degradation of the heater.

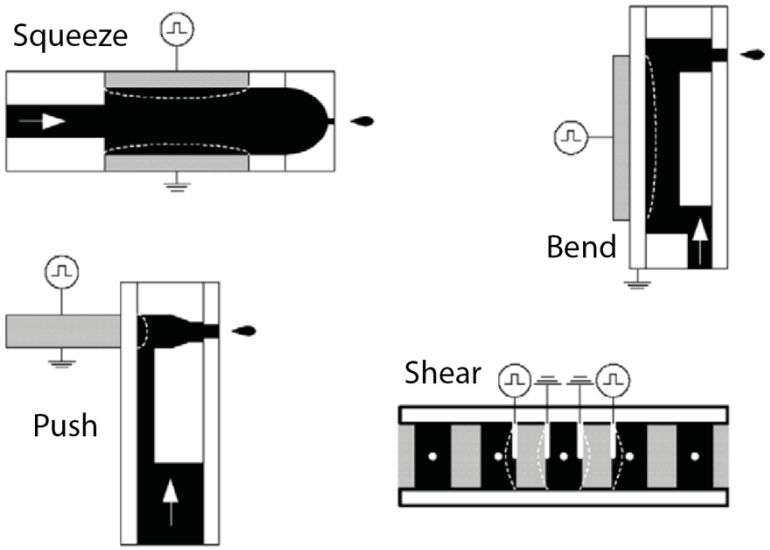

Figure 2.6: the different locations of the piezoelectric actuator for PIJ. Adapted from [23].

Piezoelectric actuation differs to TIJ as the ink meniscus at the orifice is initially drawn into the ink chamber as a voltage is applied to the piezoelectric element, causing a decrease in pressure in the chamber as the chamber volume increases. The piezo electric element is then discharged causing it to reduce the chamber volume. At the same time, the negative pressure wave is reflected causing a positive pressure wave to propagate through the ink reservoir. The synchronisation of the piezoelectric discharge and propagation of the positive pressure wave amplifies the increase in pressure ejecting a droplet from the orifice. The location of the piezoelectric element varies with different printhead designs as shown in Figure 2.6. Piezoelectric actuation is more durable than TIJ but TIJ can offer a greater nozzle packing density than PIJ as the actuator is more compact and is often cheaper.

2.1.2 Printability of DoD Inkjet Print Systems

There are many print systems that are commercially available for research applications and for industrial scale manufacturing. All IJ print systems have limitations on the properties of the fluid that can be processed and dispensed in

a suitable manner. The term printability is used when assessing the properties of the ink when predicting how suitable the formulation is for a given print system.

Printability is often described by the two dimensionless groups [24]: the Reynolds number, Re, and Ohnesorge number, Oh, which are defined as:

$$Re = \frac{\rho v d}{\mu} = \frac{inertial\ forces}{viscous\ forces} \quad 2.1$$

ρ is the density, v is the droplet velocity and d is a characteristic length of the print system, typically the orifice diameter. The Reynolds number represents the amount of energy required to form a droplet based on the size of the nozzle orifice and properties of the working fluid.

$$Oh = \frac{\mu}{\sqrt{\gamma \rho d}} = \frac{viscous\ forces}{\sqrt{surface\ tension \times inertial\ forces}} \quad 2.2$$

The Ohnesorge number represents the ability of a droplet to form based solely on the physical properties of the printing system, neglecting the energy input to the printing system.

The surface tension, γ, defined as the change in free energy when the surface area of a material is increased by one unit [25] and dynamic viscosity, μ, defined as the internal resistance of a fluid play a vital role in determining whether an ink will be printable.

Figure 2.7 shows widely accepted printability guidelines, however it must be stressed that the capabilities of inkjet printing often extend beyond the limits shown as demonstrated by studies that have printed water, which has Oh~0.012 [26].

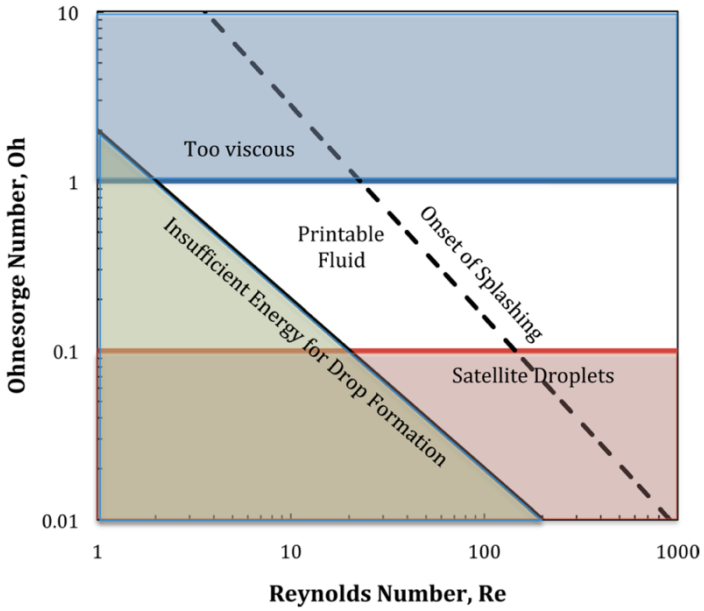

Figure 2.7 shows the region within which fluids are considered to be printable based on values of the dimensionless groups the Reynolds and Ohnesorge number [24].

However, these guidelines are also in place for optimising a print so that the droplets formed do not generate satellite droplets as shown in Figure 2.9. A satellite droplet is formed when the tail of a jet breaks up and not all the tail goes on to form the main droplet, instead multiple or single smaller droplets are also formed during the break–up process. The guidelines also ensure that droplets are of a desirable morphology, for instance double droplets do not form or the tail of the droplet does not curl at the end, known as tail hooking. The droplets should also not splash upon impact with the surface and the printing apparatus is consistently ejecting the same volume of fluid.

Further studies have considered the dimensionless Weber number, We, which considers the relationship between the inertia of a fluid and its surface tension.

$$We = \frac{\rho v^2 d}{\gamma} \qquad 2.3$$

More recent research has re–examined the region considered to be printable and defined it in terms of the Weber number and Z number, the inverse of the

Ohnesorge number. The printable region has been expanded to 0.3 < Z < 700, equivalent to 0.0014 < Oh < 3.33 in comparison to the range shown in Figure 2.7 and data verifies printability in this range between 1 < Z < 40 or 0.025 < Oh < 1 [27].

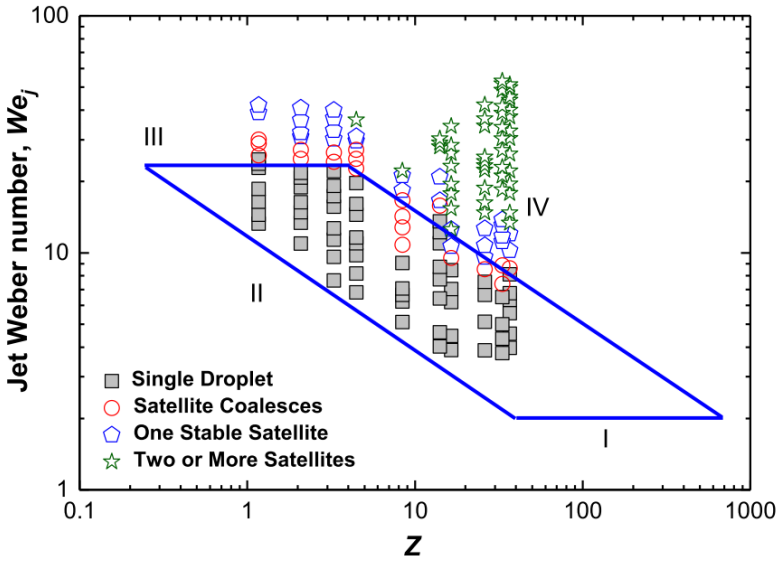

Figure 2.8 defines a region for the jetting parameters and fluid properties to be able to produce a stable single droplet during inkjet printing using the inverse of the Ohnesorge number and the Weber number [27].

To improve the printability of an ink, surfactants and viscosity modifiers are used to decrease the surface tension and increase viscosity. Surfactants will also change the spreading of a droplet on the surface it is ejected onto. Typically a surfactant will be added to an ink formulation to improve wetting, dispersion / emulsification or to preventing foaming of the ink [28], Table 2.2 provides information on different groups of surfactant that can be used for ink formulation.

Table 2.2: Examples of groups of surfactants that can be used for ink formulations, adapted from [28].

Function	Appropriate Group of Surfactants
Wetting	Acetylenic surfactants, fluorinated surfactants, fatty acids, fatty alcohols, fatty esters, fatty amines, ethylene or propylene oxide block copolymers
Dispersion	Anionic: sodium alkyl sulphates, potassium N–methyl–N–oleoyl, sodium dodecyl benzene sulphonate Cationic: dialkyl benzenealkyl ammonium chloride, cetyl pyridinium bromide, halide salts of quaternized polyoxyethylalkylamines Non–ionic: polyvinyl alcohol, carboxy methyl cellulose, polyacryl amide
Defoaming	Silicon compounds, organic esters in mineral oil base, ethylene or propylene oxide block copolymers

Commonly used surfactants in bioprinting include polysorbate 20 ($C_{58}H_{114}O_{26}$), sold under the trade name tween 20 [29], and triton X–100 ($C_{14}H_{22}O(C_2H_4O)n$ (n=9–10)) [30].

Long chain high molecular weight polymers such a polyethylene glycol (PEG) or sodium carboxymethyl cellulose (CMC) can be used as a viscosity modifier or glycerol, detailed in [4], which acts as humectant to reduce solvent evaporation at the nozzle tip or once the droplet has been deposited on a surface.

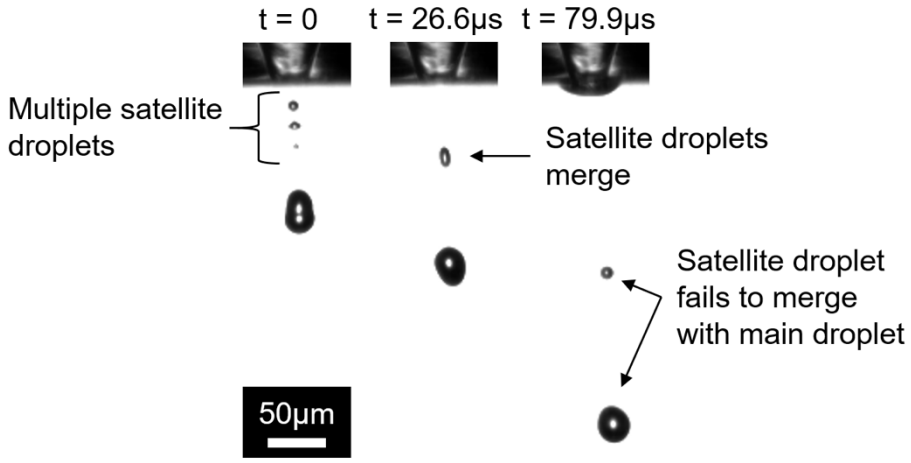

Figure 2.9: Images of HRP in PBS printed through a 30µm diameter Microfab nozzle illustrating satellite droplet formation.

2.1.2.1 Lab Scale Inkjet Systems

For lab scale systems and printheads used for research, often there is only a single nozzle or a small number of nozzles in a single row in parallel. An overview of printheads commonly used will be presented in this section and a summary of the printing capabilities of these systems, along with some industrial systems, is shown in Table 2.3. The term dots per inch (dpi) is often used as a measure for resolution and is defined as shown in 2.4.

$$dpi = \frac{25400}{drop\ spacing\ (\mu m)} \qquad 2.4$$

Table 2.3: A summary of the capabilities of different inkjet print systems.

Ref	Print System	Nozzle Diameter	Resolution	Fluid Requirements
[31]	Microfab devices (<50°C dispensing)	20–120 ± 1 µm	Setup dependent. Jetlab II up to 3µm accuracy with 1µm repeatability.	Viscosity <20 mPa s, Surface Tension 20–70mN/m, pH 2–11
[32]	DMP–2800	21µm square	Minimum drop spacing 5µm.	For optimum jetting 10–12mPa ss, 22–33mNm.
[33]	Spectra SE 128 AA	35µm	0.17˚ jet straightness. Up to 900dpi.	8 – 20 mPa s
[34]	Nova PH 256/80 AAA	52 µm	0.23˚ jet straightness.	8 – 20 mPa s

Microfab systems are used for fundamental research, typically where a single droplet is examined, DMP for prototyping and research where a larger volumetric throughput is needed and the Spectra and Nova each have >128 nozzles making them better suited for industrial applications. For each of the print systems presented in Table 2.3 the fluid requirements are all broadly within the same range. However, the ease of setting up each print system is not clear and often there is a trade–off between the ease of use of a given system compared to the tunability of the printing parameters. Often it is not clear why a specific printing system is chosen for a specific application and scale–up is not considered. Some example applications for each of the lab scale systems presented will be given but more detail on applications is presented in section 2.2.

2.1.2.1.1 Microfab Print Systems

Microfab Technologies Inc offer various printing systems intended for prototyping and research from standalone printheads to fully packaged systems. The printheads, e.g. MJ–ATP–01 or MJ–AB–01, contain the same core elements in their design. A glass tube is drawn so that the wider dimeter at the fluid inlet then tapers to the minimum orifice diameter, pictured in Figure 2.10, and the piezoelectric element is located around the circumference of the glass tube resulting in a squeeze mode actuation, detailed in Figure 2.6. The print systems are well suited for research applications because the nozzles can be integrated into custom built rigs which can image droplet generation or can be used in the pre–made packages. The Jetdrive system also enables the user to define waveforms and consequently have ultimate control over the droplet morphology.

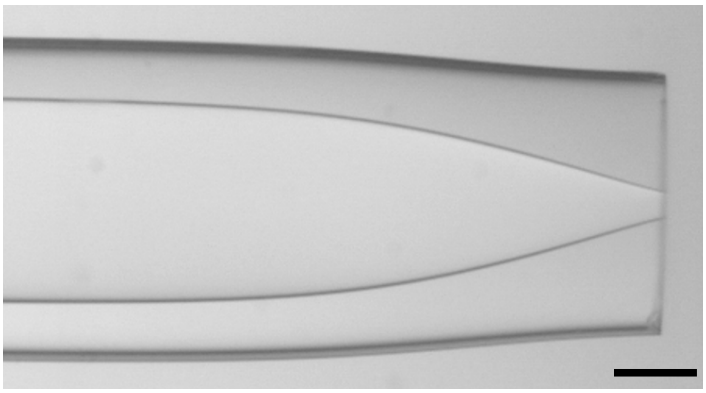

Figure 2.10: A glass tube of a Microfab printhead. The scale bar is 200µm and the nozzle tapers to a minimum diameter of 60µm.

Microfab drop–on–demand print systems have been used for different applications including reactive inkjet printing [35] [36], for the fabrication of silk nests for hosting E Coli, also deposited by IJ [37], deposition of other cells including Hep G2 hepatoma [38] and cells from the central nervous system of rats [30] and for producing oligonucleotide arrays [39]. Microfab systems have also been used for pharmaceutical applications to obtain metastable polymorphs of glycine [40].

2.1.2.1.2 Dimatix Materials Printer Systems

Fujifilm developed the Dimatix Materials Printer (DMP) Series of printers intentionally for research and prototyping. The printer enables patterning of an A4 sized substrate by a disposable piezoelectric inkjet cartridge that operates in the bend mode, shown in Figure 2.6, which has 16 nozzles in parallel that can hold up to 1.5ml of ink [32]. The printer is integrated with a camera to watch droplets forming using a strobed image capture method – images of multiple droplets captured with a micro–second scale time delay between them are built up to create a video.

The DMP cartridges have been used for a variety of applications including creating multienzyme 2D arrays of enzymes for use as logic gates [41], a functionalised silk fibroin based ink that was used for bacterial detection [42] or for tailoring the dosage of an active pharmaceutical ingredient to an individual patient [43], dispensing the poorly soluble drug piroxicam onto edible films [44] and for a study funded by GlaxoSmithKline Inc. that produced UV cured tablets containing ropinirole. Because of the DMPs flexibility and ease of use, it is used for both academic and industrial applications. The waveform can be modified, like the Microfab systems, but has slightly less flexibility as the substrate cannot be thicker than 20mm.

2.1.2.1.3 Converted Home Office Printers

It is not uncommon for commercially available home office printers to be converted into systems suitable for research applications [22] [45] [46]. The integration of these printers with existing software, such as Microsoft Word or Powerpoint, makes it easy to quickly create a design to be printed which has been popular with high throughput screening (HTS) applications. This capability serves as both an advantage and disadvantage as the setup is rapid, but the control of the printing parameters is consequently limited. Some examples of

converted home office printers used for HTS applications are shown in Table 2.4, all of the studies site a considerable decrease in volume of the assay compared to conventional 96 well plate based assays.

Table 2.4: Examples of converted home office printers being used for high throughput screening applications.

Ref	Printer	Application	Resolution
[47]	HP model 5360 compact disc printer (TIJ)	Antibiotic screening assay on E–coli transfected with green fluorescent protein.	Font size 3, 180 ± 26pl, satellites observed.
[48]	HP Office Jet Pro 8100e (TIJ)	Drug (superoxide dismutase) inhibition assay of xanthine oxidase.	20mm spot diameter created in powerpoint.
[49]	Epson R290 (PZ)	Drug screening assay of 3 immunosuppressant drugs on immune T–Cells.	1.5 – 2pl, using Adobe photoshop

2.1.2.2 Industrial Inkjet Systems

There are multiple different printheads for industrial scale applications. These printheads will have considerably more nozzles than for research applications because the printing throughput scales directly with the number of nozzles. There is limited research that uses industrial scale printheads which creates a shortfall in understanding the effect these print systems have on a functional material. A notable example of inkjet research using a Dimatix Sapphire QS 256 nozzle printhead is for the ejection of lysozyme where a loss of activity up to 40% was observed [50]. This reinforces the applicability of using research scale

printheads to determine the effect at a commercial scale but also highlights the need for multi printhead studies.

A Fuji Film Spectra SL–128 AA was used to dispense personalised dosages of the drug haloperidol onto an edible film in the shape of a QR code that could be scanned and contains patient information [51], this choice of printhead is a suitable choice as it shows the potential to scale up this technology.

2.1.3 Modelling of Inkjet Printing

The Navier Stokes equations are central for modelling droplet formation and ejection in a drop on demand inkjet printhead, which was demonstrated as early as 1994 [52] to show good agreement and reliability with predicting droplet formation. The governing Navier Stokes equations are shown in 2.5. Where ρ is the fluid density, u is the fluid velocity, p is the fluid pressure, η is the fluid viscosity, g is gravitational acceleration and $\hat{z}$ is the vector in the z direction using a cylindrical coordinate system.

$$\rho\left(\frac{\partial u}{\partial t} + (u \cdot \nabla)\mathrm{u}\right) = -\nabla \mathrm{p} + \eta\nabla^2 u + \rho g\hat{z}, \qquad \nabla \cdot u = 0 \tag{2.5}$$

Solving the Navier Stokes equations can be done through the level set method, defining a phase boundary with a contour [53], [54], or finite element analysis [55], splitting a system into smaller parts with a mesh and approximating the solution of partial differential equations in a small area.

A large field of research has examined how inkjet models compare to images of the actual printing processes. Such a comparison is difficult due to the high-speed imaging required, often in the region of 1 million frames per second. Despite this difficulty in high speed image acquisition, these studies [56], [55], [3] have shown good agreement between modelling and experimental results. Some work has also been done to compare images to modelling to improve upon inkjet delivery efficiency [57], relevant for the design of printheads and to reduce

the computational power needed to produce models through fine tuning 1 dimensional inkjet models [58].

Work has been done to verify the frequently sighted order of magnitude approximation for shear rate during inkjet printing of 10^5 s^{-1} using a 50μm diameter nozzle and assuming a Couette flow [59]. This was to build a better understanding of dispensing graphene-based inks; however, this calculation was for a single instance with a specified nozzle geometry and droplet velocity. Building upon using modelling to better understand not only the droplet velocity and droplet volumes, but also the fluid shear rate is clearly required and is a gap in the literature, particularly as no research exists in this space using biological inks.

2.1.4 Review of Micro–Extrusion

Extrusion is a manufacturing technique that has been used extensively for both metal and polymer processing for over 100 years. A solid metal billet, typically aluminium, copper or steel, is compressively forced through an opening with a cross–sectional area smaller than the input material. The metal deforms plastically and a rod is formed with the same profile as the opening it is forced through [60]. For polymer extrusion, pellets, often of polypropylene, polyethylene acrylic or another plastic, are melted and forced through a die by a rotating screw mechanism [61]. Extrusion based bioprinting (EBB) is based on these manufacturing processes but the inks used are different and include hydrogels loaded with cells [62], cell carriers often made from polymers [63] and spheroids of cells and in an extracellular matrix (ECM) [64], these examples are shown in Figure 2.11.

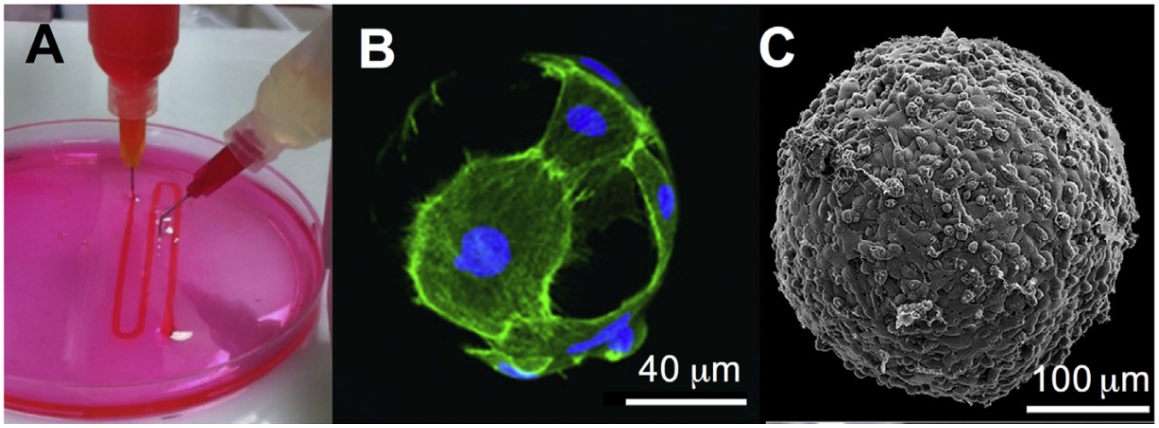

Figure 2.11: A) Extrusion using a cell laden hydrogel. B) A polymer microcarrier containing cells [63], C) A tissue spheroid used in a bioink [64]. Adapted from [62].

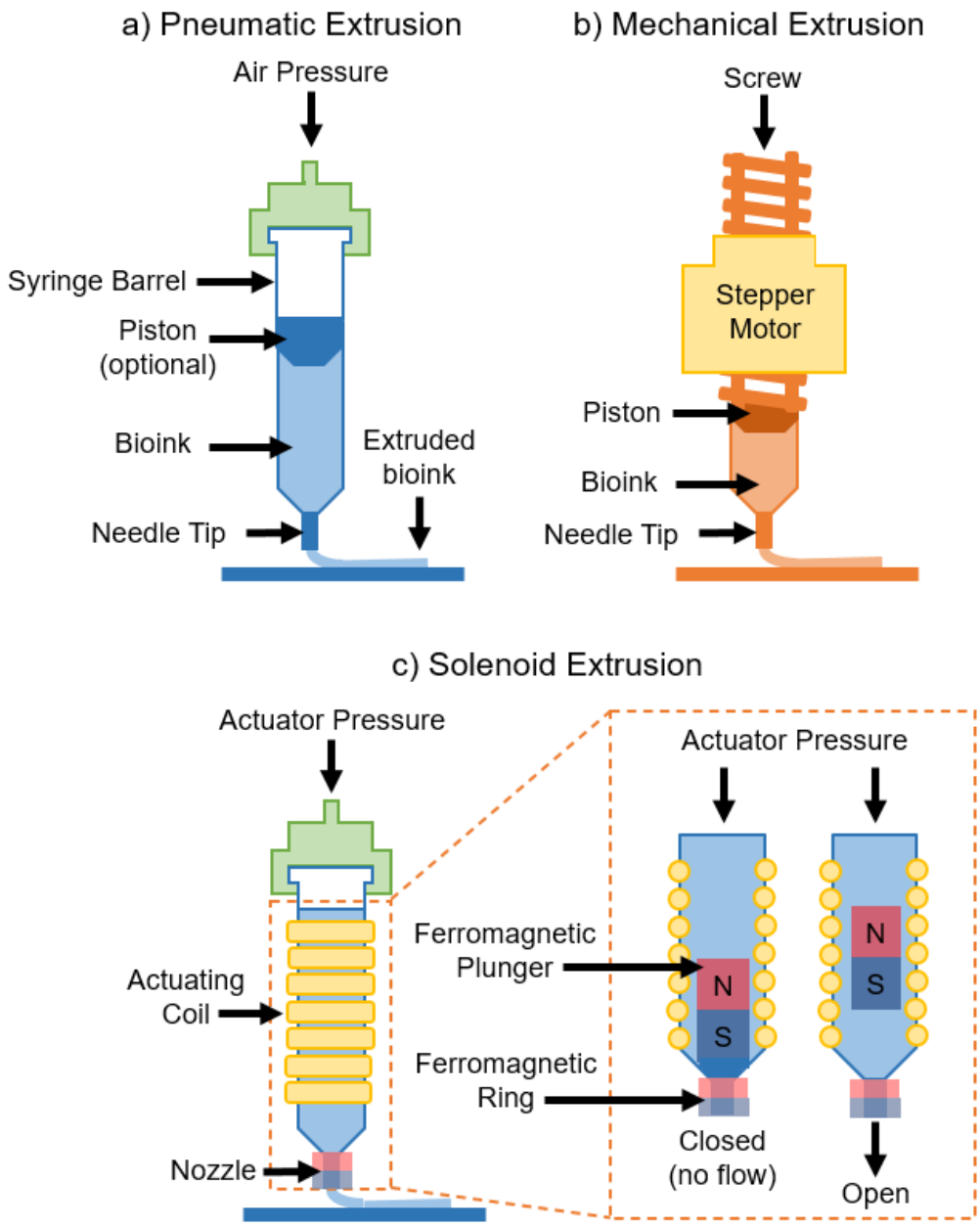

Figure 2.12: Diagrams that show the working principles of the three different micro–extrusion mechanisms used for EBB – a) pneumatic, b) mechanical and c) solenoid extrusion.

There are three main mechanisms used for the actuation of EBB: pneumatic, mechanical and solenoid based, which are illustrated in Figure 2.12. Pneumatic extrusion uses pressurised air to force the bioink through a nozzle, normally a needle tip. The air can be in direct contact with the ink or a piston can be used to seperate the bioink and air. Mechanical extrusion requires a motor to cause a

screw to rotate which forces a piston to move downwards and force bioink through the nozzle. Solenoid extrusion uses a combination of pressurised air and actuation with a ferromagnetic plunger to allow the bioink to flow through the nozzle. In all cases, the actuation method determines the flowrate of the bioink through the nozzle and the speed at which the needle tip is moving across the surface also determines the resolution of the print – a greater velocity results in a narrower line and hence higher resolution [65].

2.1.4.1 EBB Printability

The spatial resolution of extrusion systems is typically of the order of 1μm, however, as this dispensing technology is mostly used with cells, nozzles typically have a diameter of at least 150μm [66] and similar to inkjet technology, the diameter of the nozzle determines the minimum achievable resolution. Compared to inkjet, the ink used in EBB can be more viscous, typically between 30 to > 6 x 10^7 mPas [67] and because non–Newtonian hydrogels are often printed, the storage (G') and loss (G") moduli of inks is also considered, as will be discussed throughout this section. Research and application dependent, different parameters are assessed to determine the printability of a bioink and EBB system. These can be divided into the categories of (1) extrudability, (2) filament classification, (3) shape fidelity and (4) printing accuracy [10].

Extrudability concerns the force needed to push the bioink through the nozzle at a given flow rate. Using alginate–gelatin composite gels, Gillispie *et al.* determined that for hydrogels, the pressure required to achieve a given flow rate increased with both the loss and storage moduli of the gel [68], as shown in Figure 2.13.

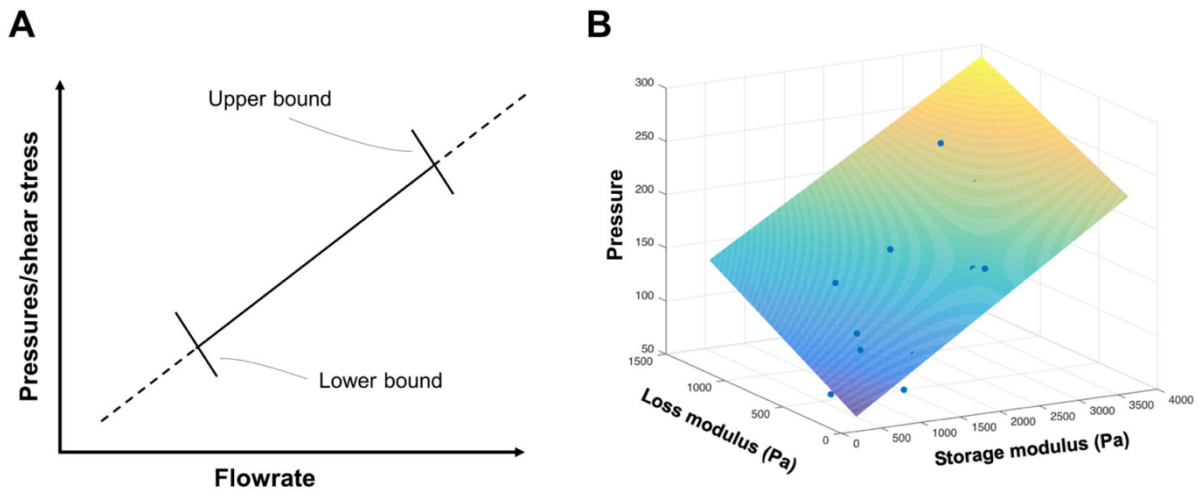

Figure 2.13: The extrudability of hydrogels relating the storage and loss moduli of the bioink with the pressure required for extrusion at a given flow rate [68].

This result is consistent with the equation relating the complex viscosity, η^*, with the storage and loss moduli and the angular frequency, ω (2.6). The Cox–Merz rule states that the apparent viscosity of a polymer solution is the same as the magnitude of the complex viscosity at a given shear rate and angular frequency [69]. The greater the viscosity of a fluid the greater the shear stress on the fluid to achieve a given flow rate.

$$\eta^* = \frac{\sqrt{G'^2 + G''^2}}{\omega} \qquad 2.6$$

Looking next at filament classification, this considers the quality of the extruded filament before deposition or when a single layer or cross hatching of filament has been deposited. A quantitative measure, Pr, is used to determine the quality of the extruded filament for retaining a square shape [66], as detailed in equation 2.7.

$$Pr = \frac{L^2}{16A} \qquad 2.7$$

The optimum filament should have a Pr value of 1. When Pr<1, the pores created by the cross–hatching flow take on a circular shape and can often be attributed

to low viscosity inks or under–gelation of the hydrogel. For Pr>1, this represents an irregular shape of the pores which could be due to over–gelation. A representation of this extrusion classification is shown in Figure 2.14.

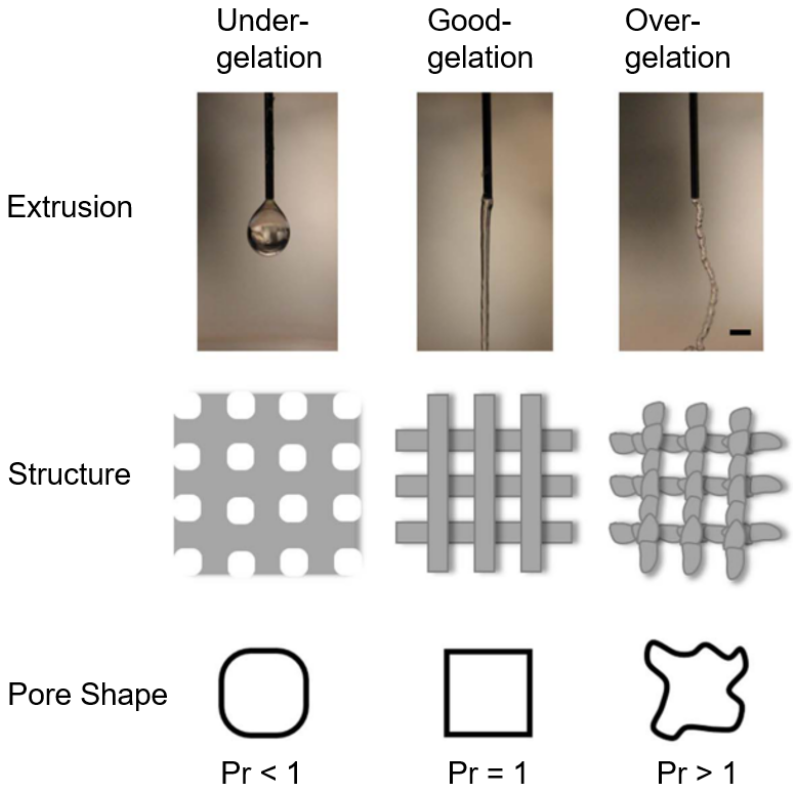

Figure 2.14: Examples of filament classification for sodium alginate, gelatin composite gels from [70]. The scale bar is 1mm wide.

In practice, the term shape fidelity (the third category of assessed parameters) looks at the entire print and assesses how much the printed structure deviates from the shape that was intended to be printed, for instance this could be based against the input CAD design. It differs from filament classification as it is concerned with the 3D result of the print rather than on the individual filament level but the Pr value in equation 2.10 can also be a relevant quantitative assessment metric for determining the spread of pores. Filaments can deform or spread after their deposition which results in poor shape fidelity. Often shape

fidelity is assessed qualitatively, for example when assessing a honey comb structure [71] or vascular constructs [72].

Further quantitative assessments for shape fidelity have included examining the collapse of filaments across a bridged gap [73] [74] and the quality of layering of filaments, hence assessing the height of the structure [68]. The collapsed area factor, C_f, is detailed in equation 2.8, where A_a^c is the actual area of collapse and A_t^c is the theoretical area. This is also illustrated in Figure 2.15.

$$C_f = \frac{A_a^c}{A_t^c} \times 100\% \qquad 2.8$$

Like the collapsed area factor, the structural integrity % is relative to a theoretical maximum. In the case of Figure 2.15, the theoretical maximum is the height of a model printed using silicon elastomer.

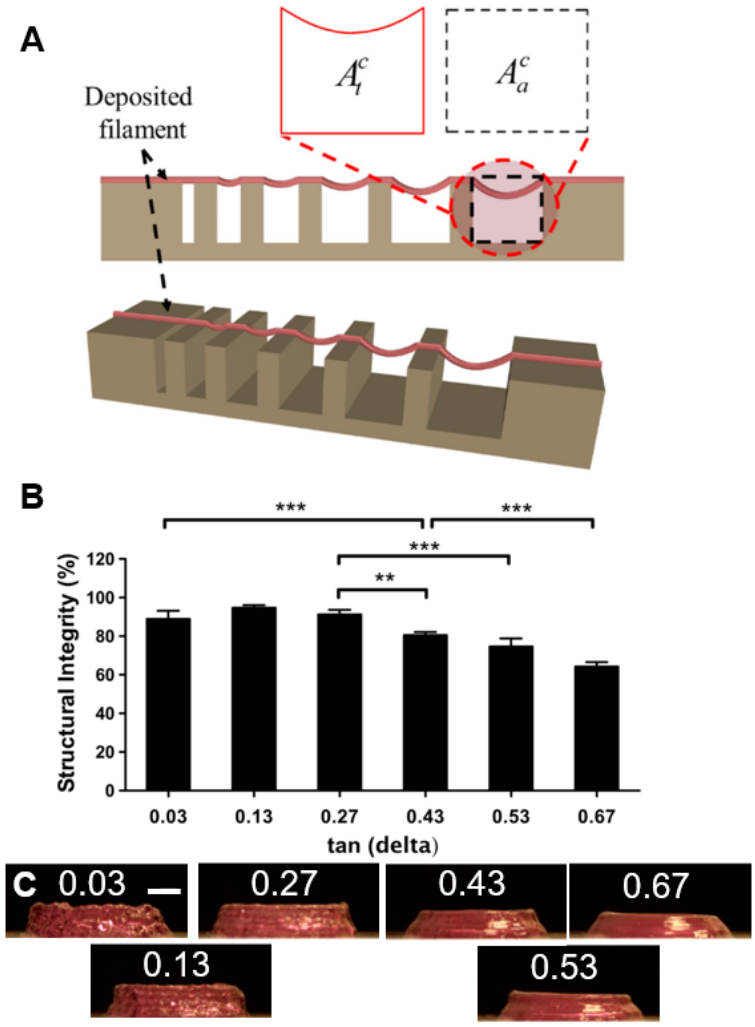

Figure 2.15: Examples of quantitative shape fidelity measures for EBB. A) shows how the collapse area of a filament is calculated [73] and B) shows and example of examining the quality of filament layering [68], C) are the printed constructs, the numbers are the loss factor of the extruded gels, scale bar 2mm.

The final category to determine the printability in EBB is the printing accuracy. Print accuracy assesses how well the chosen printing parameters perform for achieving the intended shape, size and location of a construct. Shape fidelity and printing accuracy are similar metrics, but shape fidelity is often studied using multiple bioinks whereas printing accuracy will focus on the parameters for a specific bioink.

Practically, a physical property of a print is used to determine the quality of the print and this is then examined in terms of a given print parameter. The filament width, height or cross–sectional area can all be selected and correlated with a printing parameter. The width of filaments is typically used and has been examined with respect to various printing parameters as shown in Table 2.5.

Table 2.5: Printing parameters that have been examined with respect to the printed filament width to determine the printing accuracy.

Parameter filament width correlated with	**References**	**General correlation**
Deposition velocity (feed–rate)	[65] [75] [73] [76] [77] [78] [79] [80] [81] [82]	Faster the feed rate, narrower filament
Pressure	[65] [75] [73] [76] [78] [79] [81]	Higher pressure, wider filament
Nozzle stand–off height	[73] [77] [78] [79] [82]	Greater stand–off height, wider filament
Nozzle Diameter	[81] [83]	Wider nozzle diameter, wider filament
Bioink Flowrate	[82] [83]	Higher flowrate, wider filament

There are a variety of methods to define printability for EBB and studies frequently cover elements of the printability definitions described here but not all 4 metrics. The novelty of EBB means that there is yet to be a standardised protocol to define printability which is ambiguous and makes it difficult to make cross–study comparisons. Moreover, shape fidelity, print accuracy and filament classification often consider a single layer of extruded filament and studies can neglect to consider the interactions of the substrate and the filament. Despite these drawbacks in assessing printability, it must also be noted that it is of even

greater importance to formulate bioinks for compatibility with the biological material to be printed rather than optimising for the printability. Arguably, there should be a fifth parameter of printability that examines the retained functionality of the active material that is printed. This will be discussed further in section 2.3.

2.1.5 Micro–Extrusion Systems

The three mechanisms for EBB, detailed in Figure 2.12, are utilised in commercially available systems and home–made/ custom built systems. In most EBB systems, either a standard metal needle in used as the nozzle or a drawn glass capillary. In this section, the lab scale extrusion sub–section details custom–built rigs for research applications and the commercial extrusion systems details pre–packaged setups that are commercially available.

2.1.5.1 Lab Scale Extrusion Systems

At the most fundamental level, to build an EBB system, control over the location the ink will be deposited, and actuation of the ink ejection is required. Some examples of custom–built systems are detailed in Table 2.6. Pneumatic actuation is the most popular for custom–built systems. If cells are deposited then a sterile environment and temperature control is also required, which can be achieved by placing systems in sterile enclosures and a temperature–controlled chamber.

Table 2.6: Some examples of custom-built EBB systems and the corresponding applications.

Ref	Print System	Nozzle Diameter	Application
[65]	Pressure assisted micro–syringe with glass drawn capillary tip	20–50 μm	Production of alginate scaffolds for tissue engineering.
[73]	Pneumatic pressure driven home made system.	410 μm	Production of alginate CMC composite gel for tissue engineering.
[77]	Pneumatic pressure driven home made system.	420 μm	Production of cellulose nanofibre, alginate composite

			gel for tissue engineering
[78]	Pneumatic pressure driven home made system.	250 µm	Printing decellularized skin derived ECM (majority collagen)
[79]	Pneumatic pressure driven (20kPa) home–made system.	400 µm	Printability study of sodium alginate hydrogels.

2.1.5.2 Commercial Extrusion Systems

Although EBB is still a young technology, a few commercially available bioprinting packages which can vary in price from ~£5,000, e.g. Inkredible, CELLLINK systems going up to over £100,000, for example, the 3D Bioplotter, EnvisionTEC costs around £160,000. As with inkjet printing, the throughput of printing scales directly with the number of nozzles and more nozzles enables different inks to be printed interchangeably. Table 2.7 provides some examples with applications of commercially available EBB systems.

Table 2.7: Some examples of commercially available EBB print systems and the corresponding applications.

Ref	Print System	Nozzle Diameter	Application
[76]	Inkredible+ bioprinter (Cellink)	25G (153µm), 27G (210µm), 30G (159µm)	Production of alginate, gelatin composite gel for tissue engineering.
[80]	Modified Hyrel3D, coaxial nozzle, 45 µl min^{-1} flow rate	26G (404µm) inner, 19G (910µm) outer	Dentin containing structures for regenerative dentistry.
[81]	Fab@Home Model I 3D	410–1180 µm	Optimising hydrogel printing

	printer, up to 460kPa		for tissue engineering.
[82]	Stepper motor (Kysan NEMA 17) controlled depression of a syringe.	34G (510μm)	Optimising printing of a novel chitosan–gelatin hydrogel laden with neuroblastoma cells.
[83]	Bioextruder system, stepper motor driven with the bioscaffolder 3D bioprinter.	27G (210μm)	Development and characterisation of a gelatin methacrylamide, gellan gum composite gel for tissue engineering.

Even though a print system could be sold commercially, users must still select printing parameters to optimise for the four printability factors discussed in 2.1.4.1 – (1) extrudability, (2) filament classification, (3) shape fidelity and (4) printing accuracy. Moreover, the resulting functionality of the printed bioink must also be considered for any printing application. This consideration will be examined further in section 2.3.

2.2 Inkjet Printing of Proteins

Most proteins are linear polymers consisting of amino acid groups joined by the peptide bond, the covalent bond between the carboxyl and α–amino group from adjacent amino acid groups. Unlike polymers there is not a single repeating unit, but a unique sequence built from 20 different amino acids, this sequence forms the primary structure of a protein. The secondary structure is formed through hydrogen bonding between the C=O and NH groups from different amino acids, the most common being α helices and ß sheets. The secondary structure configuration forms the tertiary structure and for some proteins multiple tertiary structures are joined to form a quaternary structure as shown in Figure 2.16.

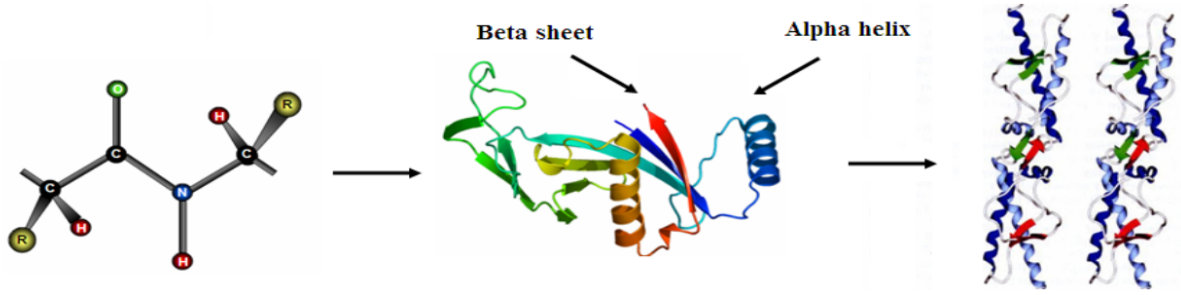

Figure 2.16: the first image shows the peptide bond between the NH and C=O groups on adjacent amino acid chains, forming the primary structure. The second image shows the tertiary structure with secondary structural motifs indicated and the final image shows a protein with a quaternary structure, where multiple tertiary structures are connected [84].

Proteins are classified into three broad categories – fibrous, globular and membrane proteins. Fibrous proteins often have poor water solubility and are found in tendons, bones, connective tissue and muscle fibres, examples include collagen and elastin. Globular proteins, such as haemoglobin, are the most water–soluble category and can often be involved in catalysing reactions. Membrane proteins are involved in cell signalling and transporting molecules, such as glucose. Examples include oxidoreductases such as horse radish peroxidase or glucose oxidase.

2.2.1 Protein Inks: Adsorption

Proteins will adsorb to surfaces when the Gibbs free energy of the system, G, decreases. Equation 2.9 states the conditions for protein adsorption to occur, H is the enthalpy, T is temperature and S is entropy.

$$\Delta_{adsorption}G = \Delta_{adsorption}H - T\Delta_{adsorption}S < 0 \quad 2.9$$

Proteins can absorb to surfaces of the ancillary equipment or printhead in an IJ system resulting in a reduction in concentration of the final printed solution. Poncin–Epaillard et al. stored the recombinant human prion protein in tubes of different materials for 24 hours at 4°C. Each of the polymers tested experienced a reduction in the amount of protein recovered with poly(tetrafluoroethene) performing the worst with 33% recovery compared to storage in an ultra–low temperature freezer [84]. To reduce protein losses, a coating of a sacrificial protein, such as bovine serum albumin (BSA), can be used [85]. Alternatively, ancillary equipment material should be coated with hydrophilic polymers, such as PEG or poly(methyl methacrylate), PMMA, to reduce electrostatic forces and hydrophobic interactions between the proteins and the surface [86], [87].

Because protein adsorption reduces the concentration of protein in the ink, care must be taken when assessing the resulting protein activity as the sample will have a reduced concentration which should be accounted for and not confused with potential losses due to droplet formation.

2.2.2 Protein Inks: Droplet Formation

For a droplet to be formed, the ink undergoes large shear forces, an extensional flow, as shown in Figure 2.17, and upon ejection the droplet is exposed to a moving air interface. The shear rate is typically of the order of 100,000 s^{-1} [1]

and the droplet can be ejected at speeds up to 10ms-¹ for a drop–on–demand printer [2],[3]. Under these conditions, it is often contested as to which effect is more adverse for inks containing proteins and enzymes: the shear force or the moving air interface and is discussed in this section.

Figure 2.17: Images showing a droplet being ejected through a 50µm Microfab nozzle. The scale bar in 100µm and the time between each frame is 6.66µs.

Walstra proposed that the energy required to deform a small globular protein is equivalent to the change in Gibbs free energy of the folded and unfolded state, typically 5×10^{-20} J per molecule [7]. This equates to a shear stress of 5×10^{5} Pa, a shear rate of $5 \times 10^{8}\, s^{-1}$ in water [6], which exceeds the magnitude experienced in an inkjet printer by a factor of 1000. When Walstra considered a 40kDa protein at a surface concentration of 2 mg/m², the interfacial surface tension between air and water supplied energy of the order 10^{-18} J per molecule, sufficient for structural alterations, insinuating that the air–liquid interface is more deleterious than the mechanical stress upon the fluid. Table 2.8 gives a summary of the effect of shear on the resulting structure and function of different proteins.

Table 2.8: The effect of shear, detailed in the induced shear rate column, on different proteins resulting structure and function, detailed in the damage column. Protein concentration and reference are also specified.

Ref	Protein, M_w, concentration	Induced Shear Rate	Damage
[88]	Horse cytochrome c, 12,384 Da, 40–50μM	2 x 10^5 s^{-1} in water, laminar flow through capillary for ~80 seconds.	No evidence of destabilisation. Damage threshold determined to be ~10^7 s^{-1} using an elongational flow model. Higher viscosity solvent and larger M_w reduces required shear.
[89]	Recombinant human growth hormone (rhGH), 22.13kDa, 2mg/ml	1.3 x 10^5 s^{-1} in water using a concentric cylinder device for 2 hours.	Slight increase in measured molecular weight, to 24.6kDa, could be low level of aggregation. Also evidence of clipping as 14kDa fragments detected. Slight change in thermal properties.
	Recombinant human deoxy ribonuclease (rhDNase), 32.74 kDa, 5mg/ml		No evidence of changes.
[90]	Bovine insulin, 5,800 Da, 0.2mg/ml	From 200 – 600s^{-1} in water in a Couette flow using a concentric cylinder device for 30 minutes.	Insulin aggregates evolved at lower shear rates and fibrillary forms were observed at the higher shear rate. The structural motif of the alpha helix was shown to be observed at reduced levels with increasing shear. Tyr fluorescence decreased with increasing shear.
[91]	α helix poly–L–lysine of M_w 15, 68.3, 205.7 and 381.2kDa (a homopolypeptide), 0.2g/ml	From 74 – 715 s^{-1} in water in a Couette flow using a concentric cylinder device for 1 hour.	Unfolding was observed as shear and time dependent with a threshold value for structural deformation of $\dot{\gamma}t = 10^5$. The unfolding of the α helix structural motif showed dependence of $\alpha \approx (\dot{\gamma}t)^{-1/2}$ and less unfolding was observed with higher molecular weight samples.

[92]	Yeast Alcohol Dehydrogenase, 146.8kDa, 1mg/ml	683s^{-1} for 5hrs at temperatures from 5–40°C in a concentric cylinder device.	No measurable activity loss, however a white precipitate formed attributed to aggregation but did not exceed 2% of the original protein in solution.
[93]	Human von Willebrand Factor, (multimeric enzyme) up to 2 x 10^4 kDa, 30µg/ml	Atomic force microscopy (AFM) probe applied a shear force 7.4 – 19nN followed by a rotational disc applying 3.5 Pa. Aqueous conditions.	Force from the AFM extended the chain conformation exposing individual globular domains. Above 3.15Pa applied with the rotating disc an unfolded 'meandering extended conformation' was observed.
[94]	Lysozyme (chicken egg white) 10mg/ml in water or 95% glycerol	Taylor–Couette flow cell – two concentric cylinders delivering 14 – 700s^{-1} shear rate.	Structural conformational changes observed in situ during shearing. More pronounced conformational change in 95% glycerol than water.

Table 2.8 summarises some of the literature investigating the effect of shear on different proteins. Shear does not seem to have a measurable effect on all the proteins in question. It seems perplexing that applying a shear rate as low as 200 s^{-1} for 30 minutes to bovine insulin [90] resulted in aggregation and reduction of the α helix structure, yet applying a shear rate 650 times greater for 2 hours resulted in no observable damage when investigating rhDNase [89]. The contrast of these results can largely be attributed to the different proteins being examined: different molecular weights and structure, but the experimental method will also influence the results.

Thomas and Geer argue that experiments investigating the effect of shear on proteins neglect to consider and isolate the damage contribution from air–liquid and liquid–solid interfaces resulting in misguided results [6]. This point is observed in [90] and [91] where there seems to be an absence of controls that

exposes the solutions to the same interfaces but without a shear applied. Interestingly, both these studies also report shear induced damage.

Another choice made in the experimental design will be the concentration of the protein in solution. The viscosity of a protein solution increases linearly with concentration, but above a threshold concentration, dependent upon the molecule, the viscosity increases exponentially [95] [96]. The viscosity is related to the shear rate through equation 2.10 shown below, where η is the viscosity in mPa s, τ is the shear stress in mPa and $\dot{\gamma}$ is the shear rate in s^{-1}.

$$\eta = \frac{\tau}{\dot{\gamma}} \qquad 2.10$$

Therefore, a fixed shear rate applied to solutions of different viscosity, which is dependent on the protein concentration, results in a different shear stress. For instance, more extensive conformational changes were observed for lysozyme in 95% glycerol than in 100% water which can be attributed to the higher viscosity [94]. For the study with the Human von Willebrand Factor, inducing a shear to the enzyme was to contribute to the understanding of thrombogenesis, the formation of blood clots, but a solution concentration greater than that found in the human body 7 µg/ml was used [93] which will increase the shear stress endured by the enzyme. This makes it harder to directly translate the result to the conditions in–vivo.

Higher concentrations also increase the frequency of protein–protein interactions which can result in tangling of the polymer chains modifying the solution viscosity. For example, *Bekard et al.* observed a greater loss of the α helix structure of poly–L–lysine for solutions containing larger molecular weights which were more viscous [91].

All the studies in Table 2.8 use dilute protein solutions but for applications where antibodies are dispensed for therapeutic use, a much higher concentration, typically 100mg/ml is required [97]. Dobson et al. studied

aggregation of 3 proteins and 3 antibodies, including BSA and concluded that the strain rate, protein concentration and sequence of amino acids that forms the protein have an influence [98].

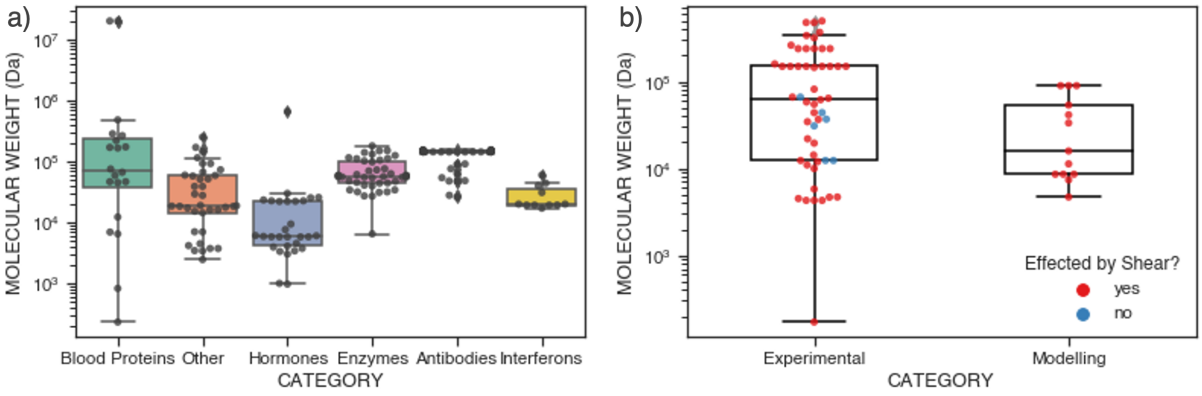

Figure 2.18: a) The molecular weights of approved protein therapeutics. b) A collation of whether proteins were affected by shear, grouped by whether this was determined experimentally or with modelling and plotted according to the molecular weight of the protein, from our recently published work [99].

Figure 2.18 shows the molecular weight of approved protein therapeutics grouped by product category and molecular weight and the figure on the right shows a collation of whether proteins are affected by shear [99]. Experimental approaches cover a more relevant molecular weight range when compared to the molecular weights of protein therapeutics. Moreover, the plot highlights that there does not seem to be a clear trend regarding molecular weight and the likelihood of a protein being affected by shear as the proteins effected by shear in these examples are in the mid–range of the molecular weights of the proteins examined in the literature.

These results have implications for inkjet printing protein solutions, particularly the experiments that reached comparable shear rates as would be endured by proteins in an inkjet printer [88][89]. Researchers have investigated the effect of inkjet printing on the retained functionality of proteins, a summary is given in Table 2.9. Although these are cases of inkjet-printed proteins, the factors

contributing to protein loss of activity could include adsorption or impact due to forces endured by the fluid.

Table 2.9: A summary of studies that have investigated the effect inkjet printing has on the resulting protein structure and function.

Ref	Protein Ink	Printer	Maximum Damage
[100]	Horse Radish Peroxidase (HRP) 10μg/ml in phosphate buffered saline (PBS).	PIJ squeeze mode.	30% retained activity, mitigated with addition of trehalose/glucose.
[4]	HRP 1.68nM in 40mM potassium phosphate buffer with CMC to reach 5mPas.	PIJ Dimatix DMP 2800	>98% retained activity and the difference not statistically significant.
[5]	Glucose Oxidase 3% wt/vol in phosphate buffered saline.	PIJ squeeze mode. Microfab MJ–AT–01–60μm diameter.	70% retained activity. No change in M_w.
[45]	Lysozyme in 30/70 glycerol/water.	Thermal inkjet. HP Deskjet 1000.	30% retained activity with 0.15 and 0.5mg/ml up to 80% 3.5mg/ml and 10mg/ml.
[45]	Ribonuclease–A in 30/70 glycerol/water.	Thermal inkjet. HP Deskjet 1000.	60% retained activity with 3.5mg/ml, 80% 10mg/ml.
[50]	Lysozyme (chicken egg white) 50μg/ml in pH 6.2 buffer	Dimatix Sapphire QS–256/80 AAA 80pl	85% retained activity for optimised ink down to 60% for 12μg/ml lysozyme concentration.

HRP dispensed with a squeeze mode piezoelectric printhead showed a loss of activity up to 30% compared to a control solution flowed through the printing apparatus at low pressure to account for adsorption losses [100]. Loss of activity

was positively correlated with compression rate, calculated from the piezoelectric crystal properties, and loss was induced above a threshold value of 2.5μm³/μs. The addition of trehalose and glucose to the ink reduced the loss, attributed to hydrogen bonding stabilising the protein secondary and tertiary structure, but the printing itself was unrepresentative of typical inkjet printers as ejection speeds were 3% of those typically experienced (10m/s). Conversely, the study by Di Risio and Yan which focused on optimising protein inks to ensure reliable jetting and no loss of protein activity found that there was no statistically significant loss of activity for HRP ink containing CMC as a viscosity modifier [4].

However, when formulating inks with proteins, property modifiers can detrimentally affect their function. Risio et al examined ink formulations containing HRP and found that solutions containing up to 0.1wt.–% of the surfactant Triton X–100 had a negligible effect on activity [4]. To reach a target viscosity of 5mPas for piezoelectric printing, seven viscosity modifiers were tested including CMC, PEG of varying molecular weights and glycerol. Most modifiers had a detrimental impact, only CMC reached the desired viscosity and had a positive impact on activity whilst solutions at or below 10wt.–% glycerol had no impact on activity. Glycerol was also found to have a detrimental impact on H+ –ATPase activity [101] and glucose oxidase [102]. Although these results cannot be directly applied to all bio–agents; care must be taken during ink formulation not to jeopardise the desired function of the printed material.

Cook et al. also used PIJ to dispense glucose oxidase (GOx) and correlated the increase in loss of activity with the voltage of the waveform [5]. Increasing the waveform voltage has been shown to increase the velocity of the ejected droplet [23] but it does not provide information on the resulting force transferred to the ink. The molecular weight and secondary structure were examined and there was no significant deviation from the control samples. However, given the large

drop in activity there is some alteration to the enzyme inhibiting its interaction with the substrate.

A further study using a TIJ printer to dispense lysozyme and ribonuclease–A found that a greater loss in activity was experienced with less concentrated solutions for both biologics [45], it was concluded there was no secondary structural change to lysozyme through circular dichroism measurements but this is an unreasonable conclusion given that the molar ellipticity changes by 1500–2000^{o}cm^{2}/dmol at 205nm.

The final study detailed in Table 2.9 uses a piezoelectric printhead with 256 nozzles in parallel and optimised the ink formulation to minimise lysozyme activity loss whilst ensuring the ink had a high printability (see Figure 2.7) Although the experimental method flowed ink through the printhead before printing, checks were not in place to ensure the surfaces were saturated and lysozyme activity losses were passed off as due to shear stress which was not quantified in the study [50].

All these studies highlight the need for a greater understanding of optimising printing parameters for IJ printing of protein solutions but have not necessarily isolated each contributing factor that could be detrimental to the printed protein activity. Results even vary across studies using the same active protein. This necessitates for an end–to–end study that examines ink formulation through to final protein stability should be conducted and must include the impact of the drop forming process and the forces endured by the ink as well as the interaction between the proteins and surfaces contacted.

When printing inks that contain proteins in their formulation there are broadly speaking two concerns that could cause a loss of protein function or effect the structure – surface interactions and forces to eject an inkjet droplet.

2.2.3 Protein Inks: Applications

Inkjet printing with inks containing proteins have a wide variety of applications from biosensing [42], to high throughput screening [102] [48] and proteomics [103] [104]. An overview of some of the instances where protein–based inks have been used for specific applications is detailed in Table 2.10.

As previously mentioned in 2.2.2 and studied in Table 2.9, there is also clear evidence that when proteins are printed for specific applications, there is frequently an observable loss of activity of the printed protein. In each study, different printers are used meaning different forces are exerted on the ink and each protein responds differently. To ensure inkjet printing is suitable for use on a larger scale, a greater understanding of the technologies effect on protein structure and function is required so that guidelines can be followed to print and minimise the detrimental effects observed.

Table 2.10: A Summary of some of the instances where protein–based inks have been used for specific applications.

Ref	Protein Ink	Printer	Application	Damage
[42]	3 wt% silk fibroin solution with HRP/ AuNP/ ampicillin/ bone morphogenetic protein 2 (BMP–2)/ Polydiacetylene and IgG	Piezoelectric Dimatix DMP 2800	Silk extends stability of functional inks for plasmonics, biosensing (bacterial detection), tissue engineering.	HRP 40% loss of activity 30 mins after deposition reduced to <5% with silk.
[41]	GOx, invertase, HRP	Omnijet 100 using DMP cartridges 30pl (21µm nozzles)	2D immobilised enzyme arrays used as logic gates	No deterioration observed due to ink formulation, printing or surface immobilisation.
[105]	Human IgG 2µg/ml	Homemade glass capillary-based system	Electrophoretically mediated microanalysis immunoassay for human IgG 10–2000ng/ml concentration detection	None reported
[106]	ß–galactosidase 0.6mg/ml in 0.1M phosphate buffer, 1.5mM EDTA, 10wt% glycerol	TIJ printhead supplied by Olivetti I–Jet. 208 roof shooter nozzles ejecting 10–12pl drops	Biosensor for colorimetric activity measurement of ß–galactosidase	15% activity drop
[46]	1.7mg/ml HRP in 0.1M phosphate buffer, 1.5mM EDTA and 10wt% glycerol	Converted TIJ Canon i905D, drops ~2pl	Amperometric biosensor for HRP detection.	Negligible loss of activity.

2.3 Extrusion Based Bioprinting Applications

Bioprinting is the production of three–dimensional biological constructs that incorporate living cells to form tissues or organs. Despite only gaining major traction from 2010 onwards, huge advances have been made. The area has applications in regenerative medicine, tissue engineering, personalised medicine, and drug screening.

To fabricate tissues or organs, one of three approaches is adopted [107]:

1. Biomimicry: Through careful and detailed observation, the design of the natural construct is copied.
2. Autonomous Self Assembly: Embryonic organ development is used as a guide. Cells are required to differentiate to provide the correct structure, function, and composition of a tissue.
3. Mini Tissues: Combining smaller tissue sections to create a larger tissue or organ construct. This method adopts elements of biomimicry and autonomous self–assembly.

Extrusion is the most common technology used for bioprinting applications. As discussed in section 2.1.4.1, the printability of a given bioink is important to consider as it will determine the resulting resolution and print quality. However, further consideration must be made when printing with inks containing active materials such as cells. The bioink is consequently assessed on how much the bioink replicates the ECM, supporting the expected cell function, if the bioink retains the cell viability after printing and whether the bioink is suitable for extrusion, requiring rheological characterisation of the ink [108].

In this section, applications of hydrogel–based inks and inks containing structural proteins, such as collagen, silk and fibroin for extrusion based bioprinting will be presented.

2.3.1 Hydrogel Based Inks

A hydrogel is a network of hydrophilic polymers, of natural or synthetic origin, produced by cross–linking monomers. A large amount of water is retained in the structure of a hydrogel, >70%, which makes them biocompatible and replicate the ECM. Hydrogels are frequently used in EBB because they enable rigid structures to be produced through cross–linking meaning during printing, the viscosity of the gel is lower which reduces the shear stress during ejection having implications for cell viability [109]. Cross–linking can be physical, through entanglement of polymer chains in the network or setting of a melt, or chemical, through the formation of covalent bonds that could be initiated by a chemical reaction or UV light.

2.3.1.1 Hydrogel Characterisation

There are multiple methods for hydrogel characterisation, commonly used testing regimes are shown in Figure 2.19. Because of the nature of hydrogels, tensile testing, for instance, is difficult to properly execute as getting a solid grip on the material is challenging. The testing regimes used are time or frequency dependent due to the viscoelastic properties of hydrogels and the time dependent nature of the mechanical properties during deformation.

A big challenge in hydrogel characterisation is the discrepancy in data across studies that can be several orders of magnitude in size [110]. For example, Oyen *et al.* examined the value of the elastic modulus for agar and acrylamide gel across several studies and found that the values can vary by 3 orders of magnitude. Even within studies, there are clear discrepancies. A study that utilised compression and indentation testing with agar gel observed an elastic modulus 52% greater with indentation [111].

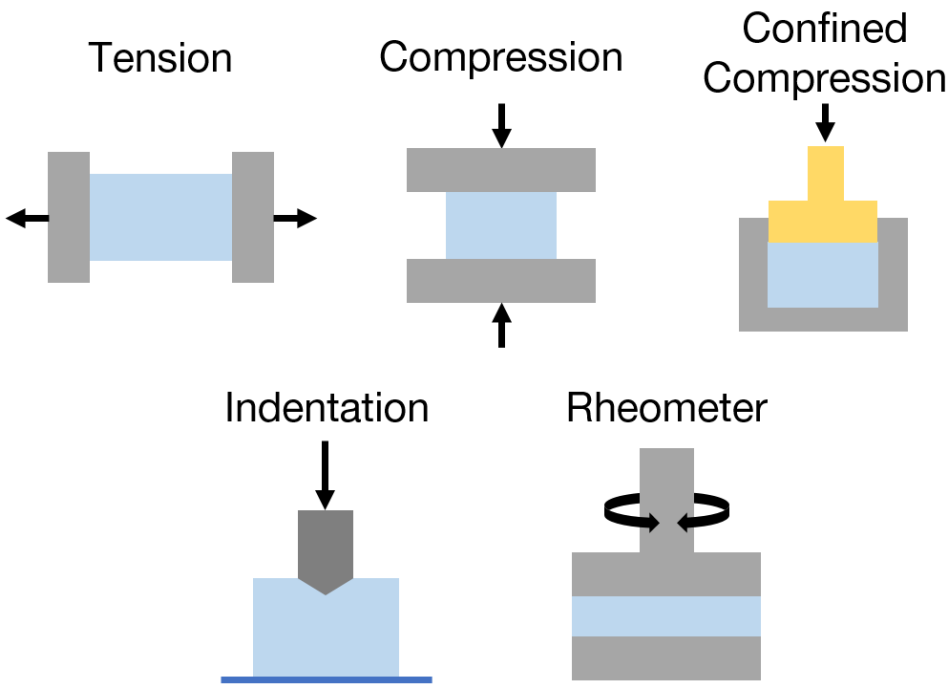

Figure 2.19: Illustrative representation of different characterisation methods used to determine the mechanical properties of hydrogels. Adapted from [110].

A large area of research in EBB is aimed at improving the mechanical properties of bio–inks through new formulations [83] [108], but if a measurement setup can result in several orders of magnitude fluctuation of data it is difficult to make an objective assessment of a formulation. Some studies have addressed this problem by clearly setting out a protocol for hydrogel characterisation using a parallel plate rheometer [112] and indentation [113]. A standard was even produced by ASTM (American Standard for Testing and Materials) for characterising hydrogels used in regenerative medicine but was later withdrawn in 2020 [114].

Many hydrogels are shear thinning, under shear force the viscosity of the gel is reduced. For preservation of cells seeded within the hydrogel this is often seen as a benefit due to reduced shear stress consequently being passed onto the cells retaining their functionality which is often the focus of research surrounding hydrogels [9], although a reduction in the viscosity of the bioink can result in reduced printing resolution [115]. However, this demonstrates that hydrogels are

susceptible to damage during extrusion based printing and is a reason for much hydrogel research focusing on gel formulations that are self–healing [116], [12], [117].

2.3.2 Inks Containing Structural Proteins

In the field of bioprinting, scaffold materials, typically made of hydrogels, are intended to resemble the ECM to as greater extent as possible [118], [119]. Structural proteins, such as collagen, fibrin and elastin, naturally occur in the ECM and therefore, incorporating these structural proteins into a hydrogel formulation helps to achieve that core objective of recreating the ECM. Collagen, a triple helical protein, is the most abundant protein found in all mammals [120]. Type I collagen has the particular benefit of having low immunogenicity, less than 90% of the population will have an immune response upon implantation making it biocompatible and highly applicable for tissue engineering and extensively used within the field [121]. Collagen based hydrogels enable cells to interact with the scaffold in similar ways as would be observed within their natural environment but have a large drawback of having poor mechanical properties in pure collagen hydrogel systems [122].

The shear forces endured by collagen based hydrogels during extrusion would be sufficient to cause modifications to the mechanical properties of the hydrogel, evident through previous studies showing that shear rates as low as $8.3s^{-1}$ have an observable effect on collagen fibre alignment [13]. Table 2.11 details some examples of collagen structure being modified due to an applied shear force.

Table 2.11: Some examples of collagen undergoing structural modifications due to an applied shear force.

Ref	Collagen Formulation	Forces Endured	Observation	Application
[123]	Rat tail collagen type I (3.64 mg/ml) in 0.2ml of 10x MEM (minimum essential medium), 8ul antibiotics and 15ul 0.1N sodium hydroxide.	Maximum 705Pa, majority of gel 56Pa for 24 hours. Parallel plate shearing by moving a parallel plate 0.5mm/h	Collagen fibres randomly situated aligned in direction of principle strain. Collagen fibres can also align in the absence of any cells.	Creating an *in vitro* cell model of the periodontal ligament construct.
[124]	Type I rat tail (2.06 mg/ml) in 2ml 10x MEM neutralised with 1M NaOH. Gelling at 37˚C, 5% CO2 30mins.	Collagen gel hung vertically slowly flowed with gravity.	Anisotropic factor (AF) = intensity 90˚/intensity 0˚ calculated at 600nm. Peaked at 2 in fluid flow setup after 60 minutes – maximum alignment reached after this duration.	Alignment of collagen of collagen fibrils across different length scales: gel fluid flow (nano scale), embossing (micro scale), layering (micro and meso scale).
[13]	Bovine dermal collagen type I 3mg/ml in 8:1:1 PBS, 0.1M NaOH	0.45 ml/min, 4 ml/min, and 11 ml/min corresponding to wall shear rates of 8.3 s^{-1}, 73.8 s^{-1}, and 203.1 s^{-1}	Higher flow rate and shear rate greater alignment, matrix density increases with higher concentration and on hydrophobic coatings. Length of fibrils increased with solution concentration and gelation time.	Microfluidic device to vary collagen solution concentration, degree of gelation, shear rate, substrate coating effect on orientation and immobilisation of fibrils.
[125]	Pepsin extracted type I	9, 20, 80 and 500	Best fibril alignment	Method to align and

	bovine collagen 3mg/ml 10xPBS and 0.1 M NaOH in the ratio of 8:1:1	s^{-1}	observed at 20 and $80s^{-1}$. At $500s^{-1}$ short and curly fibrils formed (hooks). The rate of fibril length increase was greatest for the lowest shear rate, highest for $500s^{-1}$	orient fibres which could be applied to tissue engineering.
[126]	Decellularized corneal ECM at 2% concentration containing collagen.	With a 30G needle, peak shear stress of 136.96 kPa.	30G needle caused α–SMA expression, present when the corneal myofibroblasts are wounded. Shear induced collagen alignment.	Using extrusion–based cell printing to align collagen fibrils to produce corneal stroma tissues.
[127]	2 mg/ml type I neutral bovine tendon pepsin–soluble collagen (BPSC) solution.	0 s^{-1},100 s^{-1}, 1000 s^{-1} and 2000 s^{-1} for 30 minutes at 10° C before gelation.	Higher shear rate, narrower fibre diameter and increased porosity.	Investigating the effect of pre–shear treatment on collagen gel structure
[128]	8:1:1 ratio of bovine collagen type I 3 – 3.2 mg/ml, NaOH 0.1M and 10X MEM	Shear rates of 25, 75, 150, and 225 s^{-1}	Density of deposited fibrils increased with increasing shear rate, but length decreased.	To study keratocyte behaviour by replicating the *in vivo* aligned collagen type I structures surrounding them.
[129]	Bovine type I collagen 0.8mg.ml with laponite 3mg/ml, pluronic F127 250mg/ml or Matrigel 4.2–10.1mg/ml and	Printing pressure 1–40kPa, shear rate of order $100s^{-1}$.	Collagen alignment due to molecular crowding and shear and extensional forces during	Investigating collagen fibril alignment due to drop casting and micro–extrusion,

	molecular crowders Ficoll 70kDa, Ficoll 400kDa at concentrations 6, 12, 18, and 24 mg/ml.	extrusion. Greater shear rate, greater alignment.	demonstrating applicability for tissue engineering by embedding human breast cancer cells.

From the research presented in Table 2.11 shear forces have a measurable impact upon the resulting collagen structure. This is relevant for extrusion based printing where the shear rate can be in the order of magnitude of 100 – 1000s^{-1} [11]. However, some of the conclusions presented are conflicting. For example, many examples in the literature indicate that a greater shear rate applied to the collagen fibrils results in greater alignment [13], [129] but another example indicates that above a certain shear rate alignment decreases with an optimum alignment reached for shear rates of 20s^{-1} and 80s^{-1} [125]. It is clear that the intended application for collagen–based biomaterials would be to embed cells in for further study [123], [126], [128] but when processing collagen at higher shear rates, modified cell behaviour was observed [126]. Before cells embedded within collagen–based scaffolds can be studied with confidence, it is important to establish how the shear rate caused by extrusion–based printing will affect the extruded scaffold structure.

2.4 Research Questions

Drop on demand inkjet printing and extrusion based bioprinting have several applications in drug discovery, drug delivery, personalised medicine, and tissue engineering. There are many examples of the use of these technologies at the research scale detailed in this literature review. However, there are concerns that when printing biological materials, the resulting functionality can be impaired. For example, the reduction in activity after inkjet printing of proteins (section 2.2.2), reduced cell viability and impact upon the extruded hydrogel (section 2.3.1.1). Moreover, results presented in the research can be contradictory making it even more confusing to understand how to use these printing techniques effectively and without detriment to the functional material being printed.

The broad aim of this research is to better understand how printing processes effect biological inks, particularly protein–based inks, to encourage more extensive industrial scale adoption of these technologies. The approach taken is to break down elements of each printing process to assess how much each contributing factor effects the printed bioink. To proceed with this research aim, the following research areas will be investigated in the proceeding chapters:

Chapter 4

Research aim: To assess the forces endured by aqueous inks during inkjet printing and how the chosen printing parameters effect the resulting shear forces and velocity of the ejected droplets.

Methodology: This avenue of research will be carried out by building a better understanding of the forces endured by droplets during ejection in the inkjet printing process using COMSOL Multiphysics. A simulation will be made that is representative of drop on demand inkjet printing and this will be validated by

comparing the simulation to high-speed images collected from inkjet printing with a microfab nozzle using inks containing HRP.

Chapter 5

Research aim: To determine how much different aspects of the inkjet printing process contribute to an enzymatic loss of activity.

Methodology: The journey that the ink takes in the inkjet printing process is broken down into formulation and supply, ancillary equipment, printhead, nozzle flow, droplet formation, drying and droplet stability. Each of these steps are isolated and enzymatic assays of ABTS with HRP, GOx and SOx are used to determine the impact each of these potential contributing factors has to the resulting enzyme activity.

Chapter 6

Research aim: To explore possible routes to minimise enzymatic activity losses caused by inkjet printing.

Methodology: This chapter focuses on ink formulation; adsorption and the impact drying have upon enzymatic activity; the areas highlighted in chapter 5 to be of interest for reducing enzymatic activity loss. D-Glucose and trehalose are added to ink formulations and the impact a change in formulation has on the losses due to drying and adsorption are examined with enzymatic assays of ABTS with HRP and SOx.

Chapter 7

Research aim: To investigate extrusion with a protein–based hydrogel and how the extrusion process effects the resulting integrity of the gel.

Methodology: This chapter breaks down extrusion with pure collagen gels into gel formation and processing. Piezo axial vibration rheometry is used as a

quality control technique to determine the integrity of the gels, focusing on the viscoelastic properties of the gels. A mechanical extrusion rig is used to control the flow rate collagen gels endure and control samples are compared with extruded samples. The flow rate from the rig is then compared to a COMSOL Multiphysics simulation to build a better understanding of the shear rate endured by collagen gels during extrusion.

Chapter 3 Experimental

3.1 Materials

Materials purchased from Sigma Aldrich include glycerol (≥99%), horse radish peroxidase type VI ≥250 units/mg, glucose oxidase type VII from aspergillus niger ≥100,000 units/g, sarcosine oxidase from bacillus subtilis 25–50 units/mg, sarcosine (≥98.0%), bovine serum albumin (≥98%), D–(+)–Glucose (≥99.5%), 2, 2'–Azino–Bis–3–Ethylbenzothiazoline–6–Sulfonic Acid (ABTS) ≥98%, hydrogen peroxide (≥2.5 – <5wt%), N–(3–Dimethylaminopropyl)–N′–ethylcarbodiimide hydrochloride (EDC) 98% (Sigma–Aldrich #161462), N–Hydroxysulfosuccinimide sodium salt (sulfo–NHS) ≥98%, sodium carboxymethyl cellulose M_w ~90,000, sodium carboxymethyl cellulose M_w ~700,000, poly(ethylene oxide) M_w ~1,000,000, sodium phosphate dibasic (99.95%), sodium chloride (≥99.5%), potassium chloride (≥99.0%), methanol (≥99.9%), sodium hydroxide 0.01M, glutaraldehyde solution 8%, ethanol ≥99%, deionised water

D–trehalose (≥99.0%) from Merck Life Sciences, 4–morpholinoethanesulfonic acid (MES) (>99%) from Acros Orgaincs, coomassie brilliant blue G–250, phosphoric acid (85%), Potassium dihydrogen phosphate from Fisher Scientific.

Pepsin soluble bovine atelocollagen type I 3mg/ml in 0.01M HCl was purchased from Collagen Solutions along with the neutralisation buffer.

3.2 Print System Design

Three different inkjet print systems are used for experimental work in this thesis. A research scale, single nozzle Microfab Printhead, presented in 3.2.1, a 16 channel prototyping printhead DMP-2850 presented in 3.2.2 and an industrial scale Spectra SE-128 AA with 128 nozzles, presented in 3.2.3. Each of the print systems is shown in Figure 3.1 in the corresponding order of increasing complexity from research scale through to industrial scale.

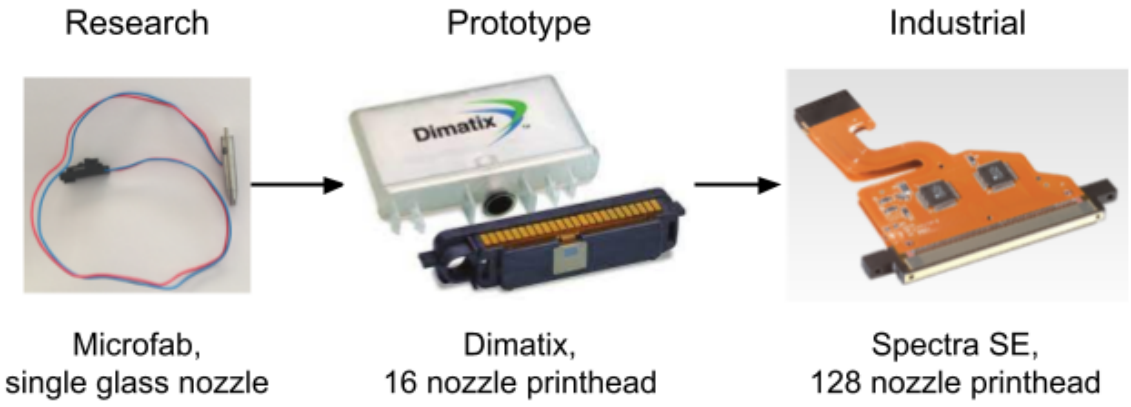

Figure 3.1: The three inkjet print systems used for experimental work, shown in the same order as the experimental flow in increasing complexity.

The rationale behind selecting these three print systems is to be able to increase the complexity gradually. Firstly, the research scale Microfab system is used that enables actuation of droplets from a single nozzle to be precisely controlled with high-speed images to be captured of droplet ejection. The next printhead used in the experimental workflow is the Dimatix printhead which had 16 nozzles introducing extra complexity to printing due to possible cross-talk between adjacent nozzles and the 128 nozzle industrial printhead is examined last in the experimental workflow.

3.2.1 Microfab Printheads

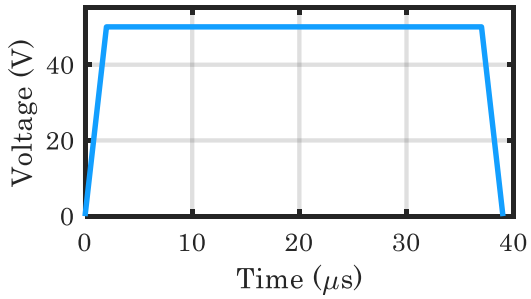

Figure 3.2: A typical square waveform used for inkjet printing with Microfab nozzles.

MJ–ABP–01 Microfab nozzles were connected to a JetDrive™ III and the JetServer™ software was used to control the waveform, typically a square waveform of varying pulse duration, typically between 30–60µs and amplitude voltage between 40–140V. The maximum frequency of the waveform is 1000Hz but a frequency between 150–250Hz was used to ensure that each droplet ejection event was independent. A typical square waveform used is shown in Figure 3.2.

The fluid reservoir consisted of an open 5ml luer lock syringe attached to a three–way valve which had a 2.5ml syringe in the horizontal position and an outlet attached to a 21–gauge needle. The horizontal syringe enabled fluid to be drawn in from the reservoir and to be expelled through the nozzle as a purge step. PTFE or ether–based polyurethane tubing formed a secure push fit to the nozzle inlet and 21–gauge needle. The fluid reservoir was attached to a screw which enabled mechanical control over the height and therefore hydrostatic pressure in the reservoir which enabled control over the meniscus level in the nozzle. The fluid should have a viscosity of <20mPa s according to the manufacturer's specifications [130].

3.2.1.1 Microfab Bovine Serum Albumin (BSA) Blocking

A sacrificial protein can be used to coat the material inside a printhead to saturate the surfaces. When another protein in the ink contacts the printhead surface, it will not adsorb due to the surface already being saturated with the sacrificial protein. This means that the active protein concentration in the ink will not be reduced when the ink makes contact and flows through the printhead.

To block a Microfab nozzle with bovine serum albumin (BSA) the nozzle is submerged in a 1wt% BSA solution in distilled water for 2 hours at room temperature. The nozzle is then air dried with compressed air.

3.2.2 Dimatix Materials Printer

A Fujifilm Dimatix Material Printer DMP–2850 was used with a Dimatix Materials Cartridge. The printer is actuated with a piezoelectric element mounted above the 16 square orifices with a side length of 21.5µm and 254µm spacing. The cartridge moves in an XY plane whilst the stage moves in the Z direction. The waveform used to generate droplets typically takes the form of a stepped square wave pulse as shown in Figure 3.3. The voltage amplitude can be varied between 0–40V and the ejection frequency can be varied between 1–15kHz. For optimised printing the fluid should have a viscosity of 10–12mPa s at jetting temperature, a surface tension of 2.2–2.8mN/m [32].

To determine the volume of printed droplets a pre–weighed glass slide is placed under the printhead and between 3–7 million droplets are ejected onto the slide depending on how many nozzles are firing. The glass slide is then weighed again, and the droplet volume is calculated by dividing the gain in mass by the number of droplets ejected.

The volume of droplets ejected with the DMP is around 10pl nominal which means they are susceptible to rapid evaporation. To prevent drying of protein

solutions the droplet volume was calculated using the method described above and droplet ejection is into a well plate containing 100µl of buffer solution.

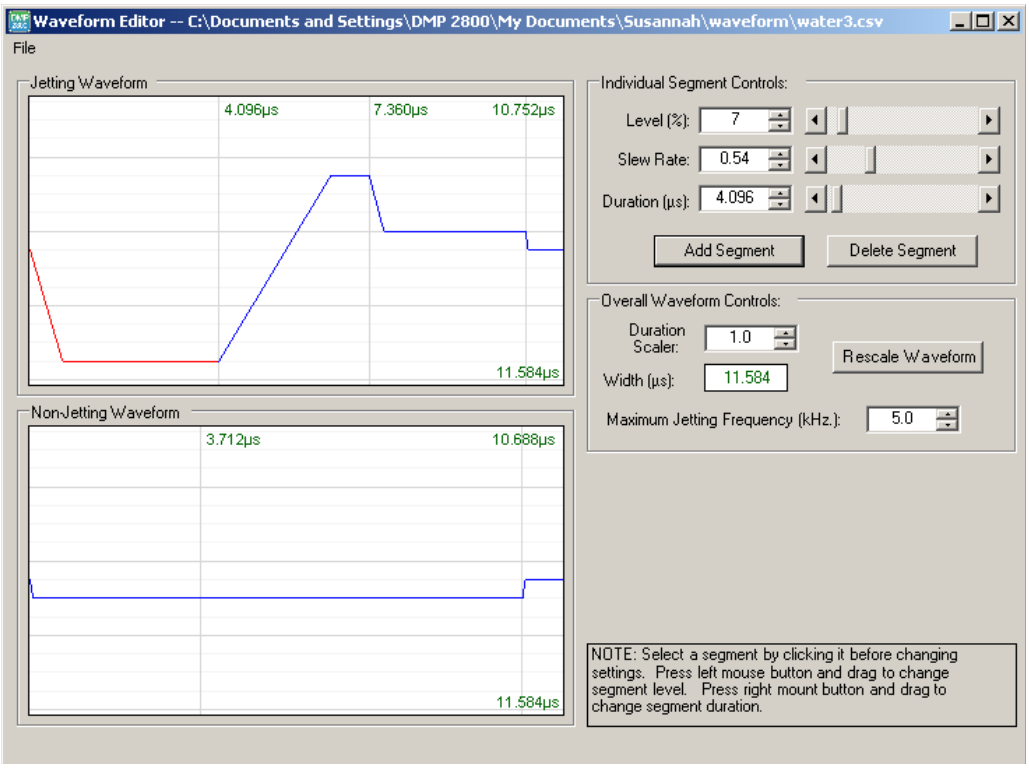

Figure 3.3: The shape of the jetting waveform used when printing with the DMP system.

3.2.3 Spectra SE–128 AA Industrial Printhead

A Spectra SE–128 AA printhead has two parallel channels each containing 64 nozzles of diameter 35µm with a 508µm spacing. Each nozzle jets droplets of 25–30pL in volume resulting in a resolution of up to 900dpi. Droplets are ejected with a nominal drop velocity of 10m/s with a standard deviation of ±5% at a jetting frequency of 40kHz. The ideal fluid viscosity is between 8–20mPa s. The printhead data is taken from the product data sheet [33]. Fluid was purged through the printhead to determine protein adsorption losses. To print with the printhead, a Pix–Dro LP–50 system was used.

3.2.4 Simulation of Inkjet Printing

COMSOL Multiphysics 5.4 is used and the level–set method and laminar flow modules are used. A 2D axisymmetric geometry is used which is shown in Figure 3.4 along with the boundary conditions. The wall and outlet, no flow boundary condition mean that the fluid velocity is 0 along these boundaries. The wall condition prevents fluid flowing through the wall. The initial fluid interface is where the ink and the air interface at the start of the simulation. The mesh for the model was generated using the physics-controlled meshing option with normal element size selected.

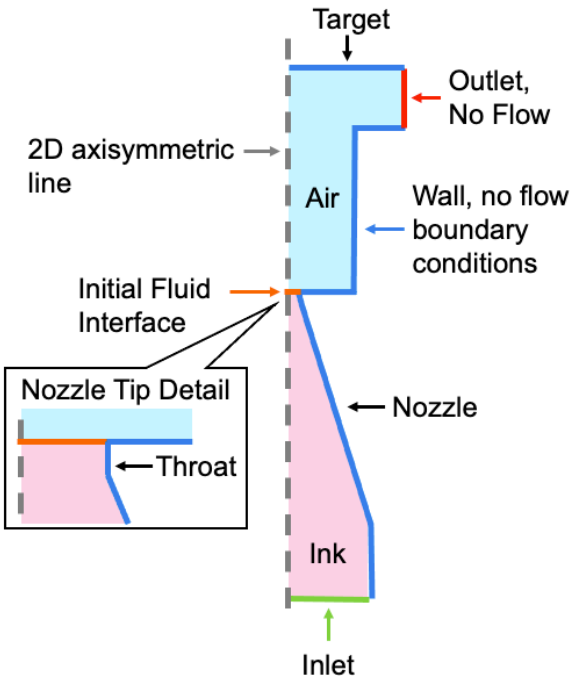

Name	Length (mm)	Description
InletR	0.1143	Inlet radius
InletL	0.211	Length from inlet to start of nozzle taper
NozzleL	0.64322	Nozzle length from tip to inlet
ThroatL	0.01	Tip length at the nozzle radius
NozzleR	0.015	Nozzle radius
AirW	0.1	Width of air channel, width of outlet
TargetL	0.4	Distance from nozzle tip to target

Figure 3.4: The geometry and boundary conditions for the inkjet simulation in COMSOL Multiphysics 5.4.

The input to the model is a built–in rectangular function, called rect within the software, with second derivative continuous smoothing and causes the ink to be forced through the nozzle as in an inkjet printer. To obtain velocity and shear rate values of the ink, filters are applied to isolate the ink.

3.2.5 Simulation of Extrusion

COMSOL Multiphysics 5.6 was used with the viscoelastic flow module. A stationary simulation based on an inlet velocity field taking the equation shown in equations 3.1 for the x and y direction. V_m is a constant that is changed for each flow rate. The viscoelastic fluid model used was Oldroyd–B.

$$x = V_m\left(1 - \frac{y^2}{4}\right) \qquad 3.1$$

$$y = 0$$

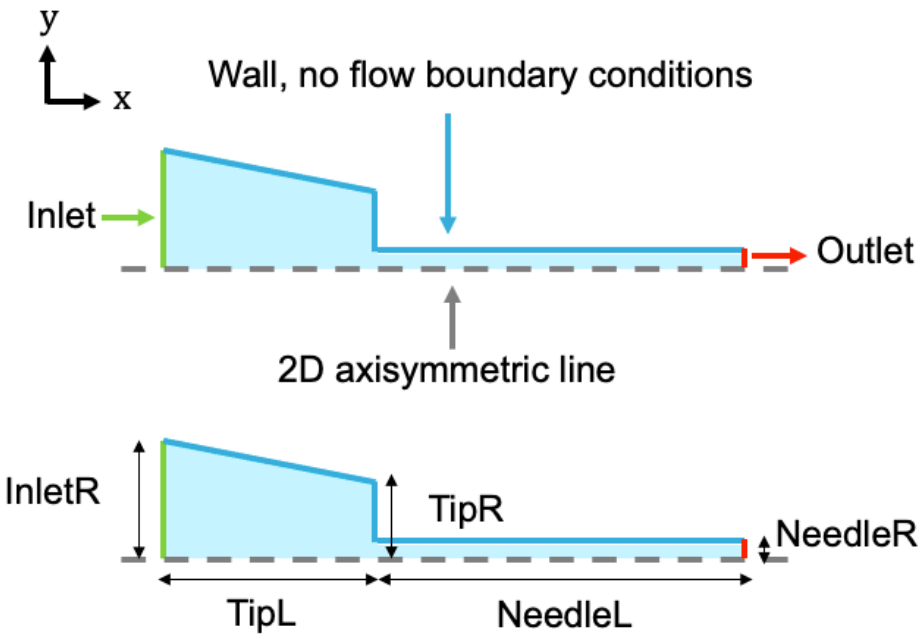

Figure 3.5: The geometry used for the extrusion simulation. The upper image shows the simulation boundary conditions for each of the edges of the needle geometry. The lower image labels the corresponding parameters that are defined based on the needle geometry.

The geometry and boundary conditions of the simulation are shown in Figure 3.5 with each of the geometric parameters detailed in Table 3.1. The geometry is based on the needles used for extrusion experiments which are detailed in section 3.3.3. The wall boundary condition prevents fluid flowing outside of the wall and at the wall there is the no slip condition so fluid velocity is 0. The mesh

for the model was generated using the physics-controlled meshing option with normal element size selected.

To ensure that the simulation was representative of the experiments conducted, the continuity equation, 3.2, where $\dot{Q}$ is the flow rate, A is the cross sectional area and v_{av} is the average velocity of fluid across the cross sectional area, was used to match the flow rate input to the syringe pump with the average velocity of the fluid at the outlet of the simulation, V_m was changed accordingly for each flow rate.

$$\dot{Q} = Av_{av} \qquad 3.2$$

Table 3.1: The geometry and boundary conditions for the extrusion simulation in COMSOL Multiphysics 5.6.

Name	Length (mm)	Description
InletR	2	The radius of the inlet.
TipL	3.675	The length of the plastic section of the needle.
TipR	1.8	The radius of the end of the plastic section.
NeedleL	6.35	The length of the metal needle
NeedleR	0.42 (18G) or 0.05 (32G)	The radius of the needle.

The physical material properties for the model are shown in Table 3.2. The solvent viscosity was chosen as the system is aqueous and the Oldroyd–B fluid viscosity was selected to be representative of the 3mg/ml collagen solution.

Table 3.2: Material Properties used for the viscoelastic fluid simulation.

Simulation Property	Value
Fluid Density	1016 kg/m^3
Solvent Viscosity	0.8 mPa s
Oldroyd–B branches	1
Oldroyd–B Fluid Viscosity	20 mPa s
Relaxation Time	0

3.3 Ink Formulation Evaluation

3.3.1 Rheology

An Anton Paar MCR 102 Rheometer was used with a cone plate attachment for protein solutions and a parallel plate for collagen gels. The operation of the rheometer for different samples is detailed in each sub section.

3.3.1.1 Parallel Plate Rheology of Collagen Gels

Collagen gels were prepared in–situ to minimise disturbances to the self–assembled fibre networks. Pepsin soluble 3mg/ml collagen was mixed with 0.01M NaOH and maintained at 4˚C until deposited onto the rheometer. Once the solution is on the rheometer, the temperature of the platform is increased to 37˚C and left covered with a solvent trap for 45 minutes to allow gelation. After the sample has gelled, the temperature of the plate is held at a fixed temperature for all subsequent tests.

To determine the limit of the linear viscoelastic region (LVE) for the sample, an oscillatory amplitude sweep was performed with constant shear stress from 0.01–100% shear strain and the resulting storage (G') and loss (G") moduli are measured. The LVE is calculated with a ±5% deviation (according to ISO 6721–10) around the plateau of the G' value.

3.3.1.2 Piezo Axial Vibrator (PAV) Rheology of Collagen Gels

A piezo axial vibrator (PAV) model TriPAV was used to determine the storage (G') and loss (G") moduli in the frequency range from 1 – 10,000Hz using a drive amplitude of 2V. The width of the shim was calibrated using an N35 viscosity standard. A sample volume of 80µl is required and a water cooling/heating system maintains the PAV at the desired temperature of 25˚C. The complex viscosity, η^* is calculated from the storage and loss modulus and is also linked to the linked to the frequency in radians/second, ω, by equation 3.3.

$$\eta^* = \frac{\sqrt{(G')^2 + (G'')^2}}{\omega} \qquad 3.3$$

3.3.1.3 Viscosity Measurements

A Viscolite 700 portable viscometer is used for measuring the viscosity of inks. The probe is submerged in the fluid and a viscosity reading is obtained.

3.3.1.4 Surface Tension Measurements

The SITA pro line t15 bubble tensiometer was used to determine the dynamic and static surface tension of fluids. The temperature probe and air capillary were submerged into the fluid. Air is pumped through the capillary into the sample fluid causing bubbles to form in the bulk. The air bubbles are compressed by the

fluid and the difference between the maximum measured pressure, when the bubble forms a hemispherical cap on the capillary, to the minimum, just before a new bubble begins to form on the capillary, is used to calculate the surface tension.

3.3.2 Flow through an Orifice Inkjet Setup

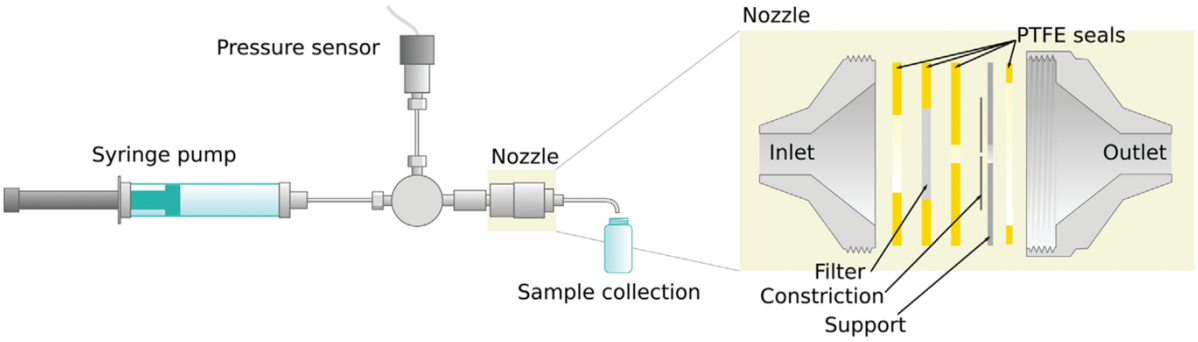

Figure 3.6: Schematic of the flow setup, figure from [131].

A setup created by Dr. Etienne Rognin, detailed in [131] and shown in Figure 3.6, was used as an experimental control to be representative of the forces endured by protein solutions, HRP, GOx and SOx, during the inkjet printing process. The sample is loaded into a syringe and the flow rate is controlled by a syringe pump. The sample flows through the apparatus, a pressure sensor is used to calibrate the setup and ensure there are no blockages in the system. The sample will flow to the nozzle, the narrowest constriction is 25µm in diameter, the sample is then collected for further analysis. To ensure that the surfaces are saturated with protein, a syringe is flowed through at a low flow rate initially before the flow rate is increased and further samples taken.

3.3.3 Flow through Extrusion Needle

A Harvard Apparatus syringe pump was used with an 8.95mm diameter syringe and 32G or 18G quarter inch needled attached. Flow rates of 30ml/hr, 45ml/hr or

90ml/hr were used, and extruded samples were collected in an Eppendorf for further analysis. The setup is shown in Figure 3.7. Collagen gels were prepared so that the gelation would occur when the samples were already loaded into the syringes. Pepsin soluble 3mg/ml collagen was neutralised with the neutralisation buffer in the ratio 9:1 and pipette mixed on ice. Pipette mixing involved pipetting the neutralised solution up and down three times with the pipette tip submerged to avoid the introduction of air bubbles. The samples were then loaded into syringes before incubation at 37 ˚C for 2 hours. Each sample of 100µl volume was loaded into a separate syringe.

Figure 3.7: The experimental setup used for extrusion and collection of collagen gels.

3.4 Image Processing and Acquisition Techniques

3.4.1 High Speed Imaging

For imaging the Microfab nozzles ejecting droplets a Phantom v310 high speed camera was used with a Navitar 12x extender attached to a Mitutoyo M Plan Apo 10x objective lens. The camera was kept at a magnification of 2.4311µm/pixel, measured by taking a snapshot of a 1mm calibration grid. The Phantom Camera Control (PCC) software was used for image acquisition and a minimum frame rate of 100,000 fps dependent on the frame size required to contain the entire droplet ejection event. The camera was either triggered manually or when synchronisation with a printing event was required, a 5V 50ms inverted square wave was used with a split output to trigger printing and image capture simultaneously. The high–speed camera was used to image droplet ejection with Microfab nozzles a schematic of the setup is shown Figure 3.8 and a photo of the rig is shown in Figure 3.9. The light source was a PhotoFluor II, 89 North®, USA.

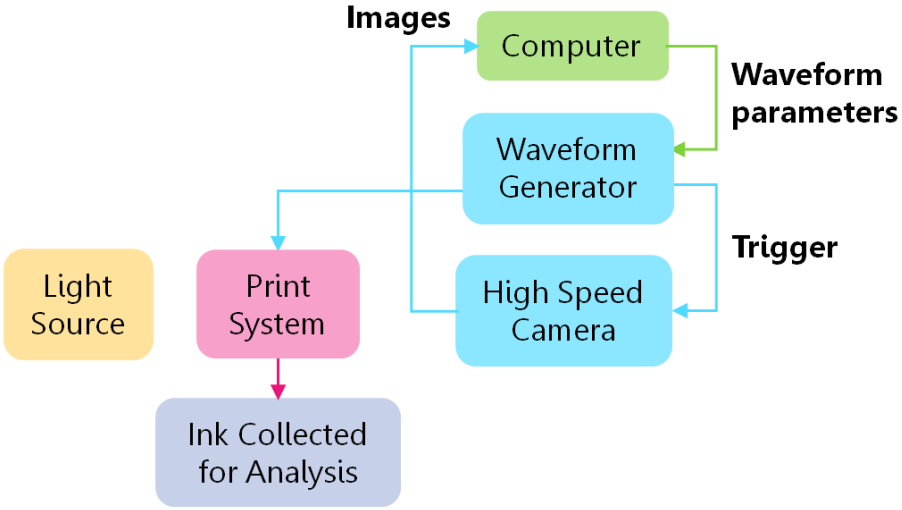

Figure 3.8: Schematic of the high–speed imaging setup with a Microfab print system.

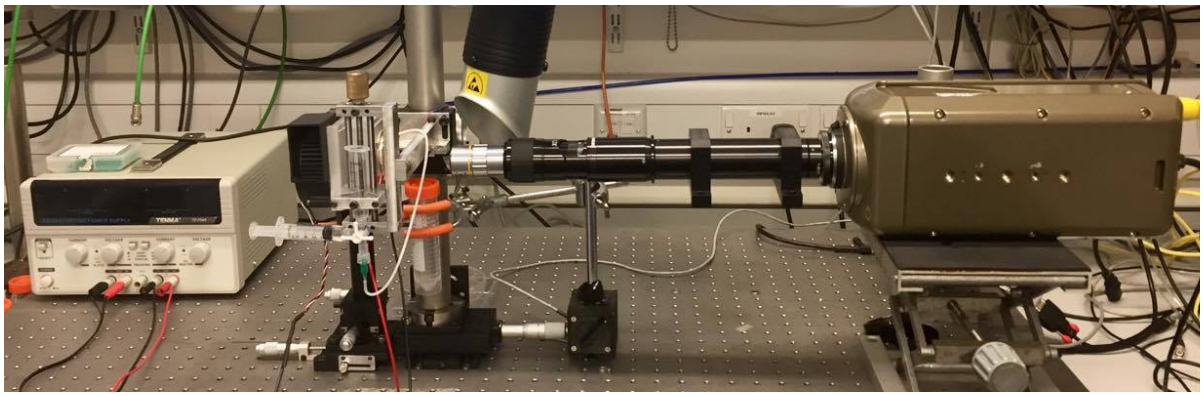

Figure 3.9: The experimental setup for highspeed imaging and inkjet printing with a Microfab print system.

To record videos of inkjet printed droplets drying a Phantom v7.3 high–speed camera, USA was used with a Navitar 12x extender attached to a Mitutoyo M Plan Apo 10x objective lens. A high intensity continuous light source, PhotoFluor II, 89 North®, USA, was used to provide illumination for image acquisition. The camera was kept at a magnification of 460 pixels/mm and a shutter speed of 40 fps was used. The camera was triggered simultaneously with the trigger of the MF printhead. The camera was positioned at an angle of 5° above the horizontal surface that droplets landed on.

3.4.2 High Speed Image Processing

All the images acquired with the high–speed cameras were in the cine format and the PCC software was used to convert the impact to bmp. All image processing was carried out using Matlab. The bmp images were firstly converted to grayscale, then converted to binary images, using predefined image thresholding functions in Matlab, so all images could be represented as logical matrices.

3.4.2.1 Droplet Generation

To isolate the fluid ejected from the nozzle, the following processing steps were executed with the code and are illustrated by Figure 3.10.

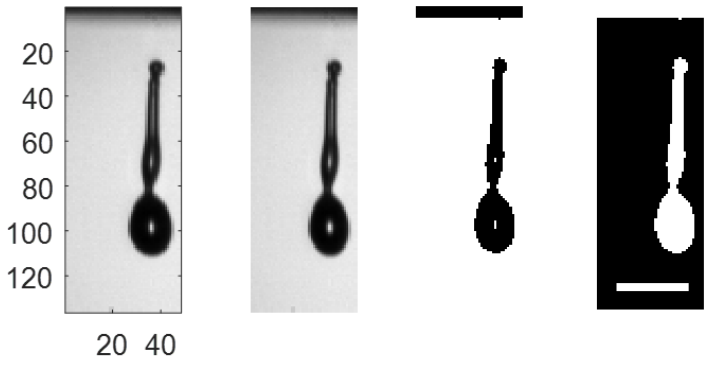

Figure 3.10: The process for taking a raw image fluid ejection, converting it into an 8 bit image, then converting it to a binary image and finally inverting the binary image. Scale bar 100μm.

1. Create an image mask of the nozzle with no fluid ejected, as shown in Figure 3.11.

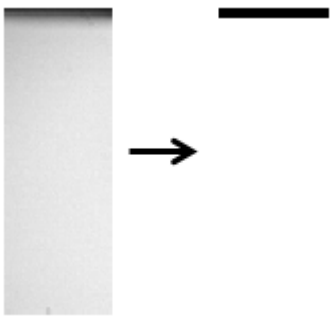

Figure 3.11: An image of the edge of the MF nozzle in grayscale which has then been turned into a black and white image to be used as a mask.

   a. The first image where no fluid has yet been ejected is selected.
   b. The image is converted to an 8–bit image.
   c. The image is converted to a binary image.
   d. Holes in the binary image are filled so there are only solid sections of black and white.

2. Using the image mask, determine the furthest Y coordinate of the edge of the nozzle. The image mask is shown in Figure 3.11.
3. Multiply the image mask with the binary image of the fluid ejected so that the pixels with ejected fluid take a value of 1 and are the only white areas in the resulting image.
4. The volume is calculated by summing discs of thickness one pixel.
5. The instantaneous velocity of the leading edge of the droplet is calculated by determining the distance from the furthest Y co–ordinate of the nozzle (step 2) to the furthest point of the droplet and dividing this value by the camera shutter speed. Subsequent images use the previous position of the droplet leading edge instead of the nozzle edge to calculate the distance travelled between images.

3.4.2.2 Droplet Drying

The following processing steps were used to determine the volume of a droplet that was ejected onto a glass slide over time.

1. The image is converted into a binary image.
2. The holes are filled in so there is a solid droplet including the reflection of the droplet.
3. The image is inverted so that pixels containing fluid are white instead of black and take the value of one.
4. The image is cropped where the droplet is at the widest point.
5. The volume of the droplet is calculated by assuming each row, of single pixel thickness, forms a disc and the sum of the volumes of the discs gives the overall droplet volume.

The processing steps are shown in Figure 3.12. In the droplet drying images 1mm is 460 pixels in length which was measured by taking a snapshot of a 1mm calibration grid, the scale bar is 0.5mm.

Figure 3.12: Images that show the processing steps for processing images of droplets drying. Scale bar is 0.5mm.

The volume of the droplet with time is then plotted and a linear fit using the predefined Matlab function polyfit is used to determine the volumetric rate of evaporation in time, which is the gradient of the linear part of the evaporation curve.

3.4.3 Scanning Electron Microscopy

A LEO GEMINI 1530VP FEG–SEM was used with EHT of 5kV and a working distance of 5mm. To prepare collagen samples for the SEM the following processing steps were taken.

1. Using 2wt% glutaraldehyde solution, leave the sample soaking immersed in the solution overnight, minimum 15 hours, to allow the sample to be fixed in place. The immersed sample is then placed on a shaker table rotating at a speed of 40rpm.
2. The glutaraldehyde solution of removed and the sample is then washed 3 times with 1x PBS. Washing consists of leaving the sample soaking in 1x PBS whilst remaining on the shaker table rotating at 40rpm and replacing the PBS after 15 minutes.
3. Solvent dehydration is then performed using increasing concentration of acetone, 30%, 50%, 70%, 90% and 100% for 15 minutes each and then repeated 3 times for the final concentration of 100%.
4. The sample is then mounted onto a silicon chip adhered to a SEM stud with silver paint.
5. The sample is then put into a desiccator for 2 hours to ensure any remaining moisture content in the sample is removed.
6. The sample is then sputter coated with a gold palladium target using an Emitech K575x sputter coater for 15 seconds at 65mA.

After images of collagen samples have been taken with the SEM further image analysis is carried out using ImageJ. The fibre diameters are measured manually using the scale bar on the SEM images for calibration. 101 manual measurements were made, and the data was collected and plotted in a box plot to show the distribution of the fibre widths with python.

3.5 Protein Analysis

3.5.1 Enzyme Assays

3.5.1.1 Colorimetric Detection with ABTS

The activity of HRP, GOx and SOx was measured with the colorimetric indicator ABTS, each reaction scheme is shown in Figure 3.13. The absorbance of 415nm light, the peak absorbance wavelength of oxidised ABTS, was measured over time with a Lambda 750 Perkin Elmer UV/VIS/NIR Spectrometer which measured the absorbance every second for 50 seconds or an Infinite M200, Tecan platereader which measured the absorbance every 4 seconds for 2 minutes.

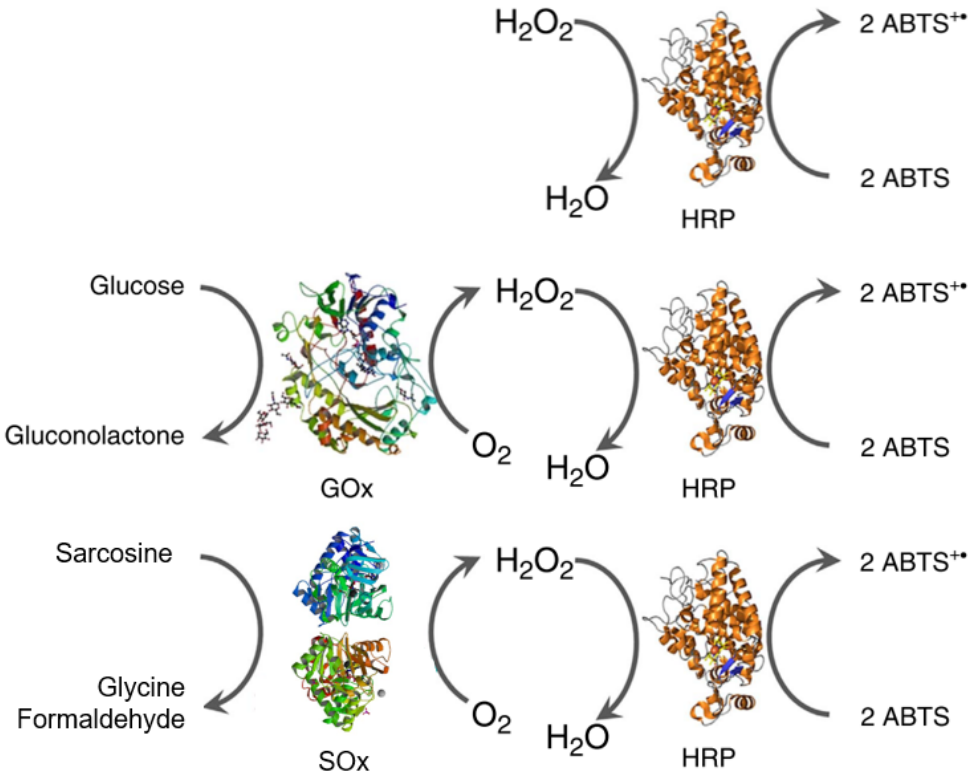

Figure 3.13: The reaction scheme for HRP, GOx and SOx with ABTS.

The resulting absorbance data is processed with a Matlab code. The files are imported in .csv format, the code reads each data file and finds the gradient of the slope. As each reading is done as triplicates the average slope for triplicates is calculated and the standard deviation for each triplicate as well. The gradient is then multiplied by a constant to give the reaction velocity in nM/s, as shown in equation 3.4, where l is the path length of the cuvette, in all instances it is 1cm, ε is the molar excitation constant which for 415nm takes a value of 36 $mM^{-1}\,cm^{-1}$ and the factor of 2 on the denominator is to account for 1 mole of hydrogen peroxide reacting to form 2 moles of ABTS.

$$Velocity = \frac{d(Absorbance)}{dt} \times \frac{1}{2\varepsilon l} \qquad 3.4$$

The final concentrations of the assays are show in Table 3.3.

Table 3.3: The concentration of reagents in the assay with HRP, GOx and SOx.

[HRP] (nM)	**[ABTS] (mM)**	**[H_2O_2] (mM)**	
1	1	200	
[GOx] (nM)	**[ABTS] (mM)**	**[D–Glucose] (M)**	**[HRP] (nM)**
1	2	0.1	50
[SOx] (nM)	**[ABTS] (mM)**	**[Sarcosine] (mM)**	**[HRP]**
10	1	150	50

3.5.2 Structural Analysis

3.5.2.1 Fourier Transform Infrared

A Frontier Perkin Elmer FT–IR Spectrometer was used with the basic instrument setup using a wavenumber of 4000cm^{-1} and a resolution of 4cm^{-1} to measure the absorbance of infrared light in a range of 650 – 4000cm^{-1}. To setup the instrument a background reading with no sample on the plate was taken which was accounted for in readings with a sample on the sensor. Samples were obtained by depositing a droplet of 50µl onto the sensor. Samples to be tested were either pure water, buffer or GOx solutions.

When analysing protein-based samples, there are certain characteristic bands to observe [132]. The repeating sub-units of protein chains are known to produce up to 9 characteristic bands. The strongest adsorption in proteins is due to the amide I band, with a peak in the range of 1600 – 1700cm^{-1} dependent on the backbone confirmation. This band is predominantly due to the stretching vibration of the C=O bonds, with some contribution from the C–N bonds. The amide II band, located between 1510 – 1580cm^{-1}, is due to a combination of N–H bending and C–N stretching. The amide III band that is pictured in Figure 3.14 is more complicated and due to contributions from side chains and hydrogen bonding.

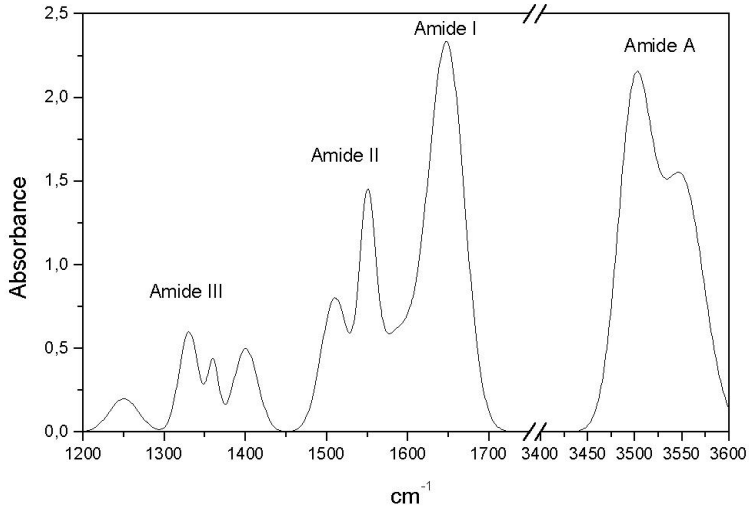

Figure 3.14: An example FTIR spectra showing the main relevant peaks for protein analysis [133].

3.5.3 Statistical Analysis

For the experimental work a minimum of 3 repeats are taken for every sample unless otherwise stated. The mean and standard deviation were calculated using Matlab for the experimental work in chapter 5 and 6, and in python for experimental results in chapter 4 and 7.

Chapter 4 Linking Experiments to Simulations: Using an Inkjet Simulation to gain insight into High Speed Image Data.

4.1 Introduction

When a droplet of fluid is ejected from an inkjet printer, the fluid undergoes shear and extensional forces. It is reported that shear rates are of the order of magnitude of 10^5 s^{-1} in DoD inkjet printers [1]. However, the shear rate will not be uniform during droplet generation and high shear rates have been reported as a likely cause of damage to biological materials contained in functional inks [5]. It is currently very challenging to both quantify the maximum shear experienced during printing and understand the percentage of the functional material that experiences this level of force. The goal of this chapter is to set up a close link between experimental images of printed bioinks and simulations, to allow these forces to be mapped out. This understanding could become an essential tool for validating reasons for changes in activity during bioprinting results and this work has not yet been carried out in the field.

This chapter will use COMSOL Multiphysics to carry out simulations to examine the velocity and shear rate experienced by ink during the inkjet printing process and examine how variables chosen for printing effect these resulting variables.

In Chapter 2, section 2.2.2 there are examples of previous research that have correlated the shear rate with conformational changes to protein structure. Although the results for different studies varied, a general trend for studies that observed aggregation or structural change was that a greater shear rate resulted in a more significant conformational change. This provides a basis for investigation of the shear rate that the ink endures during inkjet printing and if a conformational change occurs, it is more likely to occur when the shear rate is higher.

The printing variables examined in this chapter are (i) the pulse amplitude, representative of the voltage for a piezoelectric device, (ii) the time taken to reach the peak amplitude, (iii) the nozzle diameter, and (iv) the ink viscosity. Simulation results are compared with images from inkjet printing experiments with water based bioinks containing horse radish peroxidase (HRP), glucose oxidase (GOx) and sarcosine oxidase (SOx) to build a better understanding of the forces endured by these proteins during droplet generation. Before each of these parameters is examined in this chapter, the simulation setup will be described to show how it is relevant for gaining insight into the inkjet printing process.

4.2 DoD Inkjet: Droplet Ejection

Drop–on–demand inkjet is presented in section 2.1.1.2 where a thermal or piezoelectric actuator is used to generate a droplet. The droplet forming process can be separated into three distinct phases: head droplet formation, tail formation and tail break–up/ pinch off. These stages are illustrated in Figure 4.1 for a bioink printed from a Microfab printhead.

During head formation, which forms the bulk of the resulting droplet, the head will continue to grow until the velocity of the ink in the nozzle is less than the velocity of the droplet. The ink that is not travelling at a high enough velocity to

reach the head will still be ejected and form the resulting tail. The radius of the tail ligament that connects the droplet to the ink in the nozzle, will decrease in radius during the ejection event. At some point along the tail, the radius will reach a zero value and pinch–off will occur. The location of the first pinch off could be at the lower end of the tail, connecting the tail to the droplet, pictured in Figure 4.1 or it could be higher up the tail connecting the ligament to the ink in the nozzle. If pinch–off has occurred in both locations, the tail then breaks up into smaller droplets, known as satellites, and these droplets may be travelling at a sufficiently high velocity to remerge with the head droplet. An undesirable printing outcome is when the droplets do not merge by the time the head droplet impacts with the substrate and the satellite droplets land in a different location.

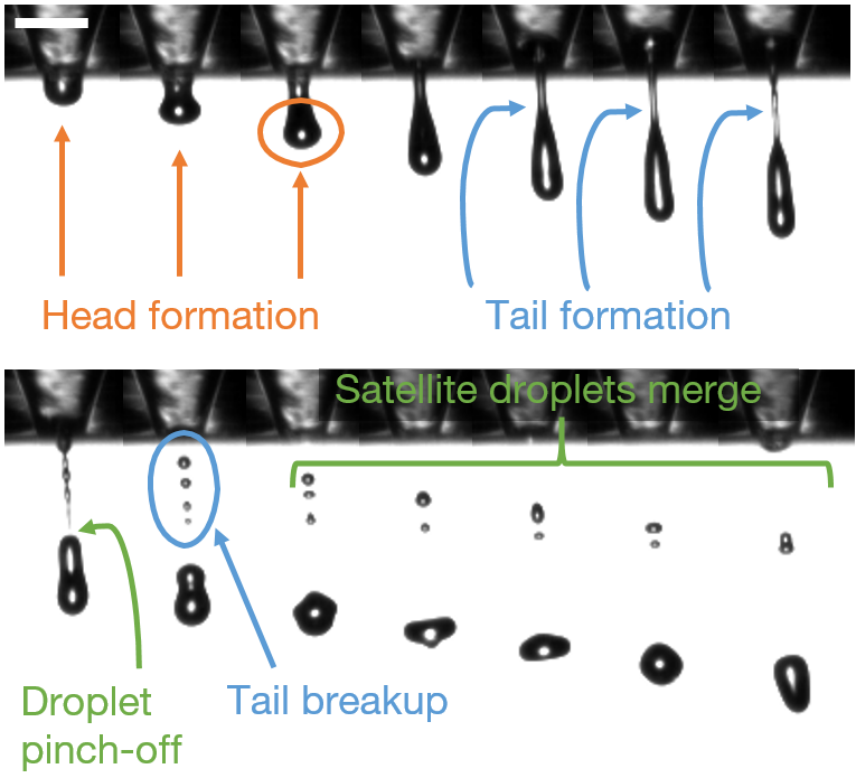

Figure 4.1: the main elements of a droplet forming event – head formation, tail formation, droplet pinch–off, tail breakup and satellite droplets merging. Scale bar is 50μm.

4.2.1 Simulation Details

For a given print system, the droplet morphology is affected by (i) the pulse amplitude, representative of the voltage for a piezoelectric device, (ii) the time taken to reach the peak amplitude – for piezoelectric actuation, the waveform used and for thermal actuation the configuration of the heating pulse, or pulses. (iii) the nozzle diameter, and (iv) the ink viscosity. discussed in 2.1.2. By simulating the inkjet printing process, these aforementioned trends can be examined, the velocity and shear rate within ejected droplets can be determined and the simulation can be used to apply this understanding to images obtained from inkjet printing with inks containing enzymes.

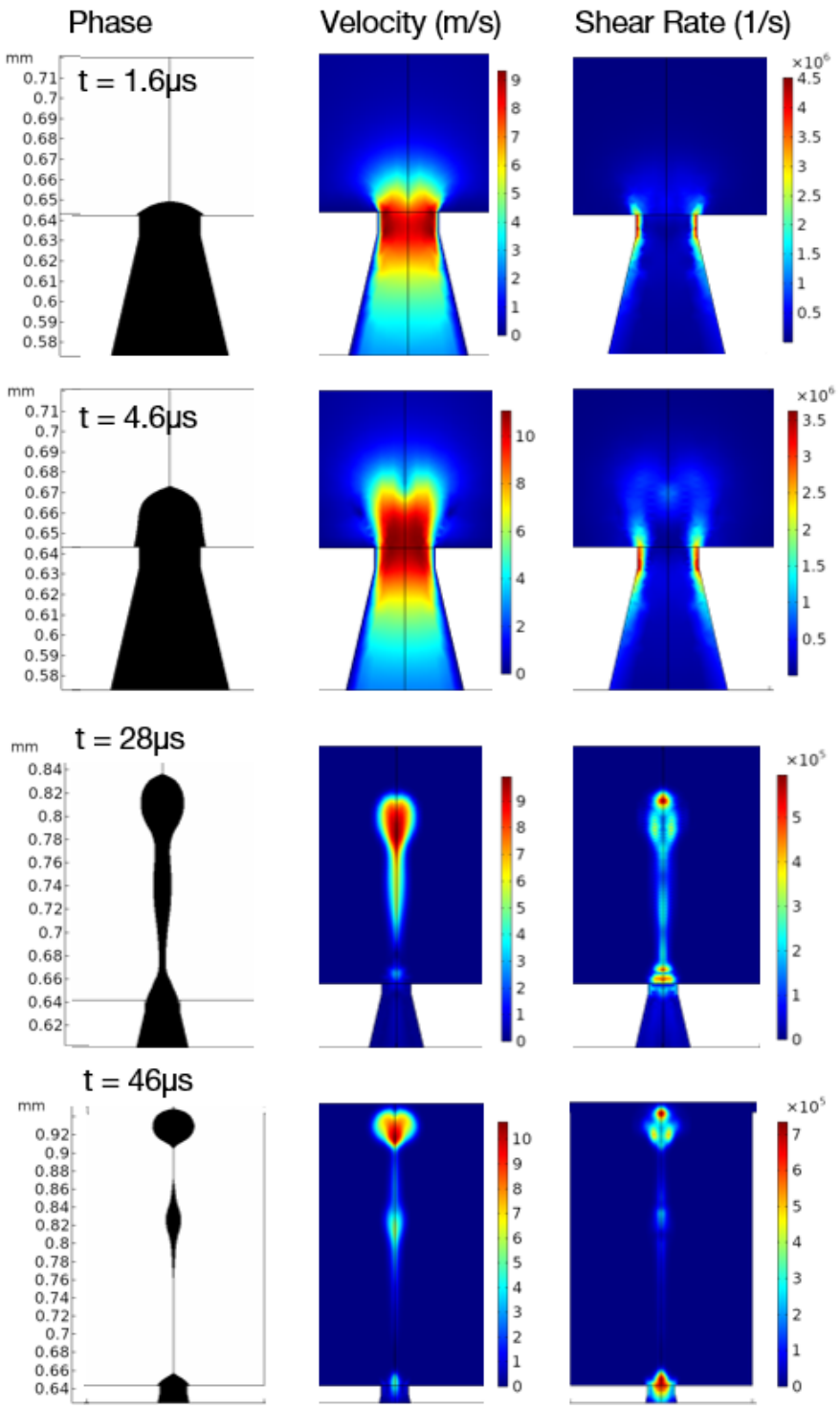

Figure 4.2: Images showing the phase, velocity and shear rate of simulated inkjet droplets, ejected with 0.1425 amplitude, at different time points. The top row is where the maximum shear rate occurs, the bottom row where the maximum velocity is measured.

A simulation of droplet ejection from a drop–on–demand inkjet printer was created with COMSOL Multiphysics 5.4, detailed in 3.2.4, using the level set and laminar flow packages. The surface plots shown in Figure 4.2 show results from the simulation in terms of the droplet morphology and phase, the velocity and shear rate at different timepoints of the drop ejection process. The results in Figure 4.4 show how the maximum velocity and maximum shear rate of a droplet changes during droplet generation. The shape of the input used to generate a droplet is shown in Figure 4.3 and the dashed lines indicate the time stamp of the simulation images displayed in Figure 4.2. The input is a rectangular pulse that triggers the droplet ejection process at the inlet to the nozzle, the amplitude is representative of the voltage in a piezoelectric printhead. The values of 0.1425 and 0.09 are scaling factors for the rectangular pulse that originally has a peak amplitude of 1 and second derivative continuous smoothing. These values represent the amplitude of the input waveform, in the case of a piezoelectric printhead, the voltage. The value of 0.1425 represents a greater amplitude, hence higher voltage input waveform than the 0.09 scaling factor. Shear rate is defined as the rate at which layers of a fluid move past each other, shown in equation 4.1.

$$Shear\ Rate = \frac{Relative\ Velocity}{Distance} \tag{4.1}$$

The maximum shear rate peaks early in the head formation phase before the maximum velocity of the ink is reached at t = 1.6μs and is located through the internal walls of the tip of the nozzle. The no slip boundary condition assumes that the velocity of the fluid that is in contact with the nozzle walls will have a relative velocity of zero which is evident in Figure 4.2 for the images at 1.6μs and 4.6μs. Despite the ink having a greater velocity magnitude at t = 4.6μs because the faster moving ink is no longer located within the nozzle the shear rate endured by the ink is consequently lower. Between 1–12μs during droplet

ejection, where the shear rate is reaching its peak value and an intermediate plateau is most likely to be when a protein conformational change would occur.

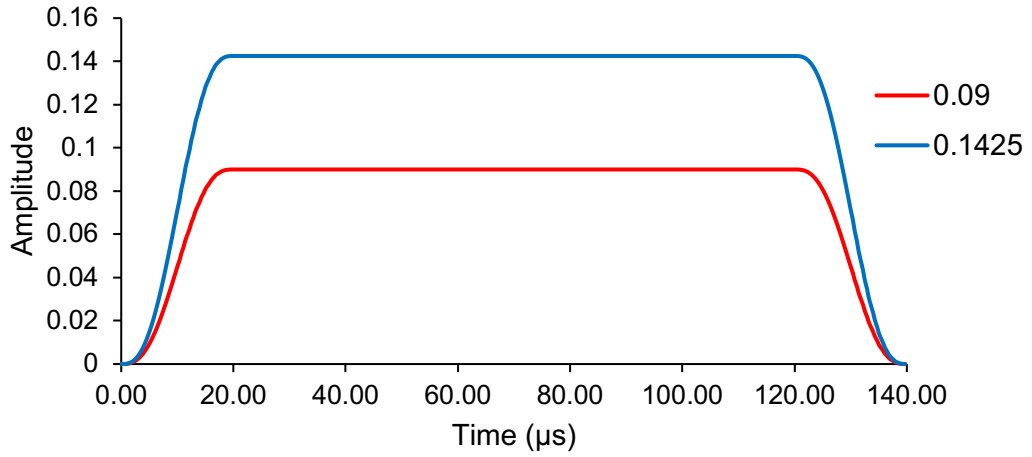

Figure 4.3: Examples of two of the input waveforms used in simulations in this chapter. The values differentiating them are the scaling factors used to adjust the waveform.

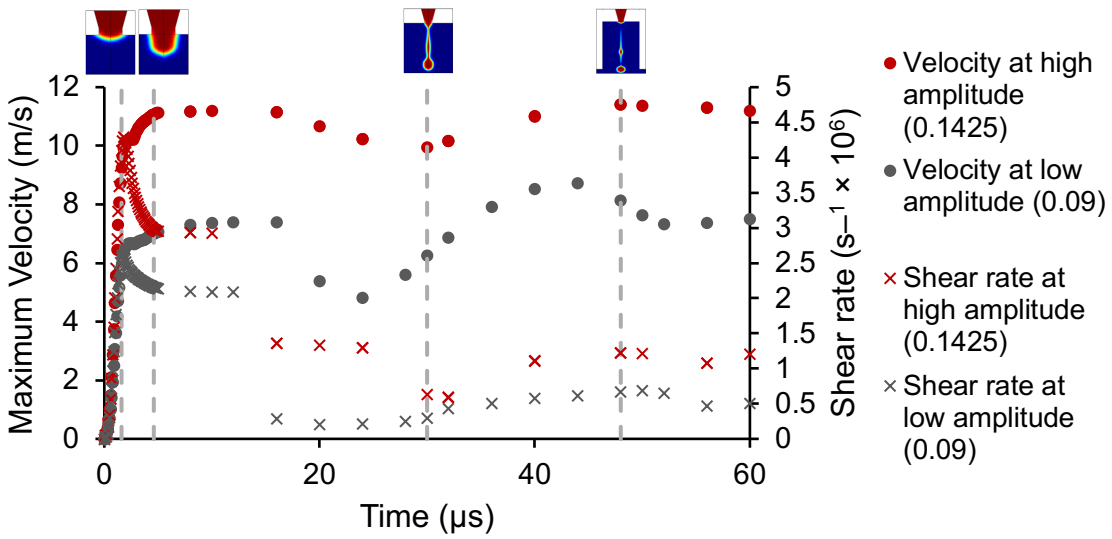

Figure 4.4: The maximum velocity (V), circles, and maximum shear rate (SR), as crosses, of a droplet in time measured with a simulation using a rectangular wave input with amplitude of 0.1425 and 0.09.

4.3 Parameters affecting Droplet Formation

There are four main parameters that can affect the droplet morphology when ejecting a single droplet that will be considered in this section: (i) the pulse amplitude, representative of the voltage for a piezoelectric device, (ii) the time taken to reach the peak amplitude, (iii) the nozzle diameter, and (iv) the ink rheology. When considering droplet ejection at an industrial scale, where printing can occur in the order of magnitude of 10kHz from each nozzle, the frequency of droplet ejection must be considered to avoid interference between droplet ejection events. A critical frequency that sets the limit for the highest frequency of droplet ejection without interference can be determined experimentally. In general, higher viscosity inks can be ejected with a higher jetting frequency due to a greater propensity to dissipate the energy from reflected acoustic waves in the nozzle [134]. Further consideration of the jetting frequency is outside the scope of this chapter because the trends are considered with respect to a single droplet. When printing with the Microfab a frequency between 150 – 250Hz was used but kept constant for all samples within an experiment set, for the DMP a frequency of 1kHz was used.

4.3.1 Waveform

For piezoelectric DoD devices, a trapezoidal waveform is the simplest input and is illustrated in Figure 4.5. The gradient of the rising edge of the rectangular input is often referred to as the slew rate. To reduce interference between droplet generation from each input, residual acoustic waves inside the nozzle can be dampened by an echo which is of equal amplitude in the negative voltage range directly after the initial positive voltage input. The rise and fall time will be equal when the rectangular pulse is symmetrical and can be referred to as the slew duration. In this section the impact of the pulse amplitude and slew

duration is examined by changing the simulation input that is representative of these parameters.

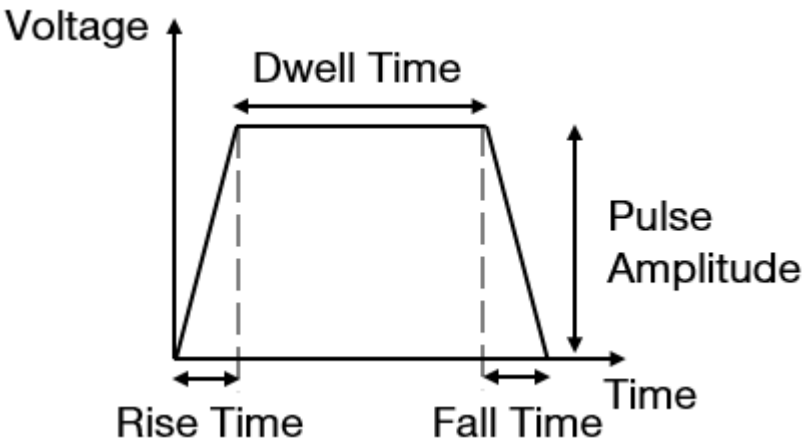

Figure 4.5: A trapezoidal waveform which can be used for a piezoelectric DoD inkjet printer. The key features of the waveform are indicated.

The software used for the inkjet printing simulation, COMSOL Multiphysics 5.4, uses finite element modelling – the entire geometry is subdivided into smaller sections that do not overlap, otherwise known as a mesh. Using a smoothing function for the input waveform ensures that are no discontinuities making it more representative of a real–life application. Second derivative smoothing of 2μs in duration is used unless specified otherwise.

4.3.1.1 Waveform Amplitude

To consider the effect that the pulse amplitude has on the resulting maximum velocity and maximum shear rate endured by the ink, the trapezoidal input was multiplied by a scaling factor that is referred to as the input amplitude. As highlighted in Figure 4.4, by using a scaling factor the dwell time and slew durations remain constant with a 2μs second derivative smoothing, but the slew rate changes because of the changing pulse amplitude. Previous research has shown that the relationship between the dwell time and droplet volume is not

linear and shows a periodic, oscillatory behaviour [135] [136]. Consequently, the dwell time is kept constant and the effect of changing the slew rate is examined in 4.3.1.2.

Subsequent results in this section use a trapezoidal waveform with a rise and fall time of 2μs and dwell time of 9μs with varying amplitudes, two examples of these waveforms are shown in Figure 4.4. The graph shown in Figure 4.6 indicates that increasing the input amplitude of the pulse increases both the maximum shear rate and maximum velocity of the ink during droplet ejection. The range of amplitudes examined in the simulation was chosen to be representative of inkjet printing of aqueous biofluids and is discussed further in section 4.4. The maximum shear rate increases approximately linearly whilst the maximum velocity increases to a lesser extent for greater pulse amplitudes.

The graph in Figure 4.7 indicates that for increasing pulse amplitude the droplet volume increases linearly. This result has been verified experimentally [137] and indicates that the simulation is consistent with experimental inkjet printing.

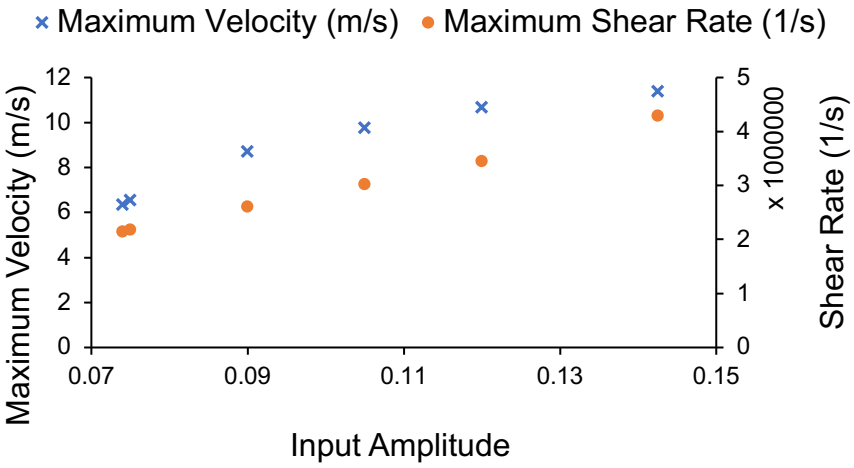

Figure 4.6: The impact of the resulting maximum velocity and shear rate experienced by an inkjet printed droplet due to varying pulse amplitude.

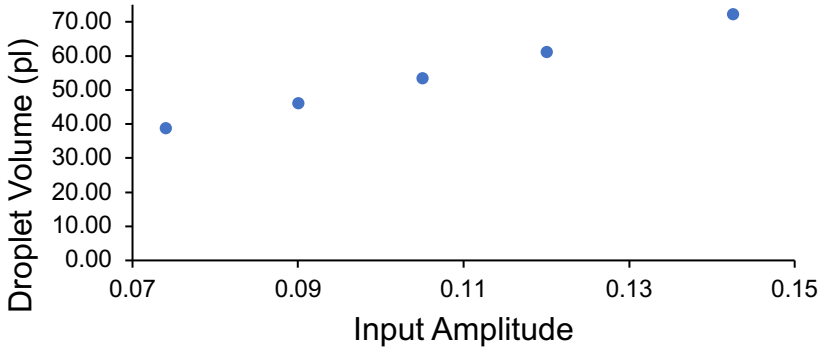

Figure 4.7: The volume of droplets ejected with different trapezoidal pulse amplitudes in an inkjet simulation.

4.3.1.2 Waveform Slew Rate

A symmetrical trapezoidal input with smoothing is used with equal rise and fall time, referred to as the slew duration. Changing the length of smoothing, changes the slew duration. A premade "rect" input was used from COMSOL Multiphysics 5.4, a rectangular shaped function with edge smoothing shown in Figure 4.3. The upper and lower limit of the function defines where the signal reaches 50% of its peak amplitude. The lower limit was 1μs and the upper limit 13μs. Transition durations of 1–2.5μs are examined, representative of the slew duration. The graph in Figure 4.8 shows the effect on the maximum velocity and maximum shear rate due to changing the slew duration. The change in maximum velocity is 0.12m/s across all the slew durations which is insignificant, but the maximum shear rate decreases as the slew duration increases.

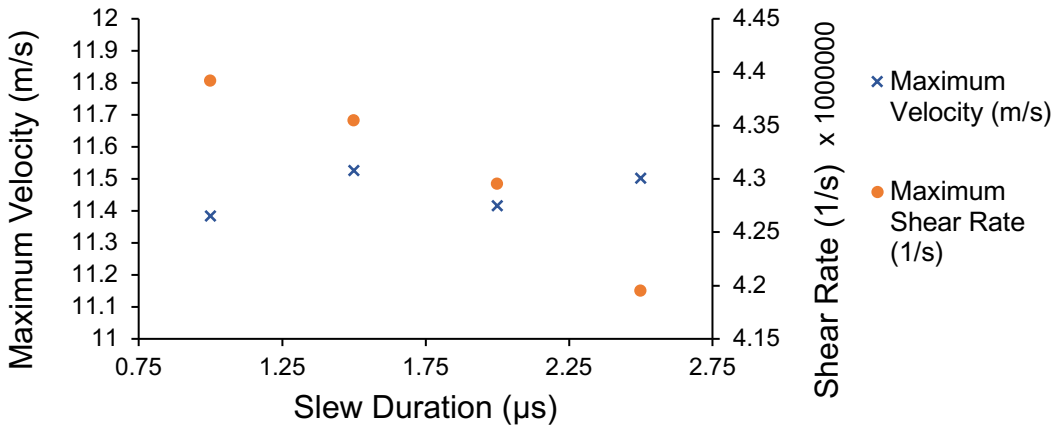

Figure 4.8: The effect of the slew rate of the rectangular pulse input has on the maximum velocity and shear rate in an inkjet simulation.

Because the point at which the amplitude reaches 50% of its maximum is fixed for all slew durations, the maximum shear rate over time for all durations overlaps at 1µs as shown in Figure 4.9. The transition zone means that for shorter slew durations, the signal start is slightly delayed, but the peak is also reached sooner. The smaller slew duration results in a faster rate of change of velocity in the fluid resulting in a steeper velocity gradient at the nozzle wall and hence a larger shear rate for small slew durations.

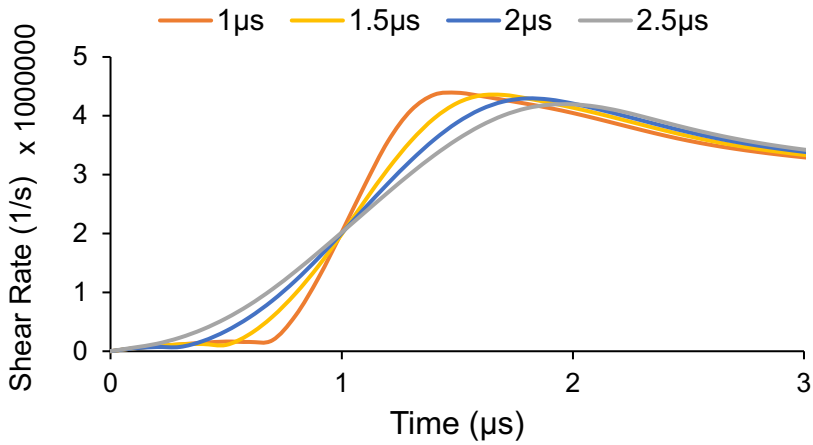

Figure 4.9: The shear rate in time across the four different smoothing durations.

The impact of changing the slew duration does not have a significant effect upon the resulting droplet volume. For a slew duration from 1 – 2.5μs the droplet volume remained at 72.5pl.

4.3.2 Nozzle Orifice Diameter

The orifice is the narrowest point within the printhead and location where fluid is ejected and forms a droplet. The orifice diameter is the limiting factor of the droplet volume and resolution of ejected droplets but fluid passing through a narrower channel has implications for the resulting force endured by the fluid as highlighted in Figure 4.10: The effect that changing the orifice nozzle diameter has on the resulting maximum velocity and shear rate in an inkjet simulation. The graph shows that for increasing nozzle diameter the maximum velocity and maximum shear rate decrease, initially more quickly and converge towards a plateau for orifices between 20–40μm in diameter. All other geometries are unchanged for these simulations and the same rect input waveform with 0.1425 scaling factor is used for each diameter.

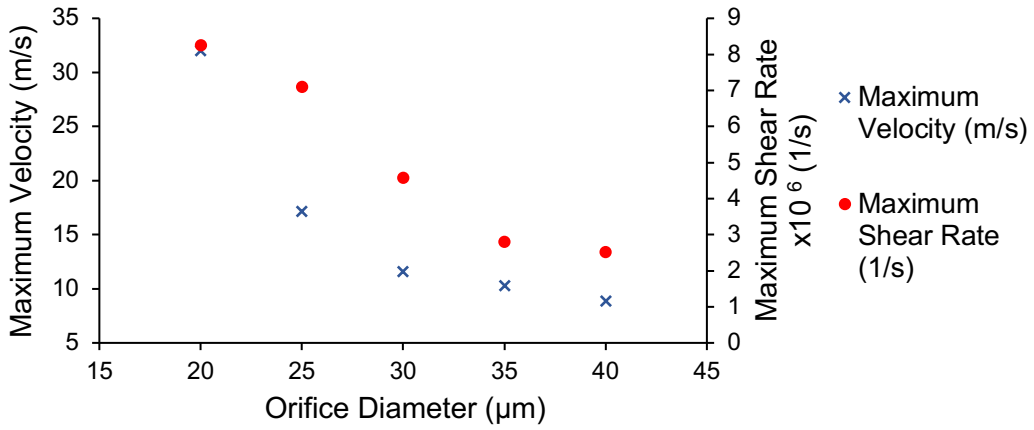

Figure 4.10: The effect that changing the orifice nozzle diameter has on the resulting maximum velocity and shear rate in an inkjet simulation.

There was an insignificant change on the ejected droplet volume attributable to using the same input for each simulation. However, in practise a user would adjust the waveform dependent on the nozzle geometry and the limiting size of a droplet is determined by the orifice diameter and nozzle geometry [23].

4.3.3 Ink Characteristics

An input with pulse amplitude 0.1425 with 2μs smoothing and upper and lower limit of 1μs and 13 μs was used and the viscosity of the simulated ink was varied from 1 – 45 mPa s, above 45mPa s with these input conditions there was insufficient energy for a droplet to form. The graph in Figure 4.11 shows the changes in the maximum velocity and maximum shear rate with ink that has different viscosity. The maximum velocity increases non–linearly with viscosity tending towards an asymptotic value of ~15m/s. The shear rate decreases non–linearly towards a value of 2 x 10^6 s^{-1}.

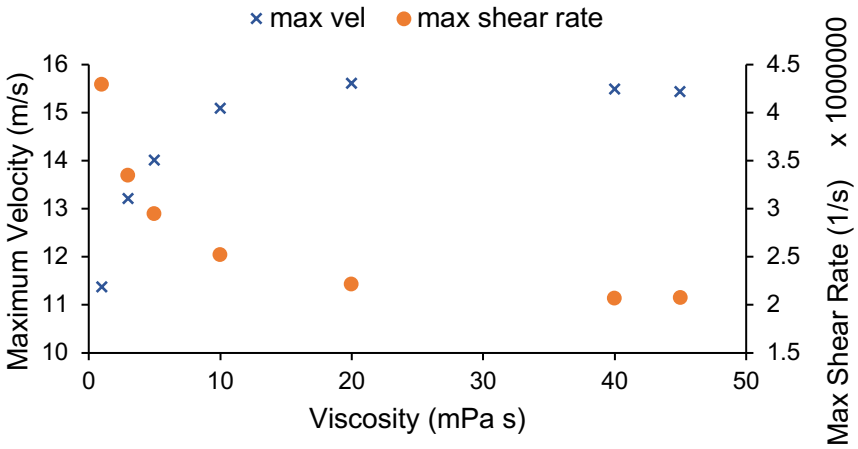

Figure 4.11: The impact on the maximum velocity and maximum shear rate determined with an inkjet printing simulation using ink with different viscosity.

The maximum shear rate is always located at the end of the nozzle at the inner walls in all simulation cases and will be due to the no–slip boundary condition on the nozzle walls. The surface plots in Figure 4.12 show the ink velocity at t = 2μs for 4 different ink viscosities. The plots show that although the higher viscosity inks have a greater maximum velocity, there is a smaller volume of ink travelling at this velocity and the peak velocity is closer to the axis of symmetry. Lower viscosity inks therefore result in a higher maximum shear rate because ink moves with a higher velocity closer to the inner wall of the nozzle than the higher viscosity inks.

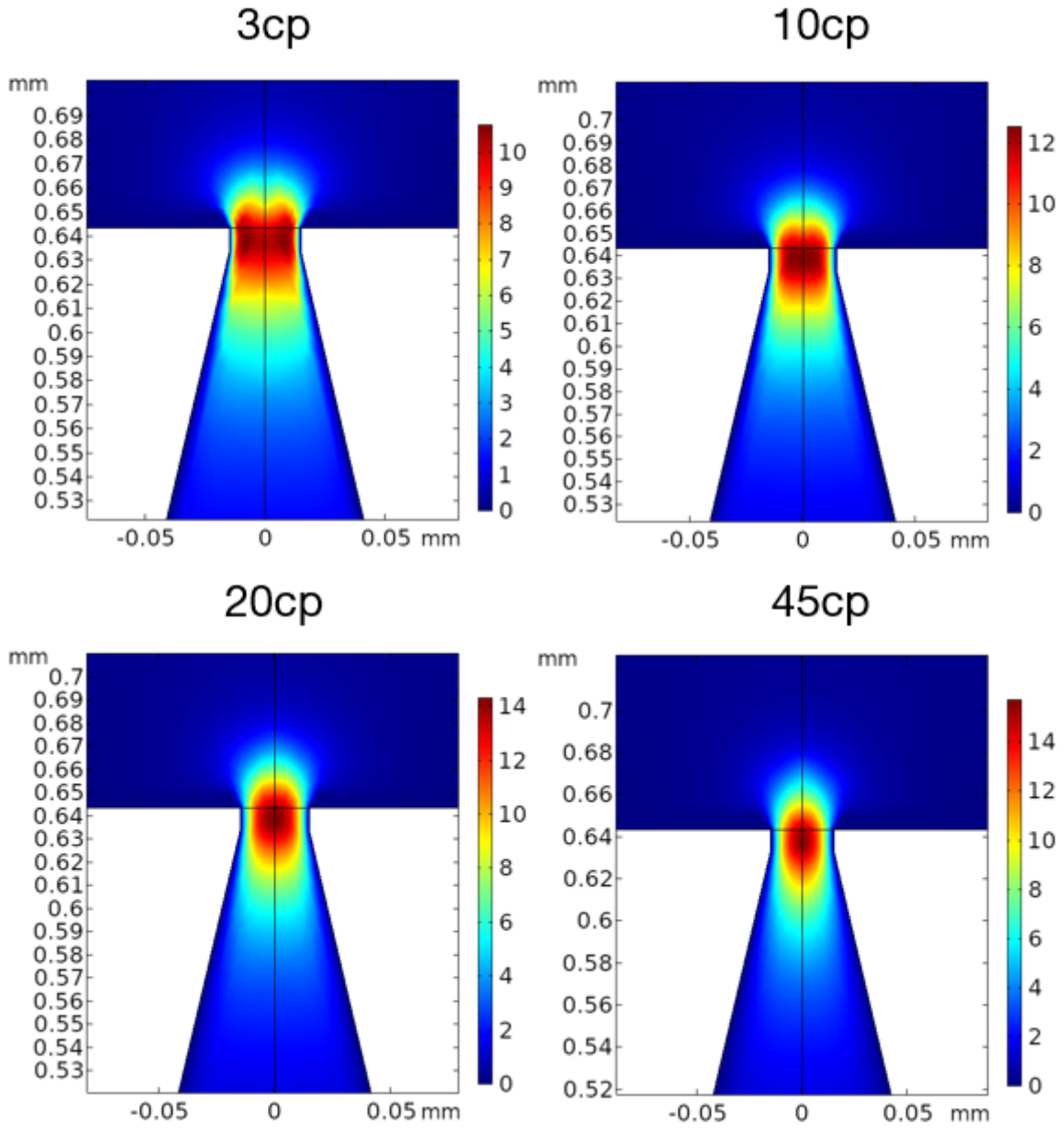

Figure 4.12: The velocity profile of the ink at t = 2μs for simulations using the same input but changing the viscosity of the inks, stated above each graph. The velocity is in m/s.

Changing the viscosity of the ink in the simulation has no significant effect on the resulting droplet volume.

4.3.4 Summary

The parameters that effect the resulting maximum measured velocity and shear rate during an inkjet printing simulation were (i) the pulse amplitude, representative of the voltage for a piezoelectric device, (ii) the time taken to reach the peak amplitude, (iii) the nozzle diameter, and (iv) the ink viscosity. A summary of the results and trends observed in this section are presented in Table 4.1.

Table 4.1: A summary of the impact of changing a given printing parameter on the maximum velocity and maximum shear rate observed in an inkjet printing simulation.

Parameter	Max. Velocity	Max. Shear Rate	Volume
Pulse Amplitude (0.074 – 0.1425)	Non– linear increase from 6 to 12 ms^{-1}.	Non– linear increase from 2 x 10^6 – 4.5 x 10^6 s^{-1}.	Linear increase from 40 to 70pl.
Slew Duration (1 – 2.5μs)	No significant change	Linear decrease from 4.4 x 10^6 – 4.2 x 10^6 s^{-1}.	No significant change.
Nozzle Orifice Diameter (20 – 40μm)	Power law decrease, converging to ~9ms^{-1}.	Power law decrease converging to ~2 x 10^6 s^{-1}.	No significant change.
Ink Viscosity (1 – 45mPa s)	Power law relationship converging to a peak value of ~15.5ms^{-1}	Power law relationship converging to a minimum value of ~2 x 10^6 s^{-1}.	No significant change.

4.4 Comparing Printing Images to a Simulation

As highlighted in section 2.2, a frequently cited concern when using inkjet printing containing biological materials such as cells or proteins, is damage to the printed active material. Attempts to quantify the shear rate required to produce a conformational change to protein structure are detailed in 2.2.2, concentric cylinder devices are frequently used [89]–[92], [94] along with AFM [93] and laminar flow through a narrow capillary [88]. Studies that have used inkjet printers to determine protein loss of activity often fail to provide an analysis of the forces the ink is undergoing that could contribute to the measured loss of activity. By examining high speed images of inkjet printed HRP, GOx and SOx and comparing these images to an inkjet simulation a clearer picture of the forces the ink endures can be built in these applications. This section will address this research gap, the disjoint between experimental protein activity measurements and detailed analysis of the droplet morphology and forces endured by the fluid during inkjet printing, by using measured instantaneous velocity values of the leading edge of inkjet printed droplets to produce an upper and lower estimate of the maximum shear rate the ink is undergoing. High speed images of the droplets formed when proteins are printed will be mapped to an inkjet simulation to provide insight into the droplet velocity and shear rate that the ink undergoes during printing.

High speed images (minimum 110,000 fps) were obtained using the setup described in section 3.4.1 and the velocity of the leading edges of the droplet were obtained using a MATLAB code described in 3.4.2.1. Briefly, the distance the leading–edge travels between frames is divided by the shutter speed and the first frame uses the edge of the nozzle as an initial reference point. The leading–edge velocity of the inkjet simulation is determined using the same methodology. It is important to have a like for like comparison of velocities because the leading–

edge velocity is not the same as the velocity of the ink travelling within the droplet, apparent in the droplet velocity surface plots in Figure 4.2.

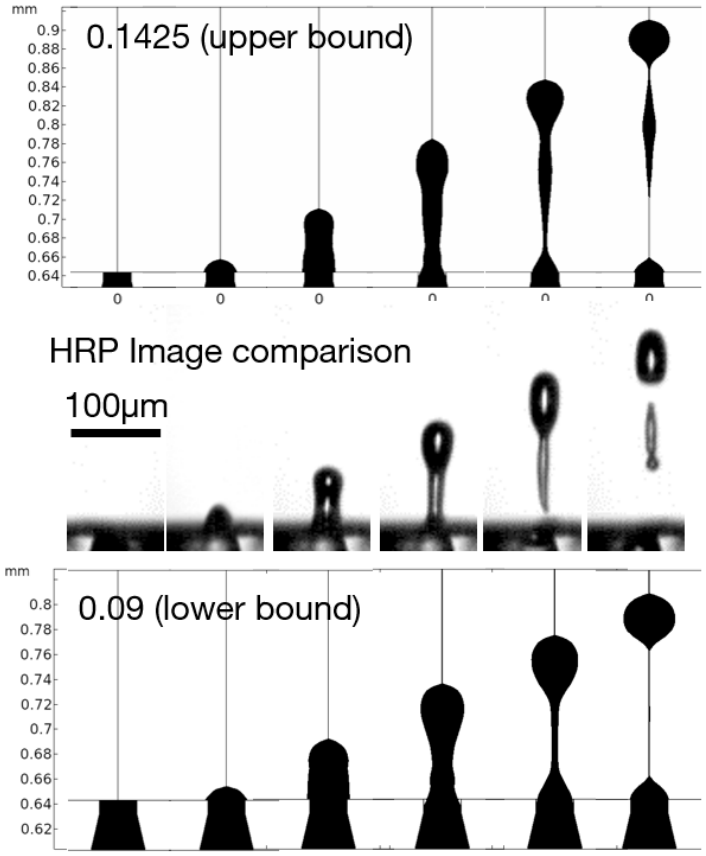

Figure 4.13: Comparison of the upper bound and lower bound images used as guidelines for velocity and shear rate data, compared with high speed images of inkjet printed HRP solution.

An example of high–speed image data from inkjet printing HRP through a 30µm Microfab nozzle is shown in Figure 4.13 with the upper and lower bounds of the simulation above and below respectively. Using the instantaneous velocity of the leading edge of the droplets shown in the high speed images in Figure 4.13, example shown for HRP, the velocity for each frame is measured and plotted in Figure 4.14. The methodology for determining the leading–edge droplet velocity is detailed in section 3.4.2.1. The upper and lower bounds of the simulation were selected to contain most of the data points for a given print as indicated in

Figure 4.14. In the first 10μs the rate of change of velocity of the droplet is rapid which is evident from the graph in Figure 4.4. The shutter speed for the high–speed images is 9.09μs which cannot provide a high enough resolution to understand what happens in the first few microseconds. However, mapping the velocity data from 10μs onwards can then be used to extrapolate what occurs in the first 10μs.

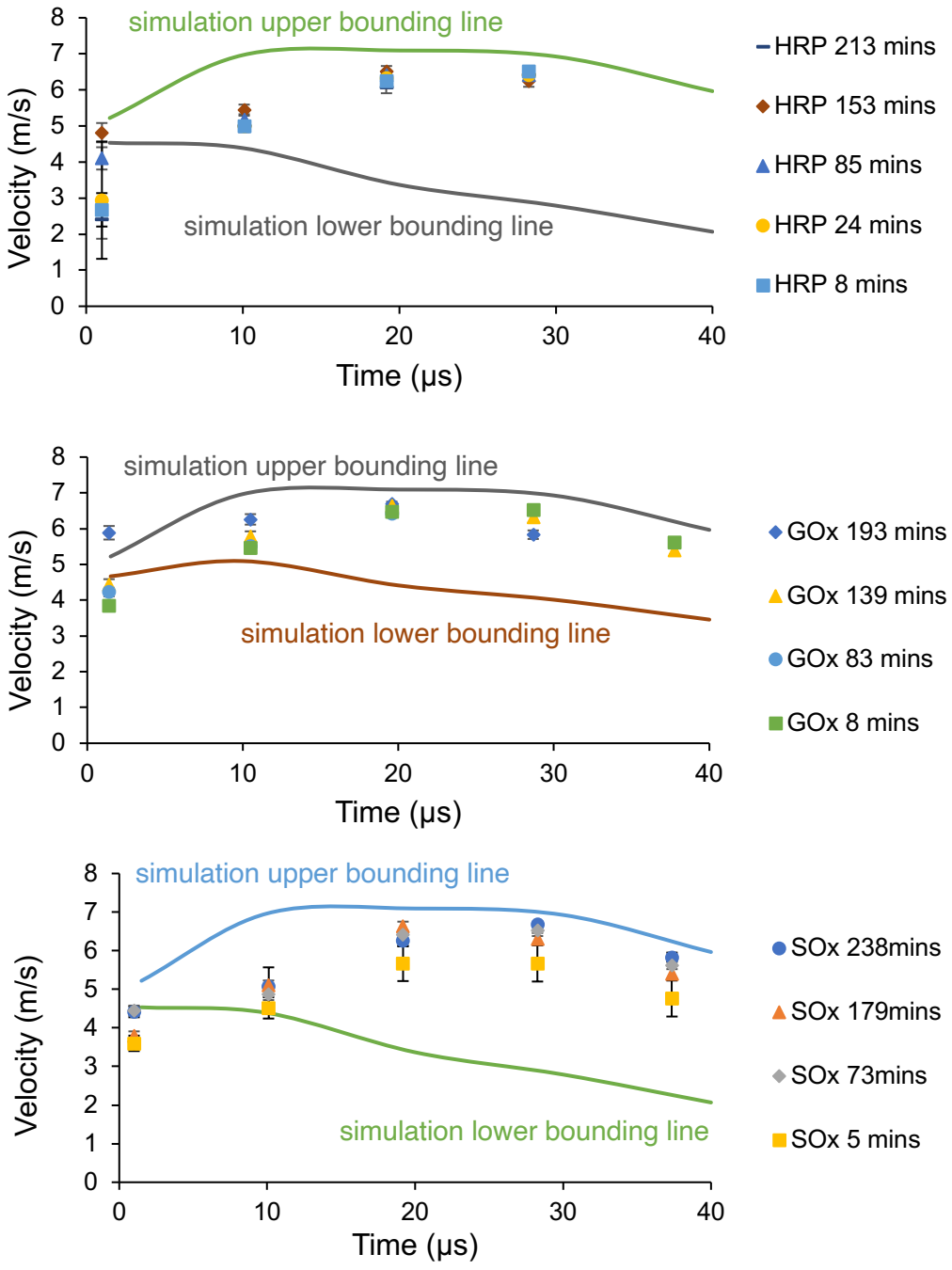

Figure 4.14: The droplet leading edge velocity over time for inkjet printed HRP (top), GOx (middle) and SOx (bottom) with n=3 for each data point, i.e. three images. The bounding lines for the graphs are from the simulations with leading edge velocity measured in the same way.

From the upper and lower bounds shown in Figure 4.14, information about the shear rate the proteins have endured can be determined. Rather than looking only at the maximum shear rate, the shear rate of the entire volume of ink within the simulation can be considered. Because the shear rate of the fluid in the ejected droplet is higher than the shear rate of the fluid inside the printhead during ejection, extra consideration of the fluid in the droplet will be analysed in this section. Based on the high speed images collected of inkjet printed proteins, the lower bound will use a scaling factor of 0.09 and the upper bound for all proteins is 0.1425. Further examination of the shear rate of the ink will consider these simulation input values.

A threshold can be applied to the simulation to isolate the fluid that is exposed to a shear rate above a given value x (spf.sr>x). An AND statement is used to combine a shear rate threshold with a further threshold upon the ink to isolate the ink and avoid inclusion of air in this analysis (ls.Vf2>0.5). The result of applying these two thresholds will exclude air and any fluid with a shear rate below the value of x. The surface plot can then be integrated over to calculate the volume of ink that is exposed to a minimum shear rate, x. The integration can be performed over the entire simulation domain, the nozzle and the domain the droplet is ejected into or either domain can be isolated and integrated over alone. By integrating over the domain the droplet is ejected into, i.e. initially the domain that contains air at t=0, information about the shear rate the droplet is exposed to can be analysed. Hence when the behaviour of the ink containing the proteins HRP, GOx or SOx, which is subsequently analysed in Chapter 5 and Chapter 6, can be better understood.

The graph in Figure 4.15 shows the percentage of ink in the droplet that is exposed to a different shear rate threshold for the rect scaling factor of 0.09. Figure 4.16 displays the same information but for the rect scaling factor of 0.1425. On both graphs surface plots are shown for droplets with heat maps for the shear rate above the threshold 500,000s^{-1}, darker blue indicates a lower shear rate and red indicates the highest shear rate. The outline of the droplet shape is also visible to give an indication of where the shear rate is peaking relative to the droplet shape. For both scaling factors all the ink in the droplet is at a minimum shear rate of 1,000s^{-1} for the entire duration of droplet ejection except for within the first couple of microseconds, 94% of the droplet is at a shear rate >50,000s^{-1} for 0.1425 and 97% for 0.09.

It is apparent that for the 0.1425 rect scaling factor during the first few microseconds a greater proportion of the ink endures a higher shear rate compared to the 0.09 scaling factor which is representative of using a higher input voltage waveform. Beyond 20μs the 0.09 scaling factor has a higher proportion of ink above the 500,000s^{-1} threshold but this can be explained by the difference in volume of the droplets. At 20μs the volume of ejected ink for 0.09 is 41pl whereas for 0.1425 scaling factor the volume is 62pl.

Instead of considering the volume of ink above a shear rate threshold in time, specific time points during droplet ejection can be selected and compared. Figure 4.17 shows the droplet volume above a given shear rate for four different time points that correspond to the same times of the droplet images in Figure 4.15 for the scaling factor 0.09. Figure 4.18 shows the same but for the scaling factor 0.1425 and corresponding to Figure 4.16. A significant volume of fluid is exposed to shear rates >$10^5 s^{-1}$. Whether this shear rate is high enough to cause conformational changes to the proteins will be discussed through experimental analysis in Chapter 5.

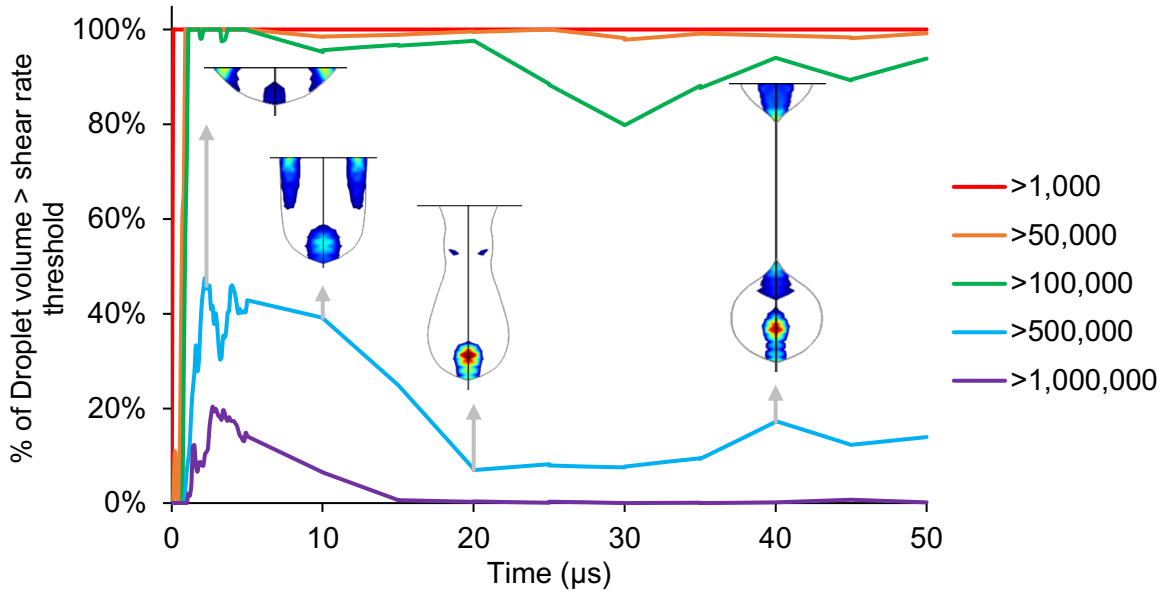

Figure 4.15: Percentage of volume of droplet above the shear rate (1/s) specified in the legend for droplets produced with a 0.09 scaling factor of the rect input waveform. The droplet images show the droplet shape outline with a heatmap for the shear rate above the 500,000s^{-1} threshold.

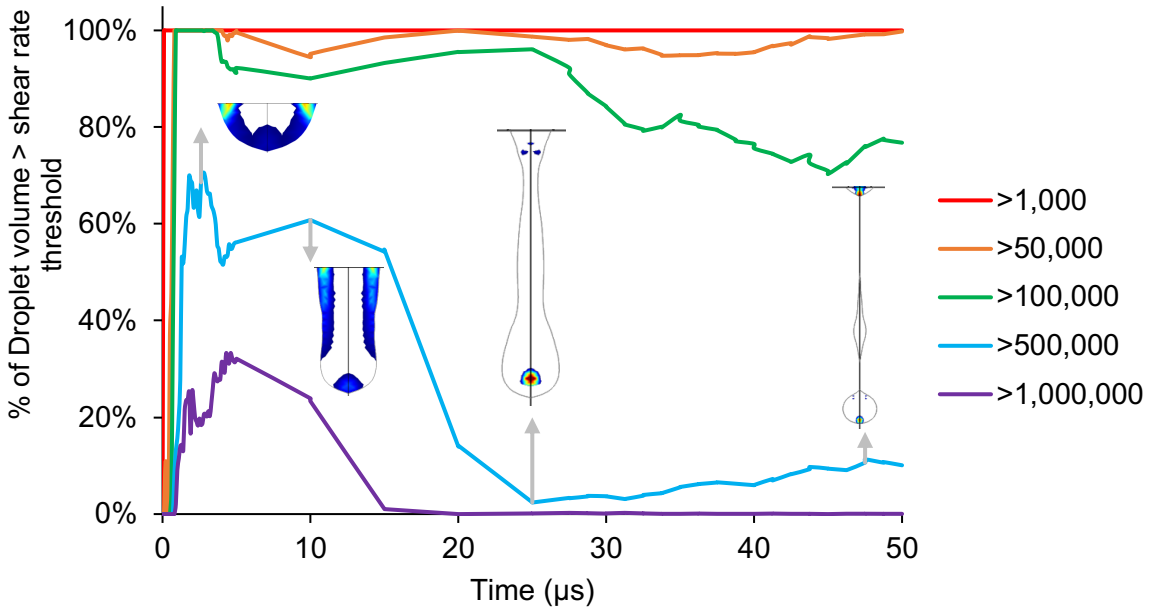

Figure 4.16: Percentage of volume of droplet above the shear rate (1/s) specified in the legend for droplets produced with a 0.1425 scaling factor of the rect input waveform. The droplet images show the droplet shape outline with a heatmap for the shear rate above the 500,000s^{-1} threshold.

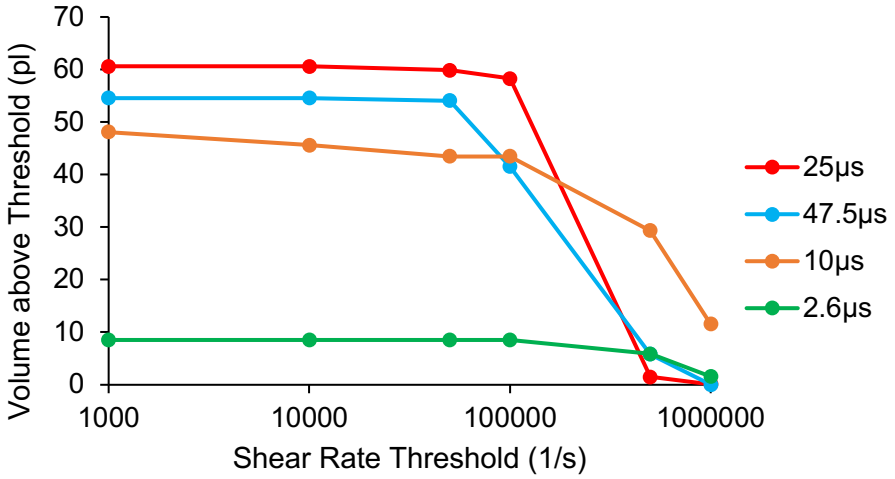

Figure 4.17: Volume of droplet above a given shear rate threshold for different times during the droplet ejection process. The input rect waveform has 0.1425 scaling factor.

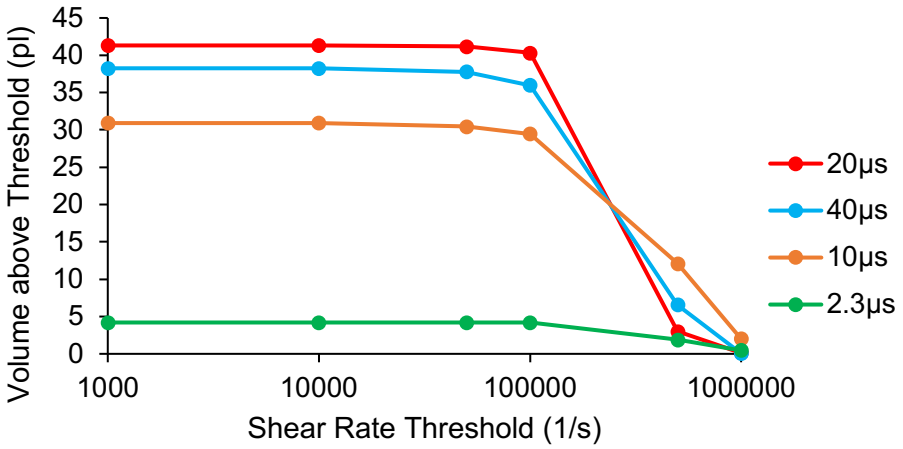

Figure 4.18: Volume of droplet above a given shear rate threshold for different times during the droplet ejection process. The input rect waveform has 0.09 scaling factor.

So far, only the ink ejected in the droplet has been considered but it is also important to consider the simulation system as a whole – the ink in the nozzle and the ink that is ejected. This is particularly important as a single inkjet printhead can be ejecting droplets at frequency in the order of 10kHz meaning

that the ink inside the printhead will be subjected to the same conditions repeatedly. Previous research examining the impact that the application of a shear rate has on a fluid containing proteins, detailed in section 2.2.2, suggests that the duration a fluid is applied to a given shear rate is important, not only the magnitude of the shear rate. A frequently used measure is defined as the shear or strain history and is shown in equation 4.2.

$$Shear = Shear\ rate \times Duration\ at\ Shear\ Rate \quad 4.2$$

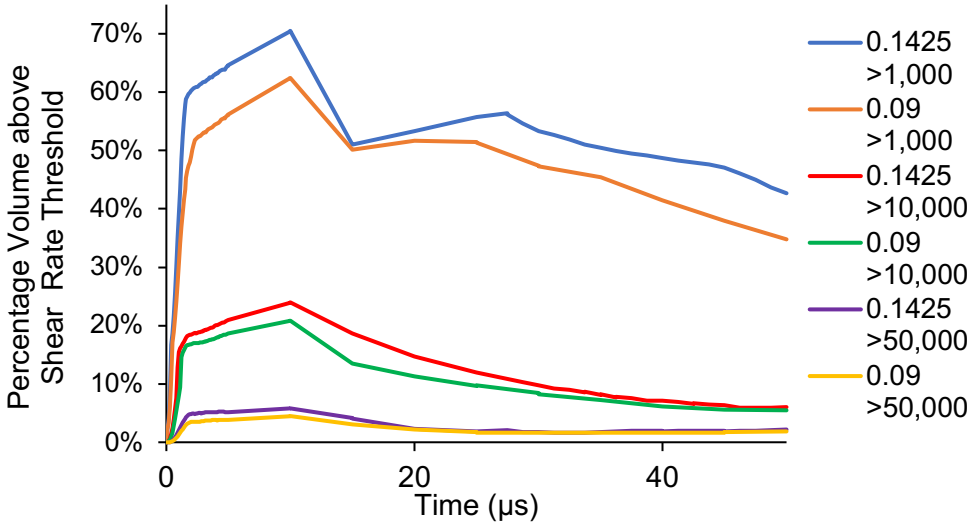

Figure 4.19: The percentage of volume above a specified shear rate threshold for a scaling factor of 0.09 or 0.1425 for all ink in the simulation.

The volume of ink inside the printhead is 15.2nl, this is three orders of magnitude larger than the volume of ejected droplets, however the ink inside the printhead is still undergoing a reasonable shear rate as highlighted in Figure 4.19. For the 0.1425 scaling factor 50% of the ink is always above $1000s^{-1}$ and for 0.09 40% of the ink is always above $1000s^{-1}$. If a printer is firing at 10kHz and the ink is exposed to $1000s^{-1}$ for half of the time and a given print takes 1 minute this would give a shear value of 30,000. A study on conformational changes of poly–l–lysine found a shear $>10^5$ was sufficient to cause such changes [91] but another study induced rhDNase to a shear of $9x10^8$ but observed no

structural change [89]. This highlights that the entire volume of the ink should be considered, not only the droplet as the impact of the shear rate upon the ink whilst still in the printhead could also influence the protein structure or activity.

Simulating the inkjet printing process and focussing on the shear rate that the ink has undergone provides tools to understand the conditions the ink undergoes in this process.

4.5 Conclusions

In this chapter a COMSOL Multiphysics 5.4 simulation has been used to build further understanding of the inkjet printing process. The velocity and shear rate of the ink during inkjet printing has been examined for different printing parameters, namely the input waveform amplitude, waveform slew rate, the nozzle orifice diameter, and the ink viscosity. To the best of our knowledge, these results are unique; matching COMSOL Multiphysics to high-speed images for inkjet printing has not been seen previously. The following conclusions were drawn:

- Waveform input amplitude (from 0.074 – 0.1425)
    - Non–linear increase in maximum velocity from 6 to 12ms^{-1}.
    - Non– linear increase from 2 x 10^6 – 4.5 x 10^6 s^{-1}.
    - Linear increase from 40 to 70pl.
- Waveform slew duration (1 – 2.5μs)
    - The only significant change was in the maximum shear rate that decreased linearly from 4.4 x 10^6 – 4.2 x 10^6 s^{-1}.
- Nozzle orifice diameter (20 – 40μm)
    - The maximum velocity had a power law decrease, converging to ~9ms^{-1}.

  - The maximum shear rate had a power law decrease converging to ~2 x 10^6 s^{-1}.
- Ink Viscosity (1 – 45mPa s)
  - The maximum velocity had a power law relationship converging to a peak value of ~15.5ms^{-1}.
  - The maximum shear rate had a power law relationship converging to a minimum value of ~2 x 10^6 s^{-1}.

High speed image data of inkjet printing with inks containing the proteins HRP, GOx and SOx were then compared to the inkjet simulation. By comparing the instantaneous velocity of the leading edge of the printed droplets and that of the simulation an upper and lower bound was determined for the printing behaviour. For both the upper and lower bounding behaviour it was observed that almost all ink in the ejected droplet is exposed to a shear rate of at least 50,000s^{-1}, 94% of the droplet is at a shear rate >50,000s^{-1} for 0.1425 and 97% for 0.09. The highest shear rates are observed within the first 10μs of droplet ejection during which time approximately 40% of the droplet is at a shear rate >500,000s^{-1} for 0.09 and 60% for 0.1425.

Through consideration of all the ink within the simulation, it is also evident that the ink inside the printhead is subdued to a low shear rate. The repetitive nature of the shear rate could also affect the protein structure.

Chapter 5 Surviving Function of Inkjet Printed Enzymes

5.1 Introduction

Inkjet (IJ) printing has been a valuable tool for the deposition of enzyme solutions as discussed in Chapter 2, HTS [102], protein microarrays [138] [29] and biosensor fabrication [46], being amongst some of these applications. However, there have been multiple cases where IJ printed enzyme solutions have endured a loss of activity after the printing process [100] [5] [45]. As noted in Chapter 2, this loss is often attributed to the effect of shear forces experienced by the biomolecules as they flow through the nozzle, with the forces driving changes to the secondary or tertiary structures. However, as discussed in section 2.2, the full journey of the active fluid through the inkjet process is not considered in a single coherent study. In addition, previous work has examined mostly single nozzle systems or lab–scale research printheads without also including a study of industrial printheads. In this chapter the full journey of the ink is examined through the printing apparatus, from formulation through to drying and the stability of the final material deposited on a control surface. A study is completed comparing three different scales of printhead, including the two most common in the research literature and also an industrial printhead. Through this approach, the work is focused on understanding the relative impact of each influencing factor on biological activity. Using enzymatic activity loss as the assessed model system, as common in the literature, the work here aims to

provide a more robust and complete testing protocol to those intending to scale up bioprinting and to help ensure delivery of the intended level of functionality.

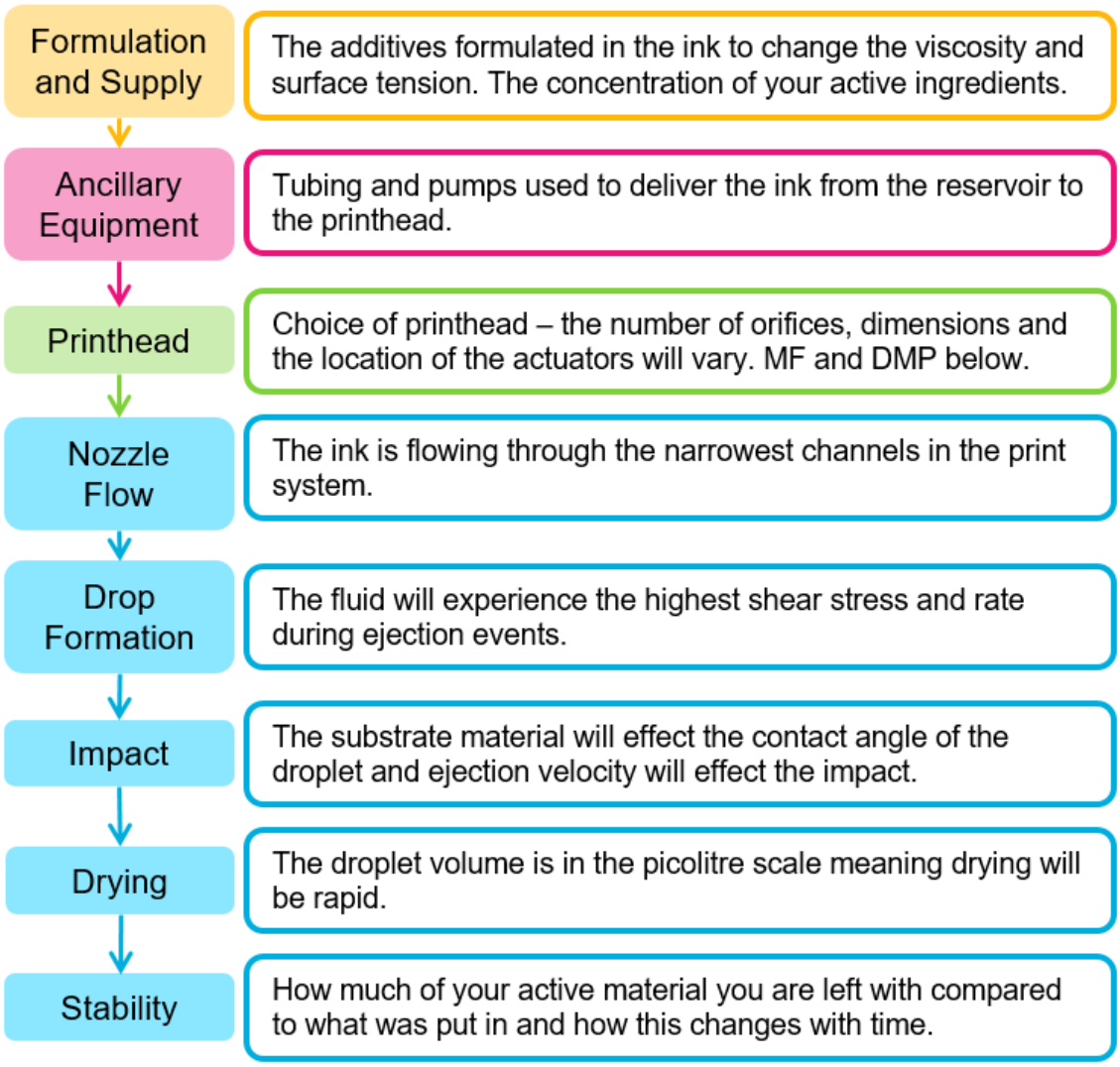

Figure 5.1: The journey of ink from preparation through to the final printed droplet. Adapted from [14].

Figure 5.1 provides an overview of the journey a fluid takes during the printing process, from ink formulation through to the final printed material stability. This chapter will discuss each element in turn and assess the impact each process has on the activity of enzymes formulated in the ink. The enzyme systems chosen to be studied in this chapter are HRP, GOx and SOx and are presented in Section 3.5.1. HRP and GOx are extensively studied model systems.

HRP has been used extensively in biochemistry as a reporter enzyme with HRP conjugated antibodies and ELISA assays and as a biocatalyst for polymerisation reactions [139]. GOx is most famously used for measuring blood glucose levels for diabetics [140] while SOx is a functional enzyme with applications in prostate cancer detection [141]. This approach in this thesis is to systematically separate out each individual contributing factor that could have an impact on enzyme activity. This has required development of novel experimental protocols that are adding to the field of bioprinting. Figure 5.2 provides an overview of the different printheads that will be examined within this chapter and highlights that each printhead is used in a different stage of a scale up process from research scale, to prototyping all the way through to industrial scale.

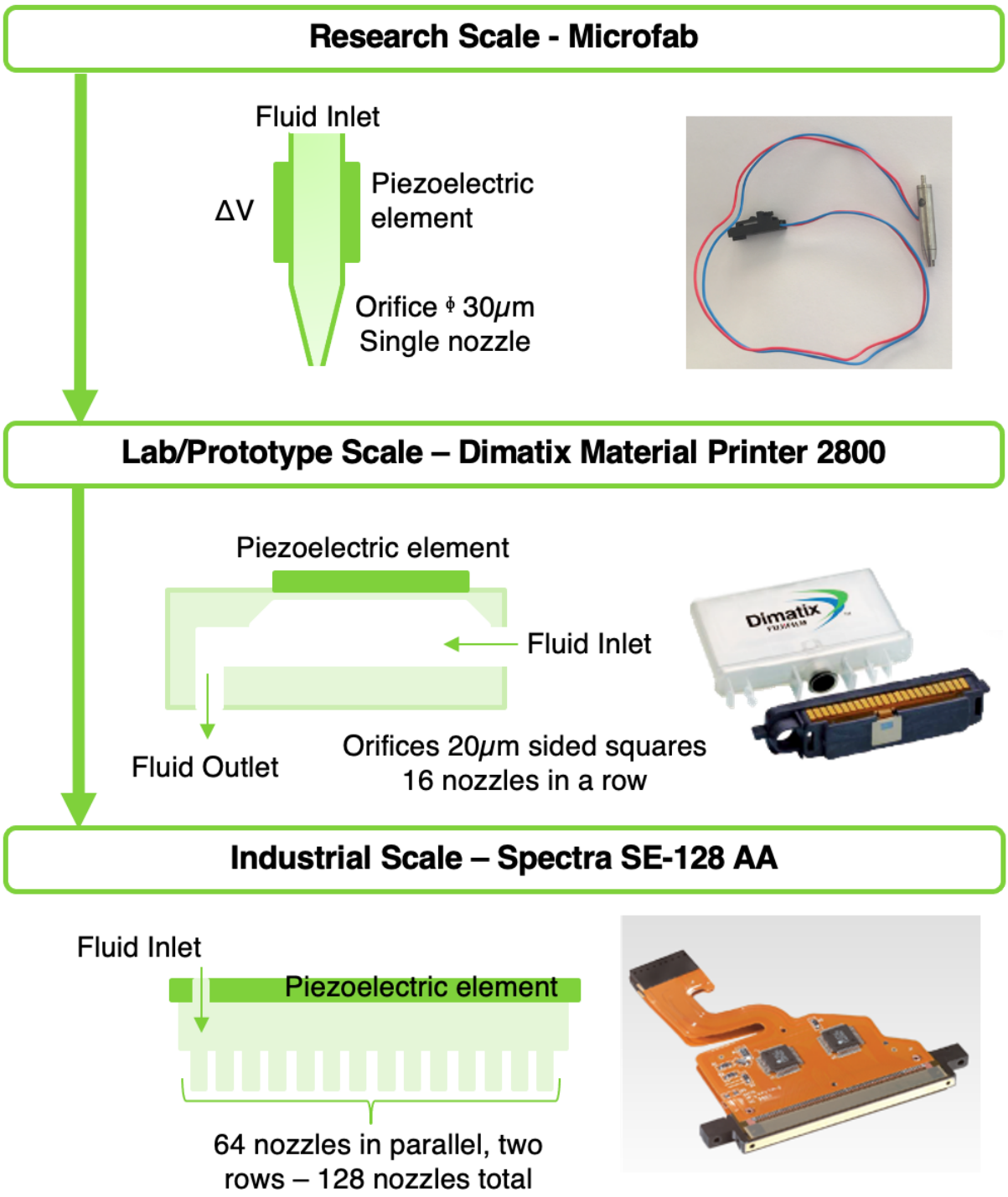

Figure 5.2: An illustration of the printheads to be examined in the chapter highlighting the different designs that are used for research applications, lab scale and prototyping through to industrial scale printheads.

5.2 Ink Formulation

The first step is to understand the role of the formulation on maintaining the biological activity. Formulation is normally tuned to print consistent droplets with a stable volume and high accuracy. To this end, it is important to formulate an ink that has a viscosity and surface tension that is within the capabilities of a print system to eject. The print system capabilities are detailed in Chapter 3.2 according to the manufacturers specifications. Secondly, as discussed in 2.1.2, if the consistency of the print is important, the ink should be formulated with consideration of the Ohnesorge number, *Oh,* introduced in equation 2.2 and Reynolds number, *Re*, introduced in equation 2.1. These dimensionless groups should be within the boundaries shown in Figure 5.3, the white area labelled 'Printable Fluid' bound by the red, blue, black and black dashed lines. The *Oh* should be between 0.1–1 and the *Re* 2–200 and consideration is also given for enough energy for droplet formation and when splashing will occur on droplet impact. Outside of these regions the print will not be optimised and have satellite droplets.

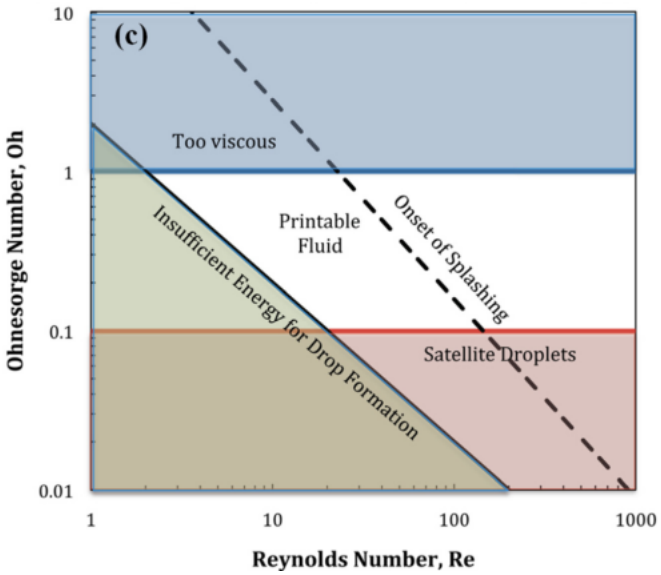

Figure 5.3: The optimum regions for ideal printing conditions of the ink, from [24].

Bioprinting is normally very challenging due to the low viscosity and high surface tension of aqueous inks. To formulate the ink to enable stable printing, viscosity modifiers, typically long chain polymers such as CMC or PEG/PEO, surfactants including tween or triton X–100 and humectants, glycerol for instance, are added. Within this chapter, the effect of viscosity modifiers on enzymatic activity and printability will be investigated. Surfactants were not added to the ink formulations to reduce the number of variables in the study. Moreover, the viscosity and flow rate of the ink is anticipated to be of greater significance as discussed in Chapter 4. Also, it is well known in the literature that in low concentrations surfactants can enhance enzymatic activity [4] [142], while at higher concentrations they impair activity and denature enzymes [143] at each stage of the printing process shown in Figure 5.1.

Research by Risio and Yan examined the impact of viscosity modifiers on HRP activity [4] and highlighted that it is of upmost importance to understand the impact each of these chemicals has on the physical properties of the fluid and to ensure that the concentration is low enough not to significantly affect enzymatic activity. All the following viscosity modifiers examined – PVA, PEG 20,000, PEG

2000, PEG 200, ethylene glycol and PVA detrimentally effected HRP activity with increasing concentration. To achieve a target viscosity of 5mPa s, none of these viscosity modifiers were suitable as they had a detrimental effect on HRP activity. Similarly lysozyme activity was negatively affected by glycerol and PEG 400 in concentrations sufficient to bring the viscosity to >5mPa s [50]. CMC (M_w not specified) and glycerol at concentrations below 0.8 wt% and 10wt% respectively did not negatively impact upon HRP activity. Therefore, the viscosity modifiers that will be examined herein are detailed in Table 5.1 and chosen to minimise losses in HRP activity. PEO 1M was selected because at low concentrations the viscoelasticity of the ink will be affected and concentrations below 5wt% were not examined by Risio and Yan but are not anticipated to have a significant effect.

Table 5.1: The viscosity modifiers and concentration range that have been examined for ink formulation.

Viscosity Modifier	Concentration Range
CMC 90k	0 – 45 µM
CMC 700k	0 – 4 µM
Glycerol	0 – 60 w/w
PEO 1M	0 – 0.025 w/w

The concentration range of the viscosity modifiers were printed through the 30µm MF nozzle without any protein in solution to ensure printing was possible. The upper limit of the concentration range was selected as printing was unreliable beyond this point and the input voltage was in excess of 140V.

5.2.1 Viscosity Modifiers for Ink Formulation

The chain length of CMC can be varied resulting in different molecular weights of the chemical. CMC with a molecular weight of 90,000kDa has a smaller chain

length than CMC 700,000kDa. A larger concentration of lower molecular weight CMC is required to reach a target viscosity as shown in Figure 5.4. For the concentrations and viscosities shown in the graphs relevant to inkjet printing, the viscosity increases exponentially with increasing CMC concentration. The same trend is observed for increasing glycerol concentration. The main function of glycerol is as a humectant rather than a viscosity modifier, but it also has an impact on the viscosity, albeit to a lesser extent than CMC 90k and 700k for the same concentration.

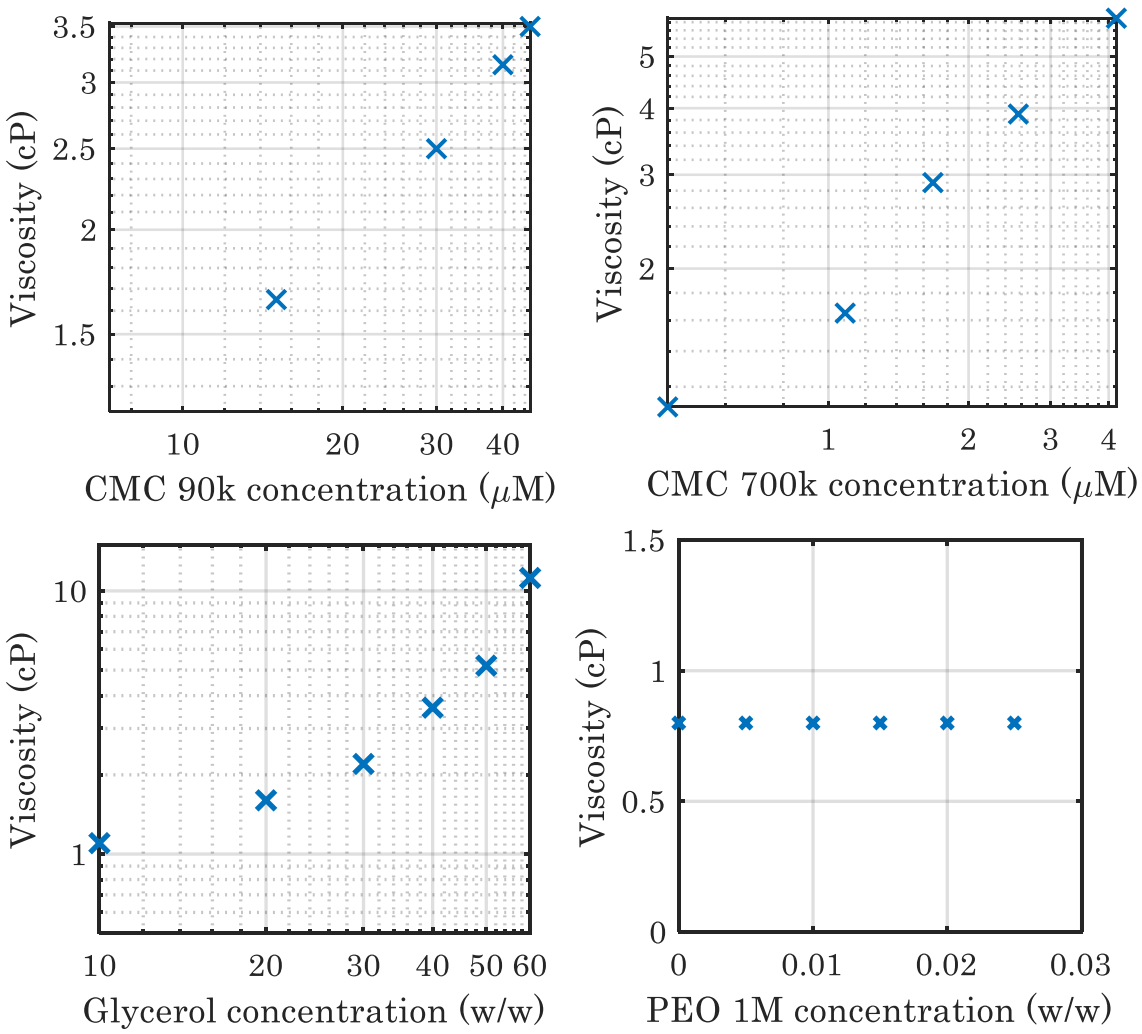

Figure 5.4: The viscosity of CMC 90k (top left), CMC 700k (top right), glycerol (bottom left) and PEO 1M (bottom right) solutions at different concentrations. Each data point has n=3 repeats with the viscometer, error bars not visible.

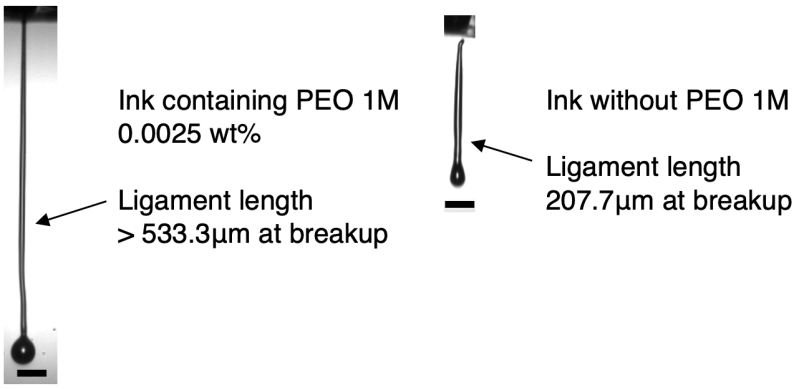

Figure 5.5: PEO 1M ejected with a 30µM MF nozzle shown on the left, without PEO 1M on the right. The droplet extends outside of the frame before breakup for the droplet containing PEO 1M, scale bars 50µm.

PEO 1M does not increase the bulk viscosity for the concentrations used in the formulation but effects the droplet morphology and ligament length during the printing process as the polymer chain is extended during droplet ejection which is shown in Figure 5.5. The ligament of the droplet formed when PEO 1M 0.0025wt% is in the formulation is more than twice the length of the ligament that forms without this viscosity modifier. The droplet goes beyond the limits of the frame size before breakup occurs.

Table 5.2: A summary of the viscosity (µ), surface tension (γ), density (ρ), Reynolds number (Re) and Ohnesorge number (Oh) of printed ink formulations to provide an overview of the printability.

Ink Formulation	µ (mPa s)	γ (mN/m)	ρ (kg/m^3)	Re	Oh
PBS (1x)	0.8	71.1 (20.7°C)	1005.6	188.6	0.017
PBS, CMC 90k 30µM	2.5	75.5 (21.0°C)	1008.3	60.5	0.052
PBS, CMC 700k 4µM	5.5	73.5 (20.3°C)	1008.4	27.5	0.117
PBS, 10wt% glycerol	1.0	70.2 (20.2°C)	1031.0	154.7	0.021
PBS, 0.0025wt% PEO 1M	0.8	75.6 (20.1°C)	1005.6	188.6	0.017

By measuring the viscosity and surface tension of different ink formulations and calculating the Reynolds and Ohnesorge numbers, as shown in Table 5.2, an assessment of how printable each resulting ink is can be made. The dimensionless groups were calculated using the constants d = 30µm, V = 5ms^{-1}, selected to be representative of the high speed image data seen in chapter 4.4, Figure 4.14. Satellite droplets formed during printing can be attributed to the low Oh number seen for all the inks.

It is important to consider the surface tension of the ink. As all the inks used are water based, the surface tension is relatively high which creates difficulty in printing as sufficient energy is required for a droplet to form. The static surface tension of PBS converges to a value of 71.1mNm. By formulating inks with a relatively lower viscosity, the amount of energy for droplet formation can be satisfied.

When inks are formulated with enzymes in solution, extra consideration must also be given to the impact each chemical in the formulation has upon the resulting enzyme activity. Consequently, an extra objective is needed when formulating with proteins, namely, to formulate to minimise loss of enzymatic activity.

The activity of HRP is assessed with different concentrations of additive in the solution, in this section glycerol and PEO 1M are examined. The addition of CMC 90k and 700k is investigated with GOx solutions. Firstly, the effect of glycerol in a sample containing 50nM HRP is examined. The glycerol concentration in a HRP sample is varied from 0–10wt% and the sample is assayed with ABTS, detailed in section 3.5.1.1. The result is shown in the left graph in Figure 5.6. For increasing glycerol concentration in HRP solutions, there is a trend that the activity of HRP decreases. The effect is only small as the mean activity from pure HRP to 10wt% glycerol varies by less than 10%. However, this result indicated it is also important to consider what happens to

HRP activity when the concentration of glycerol is kept the same across different ink formulation samples but the final concentration of glycerol in the assay changes relative to HRP.

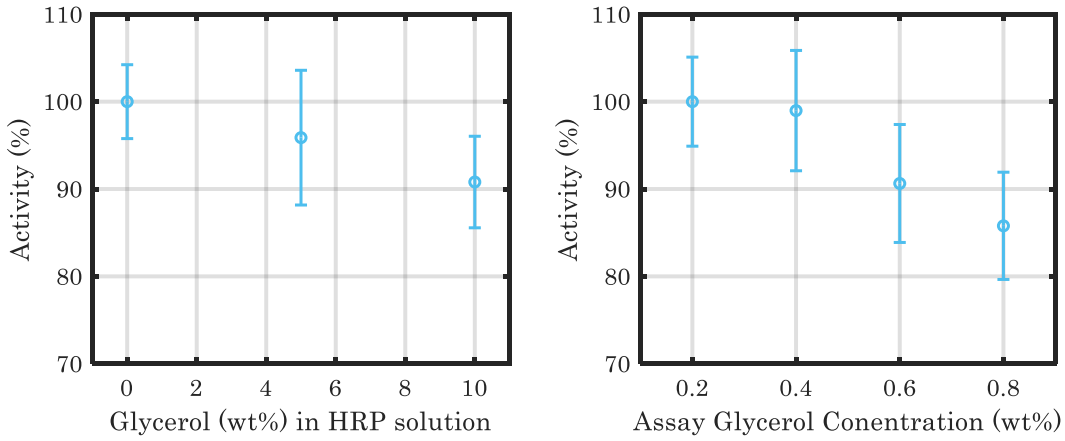

Figure 5.6: The effect of glycerol concentration on activity for HRP assays with a final protein concentration of 1nM compared to the control sample, in both graphs an assay with 0% glycerol and 1nM final HRP solution, the 0.2wt% glycerol concentration on the right has the same activity as 0% so this data point is not shown. Each data point with n=3 repeats.

In the literature, the concentration of the viscosity modifier in the printed ink is the most assessed factor. This is because it is going to be present at this concentration for the lifetime of the stable ink. In this work, Table 5.3 illustrates how the concentration of HRP has been changed in the sample being tested, but the concentration of glycerol in each sample is always 10wt%; Figure 5.7 provides a pictorial representation of the experiment for greater clarity. This means there is an increase in the relative concentration of glycerol compared with HRP. All other concentrations of every other reagent in the assay are maintained as well as the concentration of the HRP, which is 1nM, in the final activity study. The assay concentration of ABTS is 40μM for all samples, H_2O_2 concentration is 120μM. The results for each sample detailed in Table 5.3 are shown in the graph on the right in Figure 5.6. As the concentration of glycerol in the final assay increases the activity of HRP clearly decreases.

Table 5.3: The concentrations of glycerol and HRP in the samples tested and how this translates to the final concentration of each reagent in the final assay for the results shown in Figure 5.6, only the final concentration of glycerol in the assay is changing but the concentration of HRP in the sample has to change to enable this for the graph on the right.

Sample Glycerol Concentration (wt%)	**10**	**10**	**10**	**10**
Sample HRP Concentration (nM)	50.0	25.0	16.7	12.5
Sample Volume (µl)	20	40	60	80
Assay Glycerol Concentration (wt%)	0.2	0.4	0.6	0.8

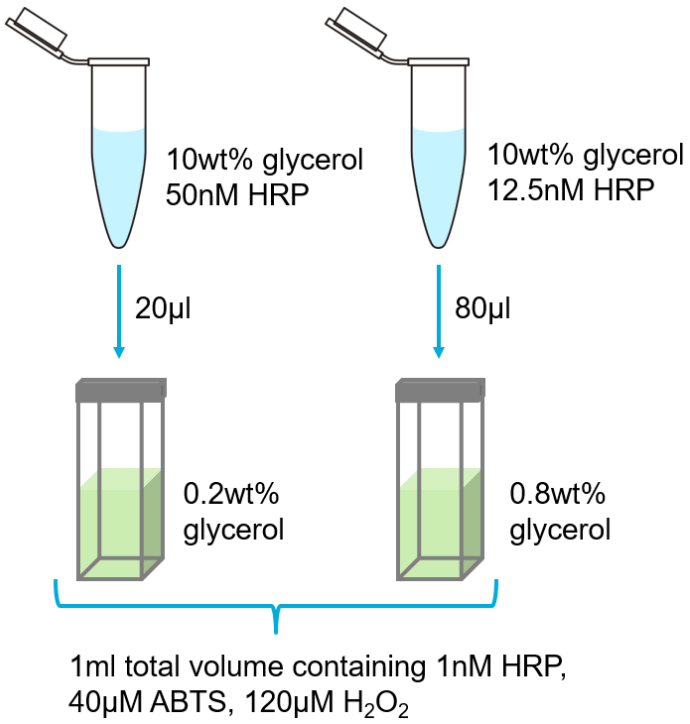

Figure 5.7: An illustration representing the first and last column show in Table 5.3.

The concentration of hydrogen peroxide has been selected so that the assay is not limited by diffusion, shown in Figure A 1 in the appendix, therefore it can be concluded the change to the diffusivity constant within the assay is not the cause of the reduced HRP activity. The effect is due to the interaction of the glycerol

with HRP, although it is not clear what the nature of this interaction is. The two graphs in Figure 5.6 demonstrate that not only the concentration of the humectant glycerol is important to consider when formulating inks with HRP, but also the final concentration of glycerol in the assay to determine HRP activity as both have a detrimental effect on HRP activity. To minimise the loss of HRP activity, inks should be formulated with no more than 10wt% glycerol.

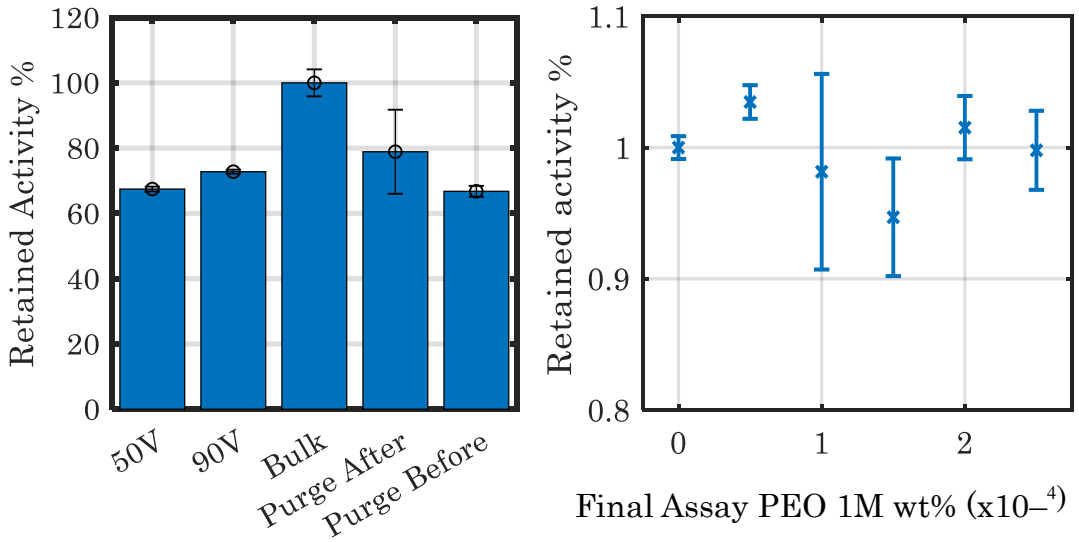

Figure 5.8: 50nM HRP with 0.0025 wt% PEO 1M printed with the MF system (left), the final PEO concentration in the assay effect on HRP activity. N=3 for each data point.

With the viscosity modifier PEO 1M a similar experimental approach was taken as represented in Table 5.3 and Figure 5.7. The final assay concentration of PEO 1M was varied between 0 – 0.0025wt% whilst the assay HRP concentration was maintained at 1nM. The results are shown in

Figure 5.8. In this case, there was no statistically significant trend. The final assay concentration of PEO 1M within this concentration range did not detrimentally affect the HRP activity in the assay. HRP solutions containing 0.0025wt% PEO 1M were then printed through a 30µm MF nozzle at varying voltages and the activity of the printed HRP solutions lies within the activity of

the solutions purged through the print system before and after the print. This result shows that there is a clear loss of activity due to some aspect of the printing process and because it lies within the boundaries of the activity loss of the purged solution it is conceivable that this is due to adsorption losses and so needs to be explored further and is examined later in this chapter in 5.4.

The impact of formulating GOx inks with the viscosity modifiers CMC 90k and CMC 700k is examined to understand the effect on GOx activity. The impact of formulating GOx solutions with increasing concentrations of CMC 90k is shown in Figure 5.9. The graph on the left indicates that for higher CMC 90k concentrations the activity of GOx is increased by 21%. This is not due to a false positive in the assay as the same assay is carried out for solutions containing only the viscosity modifier, without GOx in the samples, and the absorbance does not increase with time outside of noise from the spectrometer, therefore the increase in activity must be attributed to the interaction of the protein with the viscosity modifier. This result was also observed in HRP solutions where the impact different viscosity modifiers had on enzymatic activity was also assessed [4]. It was concluded that this effect was due to CMC being a charged polymer meaning that the viscosity of the solution was also dependent upon the charge density within the solution and meant that there was less macromolecular overcrowding in inks formulated with CMC.

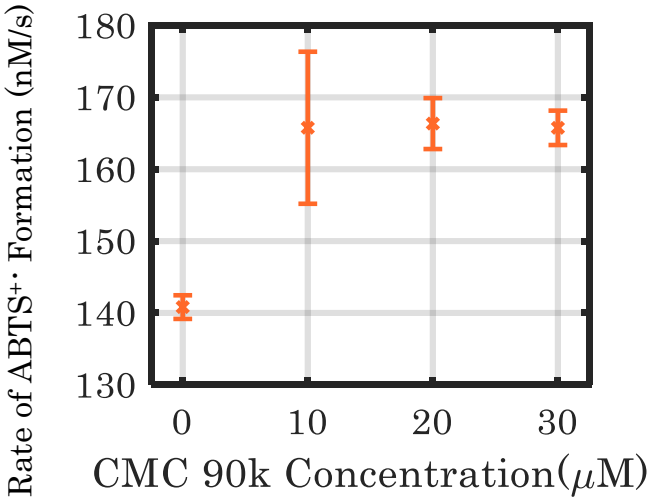

Figure 5.9: The rate of $ABTS^{+\cdot}$ formation in assays of 1nM GOx containing various concentrations of CMC 90k with n=3 for each data point, error bars ± standard deviation.

The activity of GOx solutions containing a longer chain CMC also increased in its presence, shown in Figure 5.10, which is also attributed to the interaction of GOx with CMC rather than a false positive result. When GOx ink was formulated with CMC 700k and printed through a MF 30µm nozzle, the only statistically significant loss in activity was for the sample that was collected before printing which is likely the result of a drop in GOx concentration as material in the printing apparatus, the ancillary equipment and printhead, is saturated, as shown in Figure 5.10. The impact of the ancillary equipment will be examined in more detail in the following section.

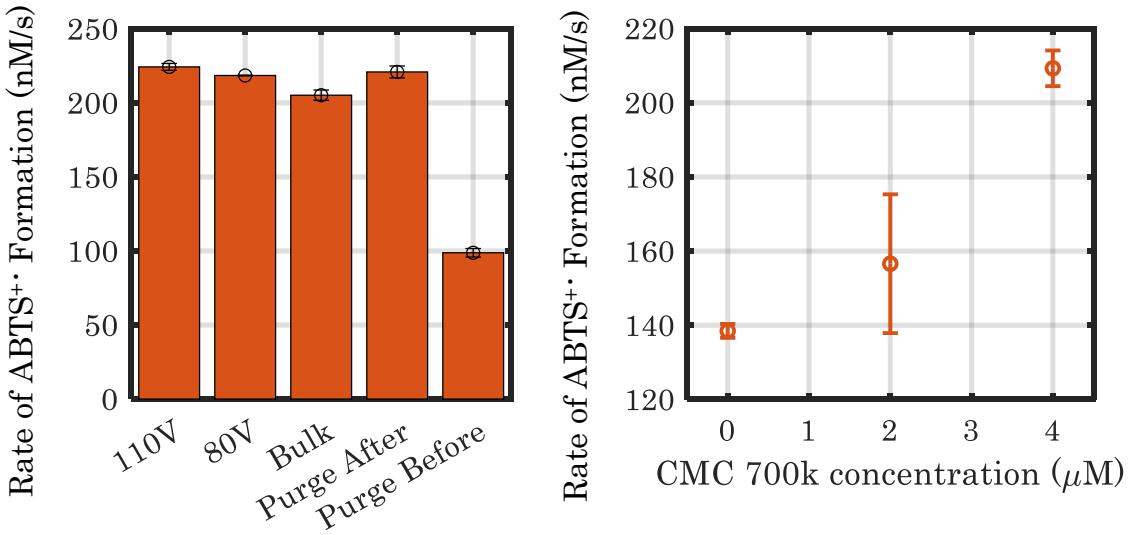

Figure 5.10: Left – ABTS assay of 50nM GOx in PBS with 30µM CMC 90k printed with the Microfab print system. Right – ABTS assay of 50nM GOx in PBS with different CMC 700k concentrations. N=3 for each data point, error bars ± standard deviation.

This section has demonstrated that viscosity modifiers can have a positive effect on enzyme activity, in the case of CMC 90k and CMC 700k, a negative effect on activity, when formulating with glycerol and no impact when using PEO 1M in sufficiently low concentrations. It has also highlighted that the relative concentration is the key measure to consider at the point when the activity is being tested in the assay. This is an important finding, because slight changes in the enzyme concentration may lead to significant changes in assay relative concentrations.

5.3 Ancillary Equipment

After ensuring a stable, printable formulation has been created that will lead to minimal or controlled losses in activity during printing experiments, it is important to consider the journey of the functional fluid to the print nozzle. The ancillary equipment of a print system encompasses all components that contact the ink but are not directly involved with fluid ejection. These components

include fluid reservoirs, pumps and tubing. Some of the previous results in section 5.2 suggested that enzyme activity may be lost due to adsorption on the printing apparatus, and so it is important to consider the impact different materials have on enzyme activity. The ink will spend more time in the ancillary equipment than the printhead. A Xaar Midas Ink Supply System is shown in Figure 5.11 and is representative of the ancillary equipment used for industrial inkjet printing applications. The flow rates in this system are at a maximum of 450ml/min with a maximum in–feed pressure of 200mbar and the reservoir holds up to 60ml of ink [144]. In contrast with industrial printing, in the MF and DMP system it is possible to forgo a pump using hydrostatic pressure or air pressure to control the meniscus, as detailed in Print System Design, Chapter 3 and there is also no in line filtration as the ink is filtered before being input into the print system. Therefore, the choice of tubing or internal bag system will have the most impact upon adsorption within the research level ancillary equipment.

Figure 5.11: A Xaar Midas Ink Supply System that can be used for industrial applications.

Protein adsorption is a common and functional phenomenon whereby a protein will adhere to a solid surface when it makes contact [145]. It is understood that the protein comes into contact with the surface via diffusion and is accepted that the tertiary structure of a protein is affected in the adsorption process. The material properties that affect the extent of adsorption are charge and

hydrophobicity and the extent of the contribution of each factor depends upon the material and protein system in question [8].

Another important factor to consider is the amount of time the protein will be in contact with a given material. The Langmuir model is often used to describe the amount of mass that has adhered to a surface. It models the adsorption of a molecule to a surface as a reversible reaction with first order reaction kinetics. The resulting rate equation, 5.1, is shown below.

$$\frac{dm}{dt} = k_a C(m_\infty - m) - k_d m \qquad 5.1$$

Where k_a is the adsorption rate and k_d is the desorption rate constant, C is the protein concentration in the bulk, m is the adsorbed mass at a moment in time and m_∞ is the maximum amount of protein that can be adsorbed to a surface. Solving the differential equation in 5.1 gives the equation shown in 5.2.

$$m = \frac{\beta}{\gamma}(1 - e^{-\gamma t}) \qquad 5.2$$

This provides a model for how adsorption progresses with time. The timescales that are relevant for printing will vary based on the application and scale. The timescales chosen here have been selected so that they cover the length of time used in any printing experiments presented herein.

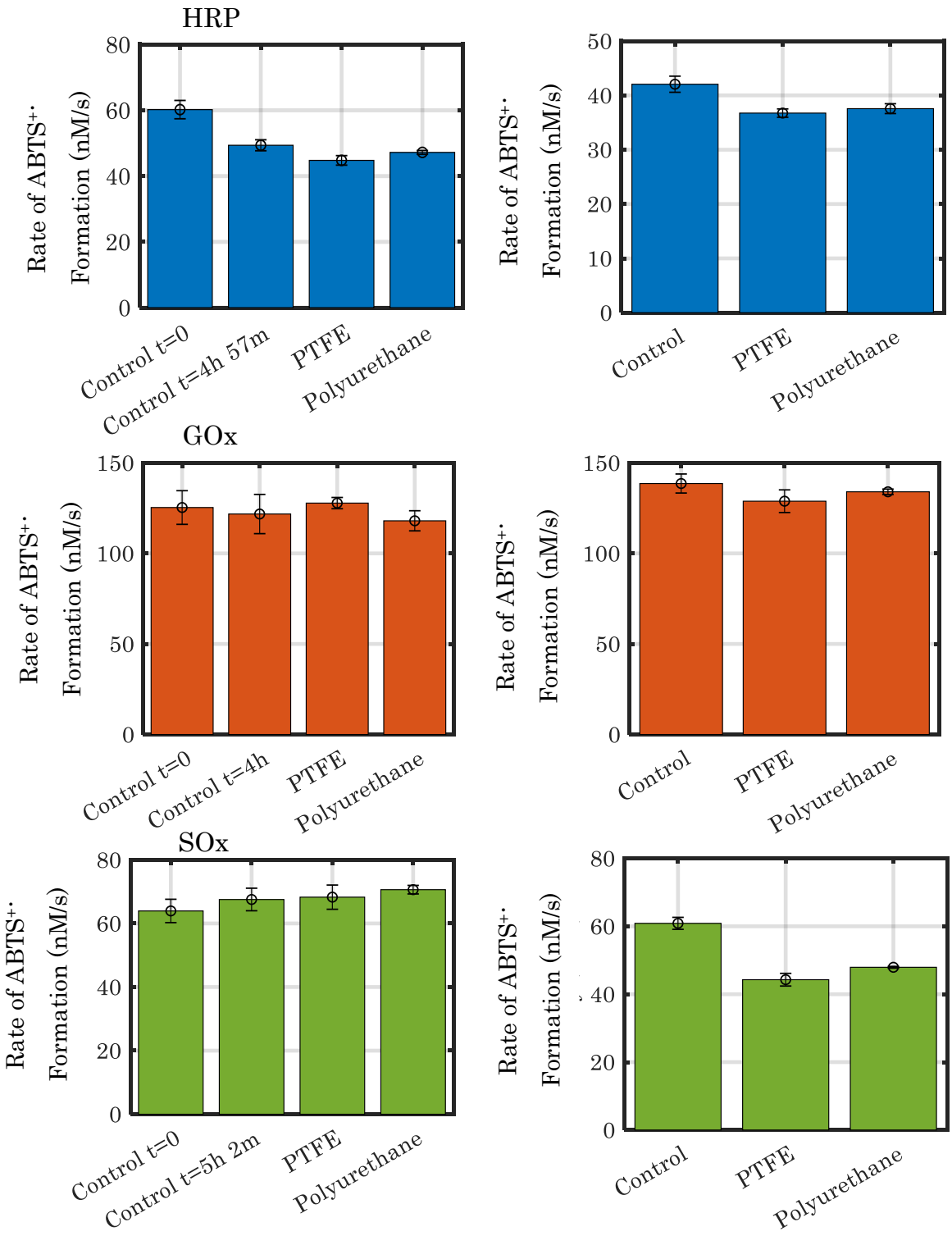

Figure 5.12: Assays with ABTS showing impact protein adsorption has on the assay using 5cm tubing of different materials in a sealed container for the time specified by the control and fast flow through (right). The protein solutions contain HRP (top), GOx (middle) and SOx (bottom). N=3 for each data point, error bars are ± standard deviation.

Experimental data assessing the activity of HRP, GOx and SOx with respect to different adsorption periods and PTFE and polyurethane tubing are shown in Figure 5.12. For all the results in the left column, a protein solution was assayed immediately (control t=0), then protein solutions were left in tubing made of PTFE or polyurethane for the duration stated in the second control, which was assayed after the stated duration. In the right column the protein solutions were slowly forced through the tubing with a low air pressure and then collected and compared to a control solution. In all cases the polyurethane tubing performed within the errors of the PTFE tubing or slightly better, however the increase in performance observed in the flow test with SOx is relatively small and hence choosing between either material is unimportant.

The results also indicate that SOx and HRP are more susceptible to adsorption losses than GOx. In the case with HRP, the duration of almost 5 hours also had a detrimental effect on the retained activity which will be in combination with the adsorption losses that are also apparent.

5.4 Printhead

Once the droplet has travelled through the ancillary equipment, it will enter the printhead. The printhead is the piece of apparatus that contains an actuator, in these cases piezoelectric elements, that cause deformations to the channel containing the ink resulting in a droplet being ejected through an orifice. In this chapter three printheads have been used – a 30μm Microfab, DMP materials printhead and a Spectra SE 128 AA printhead. The MF print system is made of glass with a stainless–steel exterior, the DMP printhead is made from silicon and the Spectra printhead has nozzles on a metal plate. Printheads can also contain nickel or polyimide. Like the ancillary equipment, it is also important to consider the impact the materials on protein adsorption so that suitable controls can be used when assessing the impact of the printing process.

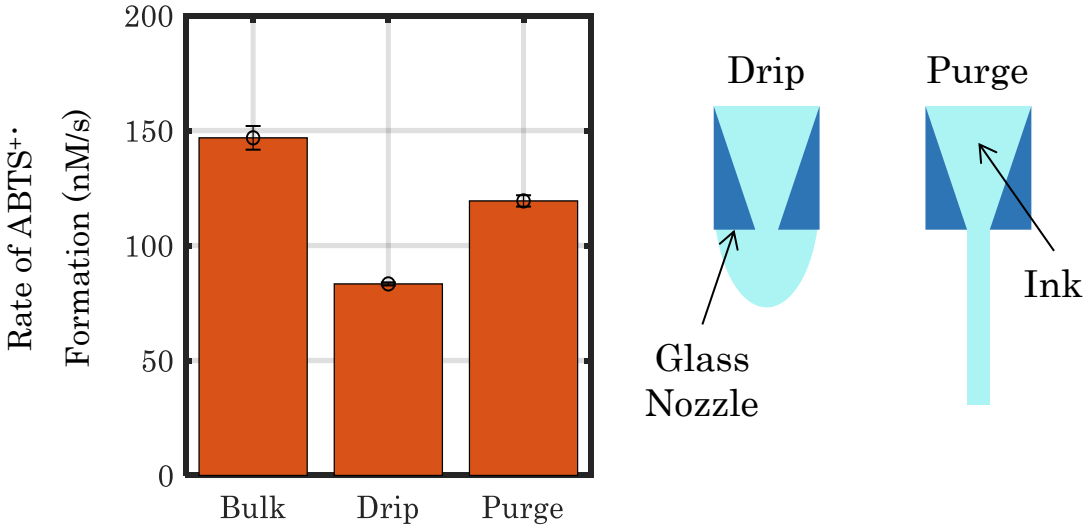

Figure 5.13: The effect of adsorption of GOx to MF (MJ–ATP–01) printing apparatus after dripping and purging, measured through observing the change of rate of $ABTS^{+\cdot}$ in enzymatic assays. The ink contacts the glass nozzle and the metal guards around the nozzle during dripping but does not with purging. N=3 for each data point, errors bars are ± standard deviation.

When considering the MF printhead, Figure 5.13 shows the effect of utilising different printing controls on the activity of GOx. In the bulk, the solution does not contact any printing apparatus. For drip, the solution drips through the printhead under gravity and wets the outside face of the glass nozzle. In the final case, the solution is purged through the printhead with a syringe at a low flow rate of 0.3ml/min. There is a greater loss of activity when the GOx solution is allowed to drip through the printhead which can be attributed to making contact with the outer face of the glass nozzle. This result justifies the use of a low flow rate purge for further printing controls as it is a fairer comparison as it retains more enzymatic activity. This is an important control to consider when reviewing the literature, as it is quite user–specific and not currently clear where the dripping control has been carried out while ensuring no contact with the external material.

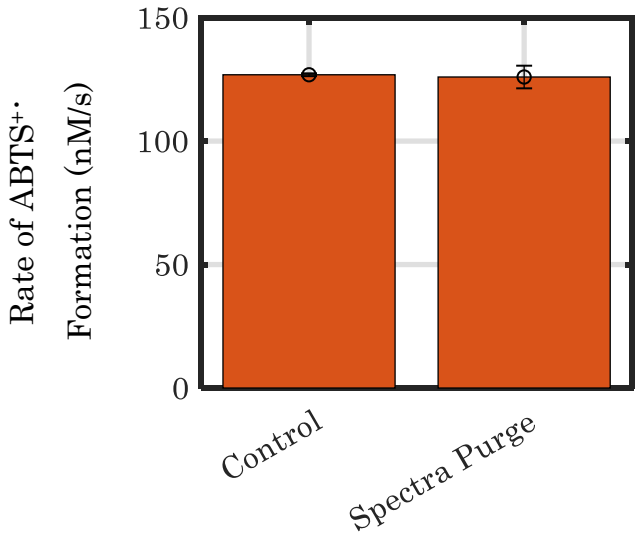

Figure 5.14: Rate of $ABTS^{+\cdot}$ formation in assay with 50nM GOx samples after being filtered (control) compared to being purged through the Spectra Industrial Printhead. N=3 for each data point, errors bars are ± standard deviation.

The silicon based printheads, DMP and Spectra SE 128 AA, should be examined separately for adsorption losses. Figure 5.14 shows a comparison of the activity of GOx solution purged through the Spectra printhead to the bulk solution. There is no statistically significant difference in activity of the two samples indicating that adsorption losses for GOx solutions on silicon based printheads are insignificant. Moreover, Figure 5.15 shows that when a GOx solution makes contact with the metal end plate of the Spectra printhead and is collected after 10 seconds, there is a slight drop in GOx activity, but it is still within the error bars of the control sample. This result is relevant for both printheads and is a positive result that silicon–based materials are suitable for protein printing.

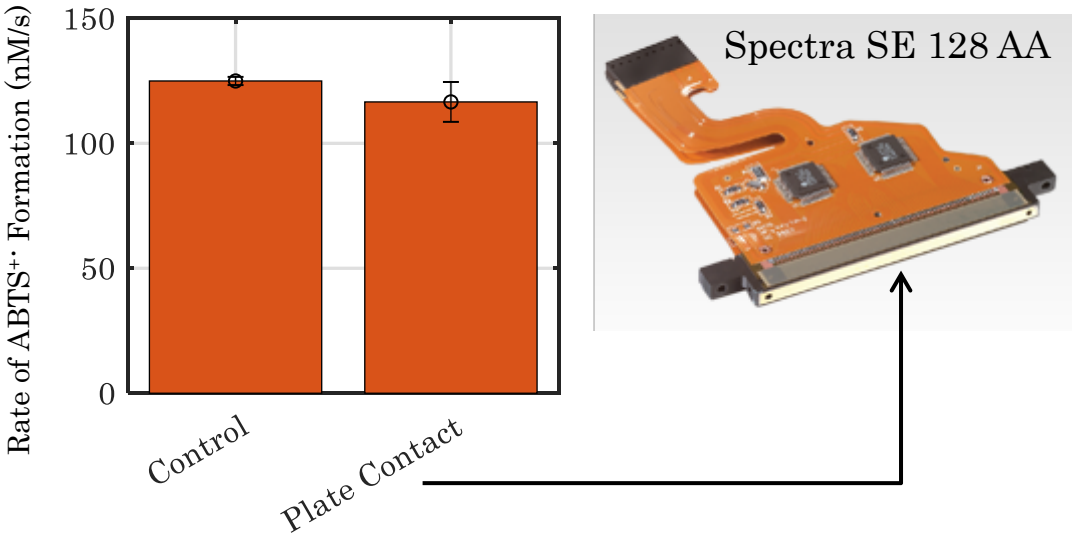

Figure 5.15: Rate of $ABTS^{+\cdot}$ formation in assays containing 50nM GOx samples after being drop casted onto the end plate of the Spectra SE 128 AA or in the bulk solution. N=3 for each data point, errors bars are ± standard deviation.

5.5 Nozzle Flow

For a droplet ejection event to occur, the ink must flow through the nozzle. The ink will flow through a channel that will narrow until it is at the finest constriction at the orifice. The geometry of the channel will depend upon the printhead design; however, the peak in the fluid shear rate will be experienced at the narrowest constriction. Therefore, it is important to consider what will occur when protein solutions are flowed through a constriction representative of the smallest dimension of the printheads examined.

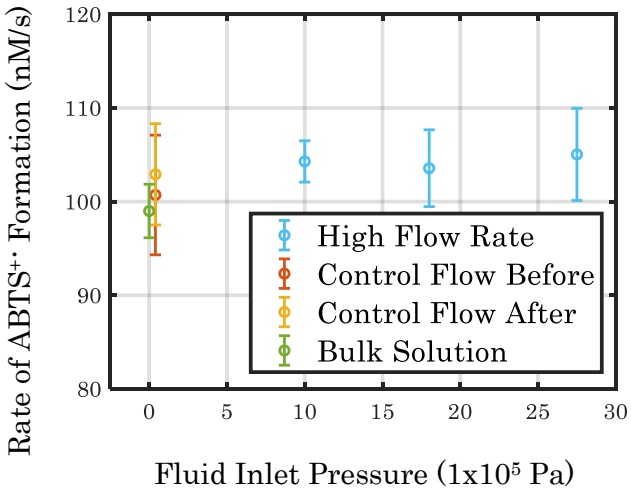

Figure 5.16: Rate of $ABTS^{+\cdot}$ formation in assays containing 50nM GOx samples in PBS flowed through a 15µm diameter nozzle at high pressure flowed through at a low pressure for the control and compared to the bulk solution. N=3 for each data point, errors bars are ± standard deviation.

The flow setup described in Chapter 3 was used with GOx and HRP solutions. The smallest constriction was 15µm diameter and protein solutions were flowed through at a high flow rate (200ml/hour), a low flow rate (20ml/h) to account for any adsorption losses and compared to the bulk solution that has not contacted the apparatus. The results in Figure 5.16 are for 50nM GOx solutions. A range of higher flow rates were tested and for every inlet pressure, even the highest flow rate, there was no statistically significant difference from the bulk or lower flow rate samples. This indicates that for the shear stress endured by the fluid due to ejection through a narrow constriction; this force is insufficient to affect the enzymatic activity. Adsorption was also not observed to be an issue in this setup.

Considering that the highest fluid inlet pressure did not detrimentally affect GOx activity, the experiment was repeated with a 50nM HRP solution shown in Figure 5.17. A bulk sample was compared with three samples at a low flow rate and three samples at the high inlet pressure. Again, it was observed that the shear stress was insufficient to negatively affect the HRP enzymatic activity.

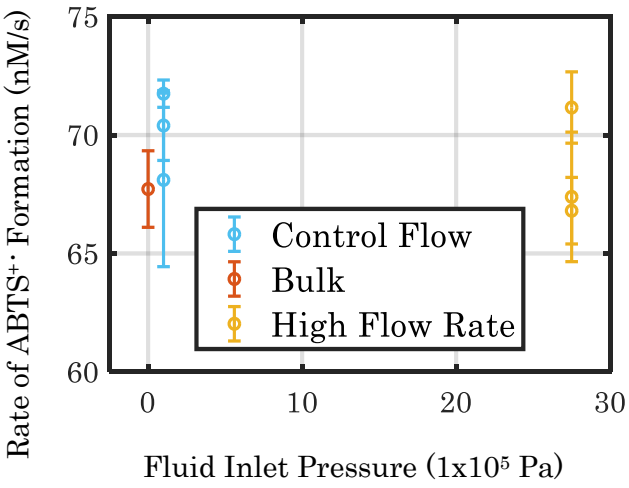

Figure 5.17: Rate of $ABTS^{+\bullet}$ formation in assays containing 50nM HRP samples flowed through a 15µm diameter nozzle at high pressure flowed through at a low pressure for the control and compared to the bulk solution. N=3 for each data point, errors bars are ± standard deviation.

These results act as a model system that isolates the contribution of the shear stress the ink will experience during inkjet printing. This suggest that for the enzymes in question the shear stress is insufficient to reduce enzyme activity meaning that in a print system the act of printing should not negatively affect the enzyme activity.

5.6 Droplet Formation – Activity after Inkjet Printing

There are many parameters that can be adjusted to achieve different droplet volumes and ejection morphologies. For the MF print system, the parameters that the user can vary are displayed and detailed in Table 5.4. As a square waveform was used in experiments an echo of the waveform, typically used for damping the vibration of the meniscus during printing, has not been considered. All the parameters except for the nozzle diameter are modified using the waveform generator whereas the nozzle can be physically changed in the printing setup.

Table 5.4 details the parameters that can be varied when setting up printing with a MF printhead.

Input Parameter	Description
Peak Voltage (V)	The peak voltage of the waveform causing the piezoelectric element to deform.
Resting Voltage (V)	The potential difference
Frequency (Hz)	The number of signals generated per second that will cause a droplet ejection event.
Rise (μs)	The time for the waveform to increase in voltage to the peak voltage from the resting voltage.
Dwell time (μs)	The duration that the waveform remains at the peak voltage.
Fall time (μs)	The duration for the voltage of the waveform to go from peak to the minimum.
Nozzle Diameter (μm)	The diameter of the narrowest constriction, the orifice, or the printhead.

The results in the upper graph in Figure 5.18 only varied the peak voltage of the waveform used; all other input parameters detailed in Table 5.4 were kept constant. The top graph in Figure 5.18 shows that there is a loss in activity of the HRP solution that lies between the loss of activity from the purge before the print and after the print. The activity is regained after consecutive prints, as the order of the print is the corresponding from left to right on the bar graph. Although the voltage is not kept constant, there is no trend with the change in voltage whereas the order is important. The results from the bottom graph with the GOx solution also confirm this as the voltage is kept constant at 110V and the activity recovers after consecutive prints. These results suggest that the

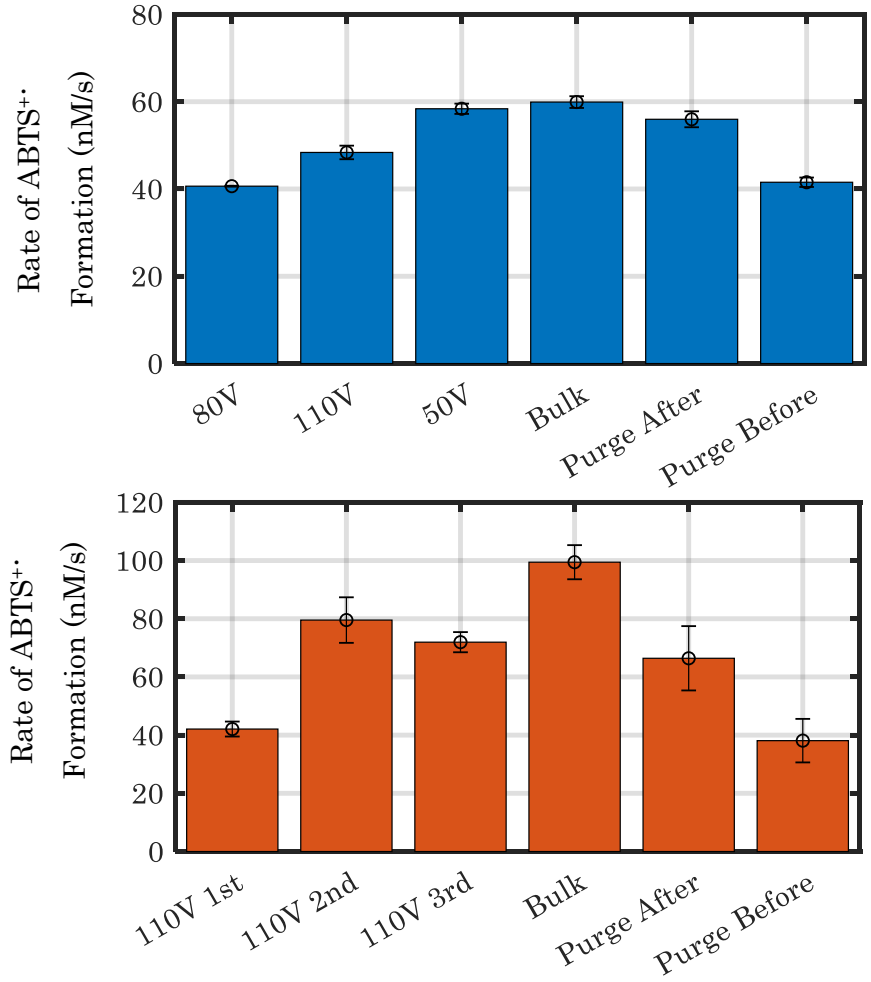

Figure 5.18 Rate of $ABTS^{+\cdot}$ formation in assays containing 50nM HRP (top) and GOx (bottom) in PBS sequentially printed with a 30µm diameter Microfab nozzle compared to the activity of the bulk solution and solution that has been through the printing apparatus before and after printing. The order of the bars shows the order of the print. N=3 for each data point, errors bars are ± standard deviation.

losses are due to adsorption and the concentration of the resulting protein solution that is assayed increases as more volume of ink is flown through the print system. This hypothesis is tested further from the results of experiments shown in Figure 5.19.

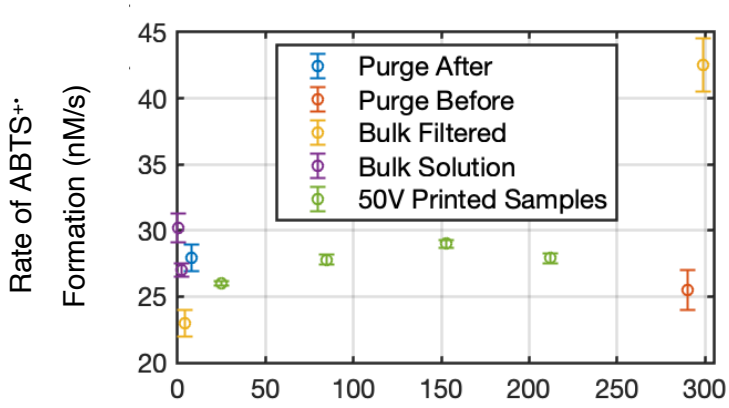

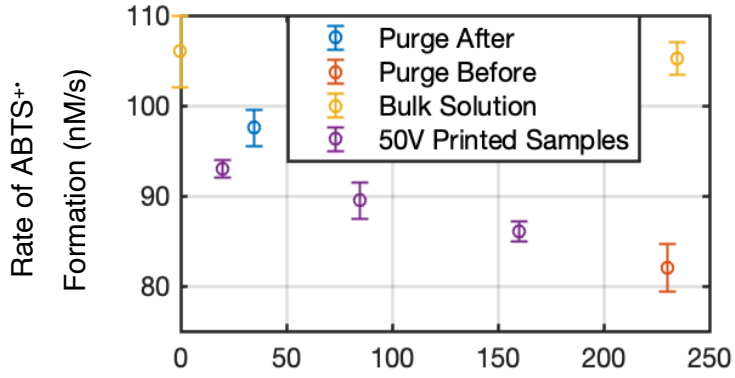

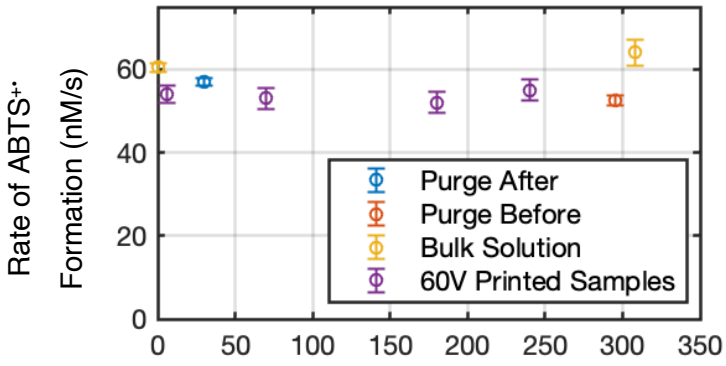

Figure 5.19: activity of protein solutions after IJ printing with the Microfab print system. N=3 for all samples, error bars are ± standard deviation.

In Figure 5.19 for each of the three proteins discussed in this chapter, HRP, GOx and SOx, the voltage is kept constant for all the prints and the time of the assay is recorded relative to when the solution was collected. In all cases, the activity of the printed solutions lies between the purge before and after the printing. The middle graph is for the GOx solution which shows the trend observed in Figure 5.18: the first sample shows the greatest activity loss and the activity then recovers with the following prints. The time of the assay relative to when the sample went through the print system also does not affect the resulting enzyme activity as the HRP and SOx samples show no trend with time.

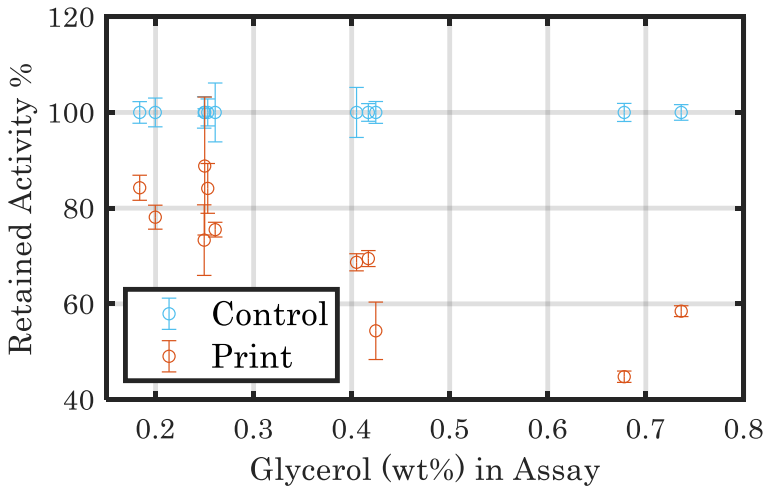

Figure 5.20: Retained activity relative to non-printed control samples of 0.3µM HRP in PBS with 10wt% glycerol printed with DMP at different voltages. Different volumes printed each time resulted in different glycerol concentrations in final assay due to the 10wt% glycerol in the ink. N=3 for each data point, errors bars are ± standard deviation.

For the DMP, 0.3µM HRP solution was ejected into wells of a 96 well plate containing 150µl PBS solution. The volume ejected was calculated by weighing the sample, the buffer and the ejected HRP solution, and then diluted to 50nM for assaying. In Figure 5.20 the printed sample also had 10wt% glycerol to slightly increase the viscosity but mainly to reduce evaporation as this was an issue for the duration of the printing when the droplets were ~20pl. Figure 5.21 shows that the activity of DMP printed 0.3µM HRP in PBS appears to exceed the

unprinted solution. This is because the printed sample was ejected directly onto a flat surface meaning that the fluid was susceptible to evaporation during the printing duration so the HRP concentration was higher in the sample. For this reason, HRP was then ejected into a well plate containing 150µl PBS.

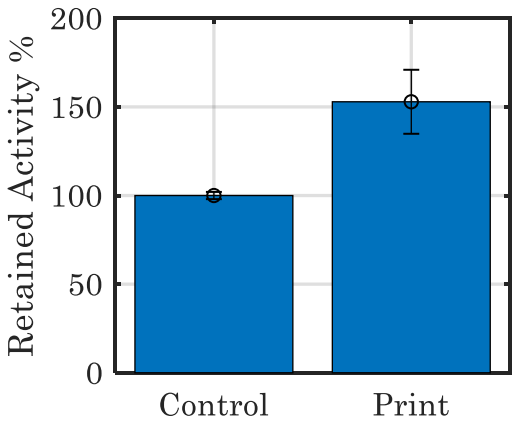

Figure 5.21: The retained activity of 0.3µM HRP in PBS printed with DMP directly onto a polypropylene surface and then collected with a syringe for the assay compared to a non-printed sample of 3µM HRP in PBS. 150% compared to the control is due to an increase in protein concentration due to evaporation. N=3 for each data point, errors bars are ± standard deviation.

The results show that for multiple print runs at various voltages, the final concentration of glycerol in the assay is of more importance than the peak ejection voltage and this result concurs with that shown earlier in the chapter in Figure 5.6, however there is a greater percentage decrease in activity in this case with the DMP so further examination into printing without glycerol in the formulation is required to understand this.

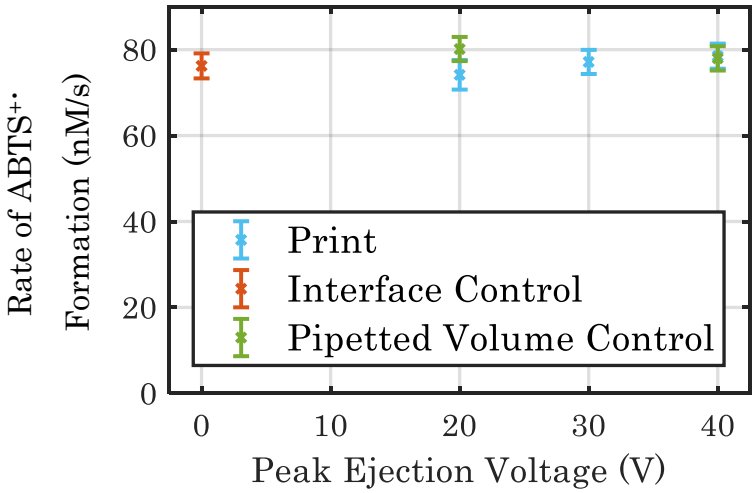

Figure 5.22: Rate of $ABTS^{+\cdot}$ formation in assays containing samples of 0.3µM HRP in PBS printed with DMP at different voltages into 150µl PBS and then diluted to 50nM for the standard ABTS assay. N=3 for each data point, errors bars are ± standard deviation.

In Figure 5.22 neither the interfaces of the DMP printhead nor the action of generating droplets detrimentally effects HRP activity. The activity of the printed samples is within the errors of the samples that have the same volume as was printed pipetted and as the sample that has been taken from the DMP cartridge and has been exposed to all the same interfaces. Therefore, it seems the glycerol is negatively affecting the HRP activity and not the DMP printing process. Moreover, evaluation of the results from flowing protein solutions through a 15 micron constriction, experimental details in section 3.3.2, which isolates the shear force component of inkjet printing combined with experiments that isolate the activity losses from adsorption and involve printing with the MF and DMP print systems, detailed in Figure 5.19 and Figure 5.22 ensures that activity losses due to evaporation and adsorption are controlled for. For the enzymes HRP, GOx and SOx, the forces endured during inkjet printing are not sufficient to cause a loss of activity and can be attributed to adsorption or evaporation. This result has not been explicit in other studies that report activity losses.

5.7 Activity Losses after Droplet Deposition

Depending on the printing application, droplets may need to be deposited in a specific location and possibly left to dry before being further processed. Microarrays of glucose oxidase, horse radish peroxidase and invertase have been produced with inkjet printing for use as logic gates [41], HRP based amperometric biosensors [46], GOx based amperometric biosensors [106] all use droplet based manufacturing techniques for instance.

Droplets ejected with inkjet printing are typically in the volume range of nano to pico litres. Evaporation of droplets this size will be rapid. It is well established that dehydration of protein solutions negatively impacts upon the resulting activity of the rehydrated protein as it causes aggregation and disrupts hydrogen bonding at the surface of the protein [146]. To build a better understanding of the drying of droplets effect on proteins, larger scale droplets are firstly examined in this section and then printed droplets are studied.

Before droplets are dried, experiments must be carried out to ensure that observed activity losses are not just attributed to adsorption to the surface the droplet is deposited onto. Figure 5.23 considers droplets of 50nM HRP solution in PBS on cuvettes made of polystyrene and shows that droplets deposited onto the cuvette surface and then assayed immediately retain protein activity, whereas droplets left in the sealed cuvette for 2 hours 30 minutes lose their activity with a trend that the smaller the droplet the great the activity loss. This implies that there are adsorption losses of the HRP solution to the cuvette surface. This is crucial to account for in subsequent drying experiments.

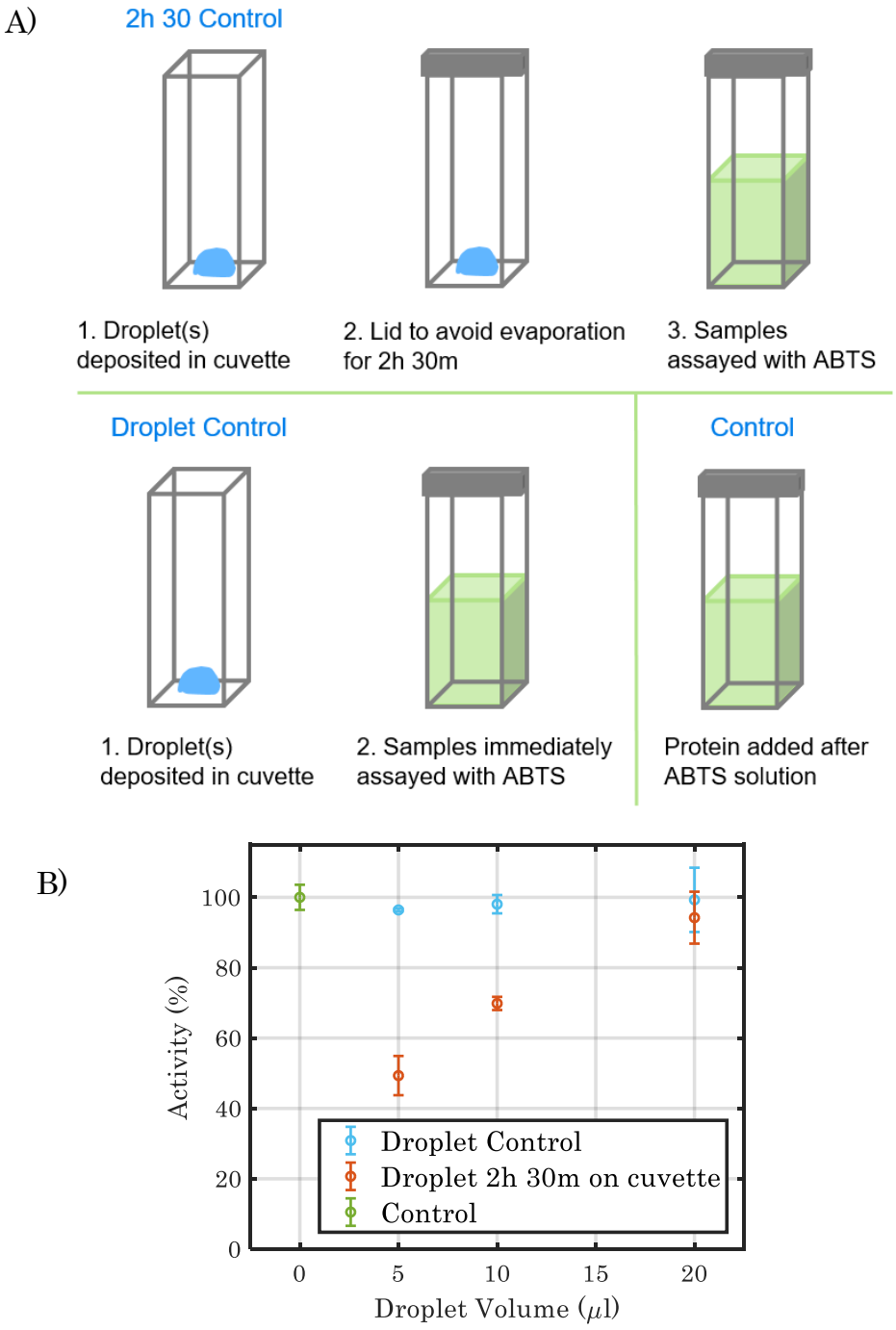

Figure 5.23: Activity of 50nM HRP in PBS after pipetting droplets onto cuvette and then assaying, leaving droplets on the cuvette for 2h 30m or through control samples adding protein solution to initiate the reaction. A) represents each scenario. B) shows the results. N=3 for each data point, errors bars are ± standard deviation.

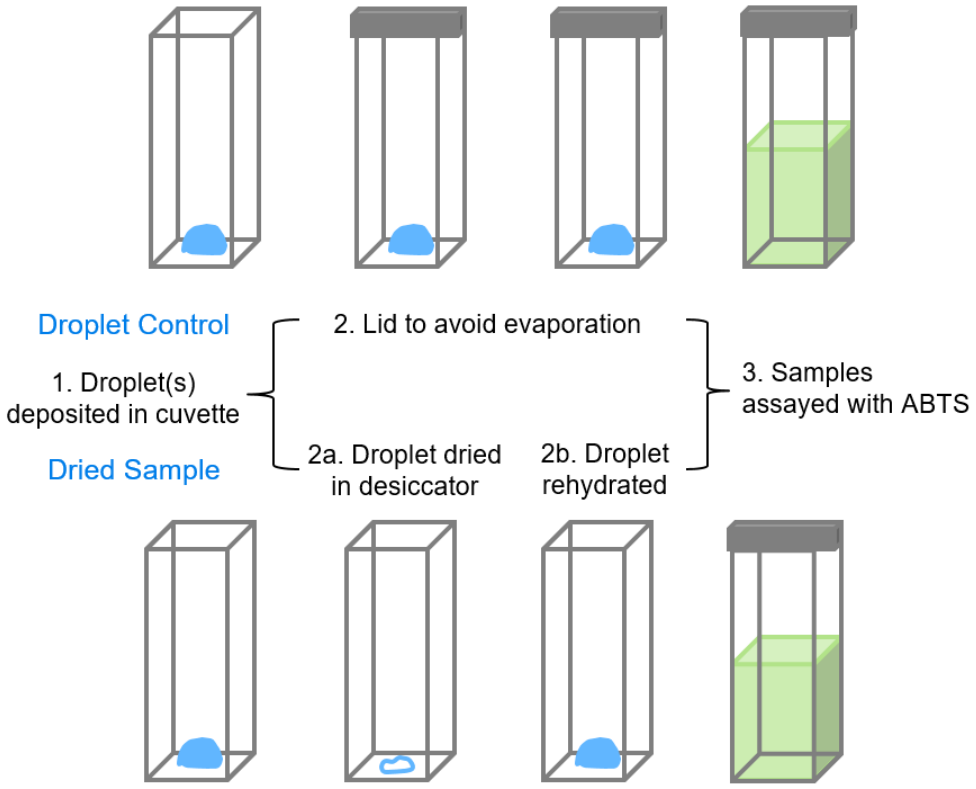

Figure 5.24: A schematic showing the experimental steps taken when drying pipette scale droplets (5–50µl).

The effect of evaporation and drying on HRP and SOx activity is examined, specifically the effect the size of the initial droplet has on the resulting activity of a dried and rehydrated protein. The experimental approach for pipetted droplets is shown in Figure 5.24, droplets of different volumes are pipetted onto the polystyrene cuvette and either sealed in the case of the control of dried in a desiccator, rehydrated and both samples are then assayed as described in section 3.5.1.1. Droplets in the sealed cuvettes are there for the same duration as the droplets that are dried in the desiccator. The control is important to understand the impact that adsorption of the protein solution to the surface the droplet is on has as this was shown to be important in Figure 5.23.

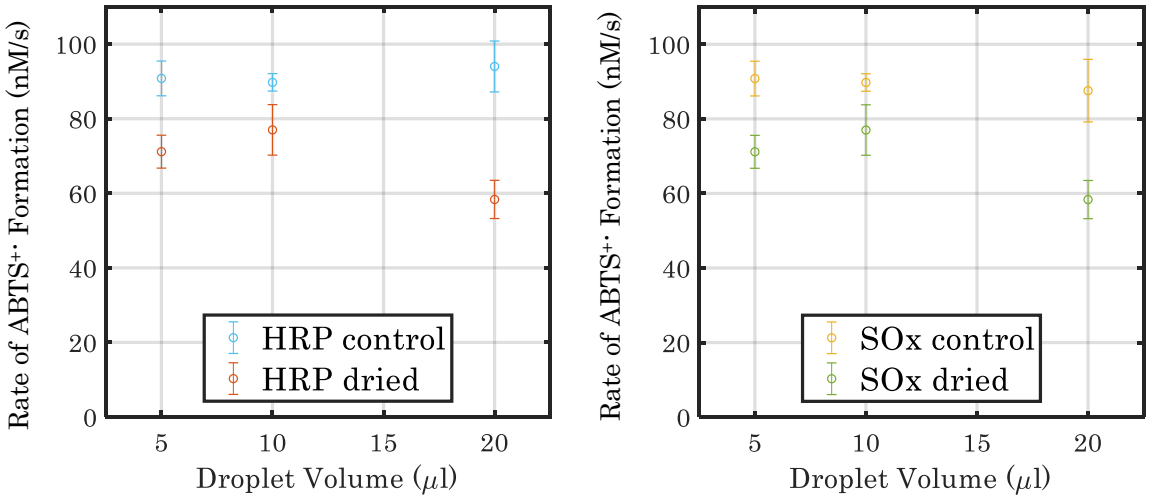

Figure 5.25: Activity of droplets containing 50nM HRP or SOx in PBS dried on a cuvette in a desiccator of various volumes against control droplets in sealed cuvettes for the same time period.

In both cases with HRP and SOx solutions the dried droplets have a greater activity loss when compared to droplets left in the sealed cuvettes. The cuvettes were purchased from Thermo fisher Scientific, information can be seen in the appendix in Figure A 4. These results combined with the finding in Figure 5.23 suggest that being in contact with polystyrene for the duration of the drying negatively impacts on protein activity but drying also has an additional negative effect decreasing activity to a greater extent in combination. For the HRP and SOx samples there is no apparent trend that the droplet volume, at this scale, has on the extent of activity loss.

The experiments in this section so far have dealt with droplets of volume ranging from 5–50µl, but inkjet printed droplets have volumes that are typically 6 orders of magnitude lower at the pico–litre scale. A DMP is used to eject pico–litre scale droplets of 20nM GOx in PBS solution into 100µl PBS in a 96 well plate, as a control, to ensure the printing is not having a detrimental effect on GOx activity, the same volume that is printed is pipetted into 100µl PBS and to observe the effect drying the droplets has, the same volume is printed into an empty well of a 96 well plate, dried in a desiccator, rehydrated and assayed. The pipetted GOx

solution is taken from the DMP cartridge to minimise discrepancies in possible losses due to adsorption to materials in a DMP cartridge. The results are shown in Figure 5.26.

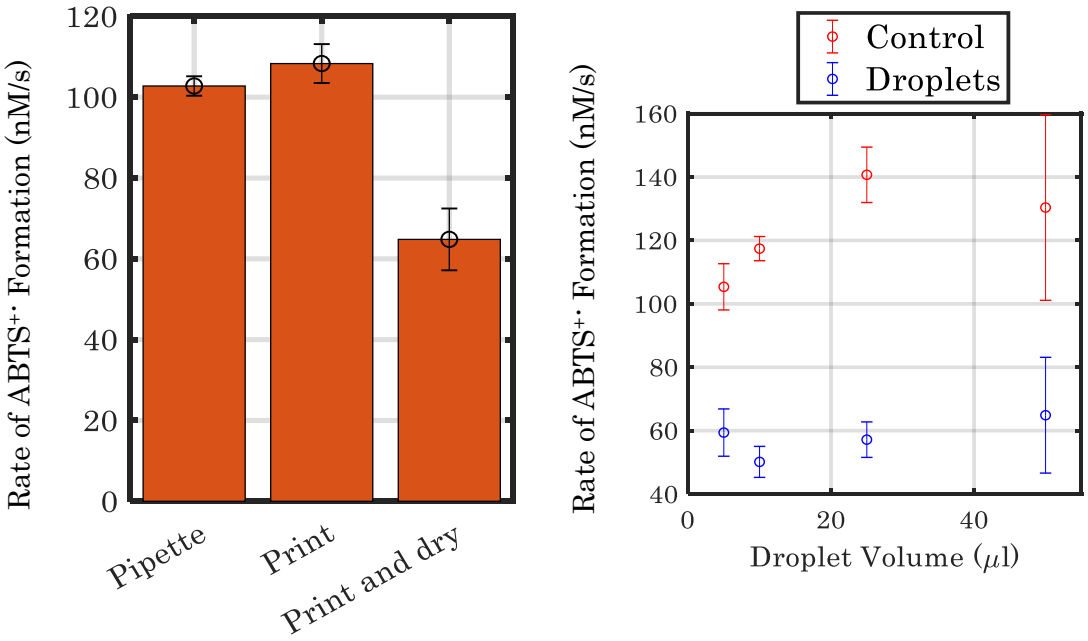

Figure 5.26: Left – Rate of $ABTS^{+\cdot}$ formation in assays containing samples of GOx pipetted or printed with the DMP into 100µl PBS, or DMP printed and dried with a desiccator, rehydrated, and then assayed. Right – Rate of $ABTS^{+\cdot}$ formation in assays containing samples GOx droplets of various volumes dried on a cuvette in a desiccator, control were in sealed cuvettes. N=3 for each data point, errors bars are ± standard deviation.

In this case the results show that there is a loss in activity that is equivalent for both micro and pico litre scale droplet sizes. On the left, GOx is either pipetted or printed into a 96 well plate containing 100µl PBS or printed into a well plate, dried in a desiccator then rehydrated and assayed. The graph on the right is showing the change in activity of dried GOx executed in the same way as detailed earlier in Figure 5.24.

The results show that printing GOx in the DMP system has no effect on the activity when compared to the pipetted solution as the errors overlap, but the

printed and dried solution shows a clear loss in activity which can be attributed to losses in drying and there could also be a contributing factor from the adsorption to the silicon, the only material the pipetted solution would not make contact with.

The reduced activity of GOx after drying was further investigated by examining the FTIR spectra of dried GOx as shown in Figure 5.27. FTIR has been shown to be a useful technique for investigation of protein secondary structure of proteins in aqueous solution and for lyophilised samples [147] From these spectra it can be inferred that there is little impact on the structure of GOx between the drying mechanisms as the spectra of air dried and desiccator dried samples are of the same shape. The spectrum of air dried and rehydrated GOx also has the same shape as GOx solution that has not been dried. The small deviations are in the fingerprint region which is noisy.

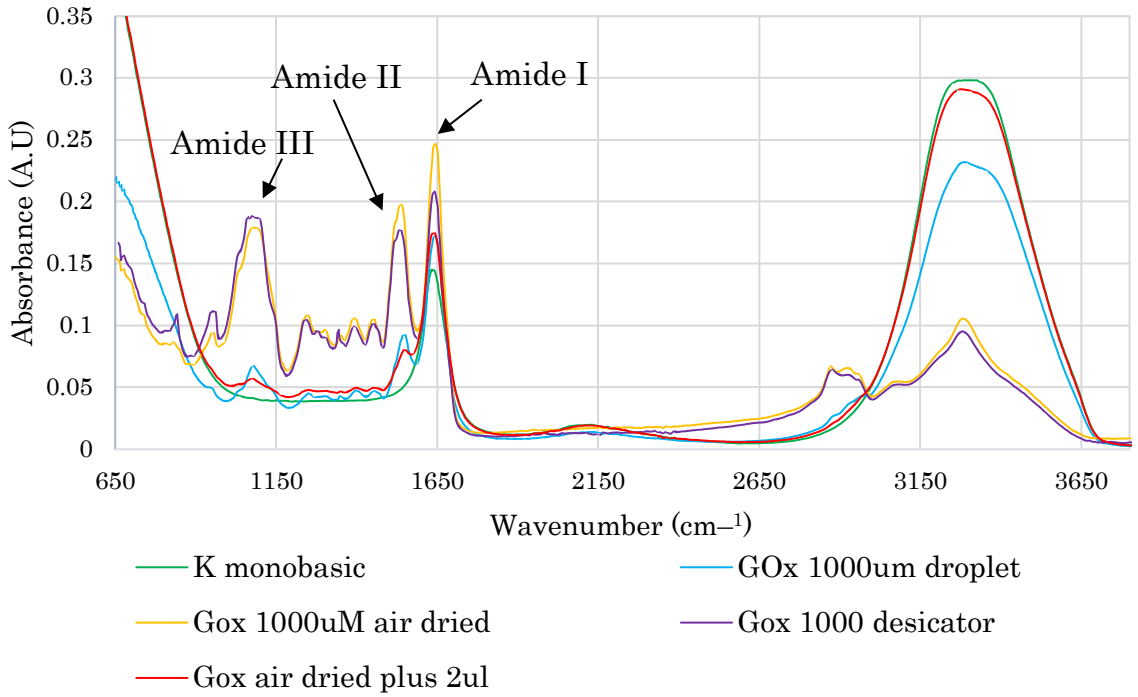

Figure 5.27: FTIR Spectra of 1000μM GOx solution air dried, vacuum dried and rehydrated, 0.01 Potassium Monobasic Buffer Solution.

5.8 Conclusions

The journey of HRP, GOx and SOx solutions have been considered from ink formulation through to deposition with research scale printheads through to systems currently used at an industrial scale. At each stage of the inkjet printing process the following conclusions have been drawn in this chapter that are relevant for enzymes of molecular weight <160kDa.

1. Ink Formulation and Supply
    i. The objectives in formulating inks are to ensure they are printable, to optimise the printability to improve print quality and to do so whilst minimise the activity losses of protein solutions.
    ii. Viscosity modifiers such as CMC 90k and CMC 700k have a positive impact on protein activity at low concentrations – a concentration of 10–30μM CMC 90k increases the activity of GOx solutions by 21%, for CMC 700k the activity increases by 50% at 4μM and this is not due to a false positive result but instead the interaction of CMC with GOx.
    iii. Glycerol, used predominantly as a humectant but also increases viscosity, has a small detrimental effect to HRP activity, at a concentration of 10wt%, HRP activity is reduced by 10%, moreover the concentration of glycerol in a final enzymatic assay also negatively effects HRP activity, for a final glycerol concentration beyond 0.4wt% the activity can be reduced by 10% for 0.6wt% and 15% for 0.8wt% even though the samples glycerol concentration is 10wt% for both.
    iv. PEO 1M has an impact on the viscoelasticity of an ink resulting in a long ligament during printing but has a neutral effect on activity at concentrations below 0.0025wt%.

2. Ancillary Equipment
    i. Losses due to protein adsorption on the tubing is the biggest concern for activity loss. Tubing is typically made from PTFE or PU with PU outperforming PTFE by a 1–5% increase in activity for the three protein systems.
3. Printhead
    i. The materials that the printheads are made from will affect the extent of protein adsorption. Protein adsorption is of biggest concern with the research scale MF printheads, in particular contact with the glass reduces GOx activity by 20% compared with a bulk solution and this activity is reduced by a further 27%, 47% total reduction, when the GOx solution makes contact with the stainless steel guards.
    ii. The materials in the DMP and Spectra SE–128 AA printheads, plastic, silicon and metal do not have the issue of protein adsorption.
4. Nozzle Flow
    i. Flowing protein solutions through a 15μm diameter nozzle provides an accurate indication as to whether the proteins in question will lose activity due to IJ printing.
5. Droplet Formation
    i. The forces during the inkjet printing ejection process do not appear to negatively affect the retained activity of the protein systems studied. More detail on the nature of these forces is detailed in Chapter 4.4. Even when the driving voltage is close to the upper limits of the print systems there is no issue.
    ii. Adsorption is an issue on the print systems but selecting the correct control appropriate for the print system in use isolates the impact of this effect.

6. Drying
    i. The volume of the droplet that is dried does not show any trend upon the resulting activity loss of HRP, GOx and SOx solutions in the rehydrated droplet and the losses can be as severe as a 50% reduction in enzymatic activity compared to a control and this control also accounts for adsorption losses.
    ii. Means to mitigate the negative effects of drying protein solutions and rehydrating them for the assay should be examined further.

These conclusions indicate that further research should be focus on the following areas:

- Modifying the ink formulation whilst maintaining or enhancing protein activity to reduce the negative effects of drying or reduce the affinity of a given protein to a material in a print system.
- Selecting printheads with materials that minimise adsorption losses from protein solutions or modifying the printheads to reduce this.
- Ensuring that the entire print system design reduces the negative impacts of droplets drying.

Chapter 6 Retaining Printed Enzyme Activity

6.1 Introduction

In Chapter 5 the impact inkjet printing has on the surviving function of HRP, GOx and SOx was examined. It was determined that the losses in the retained activity were due to drying or adsorption losses to materials within print systems. There were also activity losses for certain viscosity modifiers, an important consideration for ink formulation. In this chapter, methods to prevent activity losses of printed enzymes will focus on the ink formulation and printhead considerations to prevent the observed losses due to drying and adsorption. It serves as a proof of concept for the use of sugars within the ink formulation of inks containing HRP and SOx and the results presented are preliminary.

The novel approach taken in this chapter is approaching the addition of sugars in the ink from the perspective of reducing the impact of losses due to drying and adsorption, whereas previous instances of the addition of sugars to protein-based inks for inkjet printing have been under the premise that it would reduce activity losses due to the forces endured by the proteins during printing [5], [100]. Therefore, the specific contribution of activity losses due to drying and adsorption have been isolated and examined in this context. The challenges and unknowns to be determined in this chapter are assessing how the droplet volume affects activity loss and how the addition of sugars affects this, if protein activity loss is effected by the amount of water retained in a droplet during the drying

process, and how the surface material the droplet and ink is in contact with effects the retained activity and how sugars impact upon this.

6.2 Ink Formulation: Addition of Sugars

The aim of modifying the ink formulation is to minimise drying losses or reduce adsorption to the printing apparatus. Modifications to the ink formulation are examined in this chapter – the addition of sugars, namely trehalose and glucose as these have previously been sited to reduced activity losses of HRP solutions after inkjet printing [100]. Although proteins have different characteristics, it is proposed that sugars stabilise proteins by reducing the global and local mobility of the protein structure which prevents unfolding [148].

The addition of 10wt% trehalose and 1wt% D–glucose is examined for the HRP and SOx system. It was not appropriate to examine the effect the addition of sugars has on GOx solutions because D–glucose would interfere with the assay used to determine the GOx activity. These sugars were specifically chosen over other polysaccharides or maltodextrins because they had previously been used in inkjet studies with HRP [100] so warranted further investigation.

As in Chapter 5, it is important to consider the experimental setup to ensure that the comparison of dried droplets accounts for adsorption losses. Figure 6.1 shows the effect that leaving droplets containing 50nM HRP in PBS with 10wt% trehalose and 1wt% D–glucose on the polystyrene surface of a sealed cuvette has. The control sample is measuring the activity of HRP from an Eppendorf containing protein solution according to the methodology for activity measurements detailed in section 3.5.1.1. The droplet control sample has deposited the protein solution in droplets directly onto the cuvette just before assaying whereas the droplets with 3 hours delay have been deposited into the cuvettes, the cuvette has been sealed with a lid and then left for 3 hours. 3 hours

was chosen to be representative of the printing durations for printing with the Microfab printhead, detailed in Chapter 5. There is a loss of activity for the 10µl and 20µl droplet volume; there is also a loss for the 5µl droplet, but the error bars overlap. However, there is sufficient evidence to show that adsorption to the cuvette will detrimentally affect the activity of HRP solutions during the duration of the drying experiments.

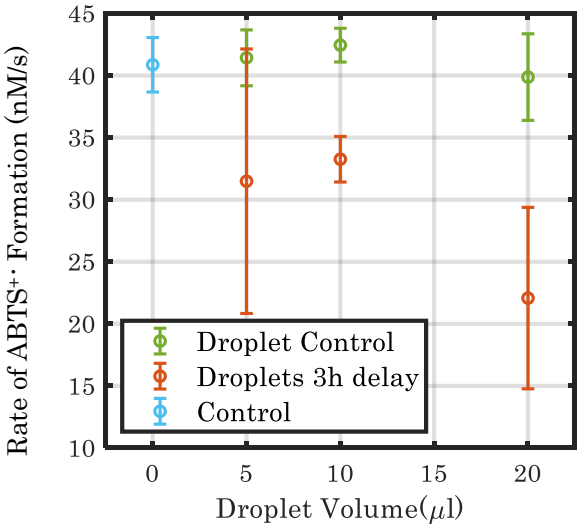

Figure 6.1: Rate of $ABTS^{+\cdot}$ formation for assays containing samples of 50nM HRP in PBS with 10wt% trehalose and 1wt% D–glucose left on a cuvette for 3 hours, deposited as droplets onto a cuvette just before assaying or assayed as normal. N=3 for each data point, errors bars are ± standard deviation.

Sugars are hygroscopic meaning that the rate of evaporation will be different than of a pure water or water and buffer solution. After 3 hours in a desiccator, it was visible that more than a coffee ring was left behind which warranted further examination of the evaporation of the droplets.

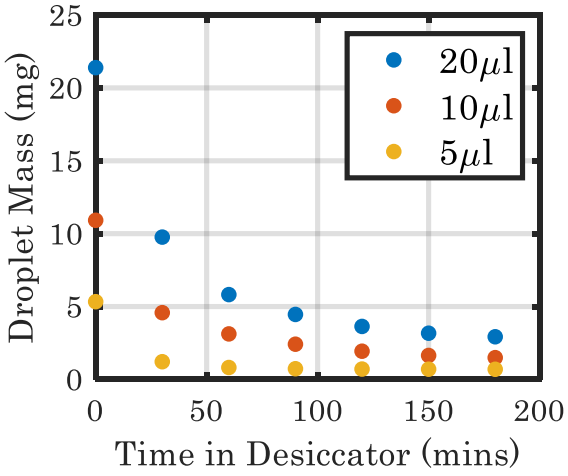

Droplet Volume (µl)	Volume of water added (µl)
20	19.46
10	19.46
5	19.59

Figure 6.2: Evaporation of 10wt% trehalose, 1wt% glucose in PBS over time and the resulting amount of water to be added to dried droplets after 3 hours.

The mass of 50 droplets of the same pipetted volume, 20µl, 10µl or 5µl, was measured for different lengths of time in the desiccator. The mass of a single droplet was determined by dividing the total mass by the number of droplets and for this reason there are no visible error bars in Figure 6.2. The graph shows that the mass of the droplets converges after 150 minutes for all droplet volumes and fastest for the smallest droplet volume, 5µl as expected as the rate of evaporation is dependent on the size of the droplet. Due to the hygroscopic nature of the sugars, not all of the water in the droplets evaporates. This meant that after 3 hours, the original droplet volume was not re–added to rehydrate the droplets, instead the amount shown in the table in Figure 6.2 was added based on the mass of the droplets after 3 hours.

Droplets containing 50nM HRP in PBS with 10wt% trehalose and 1wt% D–glucose were dried for 3 hours and rehydrated according to the table in Figure 6.2. The control sample of HRP was assayed in the usual way, the droplet control left droplets inside a sealed cuvette for 3 hours preventing them from drying but exposing the protein to the same surface as the dried droplets, whilst the dried droplets were left on the surface of a cuvette, allowed to dry for 3 hours and then rehydrated according to the table in Figure 6.2.

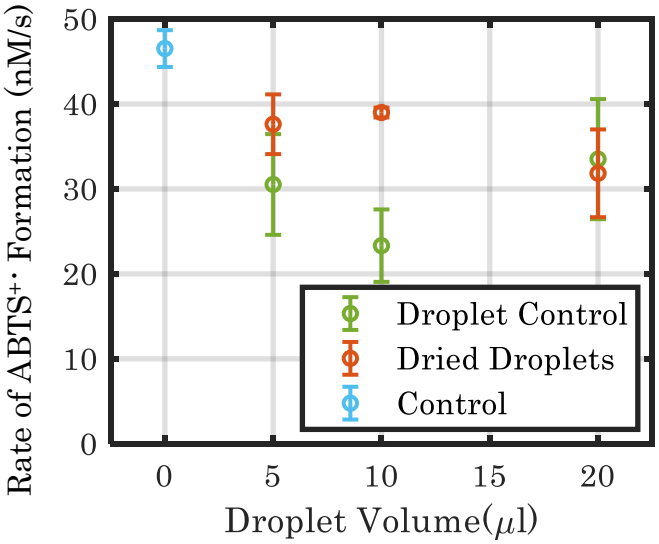

Figure 6.3: Rate of $ABTS^{+\cdot}$ formation for assays containing samples of 50nM HRP in PBS with 10wt% trehalose and 1wt% D–glucose after being dried in a desiccator for 3 hours, on a cuvette for the same duration or assayed as normal for the control.

Compared to the control, where the droplets were left on the surface of the cuvette for the same duration, the dried droplets retained overlapping activities for the 5µl and 20µl and exceeded the activity for 10µl, as shown in Figure 6.3. For the 10µl droplet, the control data point was lower than the dried data point, however when comparing the activity in Figure 6.1, the control data point is lower than expected which could be due to a level of experimental error and noise inherent to biological systems. If the measured control for the 10µl droplets was the same in Figure 6.1, the dried droplet would be close to retaining its activity in comparison.

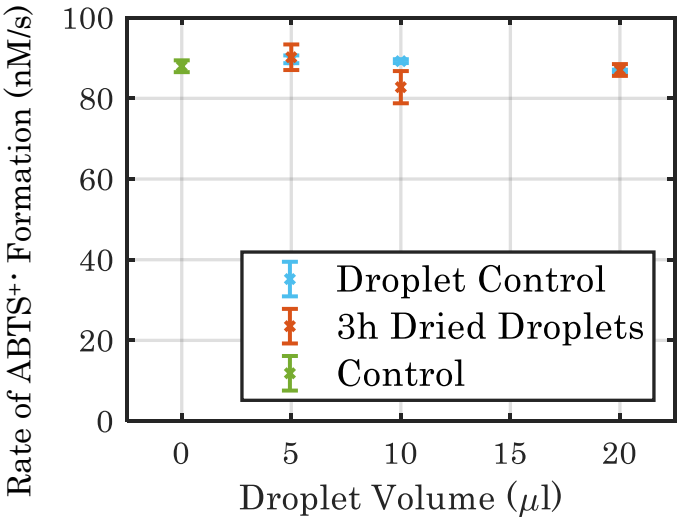

Figure 6.4: Rate of $ABTS^{+\cdot}$ formation for assays containing 50nM SOx in PBS with 10wt% trehalose and 1wt% D–glucose after being dried in a desiccator for 3 hours, on a cuvette for the same duration and assayed as normal for the control. N=3 for each data point, errors bars are ± standard deviation.

The same experiment was conducted for solutions containing SOx in PBS with 10wt% trehalose and 1wt% glucose with the results shown in Figure 6.4. With SOx it is clear that the addition of sugars to the buffer solution enabled the enzyme to retain its activity when compared to the controls except for the 10µl droplets which showed a small decrease in activity for the dried droplets but the level of retained activity is greater than for solutions which do not contain sugars which was shown in chapter 5.7 in Figure 5.25.

In both of these experiments the duration of droplet drying was fixed at 3 hours. It is also important to consider the case where droplets are partially dried, and the amount of water retained by the droplet varies because during any printing process not all droplets are deposited onto a surface instantaneously. Droplets of volume 20µl containing HRP in PBS or HRP in PBS with sugars are deposited onto a surface and allowed to dry to different extents. The droplets are weighed so that the mass of water retained by the droplet is measured, the droplets are

then rehydrated and the activity of HRP after partial drying and rehydrating can be determined, as shown in Figure 6.5.

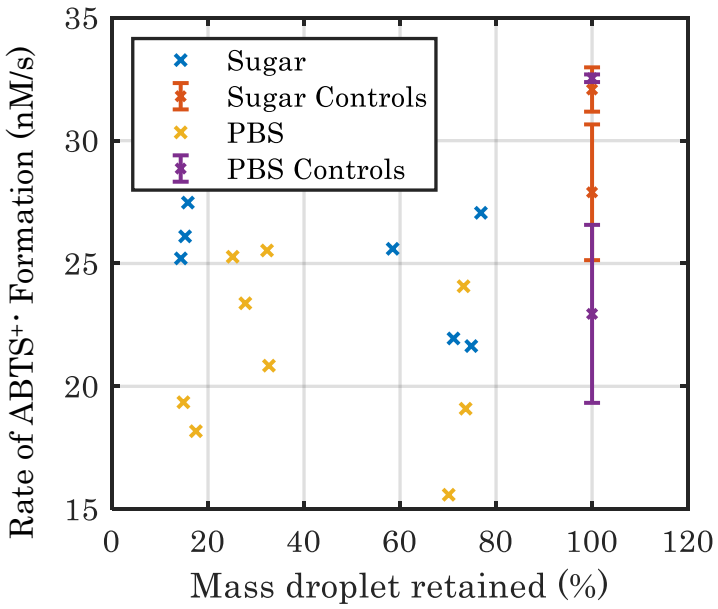

Figure 6.5: Rate of ABTS+• formation of HRP samples formulated with 10wt% trehalose, 1wt% glucose and PBS or PBS alone with different mass % of water retained in the droplets. Control droplets of 20µl are not dried but remain in contact with the surface for the same duration. For the controls N=3 for each data point, errors bars are ± standard deviation.

There is no clear trend in the results correlating the percentage of water retained with the retained activity of the HRP although the droplets containing sugars retain a higher activity than solutions without sugar but this is also consistent with the controls. These results are consistent with a study that examined freeze drying of β–galactosidase where only a significant drop in activity was observed when residual moisture is below 10% [149].

6.3 Printhead Selection

6.3.1 Material Consideration

As mentioned in section 2.2.1, one method to reduce adsorption losses is to use BSA as a sacrificial protein to saturate the surface of a material so that other proteins cannot adsorb to the surface [85]. Figure 6.6 shows the activity of GOx assayed after filtering, filtering and flowing through PTFE tubing, or filtered, flowed through tubing and purged through a 50µm MF nozzle that has been blocked with BSA or that has not been.

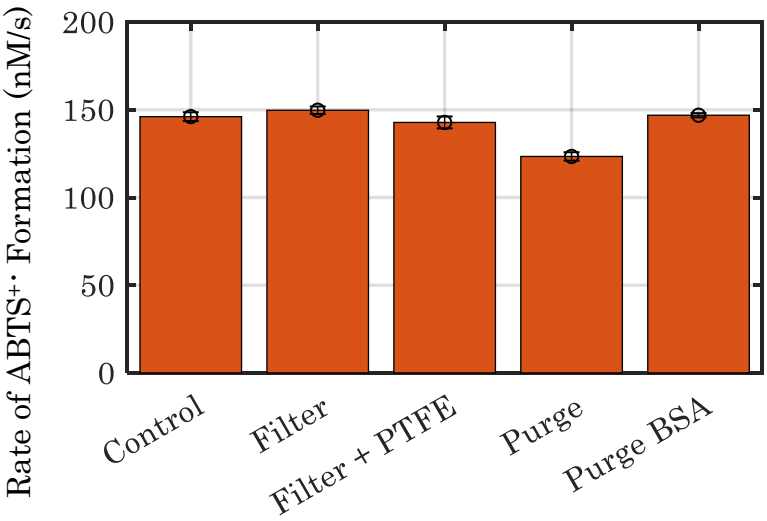

Figure 6.6: Rate of ABTS+• formation for samples of 50nM GOx, assayed from a bulk solution (control), after filtration (filter), after filtration and flow through PTFE tubing (filter + PTFE), after purging through an uncoated 50µm diameter MF nozzle, after purging through a 50µm diameter MF nozzle that has been coated with BSA. N=3 for each data point, errors bars are ± standard deviation.

There is a reduction in activity of the purge through the MF nozzle that has not been blocked with BSA. This result verifies that the BSA has saturated the surfaces of the MF nozzle and that GOx adsorbs to the surface of the glass of the standard MF nozzle resulting in a drop in concentration of GOx which lowers the

velocity of the reaction. The ink did not appear visibly different after purging through the nozzle blocked with BSA compared to purging through a nozzle without the coating.

6.3.2 Droplet Volume

The actuating waveform driving the piezoelectric element during inkjet printing can affect the droplet volume but the size of the orifice is a limiting factor on the volume of the resulting droplet that is ejected [150]. The waveform driving the piezoelectric element, predominantly the voltage will also influence the droplet volume – the greater the voltage the larger the droplet [23]. When inkjet printing is used to deposit droplets onto a surface, the choice of printhead will affect the droplet volume and hence affect the speed a droplet will dry. Drying has previously been highlighted as a concern as enzymatic activity is reduced when protein solutions are air dried, as shown in Chapter 5. Because the volume of droplets ejected during inkjet printing are in the volume range of pico–nanolitres, the droplets dry rapidly as shown in Figure 6.7, 40 droplets of PBS were ejected onto the same position, but the majority of the water has evaporated within 4 seconds of droplet deposition.

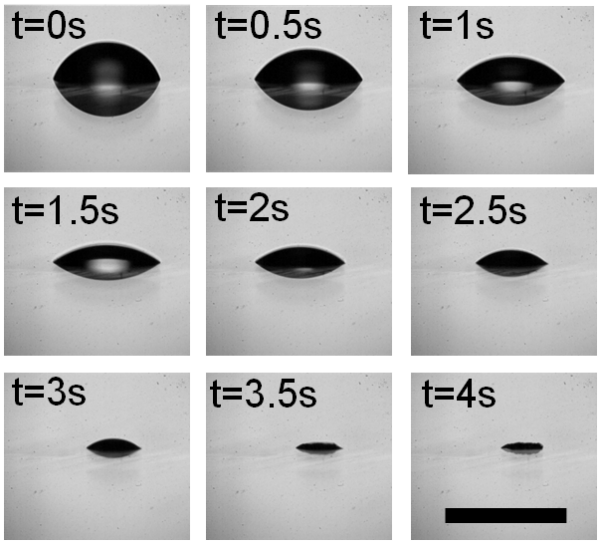

Figure 6.7: A representative droplet of PBS evaporating in time. The scale bar is 500μm in width and the time after each frame is indicated on the image.

Using a high–speed camera and the methodology detailed in 3.4.2.2, the linear evaporation rate of droplets of various size can be determined. The volume of the droplet is determined over time and the initial linear slope of the volume with time curve is determined using a least–squares fitting on Matlab. An example of the methodology is shown in Figure 6.8 where the linear fit of the initial slope of the evaporation curve is overlayed.

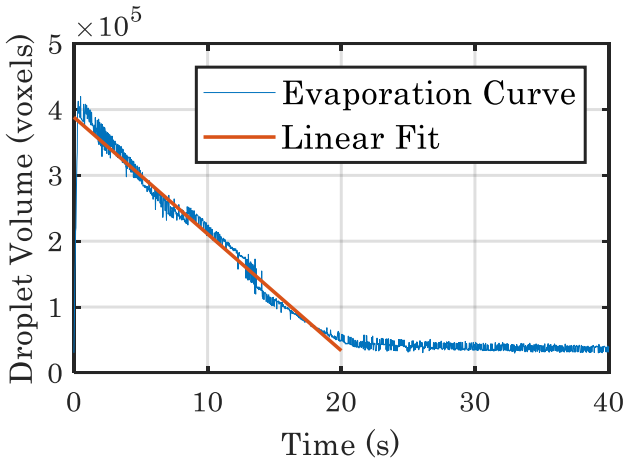

Figure 6.8: The evaporation curve for a droplet to illustrate the steady state evaporation rate linear fit.

It is difficult to determine the volume of the droplet once the droplet no longer retains the shape of a hemispherical cap, the remaining droplet is also becoming increasingly concentrated with buffer salts and sugars in the case of droplets containing trehalose and glucose. Therefore, beyond the linear fitting, the accuracy of calculating the droplet volume is limited. For different droplet volumes, representative of droplets ejected from different diameter orifices, the initial rate of evaporation is determined and plotted in Figure 6.9 with 95% confidence intervals for the linear fitting of the droplets containing PBS and sugars. The results show that there is a linear increase in the evaporation with the initial droplet volume but there is no significant difference in the linear fitting dependent on the ink formulation.

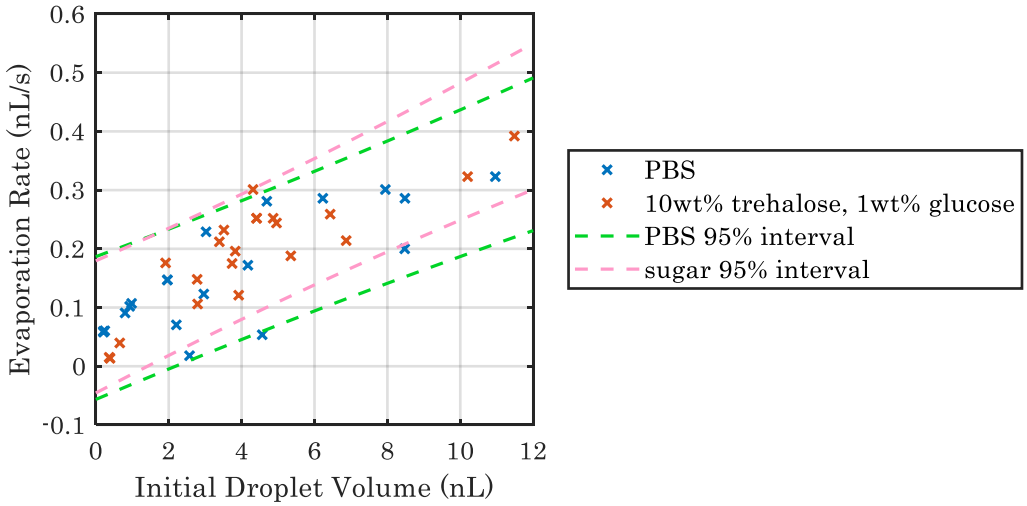

Figure 6.9: The steady state rate of evaporation of droplets containing 10wt% trehalose, 1wt% glucose in PBS or just PBS for the linear part of the evaporation curve compared to the initial droplet volume with 95% confidence intervals for each series.

6.4 Conclusions

In this chapter methods to reduce the activity loss of HRP, SOx and GOx were examined with a particular focus on losses due to drying and adsorption, the factors established as the main cause of activity loss during the inkjet printing process in Chapter 5. The following conclusions were drawn:

1. Addition of Sugars to Ink Formulations
   i. Taking into account adsorption losses to the surface of the cuvette, when drying droplets containing 10wt% trehalose and 1wt% glucose for GOx and SOx the proteins retained activity compared to droplets not containing sugars.
   ii. The moisture content retained by droplets after drying for different durations does not have any trend in terms of the retained activity and the addition of sugars also does not affect this.
2. Preventing Adsorption Losses
   i. Using a sacrificial protein, such as BSA, to coat the material in the printhead prevented all activity losses caused by the materials. This was demonstrated with the Microfab (MF) printhead.
   ii. Proteins have different propensities to adsorb to different materials, in the case of GOx with the MF printhead, the glass capillary of the printhead has a greater detrimental effect than the tubing supplying the printhead.
3. Consideration of droplet volume
   i. The rate of evaporation will be faster for larger droplets but is not affected by the addition of sugars.

Chapter 7 Collagen Integrity after Extrusion

7.1 Introduction

Hydrogel extrusion is an up–and–coming manufacturing technique used for tissue engineering and drug discovery applications, as discussed in section 2.3. Some example applications include breast cancer models for drug discovery applications [151], for drug discovery and delivery in pharmaceutics [152] and to create 3D cell models, more representative of their 2D counterparts [71]. Hydrogels containing structural proteins, such as fibrin, chitosan and collagen have been formulated into inks used for extrusion based bioprinting and offer the advantage of being highly functional, representative of the ECM seen in biological systems and provide flexibility in formulation for achieving the desired mechanical properties of the gel [153], [108]. In particular, collagen, possessing a triple helical structure is the most abundant protein found in all mammals [120]. Type I collagen has the particular benefit of having low immunogenicity, less than 90% of the population will have an immune response upon implantation making it biocompatible and applicable for tissue engineering [121].

Tissue engineering applications typically extrude the hydrogels with cells seeded and research has often focused on ensuring the cells are not damaged during this process [9]. However, the forces endured by gels during extrusion can cause changes to the gel's mechanical properties, in particular many hydrogels are shear thinning and self–healing [117]. Studies have previously investigated how shear forces can cause hydrogels containing collagen to align in the direction of

shear [154], [123], [129] clearly demonstrating that forces during extrusion based printing will impact upon collagen based hydrogels. Shear rates as low as $8.3s^{-1}$ have been shown to have an observable effect on collagen fibre alignment [13].

As discussed in section 2.3.1, hydrogels have been selected to be used so extensively for bioprinting because of their ability to replicate the ECM [108], therefore understanding the impact extrusion has on hydrogel integrity and structure is required before functional materials, such as cells are added to the gels. Moreover, as it is notoriously difficult to characterise gels, with rheological data across studies having multiple orders of magnitude differences [110]. This has clear implications for determining absolute and accurate rheological data, but also indicates that these techniques can be used effectively when looking at relative results or comparisons within a study.

In this chapter, the manufacture of collagen type I gels will be examined, in particular how the mixing process used effects the resulting gel properties. This is because the mechanical properties of the gel are extremely sensitive to the method used to form the gel and with a better understanding of collagen gel formation, the aim of guiding manufacture of these gels can be achieved. Then the extrusion of these gels will be examined to build an understanding of how this fluid deposition process effects the material characteristics of the gels. This work will also explore and validate the use of piezo axial vibration (PAV) rheology as a suitable quality control measure that can be recommended to lab usage and industrial scale–up due to its rapid response, affordability and low volume requirements which has not been used previously for characterising collagen gels. Finally, a simple simulation of extrusion with viscoelastic materials will be presented to provide insight into the shear rates and velocity the gel undergoes during this manufacturing process. The main goal of this chapter is to assist in standardising bioprinting so that fabrication using this manufacturing technique can be scaled up more effectively through linking experimental results to modelling.

7.2 Manufacturing of Collagen Gels

For any process to move from research to industrial scale, the process must be reliable and repeatable. This is particularly important when extrusion is used for an application where cells will be cultured within the gel as the properties of the cell scaffold have an impact on the resulting cell behaviour, this has been shown for gels generally [155] and specifically collagen scaffolds [156]. Therefore, an important first step to move towards tissue engineering with collagen–based gels at an industrial scale is to examine the production of the gel without any cells seeded.

Acid soluble collagen type I forms a weak gel upon neutralisation of the solution and incubation at 37°C. This is because in acidic solution the collagen lacks the N and C propeptide extensions. Once neutralised, the tropocollagen subunits of 300nm in length self–assemble and form fibrils that result in gel formation. To understand the impact gelation has upon the mechanical properties of the sample, it is important to compare the properties of the pre-gelled collagen stock solution, a gelled sample and crosslinked sample. This will provide a baseline understanding of typical mechanical properties that would be expected in further samples examined throughout this chapter.

The mechanical properties to be examined, the storage modulus, loss modulus and phase angle, are typical for characterising viscoelastic materials. The storage modulus measures how much energy is stored elastically in the material and represents solid behaviour, the loss modulus measures the viscous behaviour of the sample and represents liquid like behaviour and how much energy is dissipated as heat when a sample is deformed. The phase angle indicates the delay between when the maximum stress and strain occurs when a sample is deformed.

The storage, loss moduli and phase angle are shown in

Figure 7.1 for 3mg/ml pepsin soluble collagen in 0.01M HCl, before gelling, and the same solution after neutralisation and incubation for 2 hours at 37°C. The crosslinked collagen is the gelled collagen left for 48 hours with 2% glutaraldehyde used as a crosslinker, this is the same method used to crosslink samples for observation with a SEM. Measurements were made using a PAV rheometer, further details are given in section 3.3.1.2. This type of rheometer was selected because of the small fluid volumes required, 80µl per sample, tests can be conducted quickly, and it could be envisioned that this characterisation technique could be used for quality control in industrial processes.

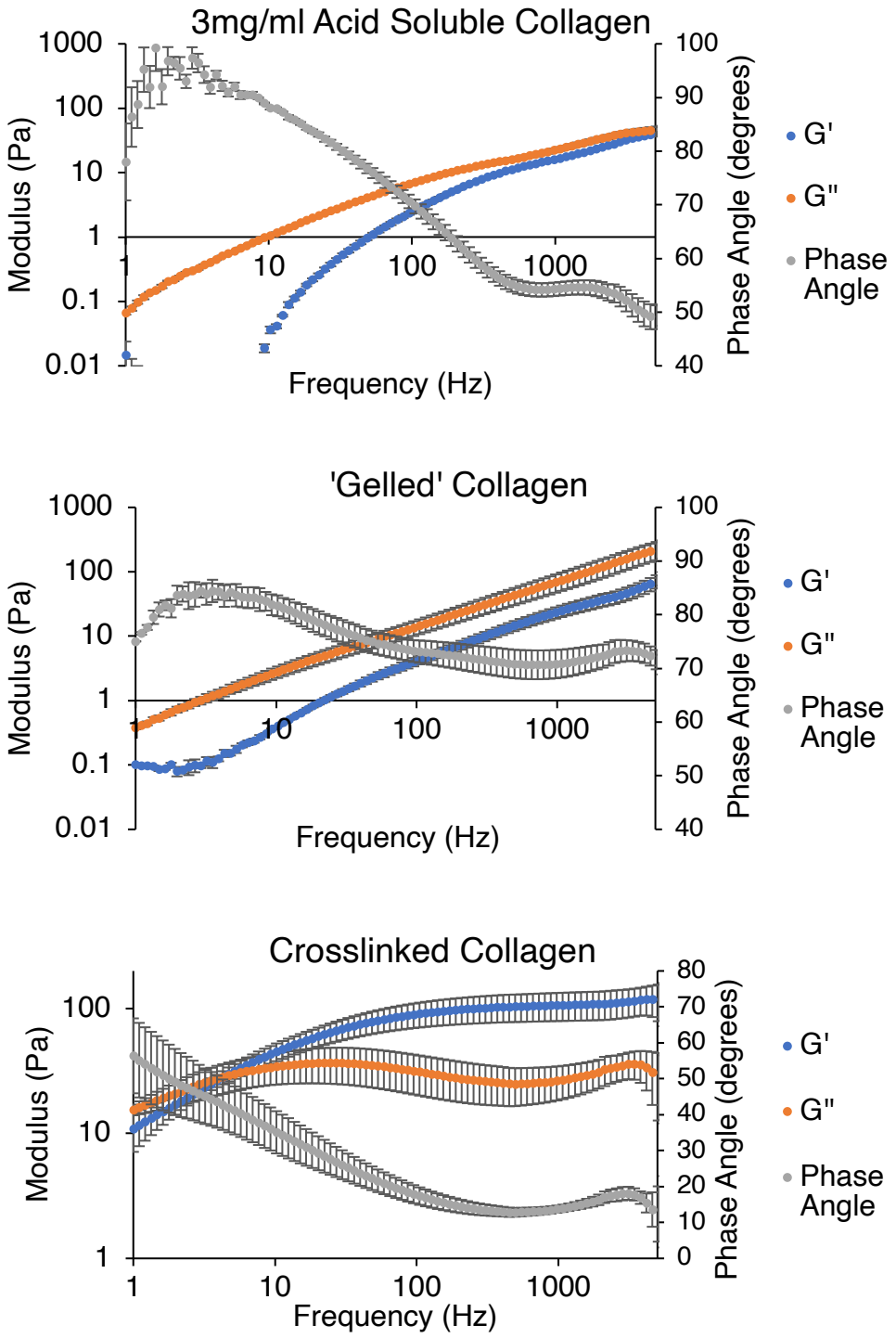

Figure 7.1: The storage modulus, loss modulus and phase angle for 3mg/ml Pepsin Soluble Atelo Collagen, type I in 0.01M HCl (top), the same collagen after neutralisation and incubation to cause gelation (middle), then the gelled collagen left for 48 hours with 2% glutaraldehyde to crosslink (bottom). N=3 for all samples and data points.

The results in Figure 7.1 show how the properties of the collagen change from the acid soluble stock solution before gelation, through to a crosslinked gel for 3 samples. The error bars can be attributed to a level of 'batch to batch' variation in manufacturing combined with some error in the measurements. The measurements are for three separate samples prepared in the same way with the average of these three measurements making up each data point and the error bars are the standard deviation of the three samples. All materials show viscoelastic properties as the phase angle is not 0°, indicative of a purely elastic material, or 90°, a purely viscous material, in any case, hence there is a delay between when the samples endure the maximum stress and when the maximum strain to the material occurs, i.e., there is a lag between when the response to the input sinusoidal wave from the rheometer is observed. During the neutralisation of the acid soluble collagen, the concentration is reduced from 3mg/ml to 2.7mg/ml, due to the mixing of the neutralisation buffer with the collagen stock solution in the ratio 9:1, but the storage and loss moduli both increase. More energy is stored within the gelled structure than before incubation and neutralisation. The phase angle is also more stable across the entire frequency range, around 70° which means that the samples could be considered viscoelastic fluids or very weak gels as gels typically have a phase angle closer to 45°. The values of G' and G" for the gelled collagen are in the same order of magnitude across the frequency range as observed when another microrheological technique, optical tweezers was used to measure collagen gel rheology [157].

As such a weak gel is formed, the manufacture of such gels is highly sensitive to the processing conditions chosen to produce the gel. Table 7.1 gives details of the components making up collagen gels in previous studies found in the literature. Where possible, the mixing technique is also specified. In these examples, only one specifies the mixing technique used, noting that vortex mixing is used, but the duration or rpm is not specified.

Table 7.1: Some examples of the components of collagen gels, how they are mixed and the application.

Ref	Gel Components	Mixing	Application
[112]	5mg/ml type I rat–tail collagen (4 parts), 1N NaOH in PBS (1 part).	On ice but not specified.	To standardise the protocol for parallel plate rheology of hydrogels.
[125]	3mg/ml type I bovine atelocollagen (8 parts), 10x PBS (1 part), 0.1M NaOH (1 part).	On ice but not specified.	Influence of shear on collagen self–assembly.
[158]	15mg/ml type I rat–tail collagen in acetic acid, 1x PBS, 10x PBS and 1N NaOH to give a final collagen concentration of 8mg/ml mixed with different cell densities of chondrocytes	Not specified.	Determining the influence of cell density in collagen gel on rheology.
[123]	Acid–soluble rat–tail collagen type I (3.64 mg/ml) mixed with 0.2 ml of 10 x MEM and 8 µl of antibiotics. Neutralized with 15 µl of 0.1N sodium hydroxide. Periodontal ligament cells added to the collagen solution to 3 x 10^5 cells/ml of collagen solution in final concentration of 1.98 mg/ml.	On ice but not specified.	Using shear stress to align collagen fibres and periodontal ligament cells in tissue constructs.
[159]	Acid soluble rat tail type I collagen neutralised with 10x DMEM, 0.25M NaOH, water, FBS and 1x DMEM to reach pH 7.4.	On ice but not specified.	Modification of collagen gel mechanical properties by changing gelation conditions.
[157]	Type I rat tail collagen diluted to with final salt concentration 273 mM NaCl, 5 mM KCl, 42 mM Na2HPO4 and 9 mM KH2PO4 (final pH= 6.9).	Not specified.	Optical tweezer micro rheology of collagen gel.
[160]	Collagen type I diluted to 2mg/ml with 10x	Not	Characterisation of

	DPBS.	specified.	collagen gels for wound healing models.
[122]	Type I rat tail collagen diluted to 1mg/ml with 10x DMEM, HEPES buffer and 0.5M NaOH to reach pH 7.4.	Not specified.	Prediction of elastic moduli of collagen gels from confocal microscopy.
[161]	100µl PBS, 0.41 ml ddH2O with 0.025M sodium hydroxide added (to reach a pH of 12.38), and 0.49 ml 8.16 mg/ml acid–soluble rat tail tendon collagen. After vortexing, the collagen concentration was 4 mg/ml and pH 7.4.	On ice, vortex mixed.	Studying collagen gel microstructure using multiphoton microscopy.

To quantify the effect the mixing technique has on collagen gel preparation, collagen samples were either vortexed to mix the neutralisation buffer and acid soluble collagen or control samples were gently mixed by slowly pipetting the mix up and down 3 times before incubation for 2 hours at 37°C, further detail on collagen gel preparation is detailed in section 3.3 and Figure 7.2 illustrates the steps to produce the vortex mixed and pipette mixed samples. The incubation temperature of 37°C was selected despite gelation for a longer duration at room temperature giving stronger material properties [122] for future applications with cell seeding in mind.

The rheology of the samples prepared with the two different methods was assessed using a PAV, further detail of the methodology is given in 3.3.1.2, briefly, the samples were measured using a frequency sweep between 1–10,000Hz at 25°C and the measurements were repeated 3 times. Although because the samples are of low viscosity, the measurements can be unreliable between 1–10Hz and is noted with a greyed–out area of the graphs when this is the case. The rheology data for the vortexed and non–vortexed samples are shown in Figure 7.3.

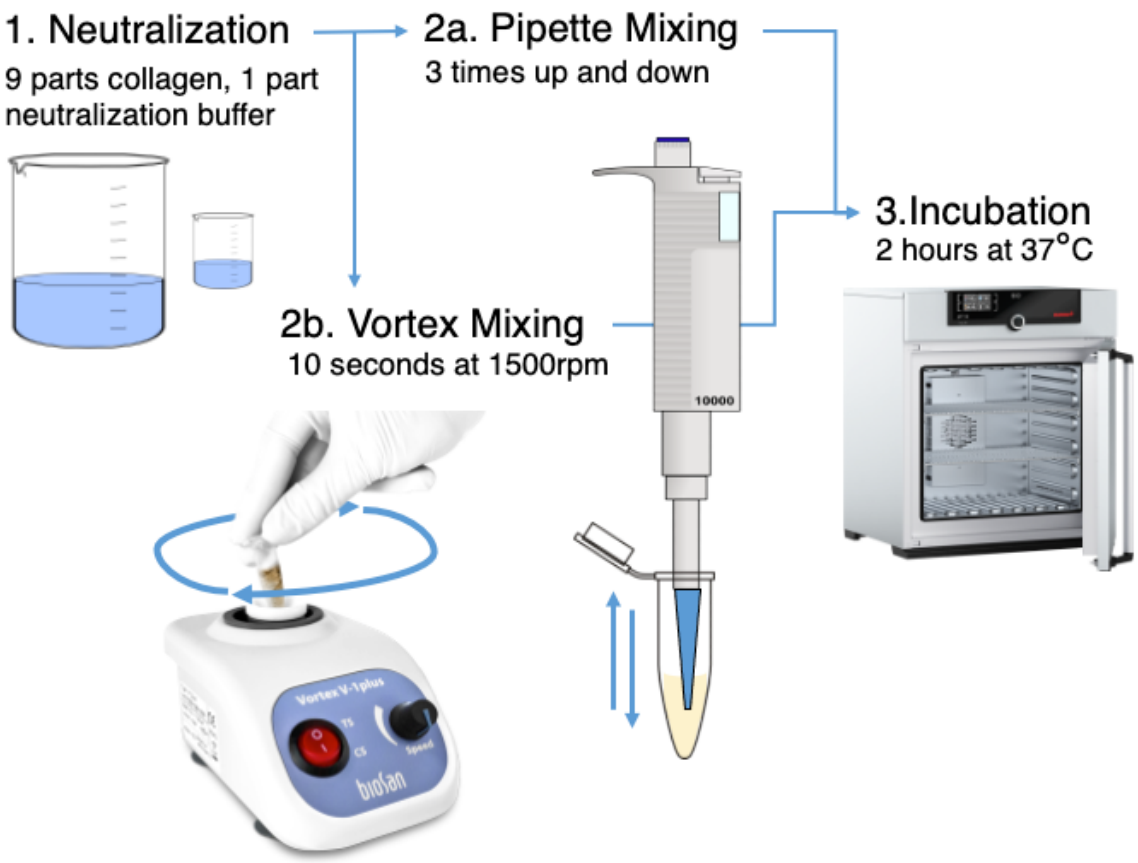

Figure 7.2: Illustration of the two preparation methods for the control, which is pipette mixed and the vortex mixing.

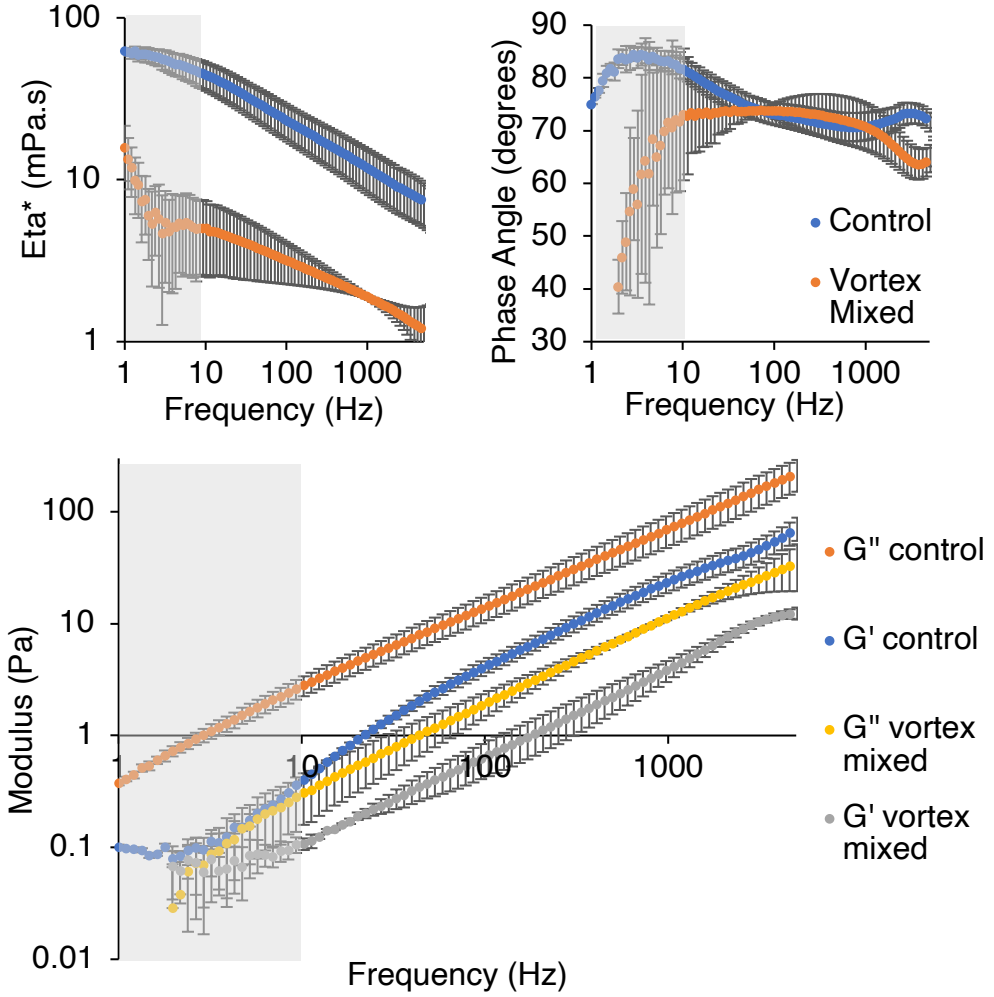

Figure 7.3: PAV rheology data for collagen samples prepared with vortex mixing before gelation or gentle pipette mixing, the control. The complex viscosity and phase angle are shown in the left and right graph, the storage (G') and loss (G") moduli are shown in the lower graph n=3 for all data points.

There is a clear difference in the rheological data for the vortex mixed and control, pipette mixed samples as indicated in Figure 7.3. The control sample follows the preparation of steps 1, 2a, 3 as shown in Figure 7.2. The complex viscosity is approximately one order of magnitude lower for the vortex mixed sample compared to the pipette mixed sample across the whole frequency range. The storage and loss moduli are also both lower for the vortex mixed samples compared to pipette mixing which suggests that the vortex mixing disrupts the

self–assembly of the tropocollagen to form fibrils to some extent. From observation, the vortex mixed sample forms small parts of gelled collagen but is not homogeneous across the entire volume of fluid. The error bars are due to a combination of error in measurement and sensitivity of each sample's properties due to preparation. A visual comparison of the two samples is given in Figure 7.4a, the pipette mixed sample sticks to the Eppendorf when upside down, a typical visual demonstration to show gel like behaviour, whereas the vortex mixed sample flows. In terms of the phase angle, the two samples show similar values, around 70°, in the reliable frequency range above 10Hz. This also supports the notion that some self–assembly and gel formation is occurring in the vortexed samples and seems likely when comparing the phase angle to the acid soluble collagen in the stock solution, shown in Figure 7.1.

Although the shear rate endured by the collagen during vortex mixing compared to pipette mixing is not examined, results from another study which expose collagen solutions up to shear rates of $2000s^{-1}$ for up to 30 minutes during fibrillogenesis also show that the sheared collagen samples have inferior G' and G" compared to non–sheared samples [127].

The box plot in Figure 7.4b shows the distribution of measurements of fibre width taken from SEM images of collagen gels prepared with gentle mixing, the control, and with vortexed mixing before gelation. The SEM images have been selected from multiple images taken and are representative of the samples. The location of the fibril width measurements can be found in the appendix, Figure A 5 and Figure A 6. ImageJ was used to measure the fibre widths after calibrating the size with the scale bar by manually drawing lines that fit the width of each fibril. The number of measurements for each sample is 101, the mean width for the control is 64nm and for the vortexed sample 49nm indicating that the fibrils in the vortexed sample do not thicken as much as the control sample during self–assembly. The mean and standard deviation were computed using python. However, the difference is not very significant as the distribution of points in the

measurement have mean values within 10nm of each other, but this result is similar to another study that examined the fibril diameter after shear pre–treatment before gelling [127].

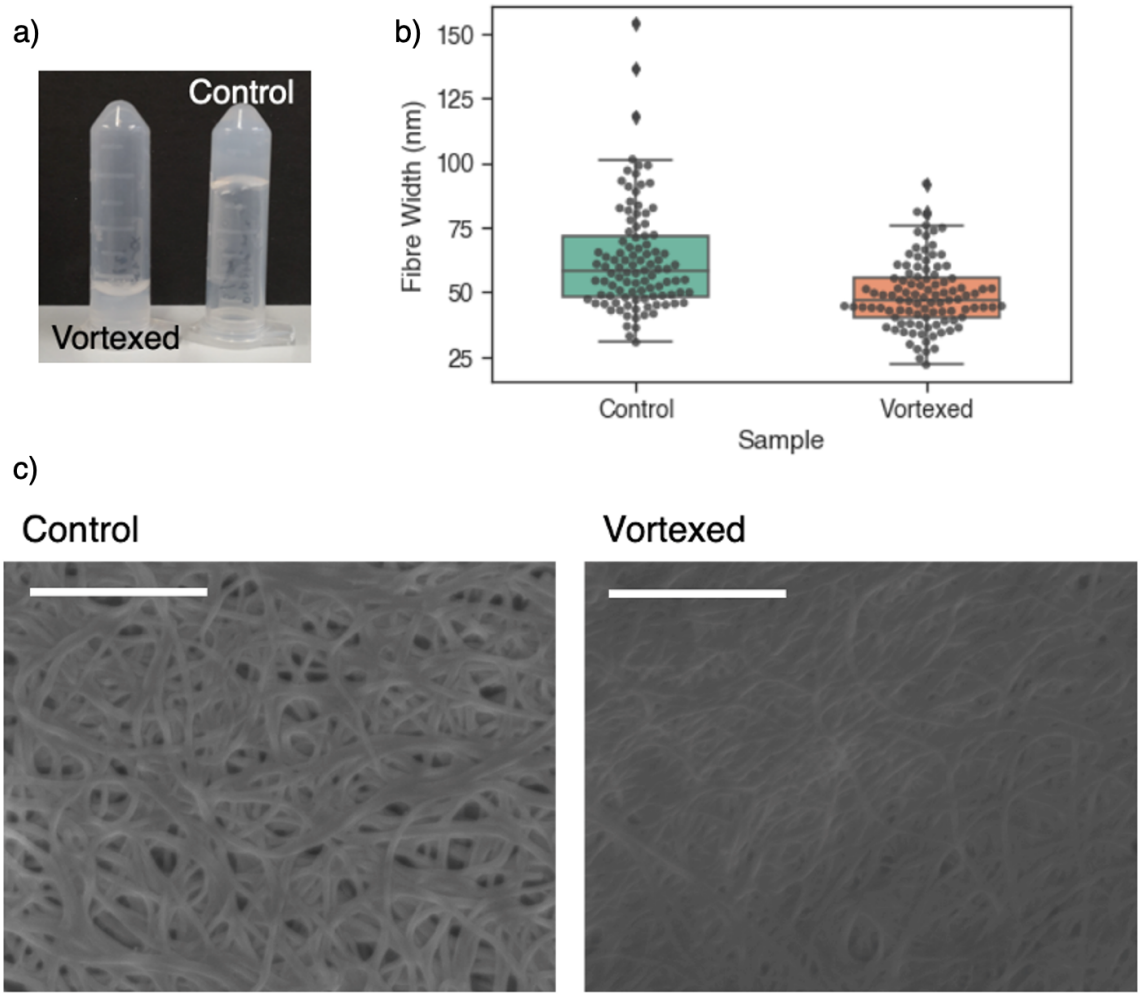

Figure 7.4: A photograph of the control and vortexed samples, a box plot showing the width of collagen fibres measured from SEM images, 101 measurements were taken. The images below show the SEM images, the scale bars are 1µm.

Looking at both SEM images for the control and vortexed it appears that the control sample has greater porosity within the network. Further measurements were completed on the images assessing the area of the holes in the mesh structure, the results are shown in Figure 7.5. The contrast in the image of the vortex mixed structure meant that it was not possible to threshold the image so

that the area of the holes could be determined automatically with the particle analysis tool on imageJ. Instead, 30 manual measurements were made for 30 randomly selected holes in the vortex control and vortexed sample. A box plot of the distribution of those 30 measurements is shown in Figure 7.5a. The mean hole area calculated using python, for the control was 13,170nm^2 and for the vortex mixed sample 2,802nm^2. Because only 30 measurements were made, these values could be seen as unreliable but when examining the SEM images qualitatively it appears that there is less porosity in the vortex mixed sample and the holes between the fibrils seem smaller. An automated measurement was made using imageJ, further detail on the method used can be found in section 3.4.3, for the control sample. The results are shown in Figure 7.5b and the thresholded image used for the analysis is presented in Figure 7.5c. In this case the mean hole area was 1,807nm^2 which is 14% of the mean value when manual measurements were made. To make the automated measurements more accurate a lower limit for hole size could have been used so that the mean was not skewed towards smaller values by inclusion of pixels due to insufficient thresholding caused by poor contrast in the image. The decrease in porosity appears as if the vortexed sample has been compressed relative to the control and can only be attributed to the difference in mixing technique used before gelation. However, the purpose of porosity measurements was to indicate that there is some noticeable difference in the microstructure of the collagen in the control compared to the vortex mixed samples. In combination with the fibril diameter measurements, there is a clear difference which could be a contributing factor to the difference in the rheological measurements shown in Figure 7.3.

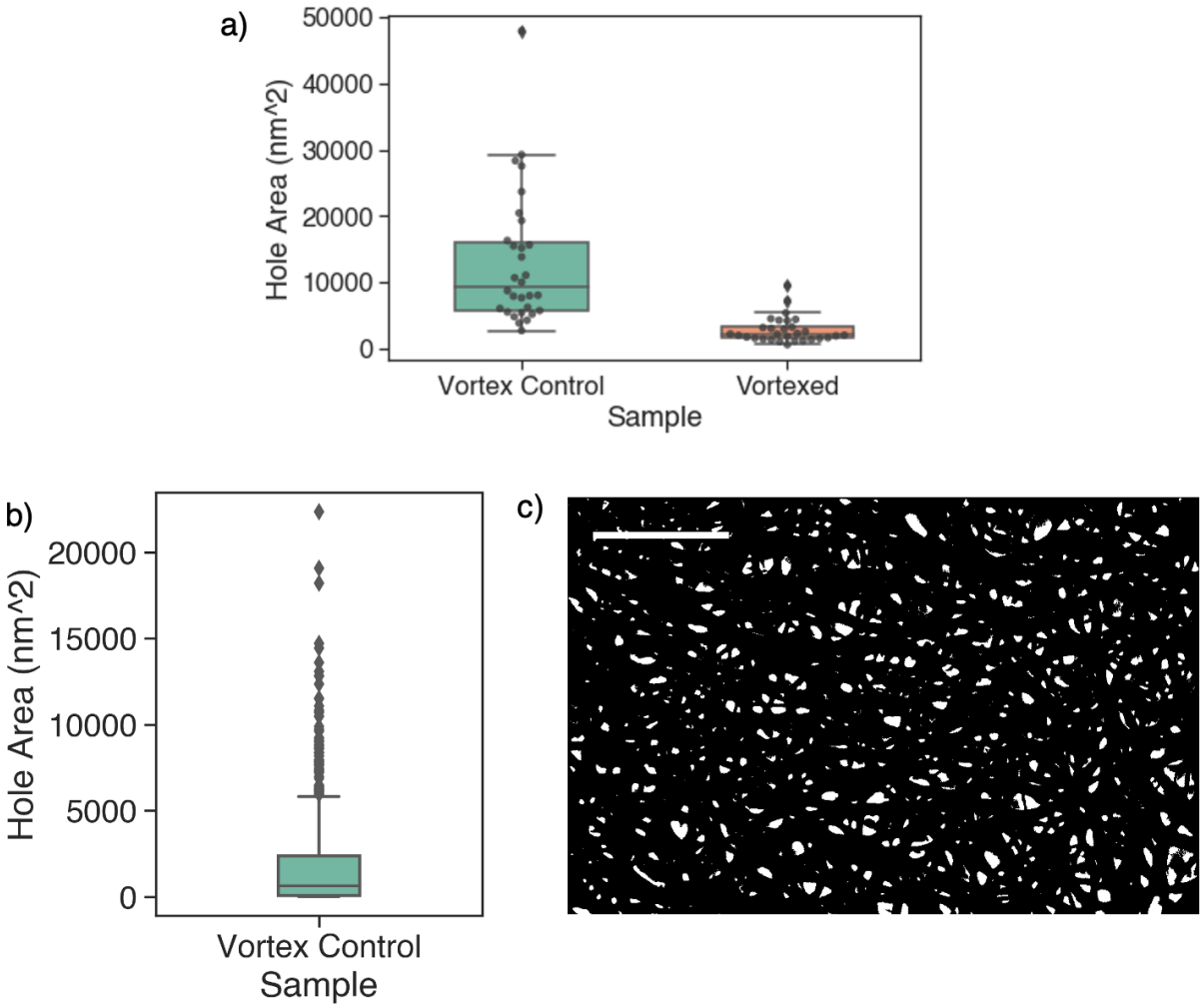

Figure 7.5: a) A box plot showing the area distribution of 30 manually measured holes in the SEM images pictured in Figure 7.4 for the vortex control and vortexed samples. b) A box plot showing the distribution of the hole areas using thresholding and particle analysis in imageJ.for the vortex control. The thresholded image is shown in c) with scale bar 1 micron.

7.3 Extrusion of Collagen Gels

7.3.1 Experimental

For investigating the impact extrusion–based printing has on collagen gels, the samples were prepared in the same way as the pipette mixed samples, detailed in Figure 7.2, but before incubation samples were loaded into syringes so gelation would occur without any further disturbance. This slight modification to the sample preparation resulted in slightly different material properties for the control samples as shown in Figure 7.6, compared to the gelled sample in Figure 7.1, the results are shown for the average of 6 control samples (N=6). The graph shows the storage and loss moduli along with the phase angle. The phase angle is lower, tending closer towards the gel value of 45°, G' and G" are both slightly higher as well suggesting fibrillogenesis occurred more optimally than when samples were allowed to gel in an Eppendorf. The main difference between these two preparation methods is that the collagen prepared in the Eppendorf has one surface not in contact with the container, a sample air interface, whereas the samples loaded into a syringe have all surfaces in contact with the solid syringe surface, i.e. the walls of the syringe and the plunger. This difference in results emphasises how sensitive collagen fibrillogenesis and gelation is to the chosen preparation method.

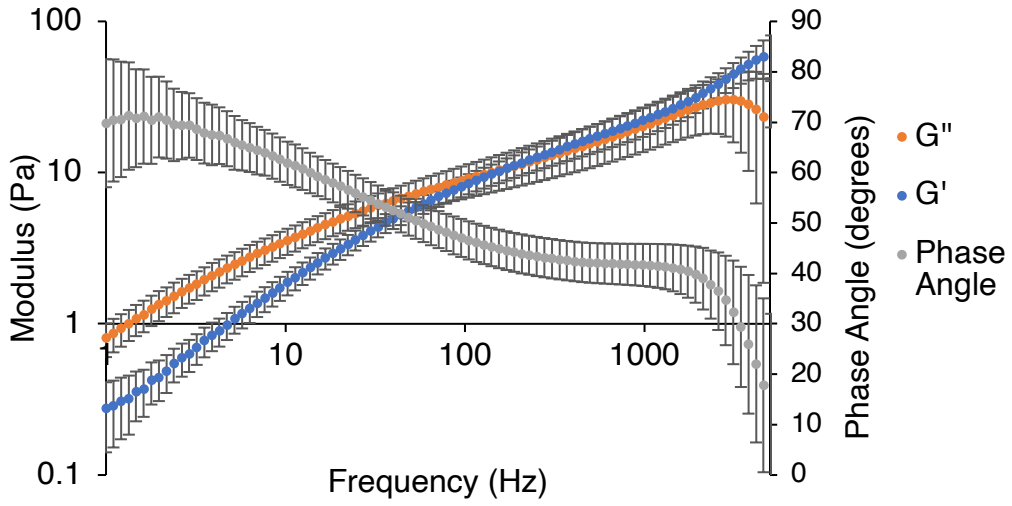

Figure 7.6: The storage (G'), loss (G") moduli and phase angle of the control collagen prepped in a syringe. N=6 for all data points.

The SEM images in Figure 7.7 are from the extrusion control sample. The sample was prepared in the same way as samples to be extruded were prepared. The sample was pipette mixed and loaded into a syringe before gelation. The image labelled a) is representative of the expected fibrillar mesh structure for the collagen gel prepared for SEM according to the procedure detailed in 3.4.3. The image labelled b) shows some coiled motifs that were observed within the sample. These motifs were not observed in the vortex control samples and could be a contributing factor to the greater material stiffness evident through the increased G' and G" values compared to the vortex control sample.

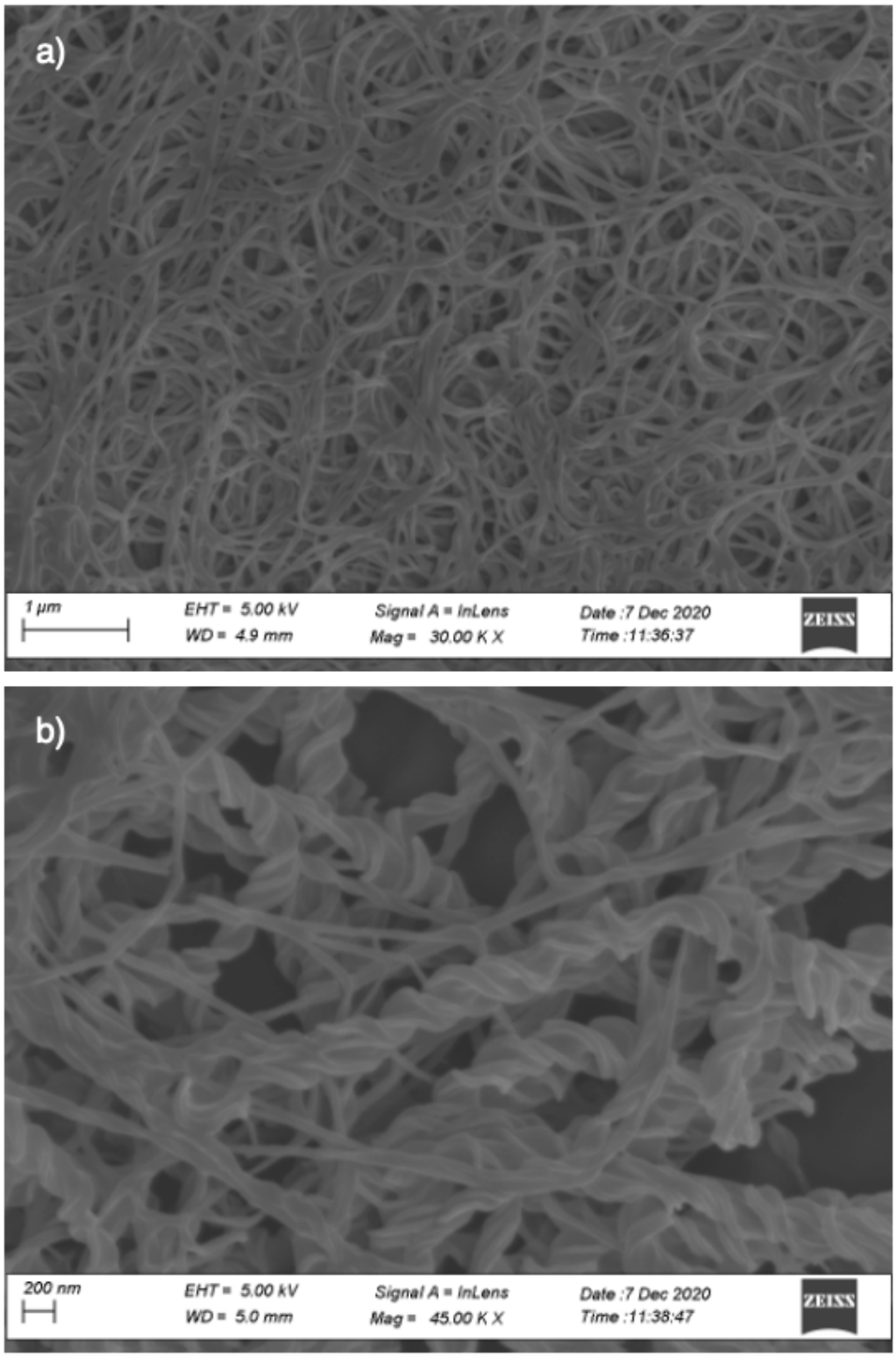

Figure 7.7: SEM images of the extrusion control sample. a) shows a less magnified image of the fibril mesh structure, b) shows a detail of some coiled fibril motifs seen in parts of the sample.

A syringe pump was used for extrusion experiments because this ensured repeatability in the resulting force applied to the collagen gels. Flow rates of 30, 45 and 90 ml/hr were investigated for two different gauge needles both a quarter inch in length – 18G, 0.84mm diameter and 32G 0.1mm diameter attached to an 8.95mm diameter syringe.

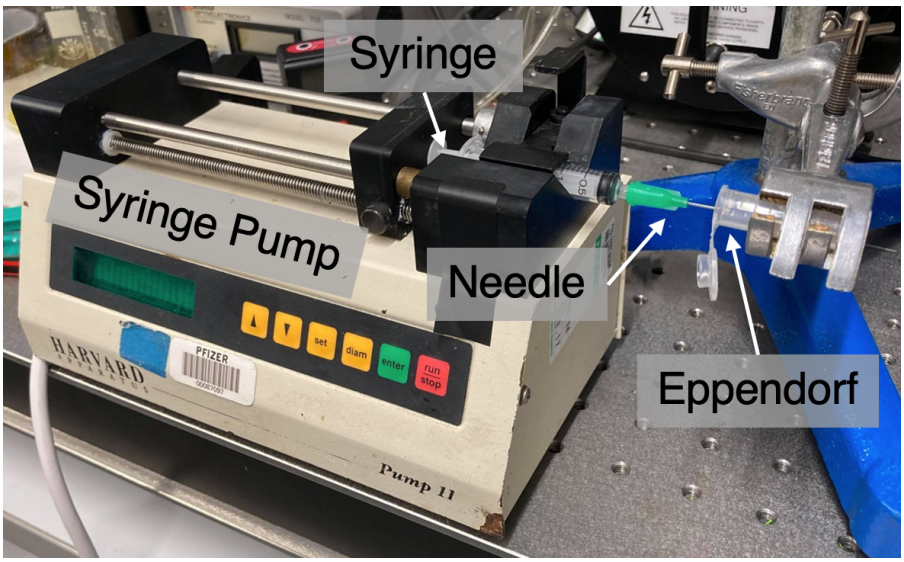

Figure 7.8: The experimental setup used for extrusion of collagen gels with a syringe pump and collection into an Eppendorf.

A labelled image of the experimental setup is shown in Figure 7.8. Further details on the experimental method are presented in section 3.3.3. Briefly, once the flow rate of the syringe pump is selected for the specified syringe diameter, the mechanical screw will turn to achieve this flow rate. The syringe has the needle attached to the end with a push fit and the extruded collagen is collected in a protein lo bind Eppendorf. The two sizes of needle were selected to examine larger shear forces, in the case of the 32G needle and because as discussed in section 2.1.4.1, a smaller orifice results in higher resolution [10], and an 18G needle was selected because less extensive shear forces would be endured by the ink. Both needle diameters are representative of extrusion systems used for extrusion based bioprinting applications. Some examples of relatively larger diameter needles [80], [151] and narrower diameters [162], [163].

The graphs in Figure 7.9 show the rheology, measured using the PAV rheometer detailed in 3.3.1.2, of the collagen gels after extrusion with an 18G needle and the graphs in Figure 7.10 are for extrusion with a 32G needle. Each data point is the average from 3 samples and the error bars are the positive and negative standard deviation within these three samples. The complex viscosity (η^*), storage (G'), loss (G") moduli and phase angle for the samples are presented and will be considered in turn.

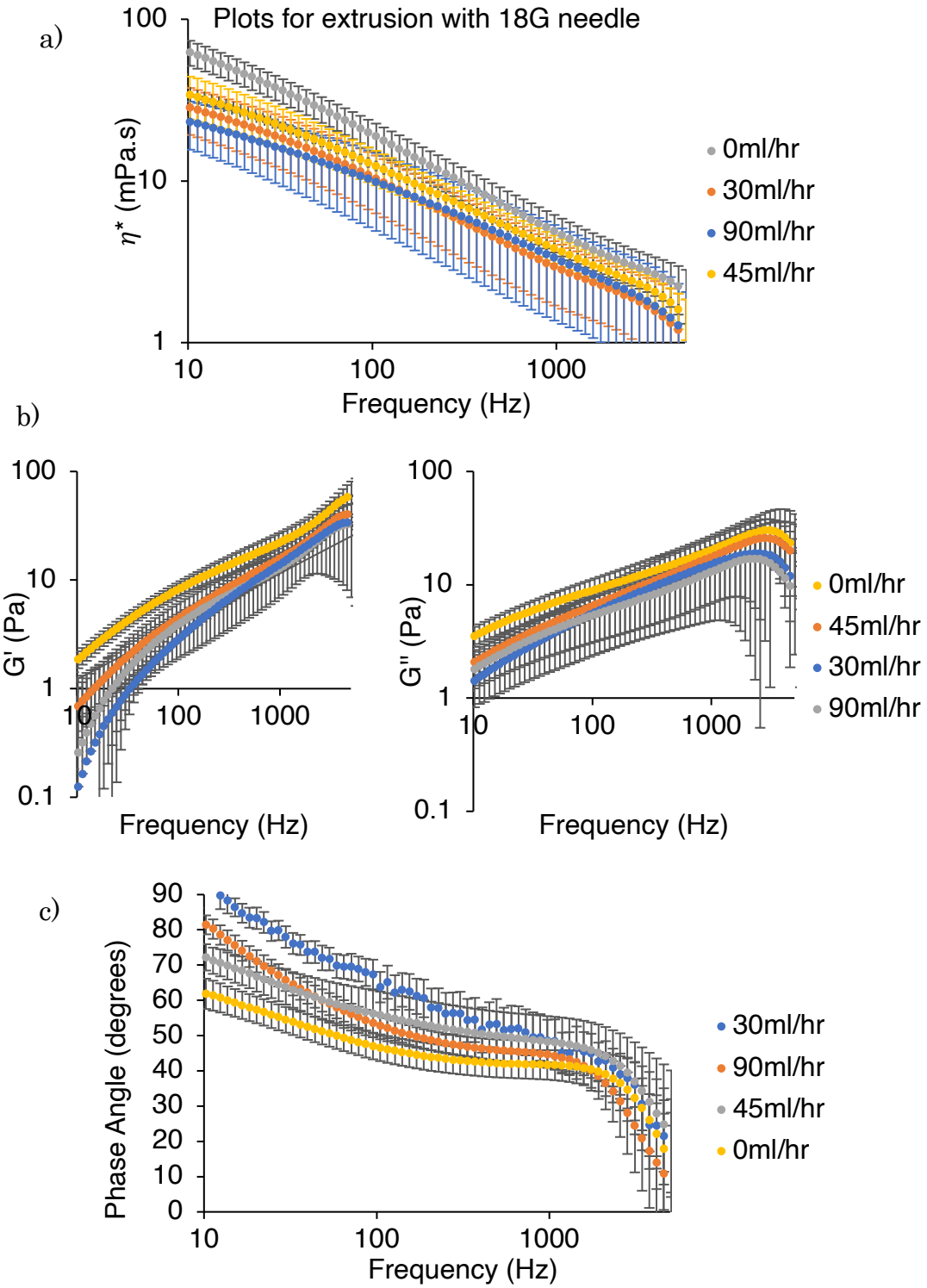

Figure 7.9: PAV results for extrusion with an 18G needle, a) complex viscosity, b) middle storage (G') and loss (G") moduli, c) the phase angle, n=3 for all data points.

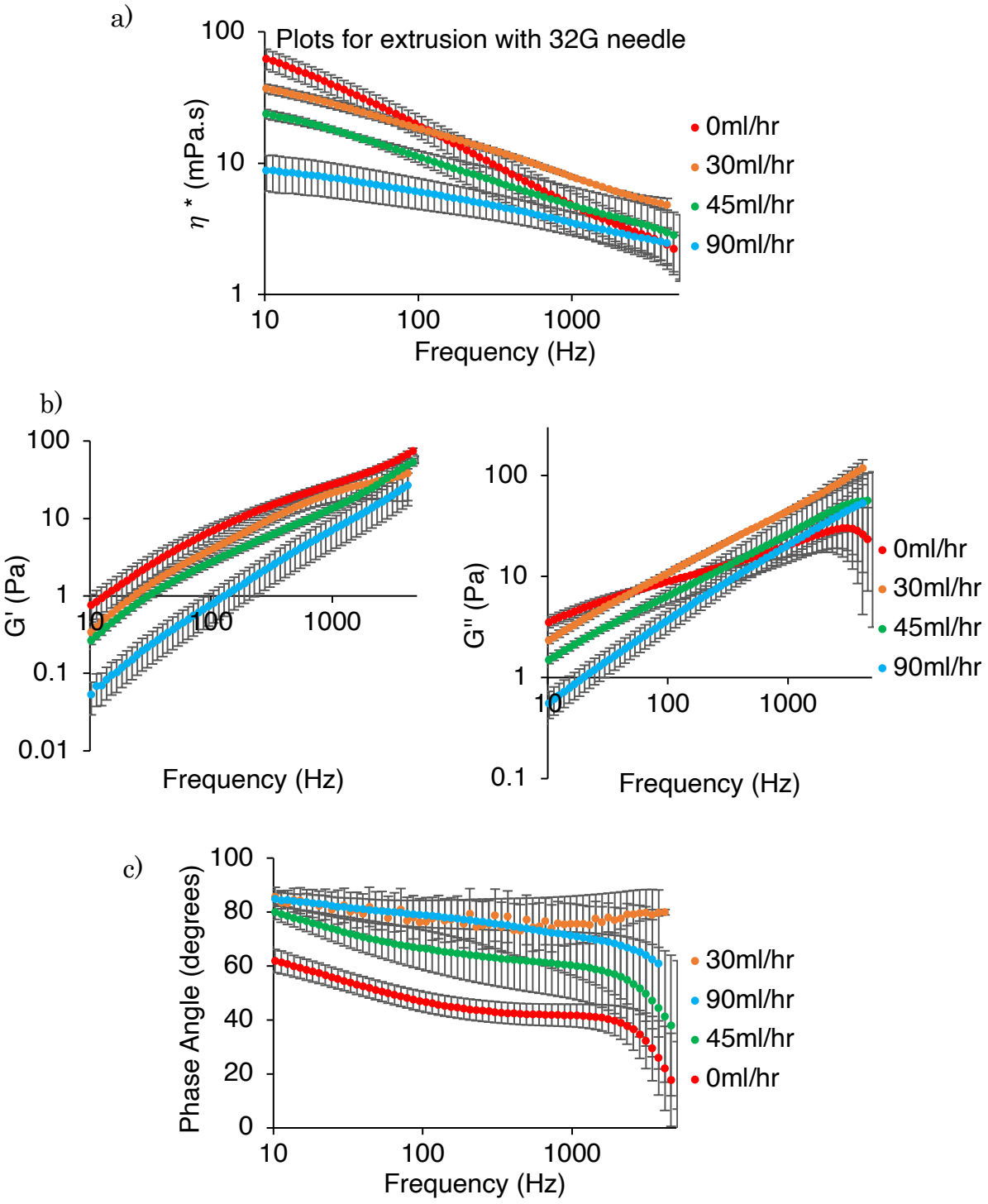

Figure 7.10: PAV results for extrusion with a 32G needle, a) complex viscosity, b) storage (G') and loss (G") moduli, c) the phase angle, n=3 for all data points.

For both gauge needles, within the range of 10–100Hz there is a statistically significant, although less pronounced for the 18G, difference between the control sample, 0 ml/hr, and the samples that have been extruded for η^*. For the 18G needle, the samples that have been extruded have overlapping errors so there is not a clear trend in terms of flow rate and η^* but for the 32G needle the higher the flow rate the lower the value of η^* will be in the 10–100Hz range.

The storage modulus (G') is lower than the loss modulus (G") for all samples which demonstrates that the samples have more dominant viscous behaviour. Consequently, all samples can be considered as viscoelastic fluids. For the 18G needle extrusion the most notable difference between the control 0ml/hr sample and extruded samples is for the values of G' between 10–50Hz. The values of the extruded samples are lower within this frequency range than the control indicating that the extrusion process seems to have the greatest impact on reducing the amount of energy stored within the structure during deformation whereas the values of the loss moduli for the samples are reduced although the error bars are overlapping so this is not as significant as the reduction in storage modulus. For extrusion with the 32G needle the differences are more pronounced, especially for the samples extruded with higher flow rates. Compared to the control 0ml/hr sample the storage modulus, G', of all extruded samples is lower within the frequency range 10–1000Hz and there is a trend that the greater the flow rate, the lower the storage modulus will be. The most pronounced difference is between the 90ml/hr sample and the 0ml/hr sample between 10–100Hz. For the loss modulus, G", between 10–50Hz the same trend is observed – the greater the flow rate of the extruded sample, the lower the value of G" will be. However, at 70Hz for the 30ml/hr sample the values begin to exceed that of the control sample and beyond 100Hz the error bars of the different samples are overlapping. A reduction in G" could signify that there are fewer entanglements within the fibrillar structure of the samples resulting in less energy being dissipated during deformation.

The phase angle for the 18G samples is higher than the 0ml/hr control sample for all extruded samples although only between 10–50Hz is this statistically significant. There is also no clear trend in the difference in phase angle as the lowest flow rate, 30ml/hr, has the highest phase angle across all frequencies. There is no significant difference between the 45ml/hr and 90ml/hr samples. For the 32G needled extrusion the phase angle for the extruded samples compared to the control is higher and statistically significant between 10–1000Hz. The error bars of the extruded samples overlap within this frequency range but the difference to the control is clear. This indicates that there is no clear trend in the phase angle for the 32G needle other than it is clearly higher than the control sample. A higher phase angle signifies the extruded samples are now exhibiting more liquid like, viscous behaviour as a purely liquid behaviour is signified with a phase angle of 90°. The phase angle is above 45° for all samples so the samples exhibit viscoelastic behaviour that is dominated by the viscous part and the increase indicates that the viscous behaviour has become even more dominant after extrusion.

In general, the greatest difference in the rheological data of the control samples compared to the extruded samples for both the 18G and 32G needle is in the 10–50Hz range. There is also a greater difference for samples extruded with the narrower 32G needle which is likely linked to the greater shear forces endured by the fluid through a narrower channel and will be discussed further in the next section, 7.3.2. These results serve to validate that PAV rheology can be used to detect differences in the characteristics of collagen gels and could be used as a quality control measure for extrusion–based manufacturing with collagen–based materials.

To examine the structure of the gels before and after extrusion, a visual examination of the 30ml/hr 32G needled extruded gel is shown in Figure 7.11a. Before extrusion the gel looked cloudy but homogenous, whereas after extrusion parts of the gel had fragmented and broken up and were floating within solution.

Going further than a visual examination, a control sample and extruded sample were prepared for SEM imaging, detailed in section 3.4.3. Briefly, the samples were crosslinked for 48 hours with a solution of 2% glutaraldehyde, washed with PBS and dehydrated with subsequently increasing concentrations of acetone solution before being mounted onto SEM stubs, dried further in a desiccator and then sputter coated with a gold palladium target. The fibril diameter shown in the SEM images, pictured in Figure 7.11c, were then measured using imageJ. 101 measurements of the fibril diameters were taken for each image and the resulting distribution of measured diameters is shown in a box plot in Figure 7.11b. The control sample shows a mean fibril diameter of 64.41nm and the extruded sample has a lower mean of 55.79nm. This difference is not very significant but noticeable. Looking at both the photographs and SEM images in combination, it seems that the main cause for the differences in rheological characterisation is due to the collagen breaking up during the extrusion process rather than a greater difference to diameter of the fibrils.

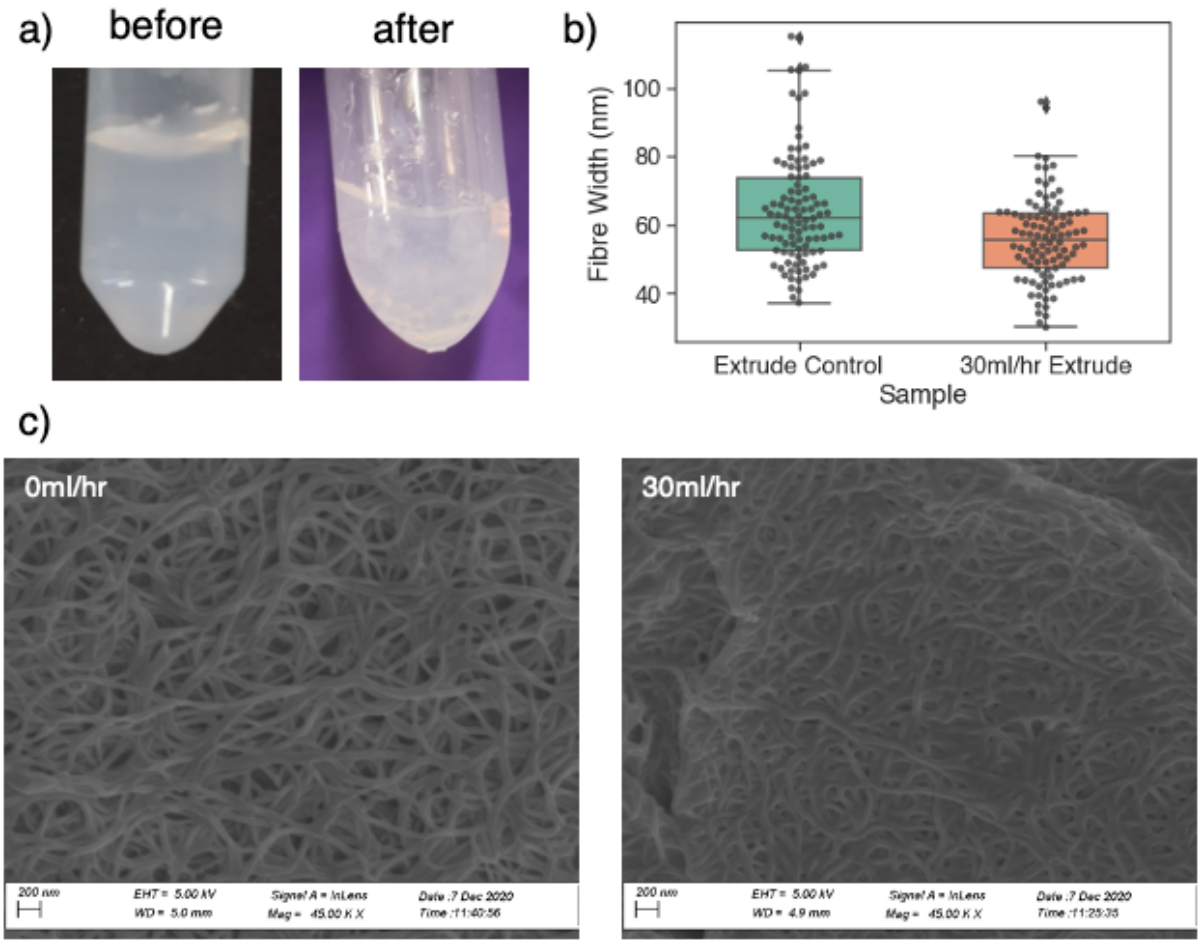

Figure 7.11: a) Picture of 30ml/hr extruded collagen through a 32G needle, b) box plot of measured fibre width from SEM images shown in c) of 30ml/hr 32G needle extruded collagen compared to the control.

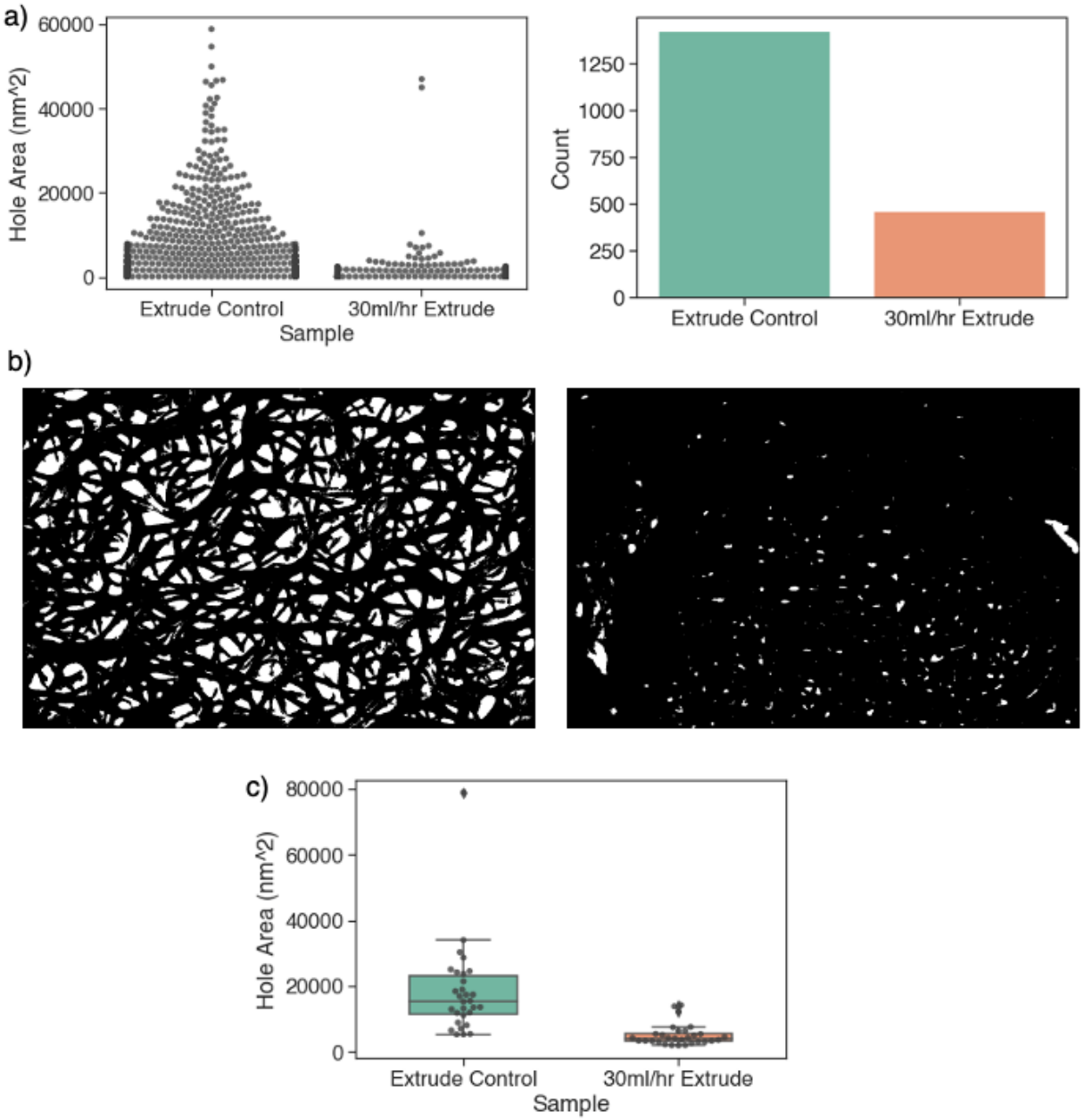

Figure 7.12: a) A plot showing the data points for the automated analysis with ImageJ of the hole area of holes in the extrude control and extruded SEM images pictured in Figure 7.11, the left plot shows the number of holes counted in the analysis. b) the thresholded images used for determining the area of holes in the SEM images. c) Comparison with 30 manual measurements of hole area in the extrude control and extruded SEM image.

As with the vortexed samples, the porosity was also investigated as a potential reason for the difference in the rheological measurements observed between the

control and extruded samples. As with the data presented in Figure 7.11, the same SEM images were used for the analysis, so the extruded sample was also from extrusion with a 32G needle at 30ml/hr. The data presented in Figure 7.12a shows the results of the automated hole area analysis using imageJ, detailed in section 3.4.3, briefly, SEM images were thresholded and the particle analysis functionality returns the measurements of the areas of the holes within the collagen mesh structure. The thresholded images are presented in Figure 7.12b. From the automated analysis, the control sample had 1426 holes with a mean hole area of 3394nm^2 and the extruded sample had 462 holes with a mean area of 873nm^2. Edge holes, i.e., holes which had contact with the boundary of the image were not included in the analysis. These results show that the porosity of the collagen structure is greater in the control sample than the extruded sample and this difference is more significant than the difference in fibre width detailed in Figure 7.11. The number of holes is 3.88 times greater in the control sample than the extruded sample and the mean hole area is twice as large whereas there is only a 15% increase in fibre width from the extruded sample to the control.

The box plot shown in Figure 7.12c is for 30 manual measurements of hole area between the extruded and control sample. In this case the mean for the control sample is 16,121nm^2 and the mean for the extruded sample is 5,073nm^2. There is clearly a difference in the values of the manually measured holes compared to the control but the trend in terms of greater porosity and hole size for the control compared to the extruded sample holds true. Similar to the vortex mixed sample compared to the control, it seems that porosity is the most obvious change to the collagen structure apparent in the SEM images which could be the main contributing factor to the differences in the rheological data shown in Figure 7.10.

7.3.2 Simulation

To determine the values of the shear rate and velocity of the collagen gel during extrusion with the syringe pump, with experimental results detailed in section 7.3.1, a simulation was made using COMSOL Multiphysics 5.6. The simulation focuses on the narrowest constrictions during the extrusion process, where the highest shear rate and velocity of the fluid will be endured. A viscoelastic fluid model Oldroyd–B was used which has previously been used to model collagen in shear flow [164]. The heatmaps for the velocity and shear rate of the simulation are shown in Figure 7.13 and Figure 7.14 respectively for the highest and lowest flow rates for each gauge needle. The images for the middle flow rate, 45ml/hr, can be found in the appendix, Figure A 9.

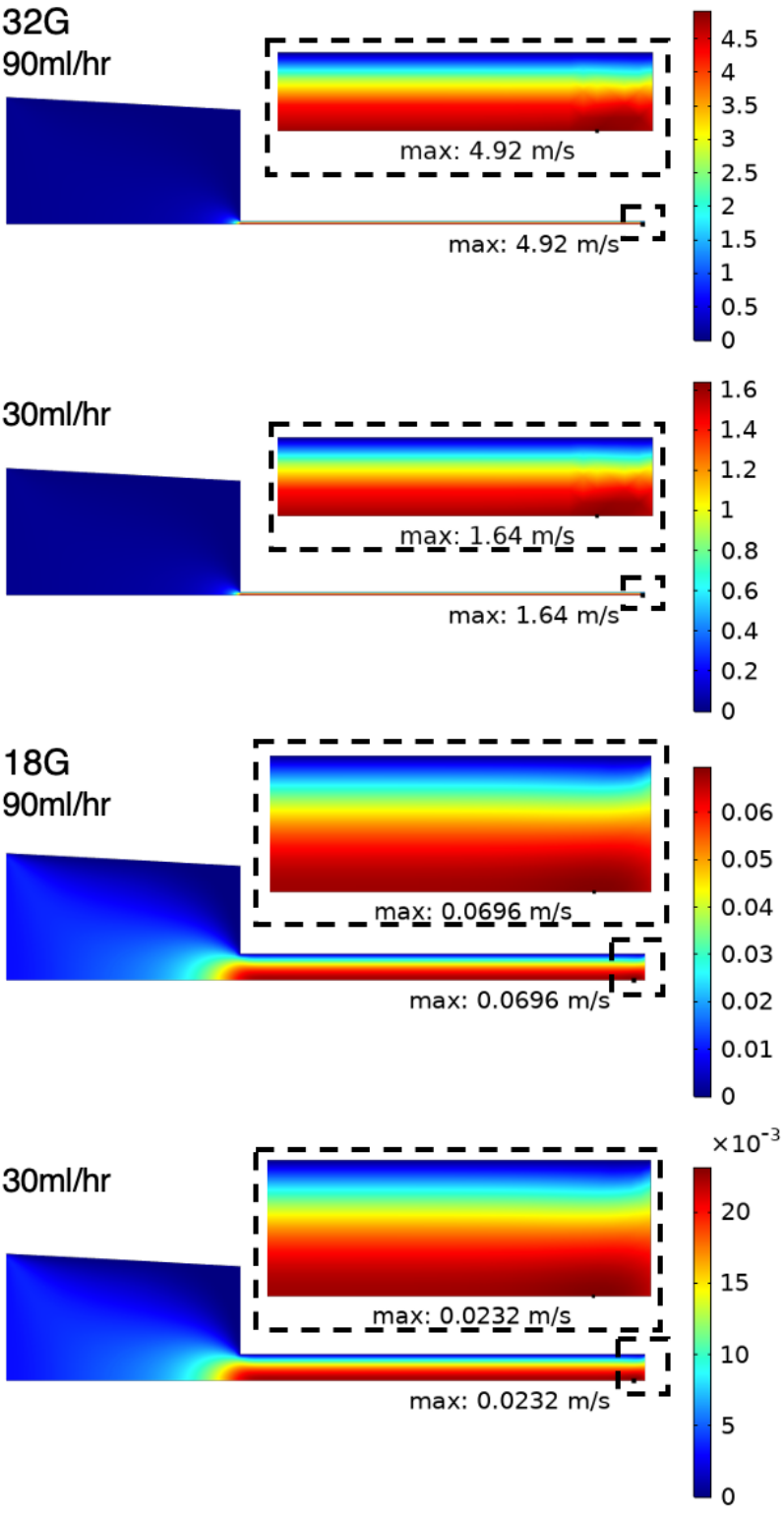

Figure 7.13: COMSOL Multiphysics 5.6 simulation of syringe pump extrusion for 18G and 32G needles. The velocity is shown as a heat map for the cross section.

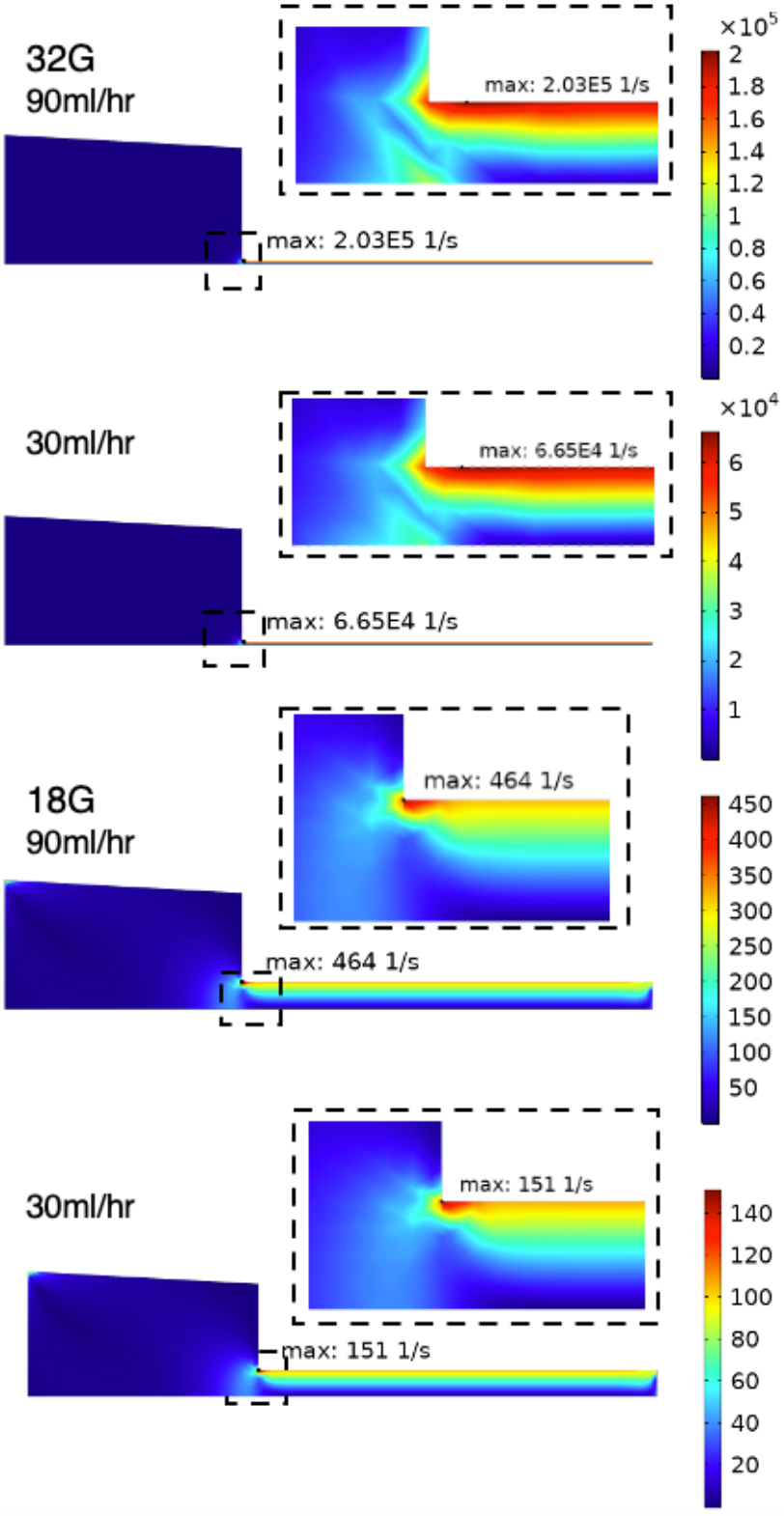

Figure 7.14: COMSOL Multiphysics 5.6 simulation of syringe pump extrusion for 18G and 32G needles. The shear rate is shown as a heat map for the cross section.

The velocity and shear rate of the collagen gel during extrusion follows the trend that the narrower the channel, the higher the shear rate and exit velocity across the fluid in the needle tip. Comparing the 32G needle and 18G needle, the diameter increases from 0.1mm to 0.84mm. For this increase in diameter the velocity increases by 2 orders of magnitude and the shear rate increases by 3 orders of magnitude for comparing the same flow rates. The location of the maximum shear rate for the 18G needle is very close to the intersection of the narrower and wider section of the needle, whereas for the 32G needle the maximum shear rate is still at the edge of the needle but slightly further along the needle. The maximum velocity for all needle lengths and flow rates is towards the end of the needle tips.

Table 7.2 gives a breakdown of the maximum velocity and shear rate for the different needle and flow rate combinations considered in the simulations. The maximum shear rate and maximum velocity is directly proportional to the flow rate for all flow rates with both needle widths.

Table 7.2: The maximum velocity and shear rate for the different flow rates and needles examined in the simulation.

Needle	Flow Rate	Velocity	Shear Rate
32G	30ml/hr	Max: 1.64m/s	Max: 6.65×10^4 s^{-1}
32G	45ml/hr	Max: 2.46m/s	Max: 1.03×10^5 s^{-1}
32G	90ml/hr	Max: 4.92m/s	Max: 2.03×10^5 s^{-1}
18G	30ml/hr	Max: 0.0232m/s	Max: $151s^{-1}$
18G	45ml/hr	Max: 0.0349m/s	Max: $229s^{-1}$
18G	90ml/hr	Max: 0.0696m/s	Max: $464s^{-1}$

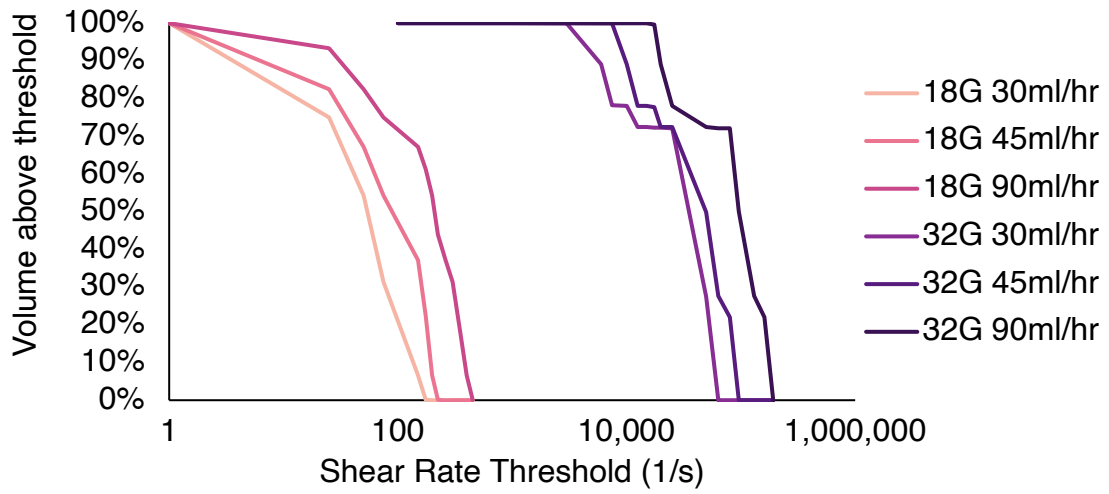

Figure 7.15: The percentage of fluid above a threshold shear rate value according to the extrusion simulation.

The structural modifications to the collagen gels will occur in the needle tip where the shear rate and fluid velocity is greatest during the extrusion process, as shown in Figure 7.13 and Figure 7.14. The graph shown in Figure 7.15 shows the percentage of fluid in the needle tip that is above the specified shear rate threshold. The 32G needle data points are 2 orders of magnitude greater than the 18G data which highlights the sensitivity of the needle diameter to increasing the shear rate endured by the extruded fluid. The minimum shear rate endured by all of the fluid in the needle during extrusion also increases with increasing needle width and flow rate. It is also evident from the heatmaps in Figure 7.13, the boundary layer of the narrower 32G needle is thicker relative to the overall diameter of the needle than the 18G needle which will have an impact on the resulting shear rate. For the narrower needle the rate of increase in shear rate for the volume of fluid exposed to the largest shear rate for 70% of the fluid increases at a rapider rate than for the lower shear rate thresholds (between 100 – 70%). For the 18G needle the shear rate there is a similar trend although the curves do not exhibit the levelling out at around 70% compared to the 32G needles. There is what appears to be a bit of a discontinuity in the

volume of fluid above the shear rate threshold around 70% for the 32G needle, this is most likely due to the limitation in the mesh size of the simulation.

7.4 Conclusions

In this chapter the manufacture of type I collagen gels has been considered along with extrusion–based printing. The extrusion process was examined experimentally using a syringe pump and with a simulation to provide further insight into the extrusion process. The mixing technique used for the manufacture of collagen gels was varied by either using pipetting or vortex mixing. For each of these elements analysed in this chapter the following conclusions were drawn.

1. Manufacture of Collagen Gels
    i. Gels formed with gentle pipette mixing compared to vortex mixing of the neutralisation buffer and collagen stock results in different rheological properties of the gel formed.
        i. The complex viscosity, η^* is approximately 10 times smaller for the vortex mixed gels than the pipette mixed across the frequency range 10–5000Hz.
        ii. The storage (G') and loss (G") moduli also follow the same trend and are at least 10 times greater in the pipette mixed samples than the vortex mixed samples across the frequency range 10–5000Hz.
    ii. The structure of the pipette mixed, and vortex mixed gels are different, as determined using SEM.
        i. The mean fibre width of the pipette mixed collagen samples is 31% wider than the vortex mixed samples.
        ii. The pipette mixed sample has greater porosity – there are more holes in the mesh structure and the holes that are present are larger.

iii. The pipette mixed gel exhibits the gel like behaviour of sticking to the top of an upturned Eppendorf, whereas the vortex mixed sample does not.

iii. The manufacture of collagen gels is very sensitive to the preparation method chosen. This was highlighted by the superior rheological properties of the collagen samples used for the extrusion control, where fibrillogenesis occurred in the syringe rather than Eppendorf, how the samples were prepared for comparing pipette and vortex mixing.

2. Extrusion of Collagen Gels

i. The rheological data for the extruded samples compared to the control is different.

i. For the samples extruded through the 18G needle between 10–50Hz the complex viscosity, η^* is lower than the control although the overlapping error bars mean that there is not a clear trend. For the samples extruded through the 32G needle between 10–200Hz there is a clear trend that the greater the flow rate, the lower the value of η^* compared to the control.

ii. There is an increase in phase angle for all the samples extruded through both 18G and 32G needles. For the 32G extruded samples the phase angle is at least 20^0 across the frequency range 10–1000Hz.

iii. The values of the storage (G') and loss (G") moduli for the 18G extruded samples are lower across the range 10–5000Hz compared to the control but there is not clear trend as the error bars are too large. For the 32G extruded samples for G' in the range 10–1000Hz, the greater the flow rate during extrusion, the lower the value of G' compared to the control,

the same trend is observed for G" but only in the range 10–50Hz.

ii. The structure of the extruded samples compared to the control show different features, a control sample is compared to a sample extruded through a 32G needle with flow rate of 30ml/hr.
    i. The extruded sample looks visibly different – the gel looks fragmented compared to an intact homogenous looking gel for the control sample.
    ii. SEM images reveal that the fibre width of the control is 15% greater on average than the extruded sample.
    iii. The porosity of the extruded sample is less than the control sample. The control sample has 3.88 times more holes and the area of the holes are 3 times greater on average.

iii. The simulation of extrusion showed that the greater the flow rate and narrower the needle diameter the greater the velocity and shear rate in the needle for the same flow rates.
    i. Considering the 30ml/hr, 45ml/hr and 90ml/hr flow rates, the shear rate in the needle for the 32G width was in the order of 10^4 to $10^5 s^{-1}$. For the 18G needle then shear rate was in the $10^2 – 10^3$ range.
    ii. The velocity of the fluid for the flow rates 30 – 90ml/hr for the 32G needle is of the order 1m/s, for the 18G needle the fluid velocity is of the order 0.01m/s.

Chapter 8 Conclusions and Future Research

8.1 Conclusions

Fluid–based manufacturing encompasses all technologies that handle fluids in a liquid or gel phase. Inkjet printing and extrusion are two examples of fluid–based manufacturing that have been the focus of this thesis. Inkjet printing was developed in the 1970s and 80s and is extensively used for printing onto textiles, ceramic tiles, in small and home offices, printing ticketing, signage and banners. More recently the use of inkjet printing has been developed for pharmaceutical and biological applications for drug discovery, drug screening and drug delivery. Extrusion is a manufacturing technique that has been used for polymer and metal processing for over 100 years. It is only within this century that extrusion based bioprinting has been developed based on this manufacturing process. Since this technology translation, hydrogels, polymers and ECM components seeded with cells have been extruded to form tissue constructs applicable for regenerative medicine, tissue engineering and pharmaceutical drug discovery and screening applications.

Due to the relative infancy of these printing processes being used for such applications, there are many barriers in greater industrial uptake of these technologies. This thesis has focused on the impact inkjet and extrusion–based printing has on the resulting structure and function of inks containing proteins after printing. For inkjet printing, the nozzles are often as narrow as 20μm with ejection speeds in the order of 10m/s. Such extreme conditions cause the ink to

endure high shear and extensional forces during droplet ejection which has previously been cited as a concern for inks containing enzymes [4], [5]. Similarly, for hydrogel–based inks undergoing extrusion, these are concerns that the shear forces endured by the ink can detrimentally affect cells within the hydrogel [9] and the hydrogel itself [12]. To investigate these impacts upon the ink the research conducted in this thesis was split into four sections.

Firstly, examining the impact inkjet printing has on proteins in aqueous ink has been focused on experimental results directly measuring the activity of the resulting protein after printing. The understanding of the shear rate and percentage of ink within the printhead enduring a minimum shear rate has not previously been examined in this context. Moreover, there is often a total absence of data examining the droplet morphology of ejected droplets containing proteins, and the metric of waveform voltage is frequently cited as a metric to resemble the amplitude of the force the ink endures. The goal of this research section is to set up a close link between experimental images of printed bioinks and simulations, to allow these forces to be mapped out. This understanding could become an essential tool for validating reasons for changes in activity during bioprinting results, particularly regarding the concern that the forces during inkjet printing are a cause for loss of activity in proteins.

Secondly, the experimental determination of the activity losses experienced by protein–based inks after inkjet printing present in the literature do not consider the full journey the ink takes from the fluid reservoir through to impacting and drying upon a surface after droplet ejection. Studies have typically focused on the nozzle and droplet generation which negates other elements of the printing process. It is well established in literature not specifically examining inkjet printing that proteins can experience activity losses due to high shear forces, adsorption to materials and from drying. Additionally, previous work has examined mostly single nozzle systems or lab–scale research printheads without also including a study of industrial printheads. In this section of research, the

full journey of the ink is examined through the printing apparatus, from formulation through to drying and the stability of the final material deposited on a control surface. Moreover, multiple printheads are examined, namely the two most common printheads used in research literature and an industrial printhead. Through this approach, the work is focused on understanding the relative impact of each influencing factor on biological activity.

Thirdly, once the contributing factors that cause a reduction in printed protein activity have been established, to pave a pathway forward for greater industrial adoption of inkjet printing technology for biological and pharmaceutical applications, methods to retain activity should be explored. The focus of research in this section is the detailing of losses due to adsorption and drying because these were identified as the elements causing protein activity losses in the second section of research. The aim of this section is to eliminate the activity losses observed due to the inkjet printing process and enable the use of this manufacturing technique.

The final section of research focuses on extrusion based bioprinting. Like inkjet printing, this process also imparts extensive shear forces to the ink being extruded. One focus of research within this field has been about retaining cell functionality and viability within the extruded hydrogel. As the hydrogel makes up the supporting environment for the cells, acting as the effective ECM, the integrity of the gel after extrusion will effect the resulting cell viability. In combination with reports that rheological measurements of hydrogels can be orders of magnitude different across studies of the same material [110] it is vital to understand how the extrusion process effects the gel and how the damage caused by extrusion could be measured in a reliable way that could serve as a quality control to permit large–scale use of extrusion base bioprinting. This would act as a first step in understanding before adding cells into hydrogel formulations, and also inform the community about rapid and controlled tests that would enable quick quality checks at every stage of formulation through to

deposition. Research in this area focused on the structural protein collagen due to its extensive use in hydrogel formulations.

The main outcomes of these four research avenues are presented and separated into the four research areas.

Firstly, the simulation data showed that the waveform input amplitude had the greatest impact on the resulting droplet morphology, ink shear rate and velocity. For the waveforms examined, the maximum velocity increased non–linearly from 6 – 12m/s, the shear rate from 2 x 10^6 – 4.5 x 10^6 s^{-1} and the droplet volume from 40 – 70pl. However, other waveform and printhead parameters also had an effect on the velocity and shear rate endured by the ink. The slew duration of the waveform also decreased the maximum shear rate linearly from 4.4 x 10^6 s^{-1} – 4.2 x 10^6 s^{-1} for slew duration increasing from 1 – 2.5 μs. The nozzle orifice diameter was varied from 20–40μm and the maximum velocity and shear rate both showed a power law decrease converging to 9m/s and 2 x 10^6 s^{-1} respectively. Varying the ink viscosity from 1 – 45mPa s resulted power law relationships with the maximum velocity converging to a maximum of 15.5m/s and the shear rate converging to a minimum of 2 x 10^6 s^{-1}. These results demonstrate that the predominant focus of previous studies on the voltage of the input waveform are insufficient to properly describe how the input waveform parameters are affecting the resulting ejected droplets. Completely novel to this field of research, high speed image data of inkjet printed HRP, GOx and SOx was compared to an inkjet simulation. It was evident that almost all of the ink in the ejected droplet is exposed to a shear rate of at least 50,000s^{-1}. The highest shear rates were sustained by the droplets within the first 10μs of droplet ejection during which time between 40–60% of the droplets were exposed to a shear rate in excess of 500,000s^{-1}. The ink that remains within the printhead during droplet ejection is also exposed to a low shear rate but the repetitive, cyclic nature of exposure to this shear rate could have implications for the integrity of proteins within the ink.

Secondly, the journey of inks containing HRP, GOx and SOx were examined splitting the journey into six sections – ink formulation, ancillary equipment, the printhead, nozzle flow, droplet formation, and drying. Inkjet printing with ink containing these enzymes has not previously been examined in such extensive detail, breaking down each part of the printing process to better understand each contributing factor. The main findings from this section of work were:

- Regarding the ink formulation, additives can have both a positive and negative effect on resulting protein activity before printing has even taken place. This has been examined in detail for the first time in this thesis. It was shown that at concentration between 10–30μM, CMC 90k increases the activity of GOx solutions by 21%, for CMC 700k the activity increases by 50% at 4μM upwards of 10wt% glycerol HRP activity is reduced.
- The main concern regarding the ancillary equipment is losses due to adsorption to the tubing, typically made of PU or PTFE. PTFE was shown to reduce activity losses for the three proteins by between 1–5% relative to PU. Similarly for the choice of printhead, adsorption is the greatest concern. Glass and stainless steel were shown to have the greatest impact on protein activity resulting in a combined reduction in activity of 47% for GOx compared to a bulk solution. The extent of protein adsorption to a surface is due to the charge and hydrophobicity of the surface [8]. The lab scale, Microfab printhead was made of these materials but the DMP and Spectra SE–128 AA composition did not cause such extreme adsorption losses.
- To isolate the impact of the forces endured by the ink during the printing process a control system flowing ink through a 15μm diameter opening and for the three proteins examined there was no evidence to suggest that activity losses during printing are due to the shear or extensional forces endured by the ink during printing.

- Drying droplets and rehydrating the proteins resulted in activity losses as severe as a 50% reduction compared to a control. These conclusions mean that for these protein systems the main concerns when using inkjet printing should be around reducing adsorption and losses due to drying.

Thirdly, as established in the second area of research, the main areas to focus on to retain inkjet printed protein activity are due to losses from adsorption and drying, at least for HRP, GOx and SOx studied in this thesis. The main conclusions in this section were that adding a small amount of sugar to the ink formulation, in this case 10wt% trehalose and 1wt% glucose, prevented activity losses due to drying. Coating a glass capillary based printhead with a sacrificial protein such as BSA prevented activity losses due to adsorption. This means that printheads with materials that would be detrimental to protein activity can still be used with protein– based inks.

The final section of research that focused on extrusion of collagen type I gels validated the use of piezo axial vibrator (PAV) rheometry as a quality control technique to determine whether collagen gels are defected or damaged due to their manufacture or processing with extrusion. It was identified that the manufacturing process used to produce collagen gels can have a big impact upon the resulting gel structure and mechanical properties, this had not been examined in detail before and was required to better understand gel manufacture and for future reproducibility of results. The complex viscosity of gels mixed gently with a pipette compared to vigorous vortex mixing was 10 times larger and the fibril width 31% greater and the structure was more porous. Extruding the collagen through 18G (0.84mm diameter) and 32G (0.1mm diameter) needles and examining the mechanical properties of the gel with the PAV demonstrated that the gel could be damaged even at low flow rates. A simulation of the extrusion process showed that shear rates in the order of magnitude of $10^2 – 10^3$ s^{-1} across the entire ink is sufficient to cause structural alterations and measurable differences to the extruded gel mechanical

properties. For the narrower, 32G needle the shear rates were in the order of magnitude of $10^4 – 10^5$ s^{-1}.

8.2 Future Printing Trends and Applications

There is a general trend for 2D and 3D printheads to increase in resolution having implications for the stresses that would be endured by the ink and functional material within the formulation. For drop on demand inkjet printheads the droplet volumes are decreasing, typically reaching a droplet volume range of 5 – 30pl [99]. For extrusion systems, the resolution of the printer is determined by the print speed across the surface and the nozzle diameter. For applications where cells are seeded within the ink, to prevent nozzle clogging it is generally advised not to go below a nozzle diameter of 150μm [66] which limits the resulting print resolution, although there are examples where cells have been deposited with narrower needles [65], [163], [151].

In terms of future applications, the use of 2D and 3D printing technology for biological and pharmaceutical applications is relatively modern. Trends in applications will be considered in 3 areas: the transition to 3D cell culture, isolating single cells for biopharmaceutical regulatory requirements and printed drug delivery applications moving from the research scale towards industrial adoption.

Extrusion based bioprinting enables 3D cell models to be produced that replicate the *in vivo* conditions better than their 2D counterparts [165], although at a greater cost per model and lower production throughput. 3D cell models have an extensive application in the area of drug screening and discovery, for instance, a 3D liver model produced more reliable predictions of *in vivo* drug toxicity than the 2D model [166] [167]. Researchers have also produced 3D cell models for studying cancer [151], [168] with an example of the 3D cervical cancer model showing greater resistance to the chemotherapy drug paclitaxel than the 2D monolayer [169]. Although the benefits of using 3D cell models over 2D cultures, advances in extrusion printing technology are required so production can match

that of 2D models and there are still regulatory hurdles that must be overcome before 3D models can replace 2D cultures for pharmaceutical applications [152]. Moreover, advancing 3D cell models towards larger tissues and even organoid constructs is currently inhibited by nutrient transport to the cells [66].

For the production of recombinant proteins, it is a regulatory imperative, from the European Medicine Agency [170], [171] and the Food and Drug Administration [172], that the proteins originate from a single cell source. The use of piezoelectric inkjet printing has been shown to be capable of achieving a single cell isolated in a single droplet with >99.99% assurance in a fully automated industrial system, Cytena's Single Cell printer [173]. There are also examples within the research literature that demonstrate the capabilities of inkjet printing to isolate single cells – adult rat ganglian and glia cells [30]. Although the research was not intended for this application it shows that there is clearly potential for inkjet printing technology to be utilised for meeting the regulatory requirement of ensuring recombinant proteins are produced from a single cell source.

Using 2D and 3D printing technology to produce drug delivery devices has been shown to have clear applications for personalised medicine [174], [175] and polypharmacy [176], [177]. 3DP of tablets offers the advantage of being able to change the shape, which can improve patient acceptability [178] and modify the release profile of the active pharmaceutical ingredient. The first 3DP oral dosage form with FDA approval was granted in 2015, a tablet containing levetiracetam to treat epilepsy [179]. Since 2015, much research has gone into many other 3D printed tablets, such as tablets containing insulin [180], prednisone and BSA used as a model system for protein therapeutics [181]. Other drug delivery devices that have been produced with printing techniques include microneedles [182] and orodispersible films [183]. Whilst neither of these examples have clinically approved examples it is clear that there is an opportunity for future instances of drug delivery devices to be produced with 2D and 3DP techniques.

8.3 Future Research

Based on the conclusions presented in this thesis, there are a number of areas where further research would aid in progressing more extensive uptake of 2D and 3D printing technologies for pharmaceutical and biological applications. The following research avenues could be considered:

- A framework for controlling inkjet printing so that each isolating factor that could cause damage to inks containing functional materials has been established in this thesis. It could be used for testing protein–based inks for specific applications to assist in moving from the research scale to industrial scale.
- A limited number of enzymes were studied in detail, this makes it difficult to find trends or similarities between groups of proteins so that it could be predicted whether formulating a certain protein would be a suitable candidate for processing with inkjet printing. To improve upon this level of understanding, further research could investigate a wider range of proteins including clinically relevant, protein therapeutics.
- Three inkjet print systems were examined in detail and as each ink and waveform is tailored to the specific printhead, it would be beneficial to examine a wider range of industrial printheads for use with protein-based inks.
- A wider range of additives to ink formulations could also be explored as although the addition of sugars served the purpose of retaining the activity of HRP and SOx after drying, trehalose and glucose were not added to GOx due to the inability to measure the activity of GOx without glucose interfering with the assay.
- For the work examining collagen gel extrusion, it would be beneficial to research into a hybrid gel formulation that has better mechanical properties, potentially with self–healing qualities so that they are suitable

for extrusion. A study seeding cells into this gel would also be beneficial to assess the resulting cell viability after extrusion and how the mechanical properties of the gel are affected by the addition of cells.

For any of the potential areas of future research, it would be important to form industrial collaborations so that the main aim of utilising 2D and 3D printing techniques on a larger, industrial scale can be achieved.

References

Academic Journals and Books

[1] K. Woo, D. Jang, Y. Kim, and J. Moon, "Relationship between printability and rheological behavior of ink-jet conductive inks," *Ceram. Int.*, vol. 39, no. 6, pp. 7015–7021, 2013, doi: 10.1016/j.ceramint.2013.02.039.

[2] S. D. Hoath, Ed., *Fundamentals of Inkjet Printing*. Wiley-VCH, 2016.

[3] G. D. Martin, S. D. Hoath, and I. M. Hutchings, "Inkjet printing - the physics of manipulating liquid jets and drops," *J. Phys. Conf. Ser.*, vol. 105, no. March 2016, p. 012001, 2008, doi: 10.1088/1742-6596/105/1/012001.

[4] S. Di Risio and N. Yan, "Piezoelectric ink-jet printing of horseradish peroxidase: Effect of ink viscosity modifiers on activity," *Macromol. Rapid Commun.*, vol. 28, no. 18–19, pp. 1934–1940, 2007, doi: 10.1002/marc.200700226.

[5] C. C. Cook, T. Wang, and B. Derby, "Inkjet delivery of glucose oxidase.," *Chem. Commun. (Camb).*, vol. 46, no. 30, pp. 5452–5454, 2010, doi: 10.1039/c0cc00567c.

[6] C. R. Thomas and D. Geer, "Effects of shear on proteins in solution," *Biotechnol. Lett.*, vol. 33, no. 3, pp. 443–456, 2011, doi: 10.1007/s10529-010-0469-4.

[7] E. Dickinson and R. Miller, *Food colloids : fundamentals of formulation*. Royal Society of Chemistry, 2001.

[8] S. J. Attwood, R. Kershaw, S. Uddin, S. M. Bishop, and M. E. Welland, "Understanding how charge and hydrophobicity influence globular protein adsorption to alkanethiol and material surfaces," *J. Mater. Chem. B*, pp. 2349–2361, 2019, doi: 10.1039/c9tb00168a.

[9] Y. He, F. Yang, H. Zhao, Q. Gao, B. Xia, and J. Fu, “Research on the printability of hydrogels in 3D bioprinting,” *Sci. Rep.*, vol. 6, pp. 1–13, 2016, doi: 10.1038/srep29977.

[10] A. G. M. Gregory Gillispie, Peter Prim, Joshua Copus, John Fisher and S. J. L. James J. Yoo, Anthony Atala, “Assessment Methodologies for Extrusion-Based Bioink Printability,” *Biofabrication*, vol. 176, no. 1, pp. 139–148, 2020, doi: 10.1016/j.physbeh.2017.03.040.

[11] J. Emmermacher *et al.*, “Engineering considerations on extrusion-based bioprinting: interactions of material behavior, mechanical forces and cells in the printing needle,” *Biofabrication*, vol. 12, no. 2, 2020, doi: 10.1088/1758-5090/ab7553.

[12] Q. Xu *et al.*, “Instant Gelation System as Self-Healable and Printable 3D Cell Culture Bioink Based on Dynamic Covalent Chemistry,” 2020, doi: 10.1021/acsami.0c08567.

[13] B. Lanfer, U. Freudenberg, R. Zimmermann, D. Stamov, V. Körber, and C. Werner, “Aligned fibrillar collagen matrices obtained by shear flow deposition,” *Biomaterials*, vol. 29, no. 28, pp. 3888–3895, 2008, doi: 10.1016/j.biomaterials.2008.06.016.

[14] R. Daly, T. S. Harrington, G. D. Martin, and I. M. Hutchings, “Inkjet printing for pharmaceutics - A review of research and manufacturing,” *Int. J. Pharm.*, 2015, doi: 10.1016/j.ijpharm.2015.03.017.

[17] H. P. Le and Hue P. Le, “Progress and trends in ink-jet printing technology,” *J. Imaging Sci. Technol.*, vol. 42, pp. 49–62, 1998, doi: citeulike-article-id:3979011.

[19] Rayleigh, “On The Instabilities Of Jets.” 1878.

[20] D. Cho, J. Lee, F. Pati, J. W. Jung, J. Jang, and J. H. Park, “Chapter 3,” in *Organ Printing*, IOP Publishing, 2015.

[21] N. I. and S. Y. Naoki Morita, Masashi Hiratsuka, Toshinobu Hamazaki, Hiroyuki Usami, Yoshinao Kondoh, Hideki Fukunaga, Hiroshi Ikeda, “Pulse and

Temperature Control of Thermal Ink Jet Printheads Without a Heater Passivation Layer," *J. Imaging Sci. Technol.*, vol. 52, no. 1, pp. 1–15, 2008, doi: 10.2352/J.ImagingSci.Technol.

[22] X. Cui, D. Dean, Z. M. Ruggeri, and T. Boland, "Cell damage evaluation of thermal inkjet printed chinese hamster ovary cells," *Biotechnol. Bioeng.*, vol. 106, no. 6, pp. 963–969, 2010, doi: 10.1002/bit.22762.

[23] H. Wijshoff, "The dynamics of the piezo inkjet printhead operation," *Phys. Rep.*, vol. 491, no. 4–5, pp. 77–177, 2010, doi: 10.1016/j.physrep.2010.03.003.

[24] G. H. McKinley and M. Renardy, "Wolfgang von Ohnesorge," *Phys. Fluids*, vol. 23, no. 12, 2011, doi: 10.1063/1.3663616.

[25] J. N. Israelachvili, *Intermolecular and Surface Forces*. 2011.

[26] G. D. Martin, W. C. Price, and I. M. Hutchings, "Measurement of Inkjet Drop Volume—The Role of Image Processing," *J. Imaging Sci. Technol.*, vol. 60, no. 4, pp. 404011–404019, 2016, doi: 10.2352/J.ImagingSci.Technol.2016.60.4.040401.

[27] Y. Liu and B. Derby, "Experimental study of the parameters for stable drop-on-demand inkjet performance," *Phys. Fluids*, vol. 31, no. 3, 2019, doi: 10.1063/1.5085868.

[28] D. R. Karsa, B. Zhmud, and F. Tiberg, "Surfactants in ink-jet inks," *Surfactants Polym. Coatings, Inks Adhes.*, vol. 1, no. 5, pp. 211–244, 2020, doi: 10.1201/9780367812416-8.

[29] D. Y. Joh *et al.*, "Inkjet-printed point-of-care immunoassay on a nanoscale polymer brush enables subpicomolar detection of analytes in blood.," *Proc. Natl. Acad. Sci. U. S. A.*, vol. 114, no. 34, pp. E7054–E7062, Aug. 2017, doi: 10.1073/pnas.1703200114.

[30] B. Lorber, W.-K. Hsiao, I. M. Hutchings, and K. R. Martin, "Adult rat retinal ganglion cells and glia can be printed by piezoelectric inkjet printing," *Biofabrication*, vol. 6, no. 1, p. 015001, 2013, doi: 10.1088/1758-5082/6/1/015001.

[32] I. FUJIFILM Dimatix, “Dimatix Materials Printer DMP-2800 Series User Manual,” *FUJIFILM Dimatix*, pp. 1–93, 2006.

[35] D. A. Gregory, Y. Zhang, P. J. Smith, X. Zhao, and S. J. Ebbens, “Reactive Inkjet Printing of Biocompatible Enzyme Powered Silk Micro-Rockets,” *Small*, pp. 4048–4055, 2016, doi: 10.1002/smll.201600921.

[36] T. Wang, R. Patel, and B. Derby, “Manufacture of 3-dimensional objects by reactive inkjet printing,” *Soft Matter*, vol. 4, no. 12, p. 2513, 2008, doi: 10.1039/b807758d.

[37] R. Suntivich, I. Drachuk, R. Calabrese, D. L. Kaplan, and V. V. Tsukruk, “Inkjet printing of silk nest arrays for cell hosting,” *Biomacromolecules*, vol. 15, no. 4, pp. 1428–1435, 2014, doi: 10.1021/bm500027c.

[38] S. Parsa, M. Gupta, F. Loizeau, and K. C. Cheung, “Effects of surfactant and gentle agitation on inkjet dispensing of living cells.,” *Biofabrication*, vol. 2, no. 2, p. 025003, 2010, doi: 10.1088/1758-5082/2/2/025003.

[39] D. I. Stimpson, W. Cooley, S. M. Knepper, D. B. Wallace, and B. College, “Parallel Production of Oligonucleotide Arrays,” *Image (Rochester, N.Y.)*, vol. 890, no. November, pp. 886–890, 1998.

[40] A. B. M. Buanz and S. Gaisford, “Formation of Highly Metastable ß Glycine by Confinement in Inkjet Printed Droplets,” *Cryst. Growth Des.*, p. acs.cgd.6b01633, 2017, doi: 10.1021/acs.cgd.6b01633.

[41] E. Gdor, S. Shemesh, S. Magdassi, and D. Mandler, “Multienzyme Inkjet Printed 2D Arrays,” *ACS Appl. Mater. Interfaces*, vol. 7, no. 32, pp. 17985–17992, 2015, doi: 10.1021/acsami.5b04726.

[42] H. Tao *et al.*, “Inkjet Printing of Regenerated Silk Fibroin: From Printable Forms to Printable Functions,” *Adv. Mater.*, vol. 27, no. 29, pp. 4273–4279, 2015, doi: 10.1002/adma.201501425.

[43] N. Sandler, P. Ihalainen, and J. Peltonen, “Inkjet Printing of Drug Substances and Use of Porous Substrates-Towards Individualized Dosing,” *Int. J. Drug Dev.*

Res., vol. 3, no. 2, pp. 26–33, 2011, doi: 10.1002/jps.

[44] D. Raijada *et al.*, "a Step Toward Development of Printable Dosage Forms for Poorly Soluble Drugs," *J. Pharm. Sci.*, vol. 102, no. 10, pp. 3694–3704, 2013, doi: 10.1002/jps.23678.

[45] M. Montenegro-Nicolini, Miranda, and J. O. Morales, "Inkjet Printing of Proteins: an Experimental Approach," *AAPS J.*, vol. 19, no. 7, pp. 234–243, 2016, doi: 10.1208/s12248-016-9997-8.

[46] L. Setti, A. Fraleoni-Morgera, I. Mencarelli, A. Filippini, B. Ballarin, and M. Di Biase, "An HRP-based amperometric biosensor fabricated by thermal inkjet printing," *Sensors Actuators, B Chem.*, vol. 126, no. 1, pp. 252–257, 2007, doi: 10.1016/j.snb.2006.12.015.

[47] J. I. Rodríguez-Dévora, B. Zhang, D. Reyna, Z. Shi, and T. Xu, "High throughput miniature drug-screening platform using bioprinting technology," *Biofabrication*, vol. 4, no. 3, pp. 1–8, 2012, doi: 10.1088/1758-5082/4/3/035001.

[48] J. Lee, A. A. S. Samson, and J. M. Song, "Inkjet-printing enzyme inhibitory assay based on determination of ejection volume," *Anal. Chem.*, p. acs.analchem.6b04585, 2016, doi: 10.1021/acs.analchem.6b04585.

[49] M. Choi, J. Hwang, J. Choi, and J. Hong, "Multicomponent High-throughput Drug Screening via Inkjet Printing to Verify the Effect of Immunosuppressive Drugs on Immune T Lymphocytes," *Sci. Rep.*, vol. 7, no. 1, p. 6318, 2017, doi: 10.1038/s41598-017-06690-2.

[50] T. T. Biswas, J. Yu, and V. A. Nierstrasz, "Effects of ink characteristics and piezo-electric inkjetting parameters on lysozyme activity," *Sci. Rep.*, vol. 9, no. 1, pp. 1–11, 2019, doi: 10.1038/s41598-019-54723-9.

[51] M. Edinger, D. Bar-Shalom, N. Sandler, J. Rantanen, and N. Genina, "QR encoded smart oral dosage forms by inkjet printing," *Int. J. Pharm.*, vol. 536, no. 1, pp. 138–145, 2018, doi: 10.1016/j.ijpharm.2017.11.052.

[52] J. Eggers and T. F. Dupont, "Drop Formation in a One-Dimensional

Approximation of the Navier-Stokes Equation," *J. Fluid Mech.*, vol. 262, pp. 205–221, 1994, doi: 10.1017/S0022112094000480.

[53] J. Der Yu, S. Sakai, and J. Sethian, "A coupled quadrilateral grid level set projection method applied to ink jet simulation," *J. Comput. Phys.*, vol. 206, no. 1, pp. 227–251, 2005, doi: 10.1016/j.jcp.2004.12.012.

[54] T. Tofan, H. Kruggel-Emden, V. Turla, and R. Jasevičius, "Numerical modeling of the motion and interaction of a droplet of an inkjet printing process with a flat surface," *Appl. Sci.*, vol. 11, no. 2, pp. 1–15, 2021, doi: 10.3390/app11020527.

[55] J. R. Castrejón-Pita, N. F. Morrison, O. G. Harlen, G. D. Martin, and I. M. Hutchings, "Experiments and Lagrangian simulations on the formation of droplets in drop-on-demand mode," *Phys. Rev. E - Stat. Nonlinear, Soft Matter Phys.*, vol. 83, no. 3, pp. 1–12, 2011, doi: 10.1103/PhysRevE.83.036306.

[56] A. Van Der Bos *et al.*, "Velocity profile inside piezoacoustic inkjet droplets in flight: Comparison between experiment and numerical simulation," *Phys. Rev. Appl.*, vol. 1, no. 1, pp. 1–9, 2014, doi: 10.1103/PhysRevApplied.1.014004.

[57] Y. Zhong, X. Dong, Z. Yin, and H. Fang, "Theoetical design of inkjet process to improve delivery efficiency," *J. Appl. Fluid Mech.*, vol. 13, no. 1, pp. 275–286, 2020, doi: 10.29252/jafm.13.01.30395.

[58] H. Jiang and H. Tan, "One dimensional model for droplet ejection process in inkjet devices," *Fluids*, vol. 3, no. 2, 2018, doi: 10.3390/fluids3020028.

[59] L. Dybowska-Sarapuk *et al.*, "Efficient inkjet printing of graphene-based elements: Influence of dispersing agent on ink viscosity," *Nanomaterials*, vol. 8, no. 8, pp. 9–14, 2018, doi: 10.3390/nano8080602.

[60] Leishik, *Aluminium Extrusion Technology*, vol. 57, no. 1. 2000.

[62] I. T. Ozbolat and M. Hospodiuk, "Current advances and future perspectives in extrusion-based bioprinting," *Biomaterials*, vol. 76, pp. 321–343, 2016, doi: 10.1016/j.biomaterials.2015.10.076.

[63] R. Levato, J. Visser, J. A. Planell, E. Engel, J. Malda, and M. A. Mateos-Timoneda, "Biofabrication of tissue constructs by 3D bioprinting of cell-laden microcarriers," *Biofabrication*, vol. 6, no. 3, 2014, doi: 10.1088/1758-5082/6/3/035020.

[64] C. Norotte, F. S. Marga, L. E. Niklason, and G. Forgacs, "Scaffold-free vascular tissue engineering using bioprinting," *Biomaterials*, vol. 30, no. 30, pp. 5910–5917, 2009, doi: 10.1016/j.biomaterials.2009.06.034.

[65] A. Tirella, A. Orsini, G. Vozzi, and A. Ahluwalia, "A phase diagram for microfabrication of geometrically controlled hydrogel scaffolds," *Biofabrication*, vol. 1, no. 4, 2009, doi: 10.1088/1758-5082/1/4/045002.

[66] J. M. C. Editor, *3D Bioprinting*. 2017.

[67] C. C. Chang, E. D. Boland, S. K. Williams, and J. B. Hoying, "Direct-write bioprinting three-dimensional biohybrid systems for future regenerative therapies," *J. Biomed. Mater. Res. - Part B Appl. Biomater.*, vol. 98 B, no. 1, pp. 160–170, 2011, doi: 10.1002/jbm.b.31831.

[68] T. Gao *et al.*, "Optimization of gelatin-alginate composite bioink printability using rheological parameters: A systematic approach," *Biofabrication*, vol. 10, no. 3, 2018, doi: 10.1088/1758-5090/aacdc7.

[69] W. P. Cox and E. H. Merz, "Correlation of dynamic and steady flow viscosities," *J. Polym. Sci.*, vol. 28, no. 118, pp. 619–622, Apr. 1958, doi: 10.1002/pol.1958.1202811812.

[70] L. Ouyang, R. Yao, Y. Zhao, and W. Sun, "Effect of bioink properties on printability and cell viability for 3D bioplotting of embryonic stem cells," *Biofabrication*, vol. 8, no. 3, 2016, doi: 10.1088/1758-5090/8/3/035020.

[71] Y. Wu, Z. Y. (William) Lin, A. C. Wenger, K. C. Tam, and X. (Shirley) Tang, "3D bioprinting of liver-mimetic construct with alginate/cellulose nanocrystal hybrid bioink," *Bioprinting*, vol. 9, pp. 1–6, 2018, doi: 10.1016/j.bprint.2017.12.001.

[72] A. Blaeser *et al.*, "Biofabrication Under Fluorocarbon: A Novel Freeform

Fabrication Technique to Generate High Aspect Ratio Tissue-Engineered Constructs," *Biores. Open Access*, vol. 2, no. 5, pp. 374–384, 2013, doi: 10.1089/biores.2013.0031.

[73] A. Habib, V. Sathish, S. Mallik, and B. Khoda, "3D printability of alginate-carboxymethyl cellulose hydrogel," *Materials (Basel).*, vol. 11, no. 3, 2018, doi: 10.3390/ma11030454.

[74] A. Ribeiro *et al.*, "Assessing bioink shape fidelity to aid material development in 3D bioprinting," *Biofabrication*, vol. 10, no. 1, 2018, doi: 10.1088/1758-5090/aa90e2.

[75] W. L. Ng, W. Y. Yeong, and M. W. Naing, "Polyelectrolyte gelatin-chitosan hydrogel optimized for 3D bioprinting in skin tissue engineering," *Int. J. Bioprinting*, vol. 2, no. 1, pp. 53–62, 2016, doi: 10.18063/IJB.2016.01.009.

[76] B. Webb and B. J. Doyle, "Parameter optimization for 3D bioprinting of hydrogels," *Bioprinting*, vol. 8, no. September, pp. 8–12, 2017, doi: 10.1016/j.bprint.2017.09.001.

[77] J. Göhl, K. Markstedt, A. Mark, K. Håkansson, P. Gatenholm, and F. Edelvik, "Simulations of 3D bioprinting: Predicting bioprintability of nanofibrillar inks," *Biofabrication*, vol. 10, no. 3, 2018, doi: 10.1088/1758-5090/aac872.

[78] G. Ahn *et al.*, "Precise stacking of decellularized extracellular matrix based 3D cell-laden constructs by a 3D cell printing system equipped with heating modules," *Sci. Rep.*, vol. 7, no. 1, pp. 1–11, 2017, doi: 10.1038/s41598-017-09201-5.

[79] Y. He, F. Yang, H. Zhao, Q. Gao, B. Xia, and J. Fu, "Research on the printability of hydrogels in 3D bioprinting," *Sci. Rep.*, vol. 6, pp. 1–13, 2016, doi: 10.1038/srep29977.

[80] A. Athirasala *et al.*, "A dentin-derived hydrogel bioink for 3D bioprinting of cell laden scaffolds for regenerative dentistry," *Biofabrication*, vol. 10, no. 2, 2018, doi: 10.1088/1758-5090/aa9b4e.

[81] K. H. Kang, L. A. Hockaday, and J. T. Butcher, "Quantitative optimization of solid

freeform deposition of aqueous hydrogels," *Biofabrication*, vol. 5, no. 3, 2013, doi: 10.1088/1758-5082/5/3/035001.

[82] K. D. Roehm and S. V. Madihally, "Bioprinted chitosan-gelatin thermosensitive hydrogels using an inexpensive 3D printer," *Biofabrication*, vol. 10, no. 1, 2018, doi: 10.1088/1758-5090/aa96dd.

[83] F. P. W. Melchels, W. J. A. Dhert, D. W. Hutmacher, and J. Malda, "Development and characterisation of a new bioink for additive tissue manufacturing," *J. Mater. Chem. B*, vol. 2, no. 16, pp. 2282–2289, 2014, doi: 10.1039/c3tb21280g.

[84] F. Poncin-Epaillard *et al.*, "Surface Treatment of Polymeric Materials Controlling the Adhesion of Biomolecules," *J. Funct. Biomater.*, vol. 3, no. 4, pp. 528–543, 2012, doi: 10.3390/jfb3030528.

[85] J. B. Delehanty and F. S. Ligler, "Method for printing functional protein microarrays," *Biotechniques*, vol. 34, no. 2, pp. 380–385, 2003.

[86] D. Beyer, W. Knoll, H. Ringsdorf, J. Wang, R. B. Timmons, and P. Sluka, "Reduced protein adsorption on plastics via direct plasma deposition of triethylene glycol monoallyl ether," *J. Biomed. Mater. Res.*, vol. 36, no. 2, pp. 181–189, 1997, doi: 10.1002/(SICI)1097-4636(199708)36:2<181::AID-JBM6>3.0.CO;2-G.

[87] F. Poncin-Epaillard and G. Legeay, "Surface engineering of biomaterials with plasma techniques," *J. Biomater. Sci. Polym. Ed.*, vol. 14, no. 10, pp. 1005–1028, 2003, doi: 10.1163/156856203769231538.

[88] J. Jaspe and S. J. Hagen, "Do protein molecules unfold in a simple shear flow?," *Biophys. J.*, vol. 91, no. 9, pp. 3415–3424, 2006, doi: 10.1529/biophysj.106.089367.

[89] Y.-F. Maa and C. C. Hsu, "Effect of high shear on proteins," *Biotechnol. Bioeng.*, vol. 51, no. 4, pp. 458–465, 1996, doi: 10.1002/(SICI)1097-0290(19960820)51:4<458::AID-BIT9>3.0.CO;2-H.

[90] I. B. Bekard and D. E. Dunstan, "Shear-Induced deformation of bovine insulin in couette flow," *J. Phys. Chem. B*, vol. 113, no. 25, pp. 8453–8457, 2009, doi: 10.1021/jp903522e.

[91] I. B. Bekard, K. J. Barnham, L. R. White, and D. E. Dunstan, “alpha-Helix unfolding in simple shear flow,” *Soft Matter*, vol. 7, no. 1, pp. 203–210, 2011, doi: 10.1039/C0SM00692K.

[92] C. R. Thomas, A. W. Nienow, and P. Dunnill, “Action of shear on enzymes: Studies with alcohol dehydrogenase,” *Biotechnol. Bioeng.*, vol. 21, no. 12, pp. 2263–2278, Dec. 1979, doi: 10.1002/bit.260211208.

[93] C. A. Siedlecki, B. J. Lestini, K. Kottke-Marchant, S. J. Eppell, D. L. Wilson, and R. E. Marchant, “Shear-Dependent Changes in the Three-Dimensional Structure of Human von Willebrand Factor,” *Blood*, vol. 88, no. 8, pp. 2939–2950, 1996.

[94] L. Ashton, J. Dusting, E. Imomoh, S. Balabani, and E. W. Blanch, “Shear-induced unfolding of lysozyme monitored in situ,” *Biophys. J.*, vol. 96, no. 10, pp. 4231–4236, 2009, doi: 10.1016/j.bpj.2009.02.024.

[96] P. Pradipasena and C. Rha, “Effect of concentration on apparent viscosity of a globular protein solution,” *Polym. Eng. Sci.*, vol. 17, no. 12, pp. 861–864, Dec. 1977, doi: 10.1002/pen.760171209.

[97] N. W. Warne, “Development of high concentration protein biopharmaceuticals: The use of platform approaches in formulation development,” *Eur. J. Pharm. Biopharm.*, vol. 78, pp. 208–212, 2011, doi: 10.1016/j.ejpb.2011.03.004.

[98] J. Dobson *et al.*, “Inducing protein aggregation by extensional flow.,” *Proc. Natl. Acad. Sci. U. S. A.*, vol. 114, no. 18, pp. 4673–4678, May 2017, doi: 10.1073/pnas.1702724114.

[99] S. E. Evans, M. C. Rodriguez Rivero, E. Rognin, T. Tuladhar, and R. Daly, “2D and 3D inkjet printing of biopharmaceuticals – A review of trends and future perspectives in research and manufacturing,” *Int. J. Pharm.*, vol. 599, no. February, 2021, doi: 10.1016/j.ijpharm.2021.120443.

[100] G. M. Nishioka, A. A. Markey, and C. K. Holloway, “Protein damage in drop-on-demand printers,” *J. Am. Chem. Soc.*, vol. 126, no. 50, pp. 16320–16321, 2004, doi: 10.1021/ja044539z.

[101] S. Uribe and J. G. Sampedro, “Measuring Solution Viscosity and its Effect on Enzyme Activity,” *Biol. Proced. Online*, vol. 5, no. 1, pp. 108–115, 2003, doi: 10.1251/bpo52.

[102] G. Arrabito, C. Musumeci, V. Aiello, S. Libertino, G. Compagnini, and B. Pignataro, “On the relationship between jetted inks and printed biopatterns: Molecular-thin functional microarrays of glucose oxidase,” *Langmuir*, vol. 25, no. 11, pp. 6312–6318, 2009, doi: 10.1021/la900071z.

[103] G. MacBeath and S. L. Schreiber, “Printing proteins as microarrays for high-throughput function determination,” *Science (80-.).*, vol. 289, no. September, pp. 1760–1763, 2000, doi: 10.1126/science.289.5485.1760.

[104] V. Romanov, S. N. Davidoff, A. R. Miles, D. W. Grainger, B. K. Gale, and B. D. Brooks, “A critical comparison of protein microarray fabrication technologies,” *Analyst*, vol. 139, no. 6, pp. 1303–1326, 2014, doi: 10.1039/c3an01577g.

[105] W. Zhang *et al.*, “The use of an inkjet injection technique in immunoassays by quantitative on-line electrophoretically mediated microanalysis,” *J. Chromatogr. A*, vol. 1477, pp. 127–131, 2016, doi: 10.1016/j.chroma.2016.11.041.

[106] L. Setti *et al.*, “Thermal inkjet technology for the microdeposition of biological molecules as a viable route for the realization of biosensors,” *Anal. Lett.*, vol. 37, no. 8, pp. 1559–1570, 2004, doi: Doi 10.1081/Al-120037587.

[107] S. V. M. & A. Atala, “3D Bioprinting of Tissues and Organs,” *Nat. Biotechnol.*, vol. 32, no. 8, pp. 773–785, 2014, doi: 10.1038/nbt.2958.

[108] J. Malda *et al.*, “25th anniversary article: Engineering hydrogels for biofabrication,” *Adv. Mater.*, vol. 25, no. 36, pp. 5011–5028, 2013, doi: 10.1002/adma.201302042.

[109] W. Sun *et al.*, “The bioprinting roadmap,” *Biofabrication*, vol. 12, no. 2, 2020, doi: 10.1088/1758-5090/ab5158.

[110] M. L. Oyen, “Mechanical characterisation of hydrogel materials,” *Int. Mater. Rev.*, vol. 59, no. 1, pp. 44–59, 2014, doi: 10.1179/1743280413Y.0000000022.

[111] K. a Ross and M. G. Scanlon, “Analysis of the elastic modulus of agar gel by indentation,” *J. Texture Stud.*, vol. 1, no. Finney 1999, pp. 17–27, 1999.

[112] J. M. Zuidema, C. J. Rivet, R. J. Gilbert, and F. A. Morrison, “A protocol for rheological characterization of hydrogels for tissue engineering strategies,” *J. Biomed. Mater. Res. - Part B Appl. Biomater.*, vol. 102, no. 5, pp. 1063–1073, 2014, doi: 10.1002/jbm.b.33088.

[113] M. Czerner, L. S. Fellay, M. P. Suárez, P. M. Frontini, and L. A. Fasce, “Determination of Elastic Modulus of Gelatin Gels by Indentation Experiments,” *Procedia Mater. Sci.*, vol. 8, pp. 287–296, 2015, doi: 10.1016/j.mspro.2015.04.075.

[114] “ASTM F2900 - 11 Standard Guide for Characterization of Hydrogels used in Regenerative Medicine (Withdrawn 2020).” https://www.astm.org/Standards/F2900.htm (accessed May 12, 2020).

[115] J. H. Y. Chung *et al.*, “Bio-ink properties and printability for extrusion printing living cells,” *Biomater. Sci.*, vol. 1, no. 7, pp. 763–773, 2013, doi: 10.1039/c3bm00012e.

[116] M. Nadgorny, Z. Xiao, and L. A. Connal, “2D and 3D-printing of self-healing gels: design and extrusion of self-rolling objects,” pp. 283–292, 2017, doi: 10.1039/c7me00023e.

[117] M. Guvendiren, H. D. Lu, and J. A. Burdick, “Shear-thinning hydrogels for biomedical applications,” *Soft Matter*, vol. 8, no. 2, pp. 260–272, 2012, doi: 10.1039/c1sm06513k.

[118] J. Patterson, M. M. Martino, and J. A. Hubbell, “Biomimetic materials in tissue engineering,” *Mater. Today*, vol. 13, no. 1–2, pp. 14–22, 2010, doi: 10.1016/S1369-7021(10)70013-4.

[119] S. F. Badylak, “The extracellular matrix as a scaffold for tissue reconstruction,” *Cell Dev. Biol.*, vol. 13, no. 02, pp. 243–249, 2002, doi: 10.1016/S1084.

[120] M. D. Shoulders and R. T. Raines, “Collagen Structure and Stability,” *Annu. Rev. Biochem.*, vol. 78, no. 1, pp. 929–958, 2009, doi:

10.1146/annurev.biochem.77.032207.120833.

[121] R. Parenteau-Bareil, R. Gauvin, and F. Berthod, “Collagen-based biomaterials for tissue engineering applications,” *Materials (Basel).*, vol. 3, no. 3, pp. 1863–1887, 2010, doi: 10.3390/ma3031863.

[122] Y. L. Yang, L. M. Leone, and L. J. Kaufman, “Elastic moduli of collagen gels can be predicted from two-dimensional confocal microscopy,” *Biophys. J.*, vol. 97, no. 7, pp. 2051–2060, 2009, doi: 10.1016/j.bpj.2009.07.035.

[123] S. G. Kim, S. G. Kim, B. Viechnicki, S. Kim, and H. D. Nah, “Engineering of a periodontal ligament construct: Cell and fibre alignment induced by shear stress,” *J. Clin. Periodontol.*, vol. 38, no. 12, pp. 1130–1136, 2011, doi: 10.1111/j.1600-051X.2011.01790.x.

[124] A. Kureshi, U. Cheema, T. Alekseeva, A. Cambrey, and R. Brown, “Alignment hierarchies: Engineering architecture from the nanometre to the micrometre scale,” *J. R. Soc. Interface*, vol. 7, no. SUPPL. 6, 2010, doi: 10.1098/rsif.2010.0346.focus.

[125] N. Saeidi, E. A. Sander, and J. W. Ruberti, “Dynamic shear-influenced collagen self-assembly,” *Biomaterials*, vol. 30, no. 34, pp. 6581–6592, 2009, doi: 10.1016/j.biomaterials.2009.07.070.

[126] H. Kim *et al.*, “Shear-induced alignment of collagen fibrils using 3D cell printing for corneal stroma tissue engineering,” *Biofabrication*, vol. 11, no. 3, 2019, doi: 10.1088/1758-5090/ab1a8b.

[127] L. He *et al.*, “Effect of pre-shearing treatment on the molecular structure, fibrillogenesis behavior and gel properties of collagen,” *New J. Chem.*, vol. 44, no. 17, pp. 6760–6770, 2020, doi: 10.1039/d0nj00054j.

[128] K. H. Lam *et al.*, “A high-throughput microfluidic method for fabricating aligned collagen fibrils to study Keratocyte behavior,” *Biomed. Microdevices*, vol. 21, no. 4, 2019, doi: 10.1007/s10544-019-0436-3.

[129] B. A. Nerger, P. T. Brun, and C. M. Nelson, “Microextrusion printing cell-laden

networks of type i collagen with patterned fiber alignment and geometry," *Soft Matter*, vol. 15, no. 28, pp. 5728–5738, 2019, doi: 10.1039/c8sm02605j.

[130] Microfab, "A Basic Ink-Jet Setup." http://www.microfab.com/a-basic-ink-jet-microdispensing-setup (accessed Oct. 21, 2017).

[131] N. Willis-Fox, E. Rognin, C. Baumann, T. A. Aljohani, R. Göstl, and R. Daly, "Going with the Flow: Tunable Flow-Induced Polymer Mechanochemistry," *Adv. Funct. Mater.*, vol. 30, no. 27, 2020, doi: 10.1002/adfm.202002372.

[132] J. L. R. Arrondo, A. Muga, J. Castresana, and F. M. Goñi, "Quantitative studies of the structure of proteins in solution by fourier-transform infrared spectroscopy," *Prog. Biophys. Mol. Biol.*, vol. 59, no. 1, pp. 23–56, 1993, doi: 10.1016/0079-6107(93)90006-6.

[133] "Determination of Secondary Structure in Proteins by FTIR Spectroscopy - JenaLib." http://jenalib.leibniz-fli.de/ImgLibDoc/ftir/IMAGE_FTIR.html (accessed Aug. 22, 2021).

[134] B. W. Jo, A. Lee, K. H. Ahn, and S. J. Lee, "Evaluation of jet performance in drop-on-demand (DOD) inkjet printing," *Korean J. Chem. Eng.*, vol. 26, no. 2, pp. 339–348, 2009, doi: 10.1007/s11814-009-0057-2.

[135] R. M. Verkouteren and J. R. Verkouteren, "Inkjet metrology II: Resolved effects of ejection frequency, fluidic pressure, and droplet number on reproducible drop-on-demand dispensing," *Langmuir*, vol. 27, no. 15, pp. 9644–9653, 2011, doi: 10.1021/la201728f.

[136] D. Jang, D. Kim, and J. Moon, "Influence of Fluid Physical Properties on Ink-Jet Printability," *Langmuir*, vol. 25, no. 5, pp. 2629–2635, 2009, doi: 10.1021/la900059m.

[137] B. Li, J. Fan, J. Li, J. Chu, and T. Pan, "Piezoelectric-driven droplet impact printing with an interchangeable microfluidic cartridge," *Biomicrofluidics*, vol. 9, no. 5, pp. 1–11, 2015, doi: 10.1063/1.4928298.

[138] I. McWilliam and and D. H. Marisa Chong Kwan, "Inkjet Printing for the

Production of Protein Microarrays," in *Methods and Protocols, Methods in Molecular Biology*, vol. 785, no. 1, 2011, pp. 363–78.

[139] F. W. Krainer and A. Glieder, "An updated view on horseradish peroxidases: recombinant production and biotechnological applications," *Appl. Microbiol. Biotechnol.*, vol. 99, no. 4, pp. 1611–1625, 2015, doi: 10.1007/s00253-014-6346-7.

[140] S. B. Bankar, M. V. Bule, R. S. Singhal, and L. Ananthanarayan, "Glucose oxidase - An overview," *Biotechnol. Adv.*, vol. 27, no. 4, pp. 489–501, 2009, doi: 10.1016/j.biotechadv.2009.04.003.

[141] T. Mazzu-nascimento, A. Gomes, C. Le, J. R. Catai, G. G. Morbioli, and E. Carrilho, "Analytical Methods Towards low-cost bioanalytical tools for sarcosine assays for cancer diagnostics," vol. c, pp. 7312–7318, 2016, doi: 10.1039/c6ay01848c.

[142] A. Shome, S. Roy, and P. K. Das, "Nonionic surfactants: A key to enhance the enzyme activity at cationic reverse micellar interface," *Langmuir*, vol. 23, no. 8, pp. 4130–4136, 2007, doi: 10.1021/la062804j.

[143] D. N. Rubingh, "The influence of surfactants on enzyme activity," *Curr. Opin. Colloid Interface Sci.*, vol. 1, no. 5, pp. 598–603, 1996, doi: 10.1016/s1359-0294(96)80097-5.

[145] J. L. Brash and T. A. Horbett, "Proteins at Interfaces," *Am. Chem. Soc.*, vol. 32, no. C, pp. 283–326, 1995, doi: 10.1016/S0065-3233(08)60577-X.

[146] W. Wang, "Protein aggregation and its inhibition in biopharmaceutics," *Int. J. Pharm.*, vol. 289, no. 1–2, pp. 1–30, 2005, doi: 10.1016/j.ijpharm.2004.11.014.

[147] A.A. Ken-ichi Izutsu, Yasuto Fujimaki, Akiko Kuwabara, Yukio Hiyama, Chikako Yomota, "Near-Infrared Analysis of Protein Secondary Structure in Aqueous Solutions and Freeze-Dried Solids," *J. Pharm. Sci.*, vol. 95, no. 2, pp. 26–33, 2006, doi: 10.1002/jps.

[148] M. A. Mensink, H. W. Frijlink, K. van der Voort Maarschalk, and W. L. J. Hinrichs, "How sugars protect proteins in the solid state and during drying

(review): Mechanisms of stabilization in relation to stress conditions," *Eur. J. Pharm. Biopharm.*, vol. 114, pp. 288–295, 2017, doi: 10.1016/j.ejpb.2017.01.024.

[149] S. Jiang and S. L. Nail, "Effect of process conditions on recovery of protein activity after freezing and freeze-drying," *Eur. J. Pharm. Biopharm.*, vol. 45, no. 3, pp. 249–257, 1998, doi: 10.1016/S0939-6411(98)00007-1.

[150] H. Y. Gan, X. Shan, T. Eriksson, B. K. Lok, and Y. C. Lam, "Reduction of droplet volume by controlling actuating waveforms in inkjet printing for micro-pattern formation," *J. Micromechanics Microengineering*, vol. 19, no. 5, 2009, doi: 10.1088/0960-1317/19/5/055010.

[151] J. M. Grolman, D. Zhang, A. M. Smith, J. S. Moore, and K. A. Kilian, "Rapid 3D Extrusion of Synthetic Tumor Microenvironments," *Adv. Mater.*, vol. 27, no. 37, pp. 5512–5517, 2015, doi: 10.1002/adma.201501729.

[152] W. Peng, P. Datta, B. Ayan, V. Ozbolat, D. Sosnoski, and I. T. Ozbolat, "3D bioprinting for drug discovery and development in pharmaceutics," *Acta Biomater.*, vol. 57, pp. 26–46, 2017, doi: 10.1016/j.actbio.2017.05.025.

[153] M. K. Włodarczyk-Biegun and A. del Campo, "3D bioprinting of structural proteins," *Biomaterials*, vol. 134, pp. 180–201, 2017, doi: 10.1016/j.biomaterials.2017.04.019.

[154] S. Yunoki, H. Hatayama, M. Ebisawa, E. Kondo, and K. Yasuda, "A novel method for continuous formation of cord-like collagen gels to fabricate durable fibers in which collagen fibrils are longitudinally aligned," *J. Biomed. Mater. Res. - Part B Appl. Biomater.*, pp. 1011–1023, 2018, doi: 10.1002/jbm.b.34194.

[155] J. L. Drury and D. J. Mooney, "Hydrogels for tissue engineering: Scaffold design variables and applications," *Biomaterials*, vol. 24, no. 24, pp. 4337–4351, 2003, doi: 10.1016/S0142-9612(03)00340-5.

[156] S. T. Kreger *et al.*, "Polymerization and matrix physical properties as important design considerations for soluble collagen formulations," *Biopolymers*, vol. 93, no. 8, pp. 690–707, 2010, doi: 10.1002/bip.21431.

[157] M. Shayegan and N. R. Forde, "Microrheological Characterization of Collagen Systems: From Molecular Solutions to Fibrillar Gels," *PLoS One*, vol. 8, no. 8, pp. 23–28, 2013, doi: 10.1371/journal.pone.0070590.

[158] N. Diamantides, C. Dugopolski, E. Blahut, S. Kennedy, and L. J. Bonassar, "High density cell seeding affects the rheology and printability of collagen bioinks," *Biofabrication*, vol. 11, no. 4, p. 045016, 2019, doi: 10.1088/1758-5090/ab3524.

[159] A. J. Holder, N. Badiei, K. Hawkins, C. Wright, P. R. Williams, and D. J. Curtis, "Control of collagen gel mechanical properties through manipulation of gelation conditions near the sol-gel transition," *Soft Matter*, vol. 14, no. 4, pp. 574–580, 2018, doi: 10.1039/c7sm01933e.

[160] O. Moreno-Arotzena, J. G. Meier, C. Del Amo, and J. M. García-Aznar, "Characterization of fibrin and collagen gels for engineering wound healing models," *Materials (Basel).*, vol. 8, no. 4, pp. 1636–1651, 2015, doi: 10.3390/ma8041636.

[161] C. B. Raub *et al.*, "Noninvasive assessment of collagen gel microstructure and mechanics using multiphoton microscopy," *Biophys. J.*, vol. 92, no. 6, pp. 2212–2222, 2007, doi: 10.1529/biophysj.106.097998.

[162] S. Laternser, H. Keller, O. Leupin, M. Rausch, U. Graf-Hausner, and M. Rimann, "A Novel Microplate 3D Bioprinting Platform for the Engineering of Muscle and Tendon Tissues," *SLAS Technol.*, 2018, doi: 10.1177/2472630318776594.

[163] D. B. Kolesky, R. L. Truby, A. S. Gladman, T. A. Busbee, K. A. Homan, and J. A. Lewis, "3D bioprinting of vascularized, heterogeneous cell-laden tissue constructs," *Adv. Mater.*, vol. 26, no. 19, pp. 3124–3130, 2014, doi: 10.1002/adma.201305506.

[164] B. Kysela, J. Skocilas, R. Zitny, J. Stancl, M. Houska, and A. Landfeld, "Simulation of collagen solution flow in rectangular capillary," *EPJ Web Conf.*, vol. 143, pp. 1–4, 2017, doi: 10.1051/epjconf/201714302063.

[165] S. Breslin and L. O'Driscoll, "Three-dimensional cell culture: The missing link in

drug discovery," *Drug Discov. Today*, vol. 18, no. 5–6, pp. 240–249, 2013, doi: 10.1016/j.drudis.2012.10.003.

[166] R. Kostadinova *et al.*, "A long-term three dimensional liver co-culture system for improved prediction of clinically relevant drug-induced hepatotoxicity," *Toxicol. Appl. Pharmacol.*, vol. 268, no. 1, pp. 1–16, 2013, doi: 10.1016/j.taap.2013.01.012.

[167] D. Yoon No, K. H. Lee, J. Lee, and S. H. Lee, "3D liver models on a microplatform: well-defined culture, engineering of liver tissue and liver-on-a-chip," *Lab Chip*, vol. 15, no. 19, pp. 3822–3837, 2015, doi: 10.1039/c5lc00611b.

[168] K. Ling *et al.*, "Bioprinting-Based High-Throughput Fabrication of Three-Dimensional MCF-7 Human Breast Cancer Cellular Spheroids," *Engineering*, vol. 1, no. 2, pp. 269–274, 2015, doi: 10.15302/J-ENG-2015062.

[169] Y. Zhao *et al.*, "Three-dimensional printing of Hela cells for cervical tumor model in vitro," *Biofabrication*, vol. 6, no. 3, 2014, doi: 10.1088/1758-5082/6/3/035001.

[171] European Medicines Agency, "Guideline on development , production , characterisation and specification for monoclonal antibodies and related products Guideline on development , production , characterisation and specification for monoclonal antibodies and related products Table of co," *EMA Sci. Guidel.*, vol. 44, no. July, 2016, doi: EMEA/CHMP/BWP/157653/2007.

[172] Food and Drug Authority, "Points to Consider in the Manufacture and Testing of Monoclonal Antibody Products for Human Use," 1997.

[173] M. Yim and D. Shaw, "Achieving greater efficiency and higher confidence in single-cell cloning by combining cell printing and plate imaging technologies," *Biotechnol. Prog.*, vol. 34, no. 6, pp. 1454–1459, 2018, doi: 10.1002/btpr.2698.

[174] M. Alomari, F. H. Mohamed, A. W. Basit, and S. Gaisford, "Personalised dosing: Printing a dose of one's own medicine," *Int. J. Pharm.*, vol. 494, no. 2, pp. 568–577, 2015, doi: 10.1016/j.ijpharm.2014.12.006.

[175] S. H. Lim, H. Kathuria, J. J. Y. Tan, and L. Kang, "3D printed drug delivery and testing systems — a passing fad or the future?," *Adv. Drug Deliv. Rev.*, vol. 132,

pp. 139–168, 2018, doi: 10.1016/j.addr.2018.05.006.

[176] S. J. Trenfield, A. Awad, A. Goyanes, S. Gaisford, and A. W. Basit, "3D Printing Pharmaceuticals: Drug Development to Frontline Care," *Trends Pharmacol. Sci.*, vol. 39, no. 5, pp. 440–451, 2018, doi: 10.1016/j.tips.2018.02.006.

[177] M. Rautamo, K. Kvarnström, M. Sivén, M. Airaksinen, P. Lahdenne, and N. Sandler, "Benefits and prerequisites associated with the adoption of oral 3D-printed medicines for pediatric patients: A focus group study among healthcare professionals," *Pharmaceutics*, vol. 12, no. 3, pp. 1–11, 2020, doi: 10.3390/pharmaceutics12030229.

[178] A. Goyanes, M. Scarpa, M. Kamlow, S. Gaisford, A. W. Basit, and M. Orlu, "Patient acceptability of 3D printed medicines," *Int. J. Pharm.*, vol. 530, no. 1–2, pp. 71–78, 2017, doi: 10.1016/j.ijpharm.2017.07.064.

[180] C. L. Nemeth, W. R. Lykins, H. Tran, M. E. H. ElSayed, and T. A. Desai, "Bottom-Up Fabrication of Multilayer Enteric Devices for the Oral Delivery of Peptides," *Pharm. Res.*, vol. 36, no. 6, 2019, doi: 10.1007/s11095-019-2618-3.

[181] T. Croitoru-Sadger, B. Mizrahi, S. Yogev, and A. Shabtay-Orbach, "Two-component cross-linkable gels for fabrication of solid oral dosage forms," *J. Control. Release*, vol. 303, no. April, pp. 274–280, 2019, doi: 10.1016/j.jconrel.2019.04.021.

[182] S. Ross, N. Scoutaris, D. Lamprou, D. Mallinson, and D. Douroumis, "Inkjet printing of insulin microneedles for transdermal delivery," *Drug Deliv. Transl. Res.*, vol. 5, no. 4, pp. 451–461, 2015, doi: 10.1007/s13346-015-0251-1.

[183] A. B. M. Buanz, C. C. Belaunde, N. Soutari, C. Tuleu, M. O. Gul, and S. Gaisford, "Ink-jet printing versus solvent casting to prepare oral films: Effect on mechanical properties and physical stability," *Int. J. Pharm.*, vol. 494, no. 2, pp. 611–618, 2015, doi: 10.1016/j.ijpharm.2014.12.032.

Webpages

[15] “Global Personalized Medicine Market 2017-2018 & 2024: Market is Projected to Reach US$194.4 Billion by 2024 from an Estimated US$92.4 Billion in 2017.” https://www.prnewswire.com/news-releases/global-personalized-medicine-market-2017-2018--2024-market-is-projected-to-reach-us194-4-billion-by-2024-from-an-estimated-us92-4-billion-in-2017--300730848.html (accessed Mar. 01, 2020).

[16] “Web of Science [v.5.34] - Core Collection Basic Search.” https://www.webofscience.com/wos/woscc/basic-search (accessed Mar. 05, 2020).

[18] S. Pira, “Future of Inkjet Printing.” https://www8.hp.com/h20195/v2/GetPDF.aspx/4AA7-4499EEE.pdf (accessed Mar. 13, 2020).

[31] M. T. Inc., “Low Temperature Dispensing Devices MJ-A Product Description.” Accessed: Jan. 04, 2020. [Online]. Available: www.microfab.com.

[33] “PDS00009 Rev. 07, SE-128 AA.” Accessed: Dec. 22, 2019. [Online]. Available: https://www.fujifilmusa.com/shared/bin/PDS00009.pdf.

[34] “Nova PH 256/80 AAA.” Accessed: Mar. 09, 2020. [Online]. Available: www.dimatix.com.

[61] E. M. M. Harold F. Giles Jr, John R. Wagner, Jr., “Extrusion: The Definitive Processing Guide and Handbook - - Google Books,” 2013. https://books.google.co.uk/books?id=noW5lmeBePMC&pg=PA128&source=gbs_selected_pages&cad=3#v=onepage&q&f=false (accessed Mar. 24, 2020).

[95] T. Palm, E. Sahin, R. Gandhi, and K. Mehrnaz, “Temperature, Viscosity, and Concentration in Parenteral Drug DevelopmentBioProcess International,” *2015-110-03*, 2015. http://www.bioprocessintl.com/manufacturing/monoclonal-antibodies/importance-concentration-temperature-viscosity-relationship-development-biologics/ (accessed Nov. 05, 2017).

[114] “ASTM F2900 - 11 Standard Guide for Characterization of Hydrogels used in

Regenerative Medicine (Withdrawn 2020)."
https://www.astm.org/Standards/F2900.htm (accessed May 12, 2020).

[130] Microfab, "A Basic Ink-Jet Setup." http://www.microfab.com/a-basic-ink-jet-microdispensing-setup (accessed Oct. 21, 2017).

[133] "Determination of Secondary Structure in Proteins by FTIR Spectroscopy - JenaLib." http://jenalib.leibniz-fli.de/ImgLibDoc/ftir/IMAGE_FTIR.html (accessed Aug. 22, 2021).

[144] "The Xaar Midas Ink Supply System - A compact fluid supply system." https://www.xaar.com/en/products/systems-components/xaar-midas-ink-supply-system (accessed Oct. 24, 2017).

[170] European Medicines Agency, "ICH Topic Q 5 D Quality of Biotechnological Products: Derivation and Characterisation of Cell Substrates Used for Production of Biotechnological/Biological Products," 1998. [Online]. Available: http://www.ema.europa.eu/ema/%5Cnhttp://www.ema.europa.eu/docs/es_ES/document_library/EPAR/.

[179] "ZipDose Technology | Spritam | Aprecia."
https://www.aprecia.com/technology/zipdose (accessed Aug. 03, 2020).

Appendix A Chapter 5 Additional Data

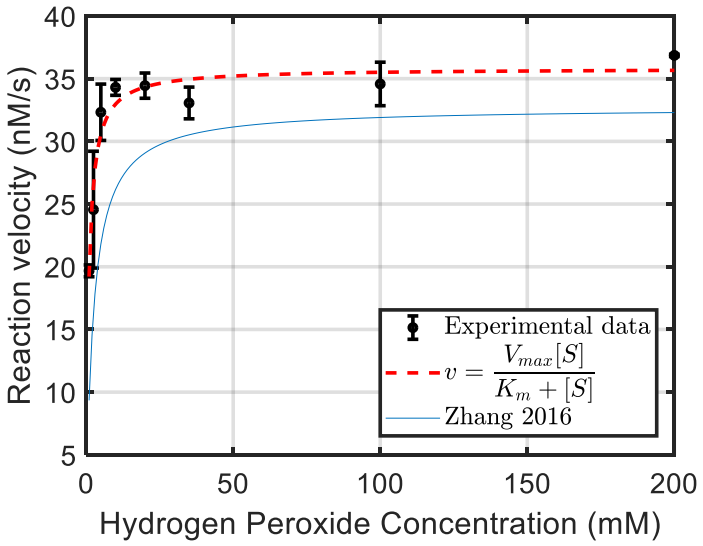

Figure A 1: The Michaelis Menten kinetics of 1nM HRP with 1mM ABTS and H_2O_2 in the concentration range from 0 – 200mM.

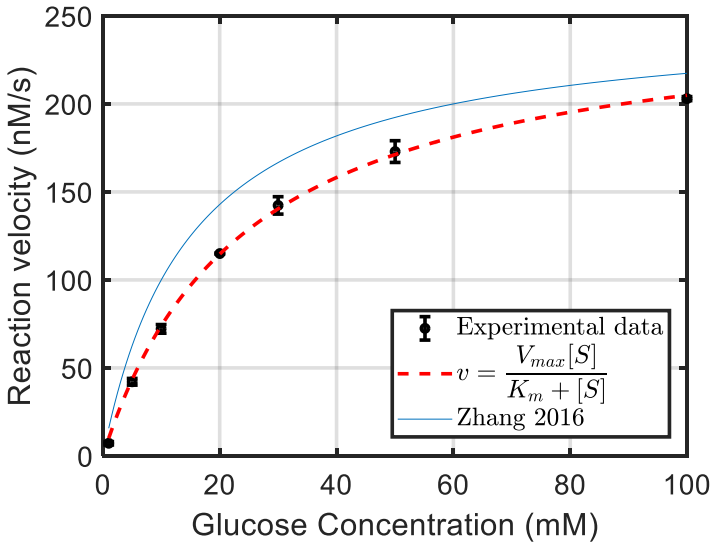

Figure A 2: The Michaelis Menten Kinetics for GOx. The V_{max} = 255nM/s and K_m = 24.5mM. The assay concentration contained 2mM ABTS, 50nM HRP, 1nM GOx and D-glucose in the concentration range of 0.1 – 100mM.

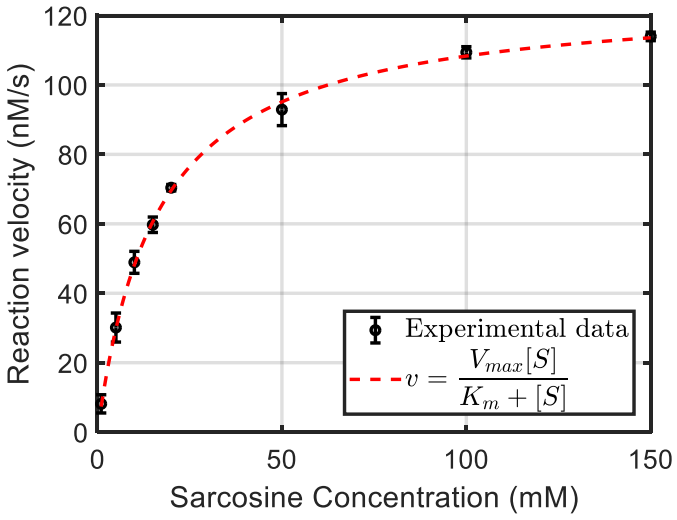

Figure A 3: The Michaelis Menten Kinetics for SOx. The V_{max} = 125.8nM/s and K_m = 16.1mM. The assay concentration contained 1mM ABTS, 1 – 150mM sarcosine, 50nM HRP and 10nM SOx.

Cuvettes, disposable, polystyrene

- Transparency: approximately 90% between 400nm and 800nm

Cat. No	Material	Dimensions, mm (w x h)	Capacity, µL	Pathlength, mm	Wavelength range, nm	Pack qty
11537692	PS	12.5 x 45	4,000	10	336 to 850	100
11547692	PS	12.5 x 45	1,600	10	336 to 850	100

Figure A 4: Specification of the cuvettes used in the contents of the thesis. The semi micro polystyrene cuvettes with 1600 µl capacity were purchased from Thermo fisher Scientific.

Appendix B Chapter 7 Additional Data

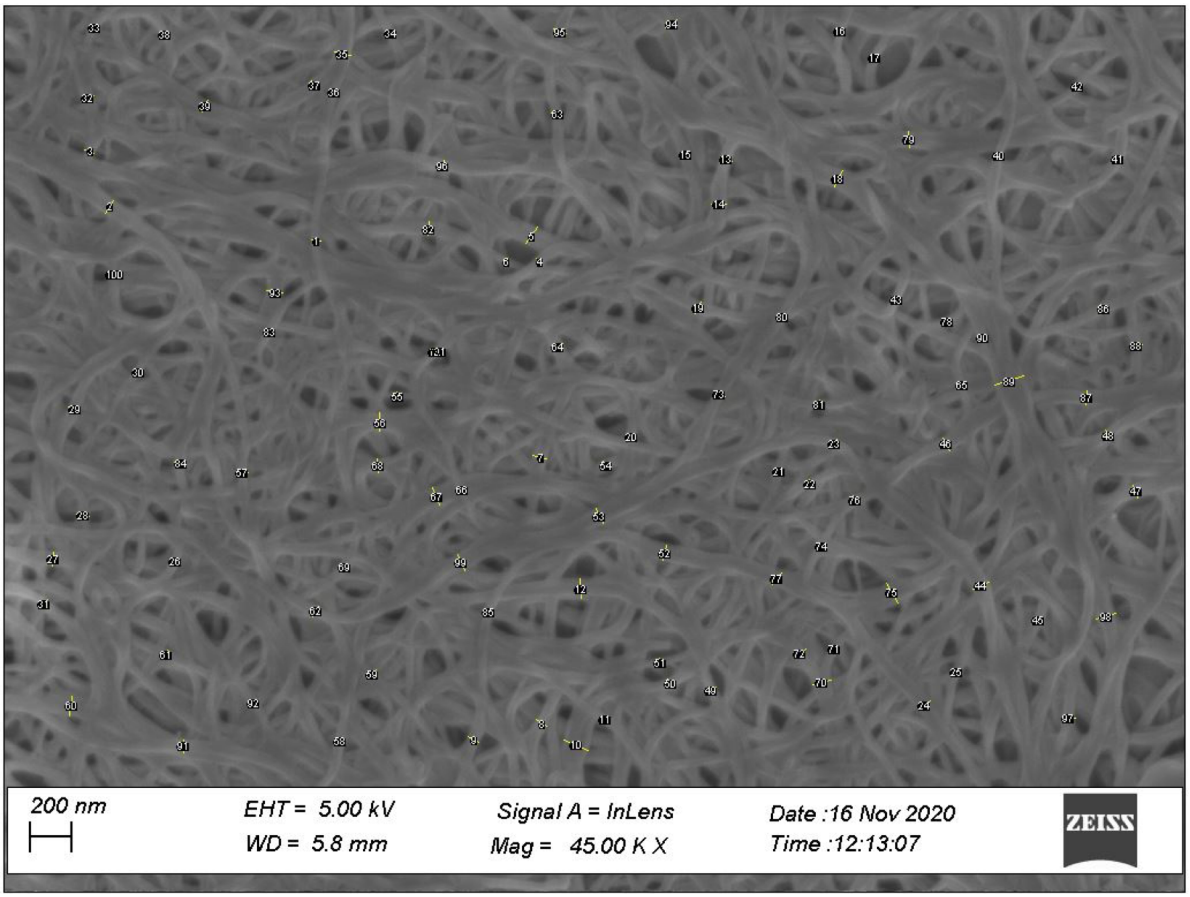

Figure A 5: SEM image with fibril width locations marked for the control, pipette mixed sample. ImageJ was used for manual measurements by calibrating with the scale bar and drawing a line of the same length as the fibre width.

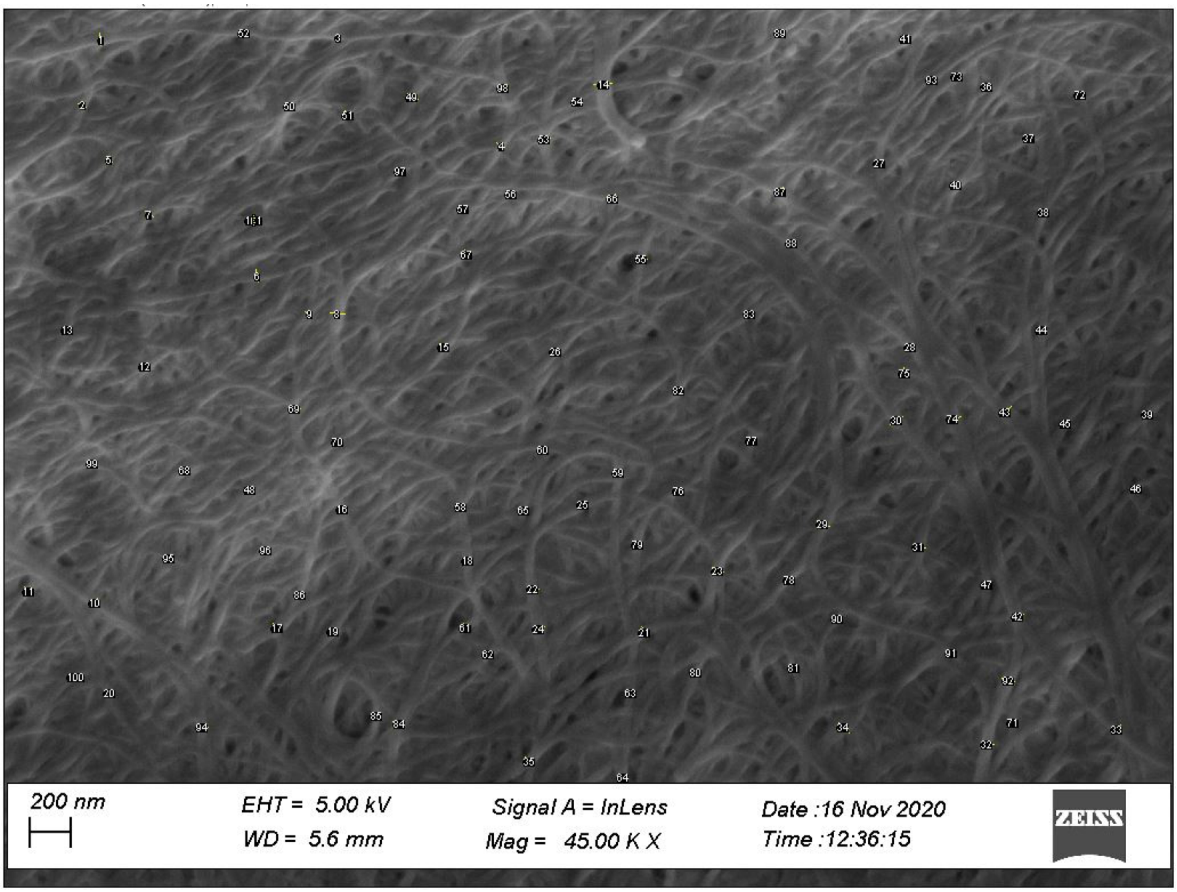

Figure A 6: SEM image with fibril width locations marked for the vortex mixed sample. ImageJ was used for manual measurements by calibrating with the scale bar and drawing a line of the same length as the fibre width.

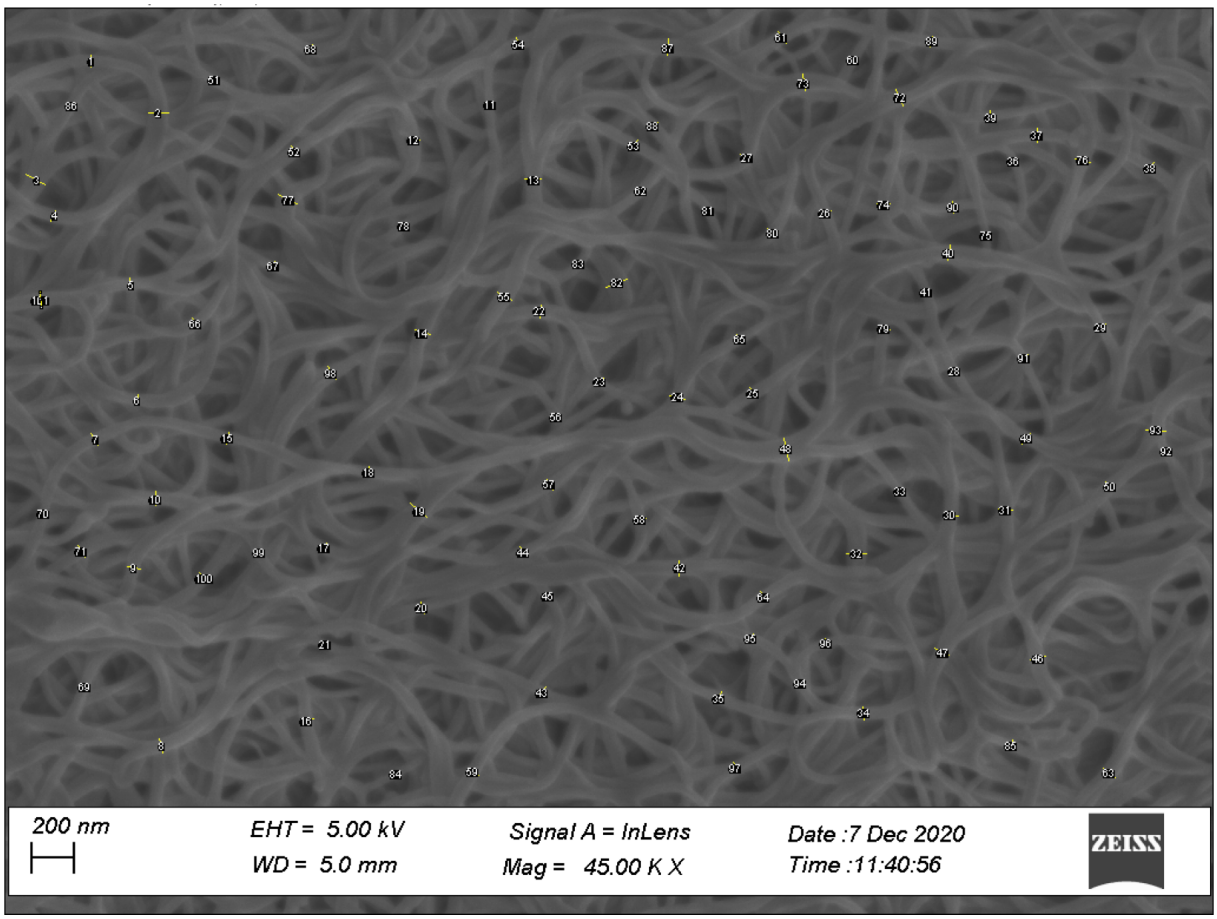

Figure A 7: SEM image with fibril width locations marked for the extrusion control sample. ImageJ was used for manual measurements by calibrating with the scale bar and drawing a line of the same length as the fibre width.

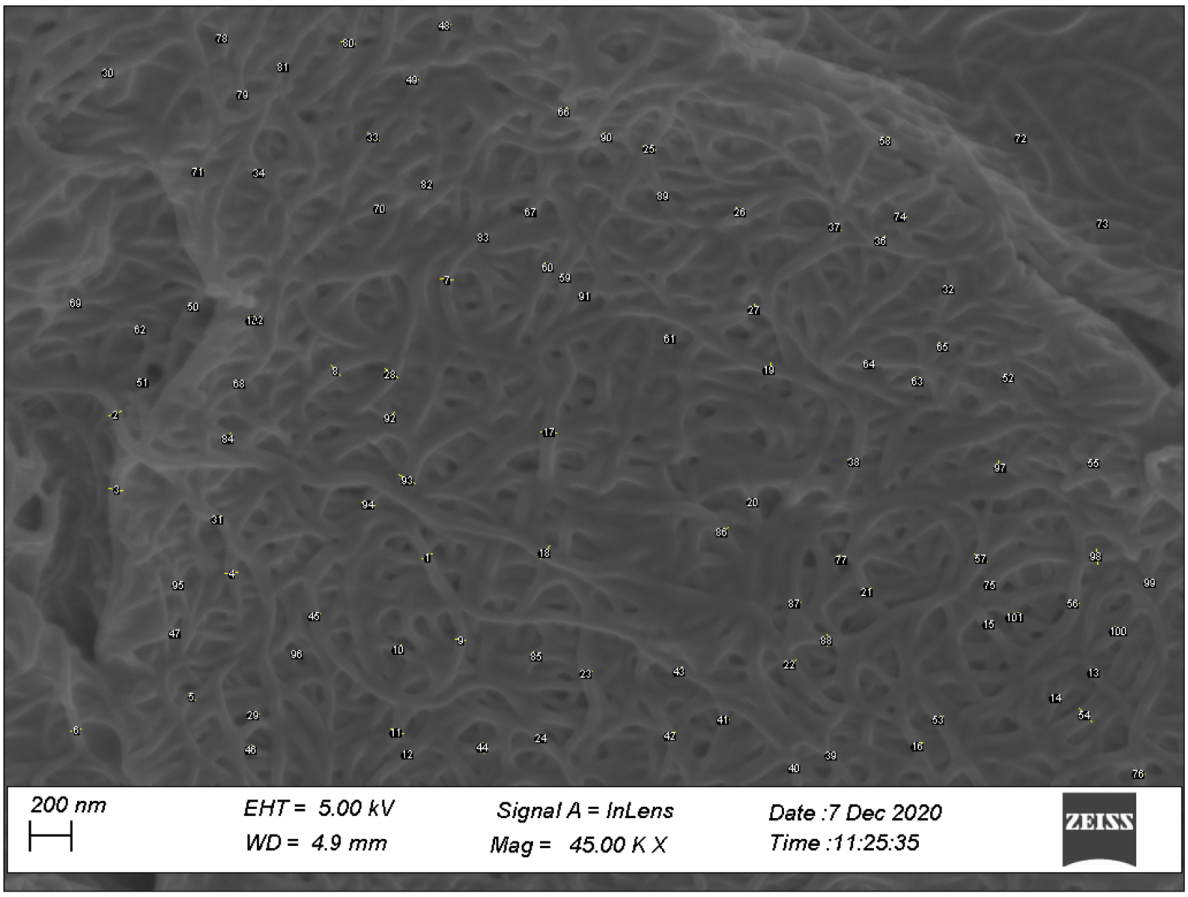

Figure A 8: SEM image with fibril width locations marked for the extruded sample. ImageJ was used for manual measurements by calibrating with the scale bar and drawing a line of the same length as the fibre width.

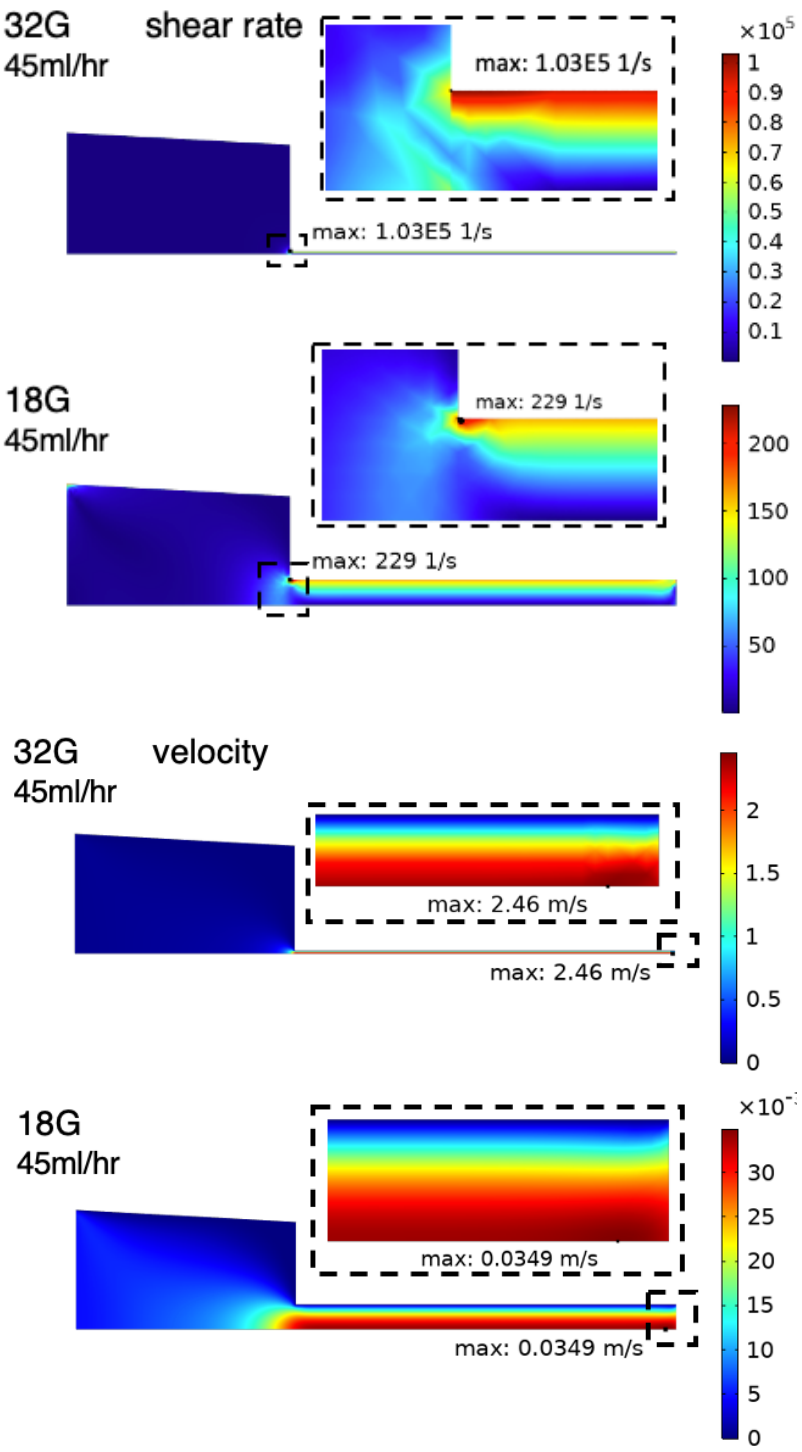

Figure A 9: COMSOL Multiphysics simulation heat maps for 45ml/hr flow rates.

Appendix C PhD Outputs

The following publications and conference presentations have been completed over the course of the PhD.

Publication:

S. E. Evans, M. C. Rodriguez Rivero, E. Rognin, T. Tuladhar, and R. Daly, "2D and 3D inkjet printing of biopharmaceuticals – A review of trends and future perspectives in research and manufacturing," *Int. J. Pharm.*, vol. 599, no. February, 2021, doi: 10.1016/j.ijpharm.2021.120443.

Conference Presentations:

Materials Research Society Fall Meeting and Exhibit, Boston, Massachusetts, Nov 26-Dec 1, 2017, Forces and Interfaces – Structural Damage to Biomolecules During Droplet Generation | S E Evans and R Daly

Institute of Physics PGS Group conference: Printing for the future 2020 15 – 16 July 2020, Forces and interfaces: structural damage to biomolecules during droplet generation